Towards optimized H2-evolving photocathodes by a molecular strategy

Emmanouil Giannoudis

THÈSE

Pour obtenir le grade de

DOCTEUR DE L'UNIVERSITE GRENOBLE ALPES

Spécialité : **Chimie Inorganique et Bio-Inorganique**

Arrêté ministériel : 25 mai 2016

Présentée par

Emmanouil GIANNOUDIS

Thèse dirigée par **Murielle CHAVAROT-KERLIDOU, CR1, CNRS**

préparée au sein du **Laboratoire de Chimie et Biologie des Métaux** dans **l'École Doctorale de Chimie et Science du Vivant**

Construction de photocathodes de production d'hydrogène optimisées par une approche moléculaire

Présentée et soutenue publiquement le **27 Novembre 2020**, devant le jury composé de :

Mme Frédérique LOISEAU
Professeure, Université Grenoble Alpes, Présidente
Mme Céline OLIVIER
Chargée de Recherche, Université de Bordeaux, Rapporteuse
Mr. Benjamin ELIAS
Professeur, Université Catholique de Louvain, Rapporteur
Mr. Ally AUKAULOO
Professeur, Université Paris-Saclay, Examinateur
Mme Murielle CHAVAROT-KERLIDOU
Chargée de Recherche, Université Grenoble Alpes, Directrice de thèse

I dedicate this thesis to the persons that offer me constant support and unconditional love.

Acknowledgments

The list of people who deserve my thanks for allowing me to carry out this thesis is long and I am afraid and sorry that I may forget some of them. This PhD thesis is the output of the effort and support of numerous persons. Writing this part was by far the most emotional, as I clearly understood that an extraordinary adventure of 3.5 years in the SolHyCat team of the Laboratory of Chemistry and Biology of Metals at CEA Grenoble comes to an end.

I would first like to thank all the members of the jury for having accepted to assess this work: Pr. Frédérique Loiseau the president of this jury, Dr. Céline Olivier and Pr. Benjamin Elias for accepting the roles of reporters and Pr. Ally Aukauloo as an examiner. I am grateful to them for the corrections on this manuscript, the comments and the discussion we had during my presentation. I would also like to thank Dr. Renaud Demadrille and Dr. Marcelo Gennari as members of my thesis monitoring committee for the interesting discussion we had and their advice. My journey in science began in 2015 in the laboratory of Bioinorganic Chemistry of Chemistry Department at the University of Crete under the supervision of Professor Athanassios G. Coutsolelos. He gave me the opportunity to discover science and to interact with amazing people.

I would like to express my sincere gratitude to Dr. D. Aldakov for the XPS analysis, C. Saint-Pierre and Dr. D. Gasparutto for the MALDI-ToF measurements, Dr. J. P*é*caut for the ESI-MS, Pr. D. Leonard for the ToF-SIMS analysis, C. Müller and Pr. B. Dietzek for the photophysical studies in solution.

The greatest thanks of all is undoubtedly for my supervisor, Dr. Murielle Chavarot-Kerlidou for giving me the chance to come and conduct my thesis at LCBM, after having mentored me for the first time during my master for 3 months. These 3.5 years that we worked together were the most productive I ever had. I understood how to organize myself in a more professional way. Your availability whenever I had any problem was remarkable. The time that you spent with me to prepare reports, abstracts, presentations and this manuscript showed your dedication to help younger people to evolve, to become better and to believe in themselves. Your thoroughness and your passion for beautiful science were all motivations to constantly improve myself. Despite the difficulties that you faced with me, I believe that we accomplished something that I can be proud of it for my whole life. Your constant smile and your impact on my life will remain indelible. I cannot find enough words to express my feelings. Thank you for everything and it was a great honor for me to work with you!

Many thanks to Dr. Vincent Artero, for welcoming me in his group and for his help and support. Your passion for science and your availability to handle all the problems in the lab are unique. I would like to acknowledge Dr. Stéphane Ménage, director of the Laboratory for Chemistry and Biology of Metals. Your accessibility and your commitment are undoubtedly one of the keys to the success and the nice atmosphere that reigns the laboratory.

I could not forget the members of the SolHyCat group. I had the opportunity to work with amazing scientists but above all magnificent personalities. The multicultural nature of the group improved me us a human being. Our daily exchange on many different topics was pleasant and unforgettable. They made me feel like home with their company and backing from the first moment I arrived in Grenoble. Sebastian, I feel blessed to meet you during this adventure. We worked together, I learned so many things next to you but most importantly, I found a good friend for the rest of my life. Bertrand, your help, support and our endless discussions will remain in my heart. I know that I found a person to trust. Matthieu, you are without any doubt a person that I will never forget and I am sure we will keep in touch. Such a passionate scientist, always available to help even though you are packed with responsibilities. Just an honor to work with you and meet you as your personality is unique and inspirational for me. Jennifer and Adina, you are two amazing persons that helped a lot from the first day that I arrived in the lab. Thank you from the bottom of my heart. Kun, Duc, Christina, Tania, Jonathan, Afridi, Nabil, Mariam, Youssef, Anthonin, Tim, Nick, Debu, Soundar, Nathan and all the other members of the LCBM, you were always next to me and I am really grateful to work with you.

Apart from the scientific field, many people were on my side during these years. I would like to thank my family starting with my parents (Kyriakos and Katerina) for their love, encouragement, and support. It is a great feeling to know that your family will be there for you regardless the difficulties. Of course, my beloved young brother (Markos). One of the most intelligent persons I have ever met. You are not just my brother, but a great friend. My friends from Greece and especially Nikos, Vivi and Christophoros. We went through a lot together from the first time that we met and started our unique relationship. But also Angeliki, Petros, Miltos, Spiros, Despina, Andreas, Nikos, Giota, Manos, Asterios, Vasilis for all the nice moments. Last but not least, the person that I spent 3 years together. Your eternal motivation, love and encouragement inspire me until today. Without you I could not complete this thesis. Thank you for being yourself and making my life happier.

Merci beaucoup à tous !!!! A bientôt !!!!

Table of contents

ABBREVIATIONS

PS I/II: Photosystem I/II
DSPEC: Dye-Sensitized Photo-Electrochemical Cell
n-DSSC: n-type Dye-Sensitized Solar Cell
p-DSSC: p-type Dye-Sensitized Solar Cell
VB: Valence Band
PS: Photosensitizer
bpy: 2,2'-bipyridine
HER: Hydrogen-Evolving Reaction
OER: Oxygen-Evolving Reaction
ITO: Indium-Tin Oxide
FTO: Fluorine-doped Tin Oxide
HOMO: Highest Occupied Molecular Orbital
LUMO: Lowest Unoccupied Molecular Orbital
CV: Cyclic Voltammetry
IEA: Irreversible Electron acceptor
LSV: Linear Sweep Voltammetry
E.A.: Elemental Analysis
ESI-MS: Electron-Spray Ionization Mass Spectrometry
HRMS: High-Resolution Mass Spectrometry
NMR: Nuclear Magnetic Resonance
ppm: parts per million
NHE: Normal Hydrogen Electrode
RHE: Reversible Hydrogen Electrode
ALD: Atomic Layer Deposition
DFT: Density Functional Theory
CuAAC: Copper-catalyzed Azide-Alkyne Cycloaddition
GC: Gaz Chromatography
MLCT: metal-to-ligand charge transfer
MWCNT: Multi-Walled Carbon NanoTube
PCET: Proton-Coupled Electron Transfer
R.T.: Room Temperature
SC: SemiConductor
SED: Sacrificial Electron Donor
SEM: Scanning Electron Microscopy
XPS: X-ray Photoelectron Spectroscopy
MALDI-ToF: Matrix-Assisted Laser Desorption/Ionization Time-of-Flight mass spectrometry
MES: 2-(N-morpholino)ethanesulfonic acid
DCM: dichloromethane
TEOA: Triethanolamine
TEA: Triethylamine
TFA: Trifluoroacetic acid
DMF: N,N-dimethylformamide
DMSO: Dimethylsulfoxyde
TBA: Tetrabutylammonium
TCO: Transparent Conducting Oxide

TMSBr: trimethylsilyl bromide
ToF-SIMS: Time-of-Flight Secondary Ionization Mass Spectroscopy
TON: turnover number
F.E.: Faradaic Efficiency
UV-Vis: UltraViolet Visible
IC: Ion chromatography
TAS: Transient Absorption Spectroscopy
TA-SEC: Transient Absorption-Spectroeletrochemistry

General Introduction

Energy is the most important tool of modern communities in order to facilitate their daily life with an annual global energy consumption of around 18 TW, which is predicted to reach 43 TW in 2100.[1] Modern energy economy is reliant on fossil fuels that cause serious environmental problems (climate change, melting of polar ice caps, air pollution, lower biodiversity) due to their combustion that produces carbon dioxide. This fact along with the depletion of fossil fuels because of their continuous use has forced the scientific community to find alternatives based on renewable and abundant energy sources, like solar, geothermal, wind power etc. (**Figure 1**).[2]

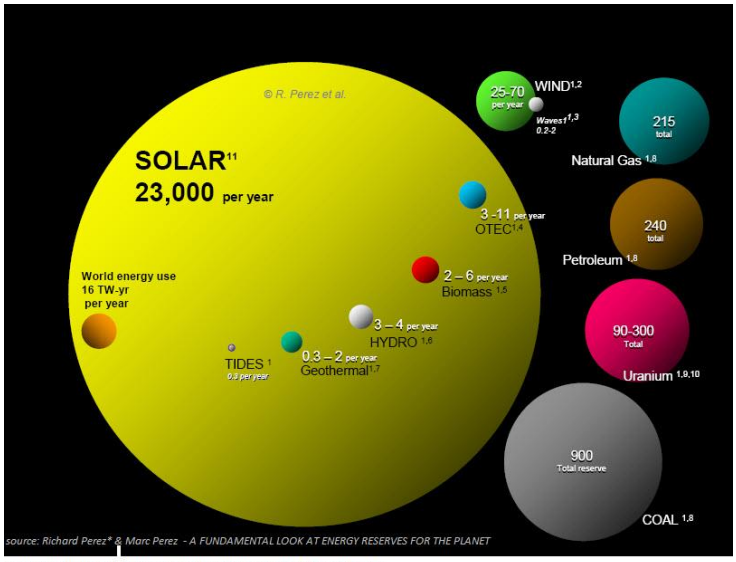

Comparing finite and renewale planetary energy reserves)Terawatt-years).
Total recoverable reserves are shown for the finate resources.

Figure 1. Total energy reserves (renewable energy sources and fossil fuels) taken from reference **2**.

Solar energy is extremely advantageous, as the most abundant energy source. The sun delivers on earth in about one hour, the same amount of energy we are currently using in one year. Unfortunately, solar energy is intermittent and diffuse. Thus, there is an urgent need to find a way to store and convert this inexhaustible source of energy. Photovoltaics is a mature existing technology to capture sunlight and convert it into electricity.

Electricity can fulfill immediate energy needs. However, it cannot be stored. To achieve long-term storage of solar energy, different approaches have been proposed. Converting it into a chemical form, like a fuel, seems a promising way and it is crucially needed due to the current technological infrastructure. Fuels that can be produced directly or indirectly by solar energy

through photo-, thermo- or electrochemical reactions are called solar fuels. Using solar energy for their production is a big challenge and scientists find inspiration from the most common natural process, photosynthesis.

In nature, there are many photosynthetic organisms, like algae, cyanobacteria and plants, called photoautotrophs, which are able to synthesize biomass directly from carbon dioxide and water using the energy from sunlight. They use the photogenerated electrons to reduce carbon dioxide and produce carbohydrates via the Calvin cycle, which are the energy reserves of the cell. Furthermore, some cyanobacteria and microalgae are capable of reducing protons to hydrogen, using enzymes called hydrogenases.[3] All these transformations are realized thanks to an amazing biologic machinery, presented schematically in **Figure 2**, consisting of two large protein complexes, the photosystem I (PS I) and the photosystem II (PS II), assisted by various redox cofactors and enzymes.

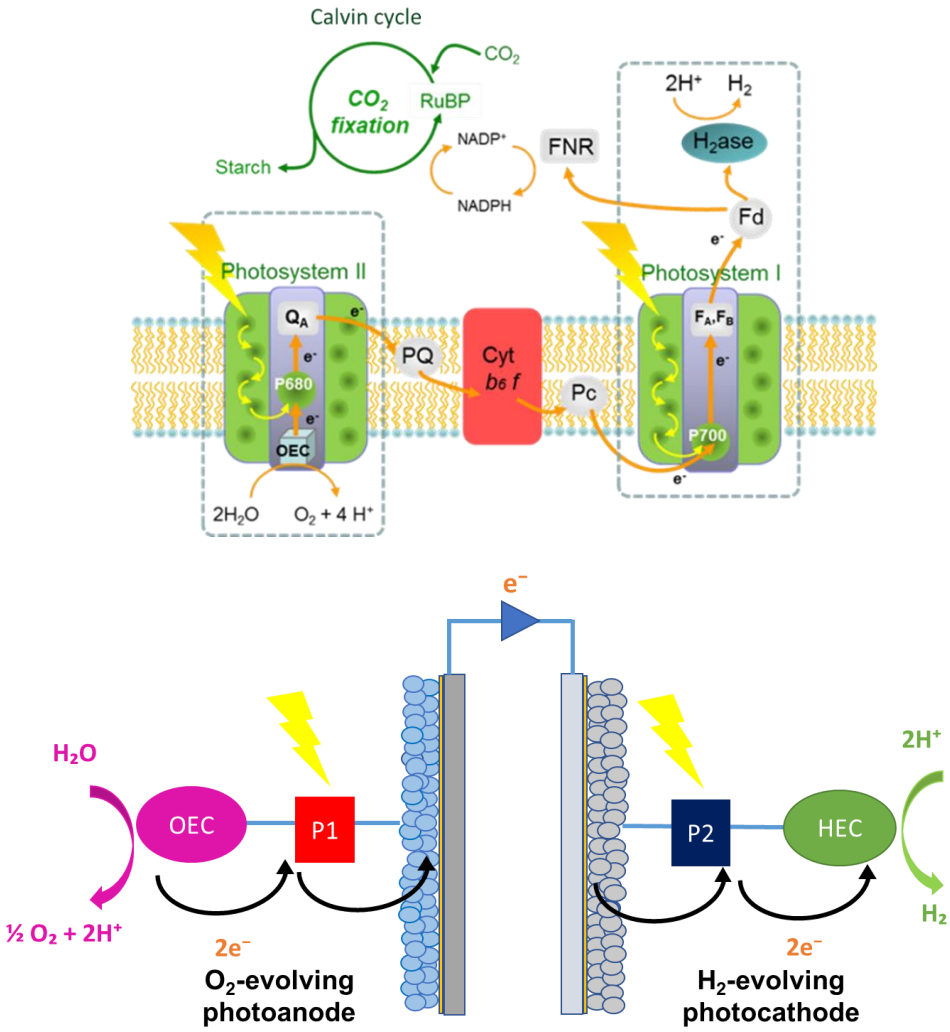

Figure 2. Schematic representation of the natural photosynthetic process (top)[4] and water splitting photoelectrochemical cell, DSPEC (bottom). Cubes correspond to light harvesters (P1, P2) and spheres to oxygen or hydrogen-evolving catalysts (OEC, HEC) accordingly.

The scientific community tries to mimic the basic mechanism of photosynthesis (artificial photosynthesis)[4,5] that consists of three elementary steps:

- initial light-harvesting thanks to molecular photosensitizers located at PSII and PSI
- proton-coupled electron transfers between redox cofactors to accomplish long-lived charge separation
- multielectronic redox catalysis involving specific enzymes and cofactors (OEC at PSII, RuBP, hydrogenases, etc)

Taking photosynthesis as a model, three main approaches exist to produce solar fuels: homogeneous photocatalytic systems using colloids, photovoltaics coupled with electrolysis and photoelectrochemical cells.[6] These systems present different degrees of technological maturity and manufacturing cost. A dye-sensitized-photoelectrochemical cell (DSPEC, **Figure 2**), that combines a photoanode in analogy to PSII, where water oxidation takes places to supply with electrons and protons the photocathode (similar to PSI), where proton (or carbon dioxide) reduction occurs, has gained an increased attention by molecular chemists. A first proof of concept was made in 1972, comprising a TiO_2 photoanode and Pt as counter electrode.[7] Since then, many efforts by different research groups have been devoted for the preparation of functional dye-sensitized photoanodes and photocathodes separately.[8,9,10,11,12,13,14] Understanding the principles that govern the activity and optimizing the performance of each component will pave the way for the preparation of competent DSPEC.

Until today, the bottleneck in a full DSPEC device in terms of performances is the photocathode part. In this sense, during my thesis, I have focused on the construction of dye-sensitized photocathodes for hydrogen evolution. This work is a continuation of what has already been done in the "SolHyCat" group in the Laboratory of Chemistry and Biology of Metals. Based on the previous expertise of the lab, the main objectives of my PhD project were:

- To compare the efficiency of different light harvesters (P2) and catalytic units (HEC) for hydrogen-evolving photocathodes
- To address the stability of the molecular-based photocathodes by performing post-operando analysis

In the first chapter, we will introduce the principles of dye-sensitized photocathodes for hydrogen production. Then, the contribution of the group to this field will be highlighted. We will show a cobalt catalyst that was used for the first covalent and noble metal-free dye-catalyst

assembly and model photocathodes based on ruthenium complexes. Next, the already reported examples of functional photocathodes will be analyzed, including the work from the group. Finally, figures of merit will be presented for all the different systems, as well as current limitations.

In the second chapter, the synthesis and characterization of a new dye-catalyst assembly consisting of a ruthenium photosensitizer functionalized with methyl phosphonate groups and a cobalt diimine-dioxime catalyst will be demonstrated.

The third chapter is dedicated to the assessment of the photoelectrochemical activity for hydrogen evolution of a NiO photocathode in aqueous media sensitized by the first dyad. Post-operando characterization to investigate the destiny of our molecular components will be carried out.

The fourth chapter will be concentrated on the preparation of a second dye-catalyst assembly with the same photosensitizer and a different cobalt tetraazomacrocyclic complex as a catalyst.

In the last chapter, the second dyad will be examined for proton reduction under the same experimental conditions with the first photocathode for direct comparison. In addition, preliminary attempts to use our novel dye-catalyst assembly for PEC carbon dioxide reduction will be presented.

Chapter I

Hydrogen and dye-sensitized photocathodes for light-driven H_2 production

Hydrogen is a chemical element with just one proton and one electron and its name arises from the Greek words hydro for "water" and gene for "forming". It is the most abundant chemical substance in the universe and the element can be found in the stars and powers the universe through the proton-proton chain reaction and carbon-nitrogen cycle. Hydrogen also plays an important role in acid–base reactions, because most of them involve the exchange of protons between soluble molecules. Furthermore, it is essential for life, and present in nearly all molecules in living organisms. Preferably it is bonded to other elements, such as to oxygen to form the most important good of life, water (H_2O).

Dihydrogen (named hydrogen in the following of this thesis), the simplest chemical compound, at standard temperature and pressure is generally nontoxic, colorless, tasteless and odorless gas. However, H_2 is not available on earth under the form of H_2. Nowadays hydrogen is almost exclusively used for industrial purposes in chemicals (ammonia, methanol) and refining. Glassmaking, production of plastics and printed circuit boards, hydrogenation of vegetables, animal oils and fats, metallurgy and weather balloons are some additional fields where hydrogen finds applications.

Hydrogen is a typical energy vector with a high energy density (120 $MJ.kg^{-1}$). 1 kg of hydrogen generates three times more energy than 1 kg of gasoline (energy density of 44.4 $MJ.kg^{-1}$). Furthermore, it is carbon-free, as its oxidation in a fuel cell, an already mature technology, produces electricity and only water as a by-product. However, the most important drawback is that its production is based mainly on fossil fuels. The most common raw materials of hydrogen are natural gas, hydrocarbon, coal and in lower scale electrolysis and biomass. Until today, the most dominant procedure for H_2 production is steam reforming from hydrocarbons, but the byproducts (CO, CO_2 and other greenhouse gases) makes this process controversial. The scientific community tries to find environmentally friendly procedures for its production, like biomass and photoelectrolysis of water (**Eqn. I.1**) to store solar energy in a chemical form. The latter approach is the one our group is keen on and has invested scientific effort for years.

$$H_2O \rightleftharpoons H_2 + \frac{1}{2} O_2 \qquad \Delta G = 237.2\ kJ{\cdot}mol^{-1}\ (298.15\ K,\ 1\ bar) \qquad \textbf{Eqn. I.1}$$

Splitting of water evolves hydrogen and oxygen and can be separated into two half reactions: water oxidation (**Eqn. I.2**) and proton reduction (**Eqn. I.3**). Throughout this work we will focus on the reductive half reaction (**Eqn.I.3**).

$$H_2O \rightleftharpoons \frac{1}{2} O_2 + 2\,H^+ + 2\,e^- \qquad E^0 = 1.23\ V\ vs\ RHE \qquad \textbf{Eqn. I.2}$$

$$2\,H^+ + 2\,e^- \rightleftharpoons H_2 \qquad E^0 = 0\ V\ vs\ RHE \qquad \textbf{Eqn. I.3}$$

Hydrogen evolution (**Eqn. I.3**) is a simple reaction, but as most of multielectronic processes, catalysts are crucial for speeding it up. Platinum and platinoids are the most widely used hydrogen-evolving catalysts (HEC). However, they are expensive and scarce (37 ppb in the Earth's crust),[15] preventing the development of functional devices in a large and sustainable scale. As an alternative, bioinspired molecular catalysts have been developed based on the active site of hydrogenases,[3] which is a binuclear complex with two iron or a combination of nickel and iron atoms. Inspired by these enzymes, molecular chemists use first row transition metals, like Fe, Co, Ni for the preparation of noble metal-free HEC.[16,17]

Homogeneous photocatalytic systems for the reductive[18,19,20] part of water splitting emerged over the last 20 years. The three most important components of a photocatalytic system for hydrogen evolution are:

1. A photosensitizer to absorb visible light
2. A catalyst to reduce protons and generate hydrogen (HEC)
3. A sacrificial electron donor to supply electrons and regenerate the chromophore

Photocatalytic systems based either on multicomponent or dye-catalyst assemblies have been developed. Supramolecular bimetallic structures, where intramolecular electron transfer and spatial charge separation can take place, seem particularly attractive. Ruthenium based-dyes coupled with noble metal catalysts (platinum, palladium) produced hydrogen in homogeneous systems.[21,22] Our group prepared supramolecular dyads with noble metal-free catalysts (cobalt complexes)[23,24] and hydrogen was evolved under light irradiation.

Today, the challenge is to integrate these molecular components into a functional device. The pioneering work from O'Regan and Grätzel on n-type dye-sensitized solar cells paved the way for intensive research of how to heterogenize light harvesters (ruthenium complexes) onto electrodes for light-driven processes.[25]

I. Design and working principle of a dye-sensitized photocathode

1) Inspiration from DSSCs and basic principles

The technological development made in the field of DSSCs can act as a base to construct devices for conversion of solar energy in different chemical forms, like hydrogen. The preparation of efficient devices, called dye-sensitized photoelectrochemical cells (DSPECs, **Figure 2**), where light-driven water-splitting can take place is far from reality. This field is still not as mature as DSSCs, even though decomposition of water with light-responsive electrodes was described for the first time in 1960s.[26] Here, we will focus on the photocathode side of a tandem device.

The first p-type DSSC (based on NiO semiconductor) was reported in 1999[27] and its basic principles[28,29,30] are depicted in **Figure I.1** (left). Light absorption by the photosensitizer generates a reactive excited state (PS^{*}), which has more oxidizing power than its ground state, and accepts an electron from the valence band of the p-type semiconductor. A charge separated state is generated with an electron on the dye (PS^{-}) and a hole on the semiconductor. Then, two pathways are possible: Regeneration of the reduced dye by a redox mediator (RM), mostly iodide/triiodide in the solution (organic media) or by the semiconductor (recombination reaction). If electron transfer from the reduced dye to the redox mediator is thermodynamically feasible and kinetically faster than recombination, the reduced mediator (RM^{-}) is formed and then oxidized at the counter electrode, producing an electric current in the external circuit.

As far as the basic principles of the dye-sensitized hydrogen-evolving photocathode is concerned, upon light irradiation, we have the formation of the excited state of the dye (PS^{*}). An electron is transferred from the valence band of the semiconductor to form a charge separated state ($PS^{-}/SC(h^{+})$). The holes (h^{+}) diffuse through NiO to a back contact, which in most cases is a glass coated with fluorine doped tin oxide (FTO). Then, an electron transfer from the reduced dye (regeneration of the dye) to the catalyst occurs. These steps will be repeated twice in order to accumulate two electrons on the catalyst for the reduction of protons to hydrogen. In this case, two different recombination processes can take place (dashed arrows). One between the reduced dye and the semiconductor, like in DSSCs, and between the reduced catalyst and the semiconductor.

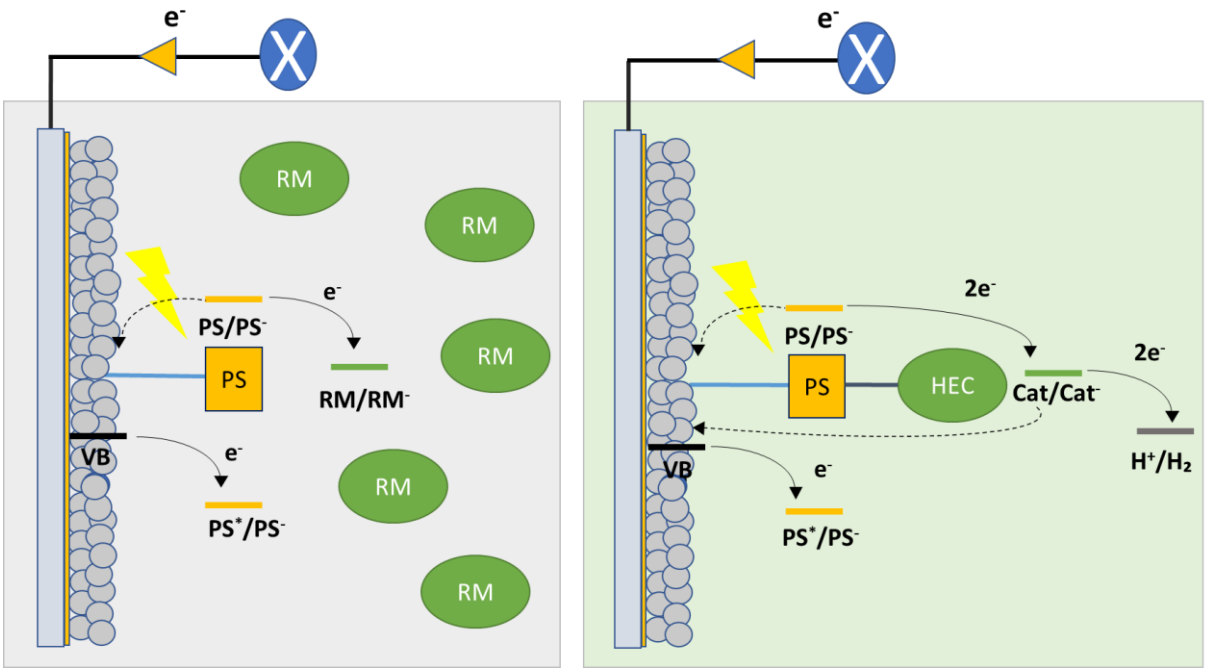

Figure I.1. Working principles of a p-type DSSC (left) and a dye-sensitized photocathode in a DS-PEC for H_2 production (right). Orange cubes correspond to light harvesters (PS) and green spheres either to redox mediators (RM) or to hydrogen-evolving catalysts (HEC).

Between DSSCs and p-type dye-sensitized photocathodes[9,10,11,12,13] (**Figure I.1**) a lot of similarities can be observed, but there are also major differences. From a kinetic point of view, in a p-type DSSC a single electron transfer process occurs to produce electricity compared to multielectronic redox catalysis for the dye-sensitized hydrogen-evolving photocathode. For the latter, aqueous medium as a proton source is needed instead of an organic electrolyte for DSSCs.

In the following section, the main components of p-type dye-sensitized hydrogen-evolving photocathodes with basic requirements will be presented.

2) NiO as semiconductor

The semiconductor is responsible for efficient charge separation. Hole diffusion away from the dye to the charge-collecting substrate (mostly fluorine tin-doped oxide), enables the catalysis to occur. An ideal semiconductor should exhibit:

- Transparency in the visible region, thus enabling the dye to perform its role by minimizing the competition for absorption.
- Photostability and stability under aqueous conditions, as water is the solvent of interest.

- Accessibility and strong chemisorption with different anchoring groups for an efficient and robust grafting with the molecular compounds.
- Mesoporosity to offer high surface area in order to increase the grafting density of the molecular components. More light harvesters mean more efficient absorption of the incident light.
- High conductivity and fast hole diffusion to reduce unwanted recombination reactions.
- A valence band with a potential able to reduce the excited dye (hole injection) in order to start the photoinduced processes.

Nickel oxide (NiO) is the most common used wide band-gap p-type semiconductor.[31] NiO is a low-cost and easy to process semiconductor with good transparency, as an indirect band gap of 3.6 eV implies that absorption in the visible region cannot occur.[32] Nickel vacancies (Ni^{2+}, Ni^{3+}) and intercalated oxygen are responsible for its p-type semiconductivity.[33,34] In addition, NiO is stable under mildly acidic aqueous conditions required for H_2 evolution. Its pH-dependent flat valence band has a value of + 0.4 V vs NHE in neutral aqueous solution,[32] which lies between the frontier orbitals of typical photosensitizers. Thus, hole injection from the HOMO orbital of excited dyes can occur.[35]

Different preparation methods exist[36] (sol-gel deposition,[37,38] electrodeposition,[39] hydrothermal synthesis[40]) and nanostructured NiO films with different characteristics (porosity, thickness, conductivity) have been developed onto transparent conductive oxide substrates, like FTO. Recently, a comparison of dye-sensitized NiO photocathodes prepared by various techniques was realized.[41] The same molecular dye and hydrogen-evolving catalyst were employed for a reliable correlation and some general trends were revealed. Thickness of around 1-2 μm and surface area of at least 40 $m^2\ g^{-1}$ were important for optimizing the performance of the photocathodes.

3) The anchoring groups

Immobilization of the components onto the surface is a crucial step for the activity. Metal oxides are the most widely used SC. Their functionalization is based on the reactivity of surface bound -OH groups with anchoring groups of the molecular components to form monolayers.[42,43] Chemical groups like carboxylic, phosphonic and cyanoacrylic acids are generally employed as anchoring groups, forming covalent inorganic ester linkages at the surface of the

semiconductor for a strong coupling. Pyridines, catechols, amines and silanes can also be used. Many parameters like pH, metal oxide, temperature, solvents affect the robustness of grafting.

Carboxylates are the most accustomed anchorages in photocathodes owing to their strong affinity to metal oxides, like NiO.[44] Different anchoring modes exist with monodentate or bidentate character due to the presence of two oxygen atoms.[45] Bidentate modes show higher stability owing to superior contact with the semiconductors. Hydrogen bonding interactions may be also present. In a comparative study, the highest grafting densities on TiO_2 were obtained with porphyrin dyes bearing carboxylates.[46]

Phosphonate is another extensively studied anchoring group, as a result of their high affinity to metal substrates.[47,48,49] The three oxygen atoms allow mono-, bi- and tridentate anchoring modes,[50] that may explain the superior anchorage stability compared to carboxylates in DSSCs.[28,46,51] Phosphonate groups were reported to offer more stable linkage under acidic aqueous conditions compared to carboxylate groups for ruthenium polypyridine complexes grafted onto TiO_2.[52] A very recent study by the groups of F. Odobel and L. Hammarström with an immobilized on NiO organic dye bearing different anchoring groups showed that the phosphonic acid was the strongest one of the series, leading to the highest dye loading.[53]

The anchoring group may influence the electronic properties of the components and the charge transfer kinetics after light irradiation. Hence, choosing the right anchoring group is an important and demanding procedure.

4) The photosensitizer

The main requirements of a photosensitizer are:

- High extinction coefficient and a broad light absorption, mainly in the visible region.
- Its highest molecular orbital (HOMO) should be more positive than the valence band of the semiconductor so that hole injection[35] can occur upon excitation.
- The reduction potential of the dye ought to have enough reducing power. This means to be more negative than the catalytic reduction potential of the catalyst.
- High photo- and electro-chemical stability under aqueous conditions.

The molecular structure of the dye is a field of extensive research. Following hole injection, the reduced state of the dye is generated. At this point, it is crucial the electron density to be transferred to the catalyst. The molecular architecture is a key for the efficiency of this electron transfer. The best-performing photosensitizers in DSSCs are donor-π-acceptor moieties.[54] The

HOMO is positioned close to the anchoring group and the semiconductor for more efficient hole injection and the LUMO away from it, slowing down charge recombination and favoring electron transfer to the redox mediator. These properties were also exploited in the context of H_2-evolving photocathodes.[9,10,11,12,13] Similar directionality of the electron transfer can be also found in ruthenium dyes.[55] Examples of push-pull organic dyes and ruthenium photosensitizers integrated in dye-sensitized H_2-evolving photocathodes will be presented later.

5) The catalyst

A catalyst for the reduction of protons to hydrogen is the final electron acceptor of the system. For catalysis to occur, its catalytic reduction potential must be less negative than the reduction potential of the dye. Stability under light irradiation, aqueous conditions and accumulation of two electrons (multielectronic processes for proton reduction) is decisive.

The development of new molecular catalysts based on non-noble metals (Fe, Co, Ni) is a crucial issue.[15] An advantage of using molecular catalysts is that their electronic properties can be modified by changing the ligands substituents. In that context, bio-inspired complexes have emerged based on the catalytic center of hydrogenases. In the field of dye-sensitized hydrogen-evolving photocathodes, cobalt and nickel complexes are the mostly used catalysts and more detailed analysis will follow.[9,10,11,12,13]

II. Contribution from the group in the field

Our group is highly involved in the field of bio-inspired chemistry and artificial photosynthesis for the production of solar fuels. Over the last years, cobalt complexes proved to be efficient noble metal-free catalysts for proton reduction.[16,18,56] In particular, a family of Co-based compounds called cobaloximes, with two glyoxime ligands (**Chart I.1**),[57] were reported in 1980s by Ziessel for hydrogen evolution under homogeneous conditions.[58] Increased research interest was revived after 2005 for electro- or photo-chemical hydrogen evolution and cobaloximes have been extensively used, including our group, due to their easy synthesis, high turnover numbers and relatively low overpotentials.[19,59,60,61,62,63] More robust catalysts, like cobalt diimine-dioxime (**Chart I.1**), have attracted our interest and in the corresponding section, an overview of the work on this catalyst will be presented.

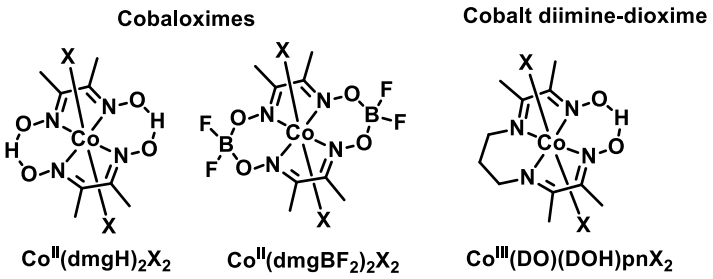

Chart I.1. Proton-bridged and difluoroboryl cobaloximes and cobalt dimine-dioxime complexes

1) The cobalt diimine-dioxime catalyst

One of the main limitations of cobaloximes is their low stability under acidic aqueous conditions.[64] Hydrolysis of the oxime bridge results in the displacement of the glyoxime ligands. This imperfection motivated our group to examine more robust cobalt catalysts for hydrogen evolution. Cobalt diimine-dioxime complexes (**Chart I.1**), promoted by Marzilli's group in late 1980s, with a single tetradentate ligand seemed a promising alternative.[65] Synthesis is based on Schiff base condensation of butanedione-monoxime on diamine compounds. Metalation can readily occur by reaction with a metal-salt and oxidation to the more stable Co(III) derivative with two axial halide ligands in an octahedral configuration.[66] The C_2 carbon of the propyl bridge can be functionalized enabling further grafting onto electrodes and covalent coupling with photosensitizers

i) Co(DO)(DOH)pnX$_2$ as electrocatalyst for proton reduction

Our group reported for the first time in 2009 a series of tetradentate diimine-dioxime complexes with Co as the central metal for electrocatalytic hydrogen evolution.[67] Their cyclic voltammograms (CV) display two reversible and monoelectronic cathodic processes attributed to two reductions, Co(III)/Co(II) and Co(II)/Co(I). In the presence of a proton source (organic acids), cobalt complexes showed catalytic activity for hydrogen evolution close to the second redox couple. Bulk electrolysis in organic media proved their ability to evolve hydrogen reaching faradaic efficiencies (F.E.) close to unity and tens of turnover numbers (TON). An increased stability at low pH compared to cobaloximes was observed and ascribed to the stable tetradentate nature of the ligand, which is resistant to hydrolysis.

When cobalt diimine-dioxime was grafted onto multiwall carbon nanotubes (**Figure I.2**) for the assessment of its catalytic activity under fully aqueous conditions, increased stability was observed.[68] The azido derivative complex was synthesized and coupled using Bertozzi's procedure (Cu-free azide-alkyne cycloaddition) on a functionalized cyclooctyne.[69] Under bulk

electrolysis at - 0.59 V vs RHE in acetate buffer (pH 4.5), current densities of 1 mA.cm^{-2} were determined. Hydrogen was evolved reaching 55000 TONs after 7 hours of operation and 97% of faradaic efficiency (F.E.). Post-operando XPS analysis and CV excluded significant decomposition that could affect hydrogen evolution.[70] Finally, this molecular cathode was tested under the presence of oxygen, which did not affect significantly the activity of the catalyst.[71] Oxygen tolerance could be beneficial as traces of oxygen can be present in DSPEC devices.

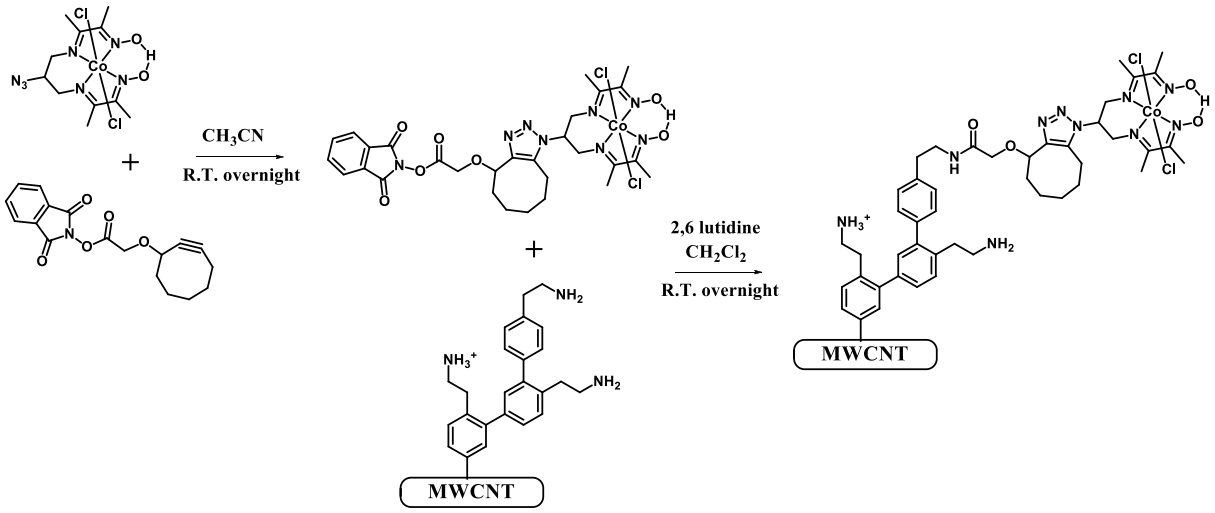

Figure I.2. Cobalt diimine-dioxime grafted onto multiwall carbon nanotubes.

The mechanism for H_2 evolution by cobalt diimine-dioxime complexes was studied by us and others (**Figure I.3**).[66] The initial Co(III)-complex is reduced twice to Co(I), which is the entry point of the catalytic process. Then, a first protonation generates a Co(III)-hydride intermediate, which is further reduced to produce a Co(II)-hydride species. Finally, a second protonation step (either external or intramolecular) drives to hydrogen evolution and the generation of the Co(II) complex, ready to launch the mechanism again. It should be noted that halide ligands are displaced during catalysis. In addition, **[Co(DO)(DOH)pnY$_2$]** complexes have an oxime bridge that can be protonated during the catalytic cycle and can act as a proton relay (**Figure I.3**). Thus, this bridge was hypothesized to be involved in the rate-determining step of the mechanism, which is the reduction to Co(I). A speculation that was further supported by DFT calculations.[72]

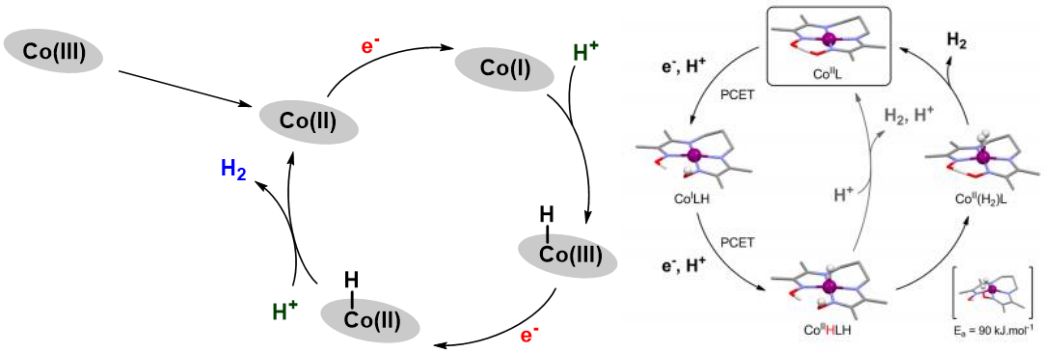

Figure I.3. Left, simplified mechanism for H_2 evolution by Co(DO)(DOH)pnX_2, right, possible pathways for hydrogen evolution, involving the oxime bridge with DFT optimized structures, taken from reference [66].

ii) Photocatalytic hydrogen evolution with Co(DO)(DOH)pnX_2

Co-diimine-dioxime catalyst and its derivatives have been operated in homogeneous photocatalytic systems using different photosensitizers and sacrificial electron donors.[73,74,75] Our group employed **[Co(DO)(DOH)pnBr_2]** in combination with an iridium photosensitizer.[75] Under optimal conditions in a mixture of organic/aqueous solvents and after 10 hours of illumination, the photocatalytic system reached 700 TON. Long-term stability was improved by addition of PPh_3, known for stabilizing low oxidation states of cobalt complexes. Thus, the catalytic activity was enhanced by stabilizing the Co(I) state, the starting point of the mechanism. The stability of the catalyst further increased the overall activity of the system for 10 hours, as the presence of a stable electron acceptor (catalyst) throughout photocatalysis, decreased the possibility of accumulating reduced dye species that can be decomposed over time. The importance of the ratio of dye/catalyst (optimal 2/1), the SED (TEA more efficient than TEOA), the pH (optimal pH 10), the amount of water in the mixture (1/1 water/acetonitrile) and the choice of photosensitizer (ruthenium complex was less active) were also examined.

2) Model dye-sensitized photocathodes

Before the preparation of dye-sensitized hydrogen-evolving photocathodes, our group developed model dye-sensitized photocathodes, where only the light harvester was immobilized in order to learn about grafting and to study the photoelectrochemical activity under pertinent conditions. Their performance was evaluated in aqueous media with the presence of an irreversible electron acceptor as a simplified replica of the catalyst.

Ruthenium polypyridine complexes were grafted onto homemade nanostructured mesoporous ITO films, prepared by template sol-gel technique.[76] We selected phosphonate as

anchoring groups based on the studies presented in the corresponding section. Complexes with two phosphonates (**RuP_2^{OH}-bpy**) were immobilized on the films by soaking overnight in a methanolic solution. CV of the electrodes showed a typical oxidation peak for Ru(II)/Ru(III). Its intensity increased linearly with increasing scan rates, an indication of efficient grafting. Dye loading of some nmol.cm^{-2} was estimated by integrating the anodic peak and by UV-Vis spectroscopy. Photoelectrochemical measurements were carried out with the presence of a cobalt complex as an irreversible electron acceptor (IEA) in aqueous solution. Photocurrent densities of - 50 μA.cm^{-2} were obtained under visible light irradiation, ascribed to an efficient electron transfer from the dye to the electron acceptor.

Continuing the work on ruthenium dyes, we compared the spectroscopic properties and the photoelectrochemical activities of NiO (prepared by screen-printing) photocathodes sensitized by different ruthenium tris diimine complexes, bearing either two or four methyl phosphonate anchoring groups and a bipyridine or a dipyridophenazine ancillary ligand (dppz) (**Chart I.2**).[55] The methylene spacers were used as they can reduce the electronic coupling between NiO and the light harvester, slowing down the unwanted recombination processes.[44,77] PEC activity was assessed in aqueous electrolyte with $[Co(NH_3)_5Cl]Cl_2$ as IEA at 0 V vs Ag/AgCl and the most active complex was **RuP_4^{OH}-dppz**. The corresponding photocathode displayed photocurrents up to - 190 μA.cm^{-2}. After light excitation, the formation of a long-lived charged separated state with a hole on NiO and one electron on the complex (PS^-) was observed by nanosecond transient absorption spectroscopy (TAS). The more extended π-ligand stabilizes the electron density away from the NiO surface, leading to increased efficiency. Two recombination pathways were proposed for all complexes. A faster one (some hundreds of ps), when the electron density is localized on the phosphonate bpy ligands closer to NiO and a slower one (2 ns) when it is localized on the ancillary ligand (bpy or dppz).

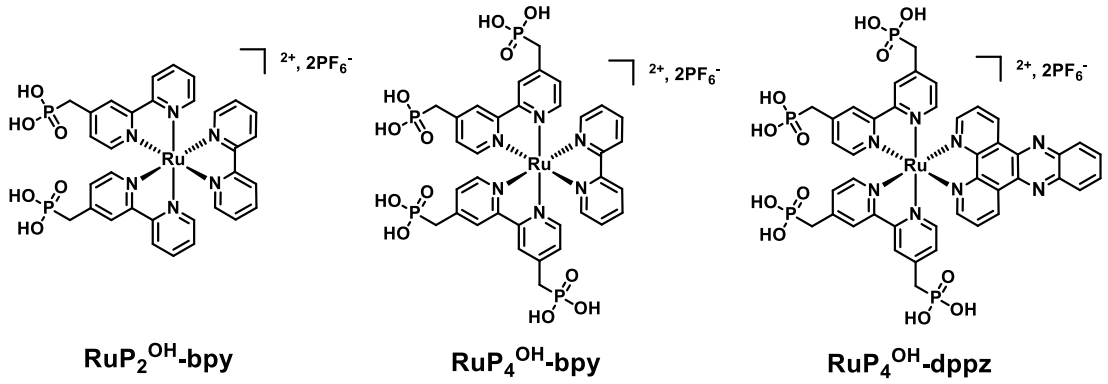

RuP_2^{OH}-bpy **RuP_4^{OH}-bpy** **RuP_4^{OH}-dppz**

Chart I.2. Ruthenium polypyridine complexes bearing methyl phosphonate anchoring groups immobilized on ITO and NiO films.

Based on the results, the anchoring groups did not affect the electronic properties of the dyes, in agreement with the non-conjugated nature of the linker. Increasing their number from two to four, the dye loading was two times higher. Furthermore, a third ligand with an electron-withdrawing nature is important for the delocalization of the electron on the bridging ligand in a dye-catalyst assembly, thus away from the semiconductor. In the literature, higher efficiencies for DSSCs were also observed for ruthenium polypyridine complexes onto NiO electrodes, when they were functionalized with an electron accepting group on the bipyridine ligands away from the anchoring groups.[78] It should be highlighted that these observations were the basis for designing the systems I worked on during this thesis.

In parallel and in collaboration with Pr. B. Dietzek and Dr. F.H. Schacher an organic push-pull dye bearing carboxylate groups was immobilized onto porous nanostructured tri-layered NiO films prepared by co-polymer template technique and deposited onto FTO.[79] Photocurrent densities of - 300 $\mu A.cm^{-2}$ were measured during PEC experiments in water (pH 4.5) with $[Co(NH_3)_5Cl]Cl_2$ as IEA at + 0.2 V vs NHE. Following this work, metallo-organic dyes, synthesized by our collaborator Dr. C. Olivier, were immobilized on NiO substrates fabricated by Dyenamo.[80] High surface coverage was observed (25 $nmol.cm^{-2}$) and PEC activity reached - 60 $\mu A.cm^{-2}$ in aqueous electrolyte at + 0.2 V vs NHE using the same IEA.

The promising activity of **Co(DO)(DOH)pnX$_2$** for hydrogen production under homogeneous conditions and the first model photocathodes sensitized by ruthenium complexes and organic dyes enabled our group to develop the first functional dye-sensitized hydrogen-evolving photocathodes based on this catalyst. They will be presented in the following part, together with the other examples of dye-sensitized photocathodes from the literature. It should be noted that some of these examples were reported during the course of this PhD thesis.

III. State-of-the-art on dye-sensitized hydrogen-evolving photocathodes

One important characteristic of a dye-sensitized photocathode is how the components are assembled together in the architecture. Four main arrangements (**Figure I.4**) exist:

- Catalyst in the solution
- co-immobilization of the dye and the catalyst on the surface
- covalent or supramolecular dye-catalyst assembly
- "layer-by-layer" approach to couple the PS with the HEC

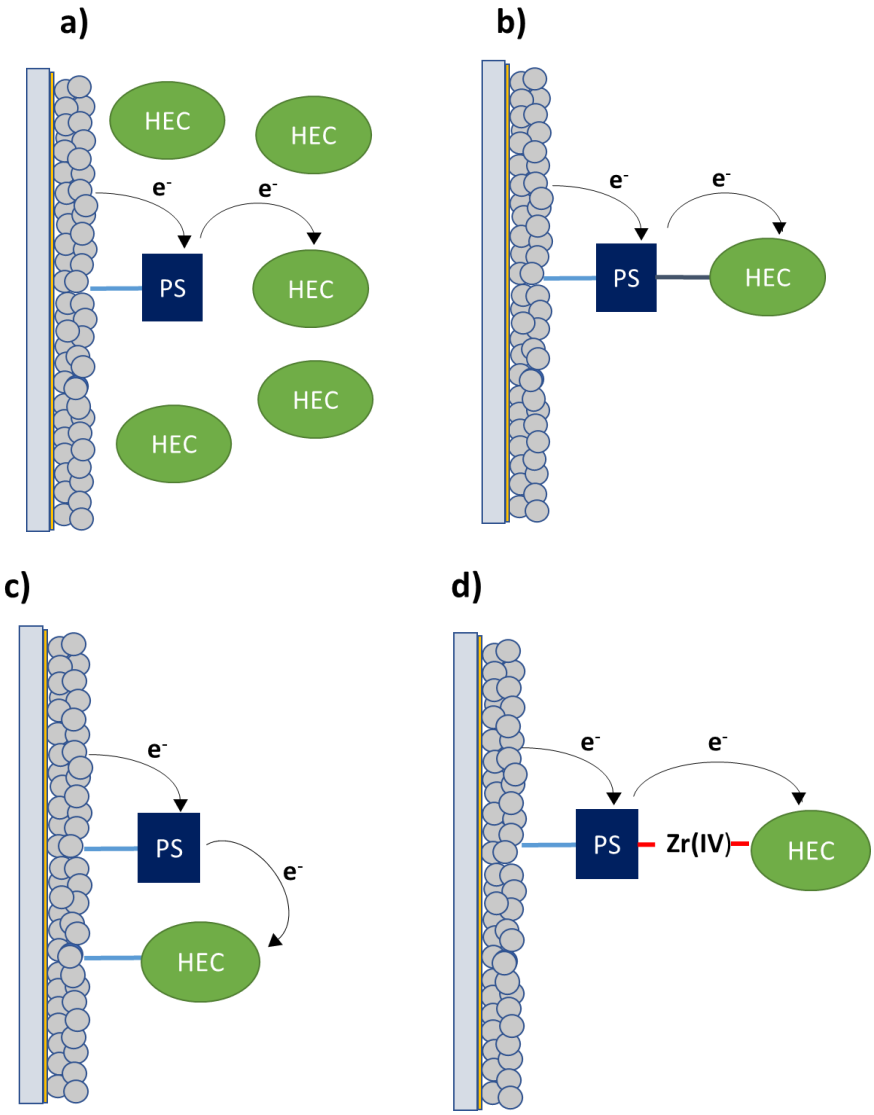

Figure I.4. Different architectures for the construction of p-type dye-sensitized hydrogen-evolving photocathodes: a) catalyst in the solution, b) covalent or supramolecular assembly c) co-grafting, d) "layer-by-layer" approach.

1) Catalyst in solution

The pioneering work of L. Sun in 2012 was the first example of a functional dye-sensitized hydrogen-evolving photocathode.[81] A molecular H_2-evolving catalyst, more specifically a cobaloxime (**HER 1**), and an organic dye (**PS 1**) were employed. The photosensitizer was grafted onto nano-structured NiO films through carboxylate anchoring groups and the catalyst was physisorbed onto the electrode. In phosphate buffer at pH 7, a photocurrent density of around - 10 $\mu A.cm^{-2}$ was observed at - 0.4 V vs Ag/AgCl. Applying this potential, hydrogen evolution was confirmed by a Clark-type electrode in the solution, with up to 90 nmol after 30 minutes of continuous visible light irradiation. Photocurrent decay due to catalyst decomposition or leaching from the surface could be solved with re-addition of fresh catalyst. Following this study, the field started to evolve and research groups around the world were keen on optimizing the activity of the photocathode counterpart of a tandem cell.

Aqueous stability is one of the main limitations for the activity of dye-sensitized photocathodes. A work published by Y. Wu in 2016 tried to address this challenge by taking advantage of the role of membranes in natural cells.[82] They constructed an organic donor-acceptor dye (**PS 2**) capable of resisting to dye desorption and semiconductor degradation at acidic aqueous solution. The hydrophobic hexyl groups created a protective layer in which water and protons cannot penetrate, whereas the two perylenemonoimide groups can act as the hydrophilic environment for interaction with the protic electrolyte. Many molecular catalysts, including cobaloximes, are unstable in acidic conditions. Hence, a cubane molybdenum sulfide cluster (**HER 2**) was chosen as a HER catalyst.[83] The activity was assessed in pH 0 at - 0.3 V vs NHE and the evolution of hydrogen was confirmed by gas chromatography, reaching an average faradaic efficiency of 50%. Higher photocurrents were observed at lower pH with maximum at pH 0 (- 300 $\mu A.cm^{-2}$ at - 0.3 V vs NHE applied potential) sustained for almost 16 hours. Such a stability is attributed to the shielding that the hydrophobic hexyl groups offer to the system. Thus, water cannot easily reach the semiconductor surface to detach the dye.

An alternative approach to stabilize the dye against desorption relies on the deposition of a thin layer of Al_2O_3 by atomic layer deposition (ALD), as reported by the group of M. R. Wasielewski's.[84] Nanostructured NiO films sensitized with **PS3** were protected by 30 cycles of Al_2O_3 ALD and the photoelectrocatalytic activity was assessed using two different molecular catalysts, a cobaloxime (**HER 1**) and a nickel Dubois-type catalyst (**HER 3**) in aqueous solution. The best performing electrode with the nickel catalyst evolved 1.82 μmol of hydrogen at - 0.4 V vs Ag/AgCl under illumination for 2 hours. The F.E. was close to unity and the TON

1.5, an indication that catalytic hydrogen evolution occurs. NiO films without ALD treatment produced less amount of hydrogen and complete loss of the dye observed by UV-Vis absorption, proving the role of the ALD as protecting layer.

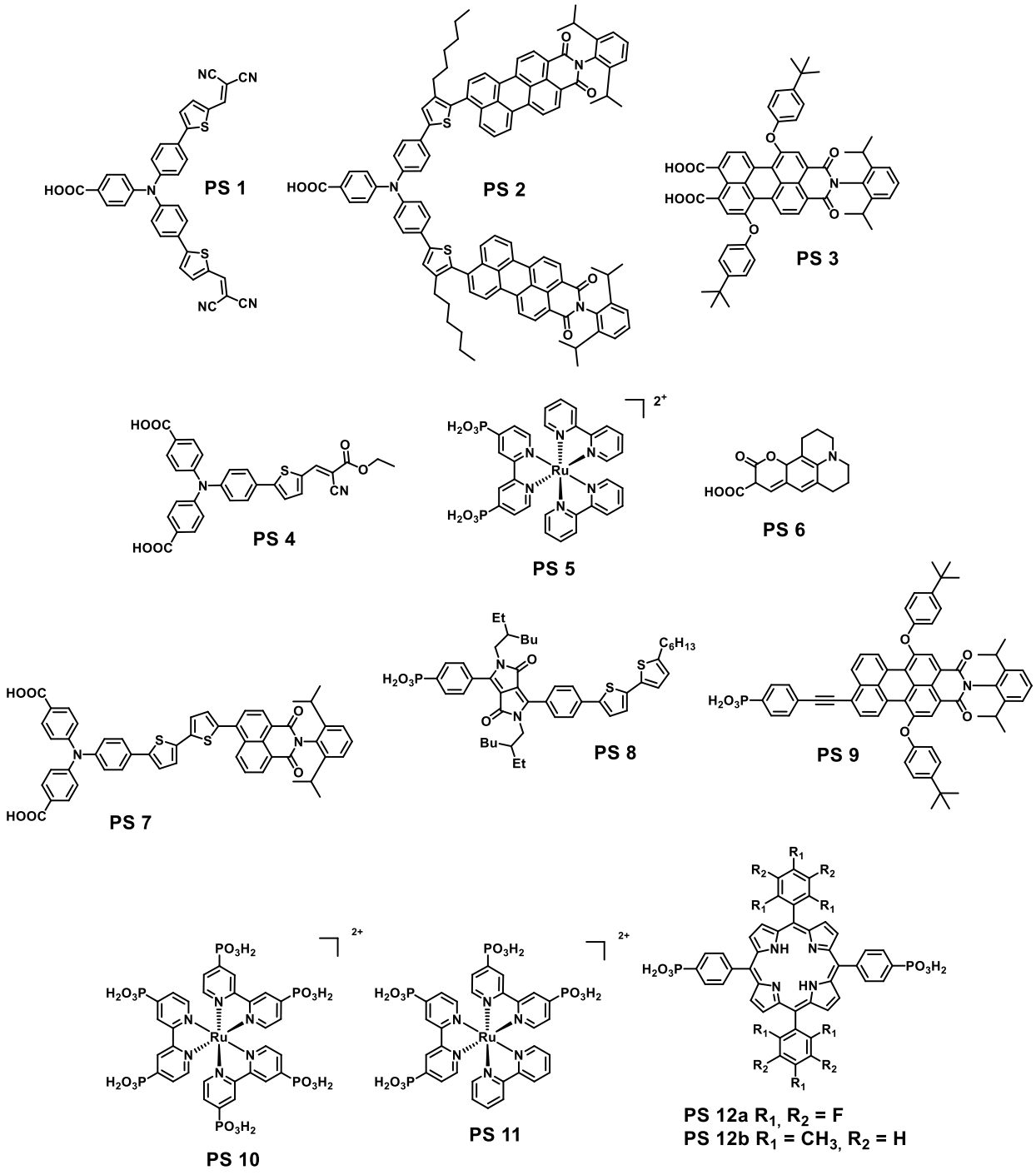

Chart I.3. Photosensitizers (**PS 1-12**) used for dye-sensitized hydrogen-evolving photocathodes.

The understanding of the electron transfer dynamics at the NiO interface and more specifically between the semiconductor and the photosensitizer and between the latter and the catalyst is quite tricky. Our group in collaboration with B. Dietzek and A. B. Muñoz-García,

recently addressed the first process using quantum chemistry and transient absorption measurements and they correlated the results with a dye-sensitized photocathode able to evolve hydrogen.[85] An organic push-pull dye (**PS 4**) was grafted onto mesoporous NiO films and was examined for PEC hydrogen evolution with a cobaloxime (**HER 1**) in solution. Chronoamperometric measurements were carried out at - 0.4 V vs Ag/AgCl for 6 hours under continuous irradiation in aqueous electrolyte with a faradaic efficiency of 3% and 12 nmol.cm^{-2} of evolved hydrogen. The key feature of this study is that a long-lived charge separated state is needed for the activity, especially when the catalyst is dissolved in the solution and diffusion governs the electron transfer.

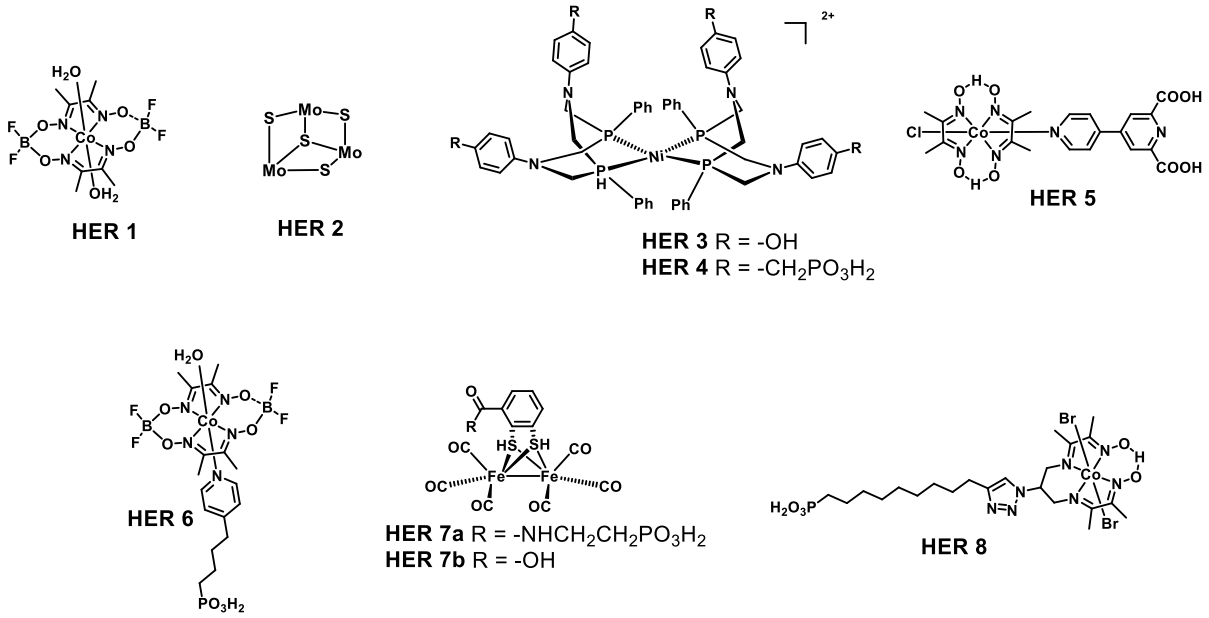

Chart I.4. Hydrogen-evolving catalysts (**HER 1-8**) used for dye-sensitized hydrogen-evolving photocathodes.

2) Covalent or supramolecular dye-catalyst assemblies

The first example of a functional dye-sensitized hydrogen-evolving photocathode based on a supramolecular assembly was reported in 2013 by the group of Y. Wu.[86] A NiO photocathode was soaked in a solution of a cyclometalated ruthenium sensitizer which was grafted onto NiO through carboxylate groups. Then, the sensitized film was placed in an aqueous solution of a cobaloxime for 5 minutes and axial coordination of the pyridyl group of the dye with the cobalt metal center resulted in **Dyad 1**. Chronoamperometric measurements at - 0.2 V vs NHE under continuous light irradiation for 2.5 hours in aqueous phosphate buffer at pH 7 were carried out and an amount of 290 nmol of hydrogen was produced, corresponding to 45% F.E. An increase of F.E. to 68%, when the photoelectrocatalytic experiments were conducted at less negative

potentials (- 0.1 V vs NHE) was observed. ALD coating before sensitization increased the photocurrent density probably due to suppression of the hole-electron recombination processes.

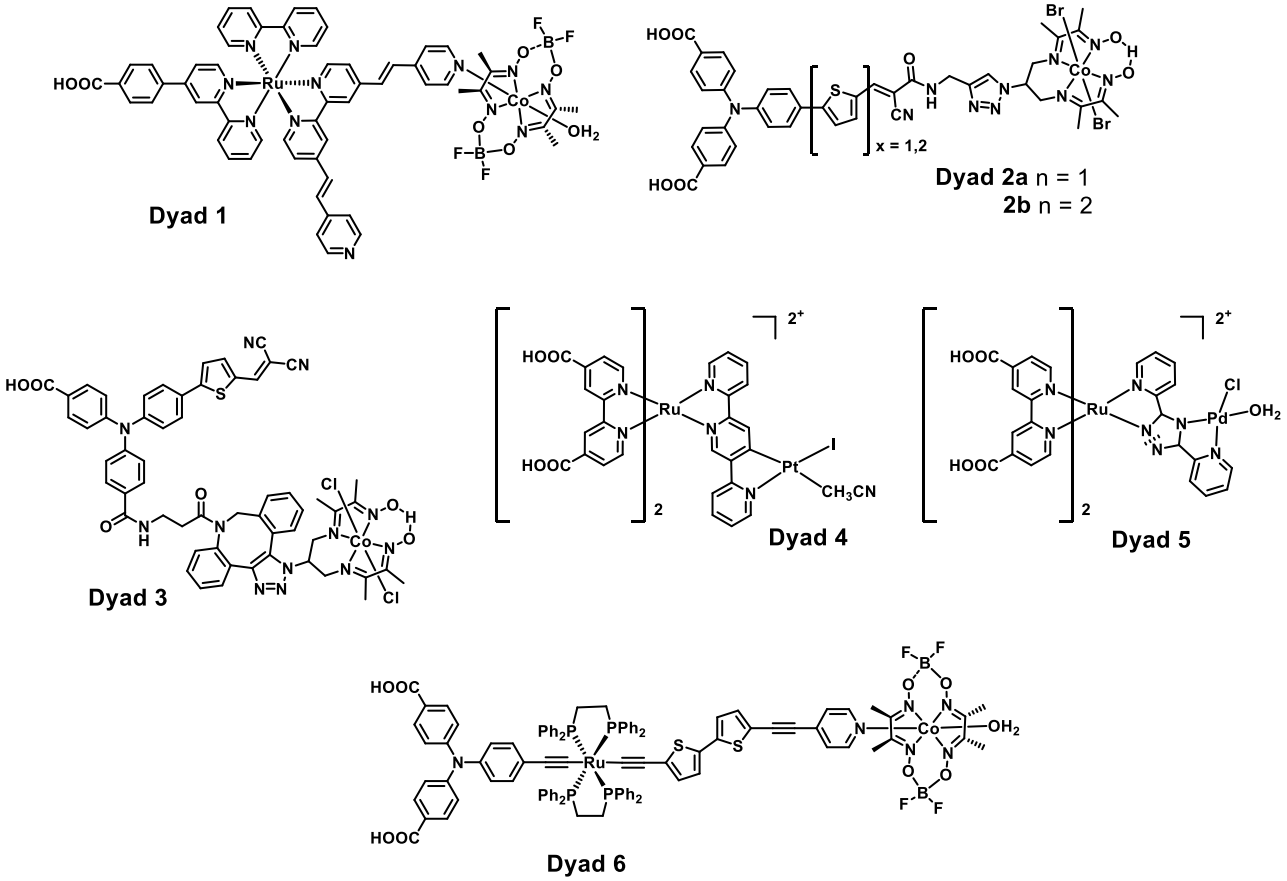

Chart I.6. Dye-catalyst assemblies (**Dyad 1-6**) used for dye-sensitized hydrogen-evolving photocathodes.

In 2016, our group designed the first noble metal-free covalent dye-catalyst assembly based on an organic push-pull dye and the cobalt diimine-dioxime catalyst (**Dyad 2a**).[87] The push-pull character appears attractive by enabling the unidirectional electron transfer from the NiO surface toward the catalyst.[54] The two components were attached using click chemistry, the copper-catalyzed azide-alkyne cycloaddition (CuAAC).[88] Long term electrolysis at - 0.14 V vs RHE in a pH 5.5 MES buffer was carried out. Chenodeoxycholic acid (CDCA) was used as a coadsorbent to avoid aggregation of the dyad on the NiO surface and hydrogen was confirmed by gas chromatography with F.E. of 8-10%. Post-operando XPS analysis revealed that one possible reason for the low faradaic efficiency can be the competitive reduction of the bulk NiO electrode, although reductive decomposition of the molecular assembly could not be excluded.[89] Re-evaluation using a microsensor Clack-type electrode for quantifying hydrogen in the solution showed 66% increase of the F.E.[90] Our group highlighted the importance to quantify H_2 in the solution and in the headspace in order to have more accurate results, as a

fraction of H_2 remains diluted in the electrolyte even after some hours of experiments. Moreover, the insertion of a second thiophene unit (**Dyad 2a**) between the donor and the acceptor part of the dye was shown to slightly improve the efficiency due to a better charge separation or a slower charge recombination.

Another dyad covalently linking an organic dye derived from **PS1** with the cobalt diimine-dioxime complex on mesoporous NiO films was prepared using a copper-free click reaction (**Dyad 3**).[91] Time-resolved fluorescence and transient absorption spectroscopy showed that upon irradiation of the photocathode, an ultrafast hole injection from the excited dye into NiO occurs, followed by an electron transfer from the reduced dye to the catalyst. The second electron transfer to reduce to Co(I) could not be identified, but hydrogen evolution was detected during photoelectrochemical experiments. In acetate buffer at pH 4.8 at 0 V vs Ag/AgCl, the system produced an average photocurrent of -10 $\mu A.cm^{-2}$ but only 2.5 nmol of hydrogen and 0.05 TON.

In 2019, dye-catalyst assemblies based on ruthenium photosensitizers and noble metal-based molecular catalysts (Pt, Pd) were grafted onto NiO films (**Dyad 4, 5**).[92] The corresponding photocathodes exhibited cathodic and stable photocurrents at pH 3. Continuous irradiation (AM 1.5 filter, 1 sun) for 1 hour with an applied potential confirmed the reduction of protons to hydrogen with faradaic efficiencies varying from 30 to 90%. At – 0.2 V vs Ag/AgCl, 46 TON were determined for the Ru-Pd photocatalyst. On one hand, post-operando analysis showed that the photosensitizer and the Pd catalyst remained stable after 1 hour of PEC tests. On the other hand, decomposition of the Pt complex and formation of nanoparticles could explain the higher performance of the system with **Dyad 4**.

Recently, the group of C. Olivier in collaboration with our group developed an original supramolecular dyad based on a pyridyl-functionalized ruthenium-diacetylide photosensitizer[80] coupled via axial coordination to a cobaloxime (**Dyad 6**).[93] Theoretical calculations showed that in the LUMO, electron density is localized on the cobalt atom of the dyad, in contrast to what observed for the HOMO. Thus, electron transfer from the excited state of the dye to the catalyst should occur. The photoelectrocatalytic activity of the NiO photocathode was assessed in acetate buffer at pH 4.5 at + 0.07 V vs RHE under visible-light irradiation for 4.5 hours. The photocurrent density was -3.2 $\mu A.cm^{-2}$ with gradual decrease during the long-term photoelectrolysis, probably due to leaching of the dyad from the surface. Gas chromatography proved the PEC hydrogen evolution with F.E. of 27%. Control experiments without the coordinated cobaloxime showed only traces of hydrogen produced.

3) Co-grafting

The group of L. Sun was the first to prepare dye-sensitized hydrogen-evolving photocathodes by the co-grafting strategy.[94] A molecular ruthenium complex (**PS 5**) bearing phosphonate anchoring groups and a cobaloxime with a pyridine-2,6-dicarboxylic acid were co-anchored onto NiO films (**HER 5**). The corresponding photocathode afforded cathodic photocurrents of -13 $\mu A.cm^{-2}$ at - 0.4 V vs Ag/AgCl at pH 7. A tandem cell with a photoanode based on the same dye and a molecular WOC was examined at + 0.4 V vs Ag/AgCl with an average photocurrent density of - 40 $\mu A.cm^{-2}$. Although the amount of H_2 produced was not reported, this study was an inspiration for the construction of full DSPECs. Moving one step forward, they prepared the first functional tandem cell for water splitting.[95] On the photocathode, an organic dye (**PS 1**) and a cobaloxime (**HER 6**) bearing carboxylate and phosphonate anchoring groups respectively were co-grafted onto NiO films. At - 0.2 V vs Ag/AgCl in a pH 7 phosphate buffer solution, the photocathode produced 290 nmol of hydrogen with a faradaic efficiency of 68% after 90 minutes of continuous irradiation. The co-grafting is clearly beneficial for the stability and activity of the photocathode compared to the previous reported system with the physisorbed catalyst.[81] The tandem cell with a TiO_2 photoanode in aqueous electrolyte at pH 7 without any applied bias evolved 330 nmol of hydrogen with a 55% faradaic efficiency.

A biomimetic Fe-Fe catalyst (**HER 7a**) was co-adsorbed with a coumarin dye (**PS 6**) on mesoporous NiO films by the group of L. Hammarström.[96] The photocathode produced 13 nmol of hydrogen (3 TON) with a 50% F.E. after 1100 s of irradiation in acetate buffer (pH 4.5) with an applied potential of - 0.3 V vs Ag/AgCl. The loss of activity was caused by the catalyst decomposition and detachment, as evidenced by FTIR spectrum. Transient absorption measurements revealed the surface electron transfer process between the molecular components in the coadsorbed system, following the ultrafast hole injection from the excited dye. It was observed that the catalyst reduction favorably competes with the relatively slow charge recombination between the reduced dye and the semiconductor. Finally, the reduced catalyst is sufficiently long-lived for catalysis to occur. This was ascribed to the distance between the iron center and the NiO surface due to the long linker.[97] This was further supported by the fact that a similar photocathode based on **HER 7b** catalyst with a shorter linker did not produce any hydrogen.

Our group contributed to the co-grafting strategy with the preparation of a NiO photocathode based on an organic dye (**PS 7**) and a cobalt-diimine-dioxime catalyst (**HER 8).**[98] After 2h of

continuous irradiation at + 0.14 V vs RHE, H_2 was detected with a F.E. of 10% and a photocurrent density in the range of previous reports using the same catalyst. Spectroelectrochemical measurements showed that at this applied potential, the grafted catalyst is at its Co(II) state and that light illumination is essential for the subsequent reduction of the cobalt center to Co(I) to enter the catalytic cycle. The group performed post-operando ToF-SIMS characterization to identify possible deactivation pathways. Detachment of both dye and catalyst from the surface, possible loss of the catalyst through cleavage of the triazole unit and cleavage of the dye either at the thiophene unit or at the triphenylamine one were hence identified. We should highlight that post-operando measurements to shed light on the destiny of the molecular components in DSPECs are limited.

Most photocathodes rely on wide bandgap p-type NiO electrodes, but the use of different p-type materials as semiconductors is investigated. Delafossites[99] in the form of $Cu^{I}M^{III}O_2$ (M = Co, B, In, Sc, Cr, Al, Ga) have been used for p-DSSCs. Reisner's group reported a photocathode for hydrogen evolution based on $CuCrO_2$ films co-sensitized by an organic diketopyrrolopyrrole dye (**PS 8**) and a molecular Ni-catalyst (**HER 4**).[100] Thermodynamically, hole injection from the excited dye to the valence band of $CuCrO_2$ and electron transfer from the reduced dye to the catalyst are feasible. PEC measurements were conducted under UV-filtered simulated solar irradiation in aqueous Na_2SO_4 at 0 V vs RHE over 2 hours. The amount of the co-immobilised Ni-catalyst estimated by inductively coupled plasma optical emission spectroscopy and H_2 generation reached 94 nmol (126 TON) with F.E. of 34%. Moderate F.E. could be due to reduction of Cu(II) and remaining oxygen, like in NiO-based systems. Post-operando characterization with ICP-OES showed significant desorption of the catalyst (45% after 2h of PEC test), that limits the long-term activity. Direct comparison with a NiO electrode proved the superior activity of the $CuCrO_2$ electrodes. More recently, in collaboration with the group of F. Odobel inverse opal (IO) $CuCrO_2$ electrodes were developed to increase the surface loading.[101] IO-$CuCrO_2$ photocathode with **PS 8** outperforms in activity the one with $CuCrO_2$. Higher dye loading and stability against detachment are the main reasons for this improvement. The best performing photocathode was a NiO co-sensitized with a perylene monoimide dye (**PS 9**) and **HER 4**. 215 nmol.cm^{-2} of hydrogen, 48 TON and 41% FE after 2 hours of continuous irradiation at 0 V vs RHE in aqueous electrolyte (pH 3) were determined. One of the main reasons for this higher activity is the higher light harvesting efficiency in the visible region of **PS9** compared to **PS8**.

In 2019, our group in collaboration with O. Ishitani and R. Abe reported a functional tandem photoelectrochemical cell.[102] An organic push-pull dye (**PS 7**) and a cobaloxime (**HER 5**) were

grafted onto NiO electrodes. P-type semiconductors like $CuGaO_2$, which are more conductive and with a more positive flat band potential compared to NiO, were also tested.[103] Under the best conditions, the $CuGaO_2$ photocathode was more efficient reaching 555 nmol of H_2 with a 75% F.E. and TON ranging from 82 to 640 over 2 hours of continuous irradiation at 0 V vs RHE. With this photocathode in hand, which is the most efficient in the literature in terms of TON, a tandem cell with a photoanode was prepared. The $TaON/CoO_x$ photoanode and the photocathode split water into hydrogen and oxygen with comparatively activities of the separate electrodes. After performing ICP-OES measurements, leaching of the cobalt complex from the surface was evidenced probably due to weak interaction between the pyridyl group and the metal center.

4) "Layer-by-layer" assembly

"Layer-by-layer" assembly can contribute to spatial separation similarly to the covalent approach but without involving demanding synthetic steps for a covalent coupling. The first example of a dye-sensitized photocathode based on this architecture was reported in 2016 by the group of E. Reisner.[104] NiO films were first sensitized by a Ru-PS (**PS 10**), then the electrode was dipped in a solution of $ZrOCl_2$ for the bounding of the phosphonic acid groups of the Ru-complex to Zr(IV). Finally, the nickel catalyst (**HER 4**) was attached to Zr(IV) and the assembly was assessed in aqueous electrolyte (pH 3) at + 0.3 V vs RHE under continuous irradiation. Moderate amounts of hydrogen (6 nmol in the headspace) and F.E. (around 9%) were obtained. Slightly higher activity was observed with two layers of the Ni-catalyst after two immobilization cycles, showing that the ratio of dye/catalyst influences the performance. The low activity of this assembly was attributed to inefficient charge transfer dynamics at the interfaces, as well as a low loading of the catalyst (around 5 $nmol.cm^{-2}$). Direct comparison with a co-grafting approach, which exhibited negligible photocurrents, indicated its superior activity. A possible explanation is the proximity of the catalyst with the semiconductor for the co-grafting method, leading to fast recombination processes. Furthermore, the "layer-by-layer" assembly had a positive impact on the stability of the system, as 50% of the light harvester remained grafted on the surface after 2 hours of PEC test compared to some traces when the two molecular components were immobilized on the surface.

The same year, T. J. Meyer's group prepared a tri-layer photocathode based on a donor-dye-catalyst assembly to further increase the distance of the catalyst **(HER 4**) from the surface.[105] The insertion of dianiline as electron donor in between NiO and the light harvester (**PS 11**)

allows ITO to be used as SC instead of p-type NiO. Transient-absorption measurements revealed relative slow recombination processes between the reduced dye and the hole in NiO. Hence, electron transfer to the catalyst can favorably compete and this is the basis of the efficiency of this system. PEC tests on macro-mesoporous IO-ITO offered high surface loading and higher activity to previously reported photocathodes with 53% F.E. in MES buffer (pH 5.1) at + 0.05 V vs RHE. Initial photocurrent density of − 56 μA.cm^{-2} dropped by 50% within 4 h of operation. Post-operando analysis showed that desorption or degradation of the catalyst are the two main problems for the decay of the photocurrent. In contrast, negligible H_2 evolution was observed using meso-ITO films, demonstrating that macromesopores ensure sufficient assembly coverage.

Continuing their work, the preparation of multilayered assemblies with atomic layer deposition was accomplished.[106] Thin layers of various metal oxides (Al(III), Sn(IV), Ti(IV) or Zr(IV)) were deposited by ALD on top of the NiO film sensitized by **PS11**, further allowing to anchor catalyst **HER 4**. Transient absorption measurements correlated the increased photocurrent efficiencies with the slowest rate of the back electron transfer due to the ALD treatment. Photocurrent densities as high as - 40 μA.cm^{-2} for the full assembly were achieved at - 0.2 V vs Ag/AgCl in an aqueous electrolyte (pH 4.65). In a recent study, they tried to increase the internal driving force for hole transport of the NiO electrodes.[107] Two layers of doped NiO, 2% of K-doped as the inner layer and 2% of Cu-doped, showed the higher driving force for hole transport. Loading of the molecular components on the surface was increased by adding a third layer of IO-ITO. A trilayered photocathode with **PS 11** and **HER 4** as previously, produced 700 nmol of hydrogen with 86% F.E. and photocurrent densities of - 40 μA.cm^{-2} during 2 hour of PEC tests at - 0.25 V vs NHE. Reversing the inner and outer layers or using non-doped NiO films, the PEC activity was significantly reduced. Control experiments without NiO electrodes gave anodic photocurrents, highlighting the role of NiO as a p-type semiconductor. Interestingly, excited-state quenching of the dye by the Ni-catalyst (oxidative quenching) seemed to be faster than quenching by NiO (hole injection-reductive quenching), implying that thermodynamically it is more favorable to achieve photoinduced intramolecular electron transfer to the catalyst than hole injection. Using porphyrins as photosensitizers (**PS 12**) decreased the efficiency of the photocathodes mainly due to their highly conjugated nature that accelerates back electron transfer.

5) Narrow band gap photoactive semiconductors

Fabrication of hydrogen-evolving photocathodes with narrow band gap semiconductors, which can behave as light harvesters and achieve charge separation, is an alternative to p-type semiconductors. Although the scope of this thesis is different, some recent breakthroughs on this field and particularly when combined with molecular photosensitizers will be presented.

P-type silicon (second most abundant element in the earth's crust) materials are attractive photocathodes due to their low-cost, visible light absorption and has been already used for hydrogen evolution.[108] A nanostructured p-Si photocathode in water with the Ni bis(diphosphine)-based catalyst (**HER 4**) anchored on the surface has been prepared by the group of E. Reisner.[109] In a more elegant approach by T. J. Meyer, a p-Si photocathode modified by a "layer-by-layer" assembly of an organic dye (derivative of **PS3**) and the same nickel-catalyst (**HER 4**) showed significant activity for hydrogen evolution with photocurrent density of - 1 $mA.cm^{-2}$ at 0 V vs NHE.[110] The additional dye (heterojunction) was used as an electron transfer mediator between the photo responsive p-Si electrode and the catalyst. A tandem cell with a SnO_2 photoanode with two Ru-complexes as PS and OEC achieved water splitting and the efficiency seems to be hindered by the performance of the photoanode. Thus, in this case the limiting factor for an efficient tandem cell is the photoanode and not the photocathode. This work is an inspiration for utilization of both a photoactive semiconductor and a molecular photosensitizer in order to afford more efficient light absorption and higher performances.

Mesoporous perovskite $LaFeO_3$ is a stable material under irradiation and in aqueous solutions and has a proper band gap energy for visible light absorption.[111] Hence, potential candidate as a p-type visible-light-absorbing semiconductor for light-driven H_2 generation. Successful modification with a molecular dye and **HER 4** produced hydrogen with photocurrent densities of - 20 $\mu A.cm^2$ and 48% F.E. at + 0.6 V vs RHE by the group of L. Sun.[112] Inferior activity was obtained for the photocathode without the grafted dye. ICPE spectra indicated that both the perovskite and the molecular dye absorb light and contribute to the photocurrent generation.

IV. Figures of merit and current limitations

1) Performance of the state-of-the-art photocathodes

The development of artificial photosynthetic systems, capable of harvesting light energy and converting it into an electrochemical gradient of potential to perform catalytic reactions of interest (oxidation of water, reduction of protons, carbon dioxide, etc.) is a field of intensive research. Over the last years, dye-sensitized photoanodes for water oxidation have reached milestones with high catalytic efficiencies and photocurrent densities of 1 $mA.cm^{-2}$.[113] For the construction of an operating tandem DSPEC, the two counterparts should exhibit similar activity.

The reported dye-sensitized photocathodes are based on four different architectures, as already presented. The first architecture follows the concept of p-DSSCs but with a H_2-evolving catalyst in the solution instead of a redox mediator. This approach is not promising, as the electron transfer is diffusion-limited and recombination reactions can be favored. Systems that bring the molecular components in closer contact are needed. The second arrangement based on a covalent or supramolecular dye-catalyst assembly can enhance the directionality of electron transfer and the charge separation, because the catalyst is placed away from the semiconductor. In addition, the dyad enables to perform analytical studies in solution prior to grafting. It is also a logical continuation of the work already done with dyads or triads in the field of artificial photosynthesis. [114,115,116] For these reasons and based on the previous expertise of the group, we decided to adopt this architecture in this work, even though it is synthetically challenging. Co-grafting of the catalyst and the photosensitizer on the surface is a more straight-forward procedure and it gives the opportunity to deconvolute the effects of the photosensitizer and the catalyst on the performance. Although the electron transfer between the dye and the catalyst is efficient due to the attachment of both on the electrodes, the proximity of the catalyst to the semiconductor can enhance unwanted recombination processes. In this approach, the ratio of adsorbed dye/catalyst is also difficult to be determined. Furthermore, the surface coverage of the film with the photosensitive unit is limited, as there is a competition for attachment with the catalyst. A way to overcome the complexity of synthesis and keep the directionality of the electron transfer is the "layer-by-layer" assembly of the molecular components. Nonetheless, the ratio of the two subunits is doubtful, arising questions about the influence of the dye and the catalyst on the activity.

In **Table I.1**, the figures of merit (the photocurrent densities (*j*), the amount of produced hydrogen, the turnover numbers and the faradaic efficiencies) together with the different

experimental conditions of the hydrogen evolving photocathodes reported up to date are presented.

-*Photocurrent density:* Overall, the different photocathodes exhibit low photocurrent densities, in the order of some tens of $\mu A.cm^{-2}$, far away from the goal of 1 $mA.cm^{-2}$. Only two examples with values higher than 100 $\mu A.cm^{-2}$ exist.[82,84]

- *Amount of H_2 produced*: Gas chromatography was mainly used for the quantification of the amount of hydrogen produced. High-sensitive micro Clark-type electrode was also employed in some cases for the determination of diluted hydrogen in aqueous solution. Recently, our group highlighted the importance to combine both techniques in order to have more accurate results especially when low photocurrents are observed, as a fraction of H_2 remains in the electrolyte even after some hours of experiments.[90] In many cases, the surface of the electrode is not indicated in order to perform a comparison taking into account the size of the photocathodes. Thus, comparing the different systems with the amount of H_2 produced is not so accurate.

-*TON*: In order to correlate the overall performance of the system with the intrinsic activity of the molecular components, the loading of the molecular components needs to be taken into consideration. Turn-over number (TON) is a reliable factor for direct comparison between the different photocathodes, at it excludes material- and device-based parameters. It indicates how many times the catalyst has participated in the catalytic cycle for the reduction of a substrate (proton, carbon dioxide, etc). Nevertheless, a lot of studies do not provide TON values, as surface characterization techniques are scarce and the amount of the loaded catalyst is not determined. In particular for co-grafting and "layer-by-layer" approaches, the surface organization that can affect the activity is questionable.

-*Faradaic efficiency:* The faradaic efficiency shows the percentage of charge converted to hydrogen (2 electrons per molecule of H_2). We could say that it is a selectivity index for proton reduction. F.E. close to unity are favorable, indicating that all the photo-driven electrons are used for H_2 evolution. The reported values drastically vary from < 10% to almost 100%, from one system to the other.

Until today, comparing the four different figures of merit, no direct proof can be extracted of which architecture or molecular components (photosensitizers and hydrogen-evolving catalysts) are the most appropriate for a functional photocathode. It is important to highlight that from one study to the other, too many parameters vary (different pH, electrolytes, applied potentials, film preparation and light intensity) for an accurate comparison to be made.

Electrode architecture	Components	Electrode material	pH[1]	Applied potential (V)	*j* (µA.cm^{-2})	H_2 (nmol) (nmol.cm^{-2})	TON	F.E. (%)	Reference
a	HER1/PS 1	NiO	7	- 0,4 (Ag/AgCl)	-10	90 (90[2])	<1[2]	n.r.	L. Sun et al. 2012[81]
a	PS2/HER2	NiO	0	-0,3 (NHE) 0 (NHE)	-300 183 ± 36	n.r.	n.r.	49 ± 11	Y. Wu et. al. 2016[82]
a	PS3/HER1 PS3/HER3	NiO	n.r.	-0,4 (Ag/AgCl)	-200 -100	130 ± 90[2] (342) 1820 ± 20 (4789)	<1[2] 1.5	60 ± 10 98 ± 10	R. Wasielewski et al. 2017[84]
a	PS4/HER1	NiO	4,5	-0,4 (Ag/AgCl)	-6	~40 (12)	<1[2]	3	M. Chavarot-Kerldou et al. 2019[85]
b	Dyad 1	NiO	7	-0,2 (NHE)	-15	290 (290[1])	n.r.	45	Y. Wu et al. 2013[86]
b	Dyad 2a	NiO	5,5	-0,4 (Ag/AgCl)	-15	37 ± 6 (26 ± 10)	<1[2]	9 ± 1	V.Artero et al. 2016[87]
b	Dyad 2b	NiO	5,5	-0,4 (Ag/AgCl)	-11	16 ± 5	n.r.	13 ± 1	V.Artero et al. 2018[90]
b	Dyad 3	NiO	4,8	0 (Ag/AgCl)	-10	2,5	0,05	n.r.	H. Tian et al. 2017[91]
b	Dyad 4	NiO	3	-0,2 (Ag/AgCl)	-33 ± 7	<300 (<380)	47	96	E. A. Gibson et al. 2019[92]
b	Dyad 5	NiO	3	-0,2 (Ag/AgCl)	-36 ± 2	500 (400)	46	98	E. A. Gibson et al. 2019[92]
b	Dyad 6	NiO	4,5	-0,4 (Ag/AgCl)	-3,2	109 (33[2])	2,5	27	C. Olivier et al. 2019[93]
c	PS5/HER5	NiO	7	-0,4 (Ag/AgCl)	-13	n.r.	n.r.	n.r.	L. Sun et al. 2014[94]
c	PS1/HER6	NiO	7	-0,2 (Ag/AgCl)	-35	290 (290[2])	n.r.	68	L. Sun et al. 2015[95]

c	PS6/HER7a	NiO	4,5	-0,3 (Ag/AgCl)	-10	12,4 (12,4[2])	≤ 3	50	L.Hammarström et al. 2016[96]
c	PS7/HER8	NiO	5,5	-0,4 (Ag/AgCl)	-8	n.r.	n.r.	9,3 ± 1.5	V. Artero et al. 2018[98]
c	PS8/HER4	$CuCrO_2$ NiO	3	0 (RHE)	-15,1 -5,8	94 ± 10 (376 ± 40)[2] 35 ± 2	126 ± 13	34 ± 8 31 ± 8	E. Reisner et al. 2018[100]
c	PS7/HER5	$CuGaO_2$ NiO NiO	7 7 5.5	0,41 (RHE) 0,14 (RHE) 0,14 (RHE)	-45 -12 -12	555 540 ± 80 347 ± 29	82-640 14-84 n.r.	74 80 ± 8 71 ± 2	R. Abe, O. Ishitani, V.Artero et al. 2019[102]
c	PS9/HER4	IO-$CuCrO_2$	3	0 (RHE)	-25	54 ± 3 (215 ± 10)	48 ± 2	41 ± 8	E. Reisner et al. 2019[101]
c	PS8/HER4	IO-$CuCrO_2$	3	0 (RHE)	-18	40 ± 6 (160 ± 24)	36 ± 5	40 ± 14	E. Reisner et al. 2019[101]
d	PS10/HER4	NiO	3	+0,3 RHE	-9	7 ± 1	n.r.	10 ± 2	E. Reisner et al. 2016[104]
d	PS11/HER4	io-ITO	5,1	+0,05 RHE	-56	>1000	>15[2]	53 ± 5	T. J. Meyer et al. 2016[105]
d	PS11/HER4 PS12/HER4	Doped NiO/ioITO	5	-0,25 NHE	-40 ≥ -15	700 ± 80 (700 ± 80)[2] n.r.	20[2] n.r.	86 ± 3 n.r.	T. J. Meyer et al. 2017[107]

Table I.1. Figures of merit of the reported dye-sensitized hydrogen-evolving photocathodes together with the different experimental conditions employed.

1. The nature of the electrolyte is not taken into account in this table.

2. Calculated based on the numerical values provided in the studies.

2) Kinetic issues

The few reported NiO-photocathodes still exhibit low activity in terms of photocurrent densities and TON compared to TiO_2 photoanodes. In **Figure I.5**, the photoinduced processes occurring in dye-sensitized photocathode based on a covalently linked dye-catalyst assembly are depicted. Upon light excitation, fast hole injection occurs resulting in a charge separated state with a hole on NiO and an electron on the photosensitizer. Competition between charge recombination and catalysis, after thermal electron transfer from the reduced dye to the catalyst, is believed to be the main kinetic issue (**Figure I.5**).

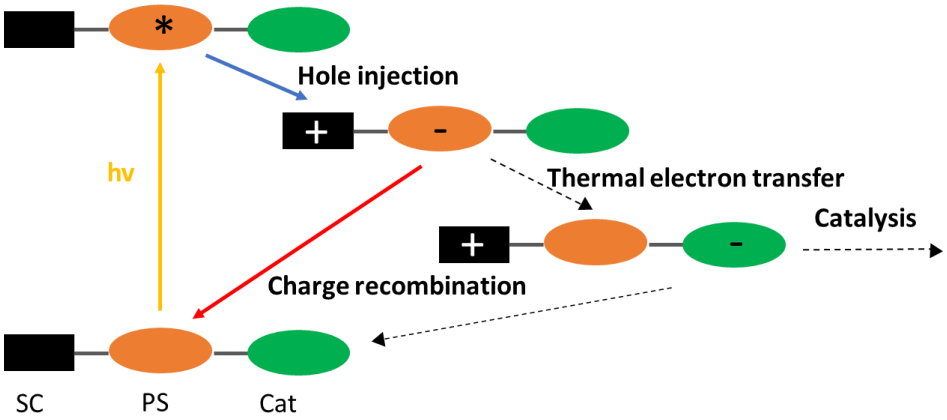

Figure I.5.Photoinduced processes in a dye-sensitized photocathode based on a covalent dye-catalyst assembly.

The origin of these unwanted recombination pathways was enlightened for NiO-based DSSCs.[117] One of the sources behind these detrimental procedures is the hole extinction coefficient 10^{-8}-10^{-7} cm^2 s^{-1}, which was estimated two times lower than for TiO_2 photoanodes.[118,119] In addition, Ni^{3+} defect species can act as hole (Ni^{4+}) and electron traps.[117,120,121] Atomic layer deposition (ALD) of thin layers of insulating Al_2O_3 onto NiO electrodes before sensitization was employed to slow down the recombination processes,[122,123] but undesirable slower electron injection from the semiconductor to the photosensitizer can occur with increasing number of ALD cycles.[124] Hence, a compromise between slower recombination and slower electron injection should be considered for optimization of the systems. Nevertheless, ALD-treatment was used for hydrogen-evolving photocathodes, showing a beneficial impact.[86,105] Efforts to replace NiO with other materials to increase the efficiency of H_2-evolving photocathodes are ongoing with some interesting preliminary results. Delafossites (such as $CuGaO_2$, $CuCrO_2$)[99,100,101,102,103] is another family of metal oxides with interesting

properties for both p-type DSSCs and DSPECs. Materials like CuO[125] and conductive ITO[105,126] with fast hole mobility could also offer alternative solutions.

It should be noted that most photophysical studies performed on NiO-photocathodes to address the kinetics of electron transfers were not recorded under operando conditions and especially under the potential applied for the PEC tests. However, recent studies by the group of L. Hammarström and T. J. Meyer revealed that charge recombination kinetics are strongly affected by the potential applied to the NiO film.[117,121] In particular, transient absorption measurements recorded on films sensitized with the ruthenium phosphonate complex $[(Ru(bpy)_2\ (bpyPO_3H_2)]^{2+}$ established that the lifetime of the charge separated state (hole on NiO and reduced dye) is drastically increased when potentials more negative than OCP are applied to the electrode.[121] This has also prevented to study the following processes that are the thermal electron transfer from the reduced dye to the catalyst and the charge recombination between the reduced catalyst and the NiO. In particular, the formation of the reduced catalyst has never been observed for dye-sensitized hydrogen-evolving photocathodes based on cobalt catalysts.

3) Stability issues

Long-term stability is another limiting factor for the efficiency of the dye-sensitized photocathodes. However, only a few studies addressed this issue by performing post-operando analysis to find out the destiny of the molecular components.[98] Most of the systems exhibit low stability due to desorption of the molecular components from the surface. Thus, more robust anchoring groups or stabilizing methods should be found. Atomic layer deposition of thin layers of Al_2O_3 can also contribute to decrease desorption.[84] Meyer's group proposed a what he called "mummy" strategy.[127] After grafting of a Ru-complex onto TiO_2, Al_2O_3 ALD used for protection and for consequent grafting of a WOC. In a final step, Al_2O_3 ALD was employed for further catalyst stabilization and the photoanode successfully oxidized water.

For the different systems, the same catalysts are repeated and notably complexes based on cobalt and nickel. As far as cobalt catalysts concern, their decomposition under experimental conditions is speculated to be a limiting factor. More stable and robust catalysts should be employed to face this detrimental phenomenon, like polypyridyl cobalt complexes that showed resistance under reductive conditions.[128,129,130]

Analyzing the state-of-the-art photocathodes, ideas of the path that we should follow can be extracted and more specifically:

- *The various reported experimental parameters make it difficult to rationalize the activity of the different systems. Thus, we will assess the performance of the new photocathodes under strictly identical conditions to rationally improve the molecular design.*
- *The kinetics of the electron transfer under the potential applied for the photoelectrochemical experiments are unexplored. In this sense, we will undertake photophysical studies under quasi-operando conditions in order to understand the bottleneck of the electron transfer.*
- *Post-operando analysis is insufficient for a clear understanding of the fate of the molecular components. Undertaking in-depth characterization could help selecting more robust components and optimizing the molecular assemblies.*

Chapter II

Synthesis and characterization in solution of a novel dye-catalyst assembly based on the cobalt diimine-dioxime complex

In this chapter, the synthesis and characterization of a dye-catalyst assembly, **RuP_4^{OEt}-Co**, relying on a ruthenium tris-diimine photosensitizer functionalized with four methyl phosphonate groups for a covalent anchoring onto semiconducting films and covalently linked to the cobalt diimine-dioxime catalyst is presented (**Scheme II.1**). The choice of the components is not random, as we will rely on existing knowledge from the group and this part of my thesis project directly follows-up on Nicolas Queyriaux PhD thesis (defended in March 2016). In our effort to obtain a rational study for dye-sensitized photocathodes, we decided to synthesize a molecular architecture similar to the first reported dyad (**Dyad 2**)[87] with a different light harvesting unit, keeping the catalyst and the triazole assembly identical.

The structure of the light harvester, bearing a functionalized imidazo [4,5-f][1,10]phenanthroline ligand, stems from supramolecular ruthenium-based assemblies studied for photocatalytic proton reduction.[23,24] Furthermore, the decision to functionalize the dye with four methyl phosphonate groups is inspired by our model NiO photocathodes sensitized by ruthenium complexes.[55] Finally, an optimized protocol using copper-catalyzed azide-alkyne cycloaddition for coupling the two subunits will be employed for the construction of the final assembly.[87,131]

The redox and spectroscopic properties of the final dyad will be also evaluated. Thermodynamic considerations supported by transient absorption spectroscopy and spectro-photochemical measurements will be presented to analyze the feasibility of the working mechanism onto NiO electrodes. We should note that the anchoring groups were protected until the end of this chapter for solution studies.

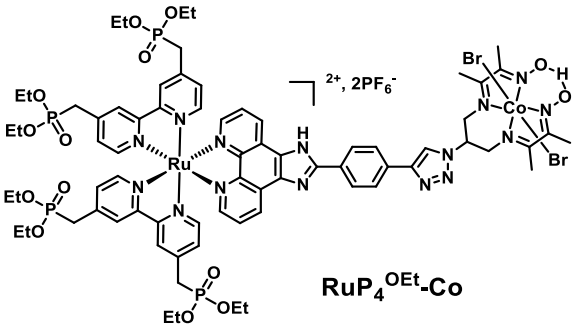

Chart II.1. Structure of **RuP_4^{OEt}-Co**.

I. Synthetic strategy

In **Scheme II.1**, two proposed synthetic routes are depicted for the preparation of **RuP_4^{OEt}-Co**, which will be analyzed in the following part.

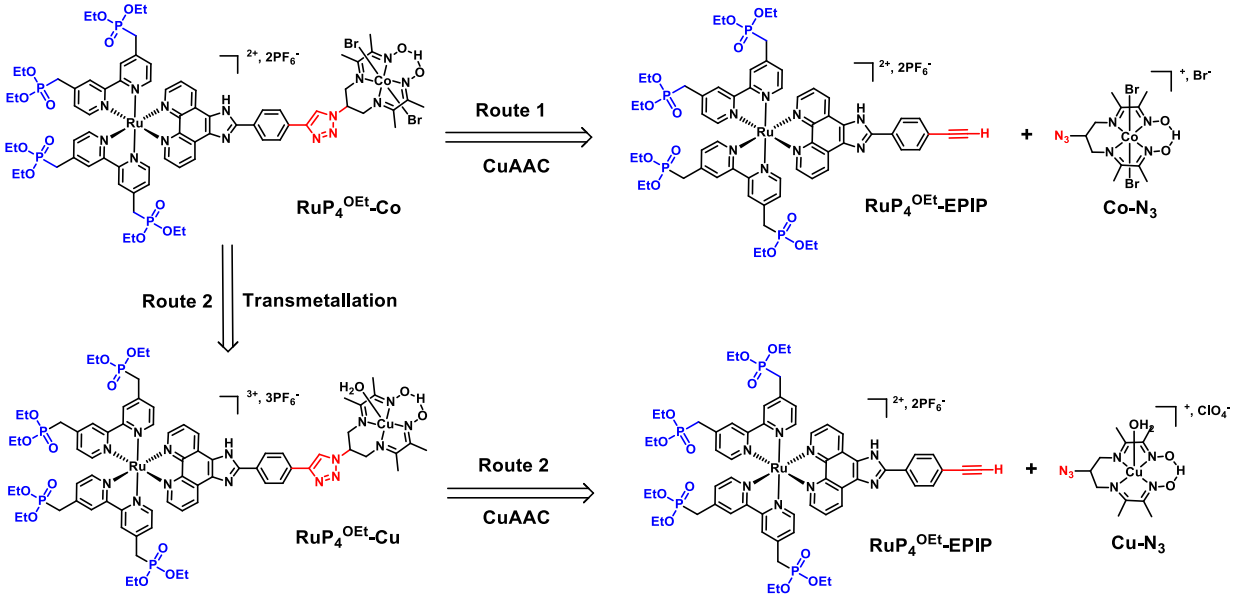

Scheme II.1. Two proposed synthetic routes for the preparation of **RuP_4^{OEt}-Co**.

1) Copper-catalyzed Azide-Alkyne Cycloaddition (CuAAC) coupling

Efficient and modular synthetic strategies to combine in a single molecule a photosensitizer and an electroactive catalytic unit appear particularly interesting, even though the preparation can be synthetically demanding. We selected Copper-catalyzed Azide-Alkyne Cycloaddition (CuAAC), established by Sharpless in 2002,[132] one of the most famous examples of "click" chemistry.[88] Regioselectivity to give 1,4-disubstituted 1,2,3-triazoles, mild experimental conditions, high yields and compatibility with most organic and metallo-organic functions are the main advantages of this synthetic tool. Examples of ruthenium tris-diimine assemblies coupled with a molecular moiety using CuAAC have been already reported.[133,134]

Route 1, where **Co-N_3** can be coupled through CuAAC with **RuP_4^{OEt}-EPIP**, is the most obvious one to build the dyad. However, we observed that under standard copper-catalyzed conditions for the azide-alkyne cycloaddition reaction, partial substitution of the cobalt center of the catalyst by copper ions can occur.[68] In parallel, a second route was developed by our group based on the use of the copper diimine-dioxime complex **Cu-N_3**, to perform the CuAAC coupling either with a push-pull organic dye[87] or a ruthenium tris-diimine complex functionalized with an alkyne group, which was the first example of a paramagnetic binuclear Ru(II)-Cu(II) complex (**Ru-Cu**) efficiently produced using click chemistry (**Scheme II.2**).[131]

In the case of the push-pull organic dye, the targeted dyad (**Dyad 2**) was isolated after performing transmetallation from copper to cobalt. Thus, the second route will be employed in order to prepare our final dye-catalyst assembly (**RuP$_4^{OEt}$-Co**).

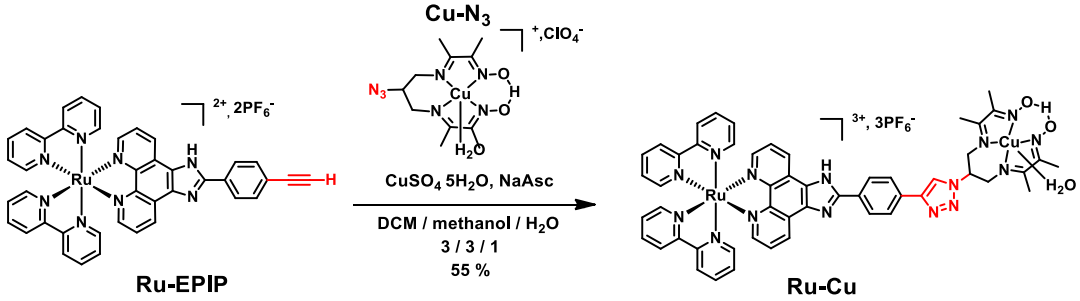

Scheme II.2. CuAAC to obtain the paramagnetic **Ru-Cu** dyad.

2) Functionalization with methyl phosphonate groups

Grafting of the molecular components onto semiconducting materials is crucial for the overall activity. Ruthenium-polypyridine photosensitizers are widely used for both photoanode and photocathode applications due to their long-lived photoexcited state, strong visible absorption and chemical stability.[135] Various synthetic modifications, consisting of two main steps, are well-described to tune their redox and spectroscopic properties. Initially, ligands are synthesized and purified and coordination on ruthenium follows. Despite its dominant role for the synthesis of ruthenium polypyridine complexes, 'chemistry on the complex' is an alternative with limited usage.[136] Different coordination routes have been developed starting by various ruthenium precursors, like $[Ru(DMSO)_4Cl_2]$, $[Ru(arene)Cl_2]_2$ where arene = cymene, benzene, etc. or $RuCl_3$ hydrate.[137,138]

Based on the model photocathodes sensitized by ruthenium complexes from the group, four methyl phosphonate anchoring groups increased the dye loading onto NiO films, without modifying the electronic properties of the complex.[55] Two main synthetic routes to prepare ruthenium dyes with four methyl phosphonate anchoring groups (**Scheme II.3**) have been reported. The first one, called traditional route[22,139,140,141,142] relies on the preparation of the [cis-$Ru(4,4'-(CH_2PO_3Et_2)_2\text{-bpy})_2Cl_2$] intermediate, while the second approach developed in 2010 exploits the properties of organometallic ruthenium complexes.[138,143,144] With the traditional route, the anchoring groups are introduced first followed by the substituted bpy ligand, while the latter route proceeds in the opposite order.

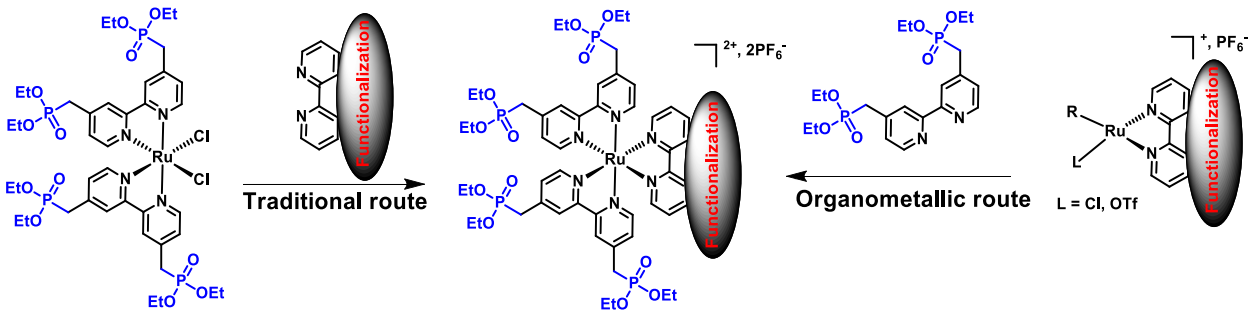

Scheme II.3. Schematic representation of the two synthetic routes to prepare ruthenium complexes with four methyl phosphonate groups.

In a recent publication, we evaluated the efficiency of both methods for the preparation of ruthenium complexes with substituted bpy or phen ligands.[145] Poor orthogonality due to reactive organometallic intermediates prevented us to prepare **RuP4^{OEt}-dppz** or **RuP4^{OEt}-phendione** by the organometallic route (**Chart II.2**). In addition, protection of the **EPIP** ligand[146] by a trimethylsilyl group (**TMS**) was mandatory to avoid alkyne coordination to the Ru center or hydration of the triple bond.[147]

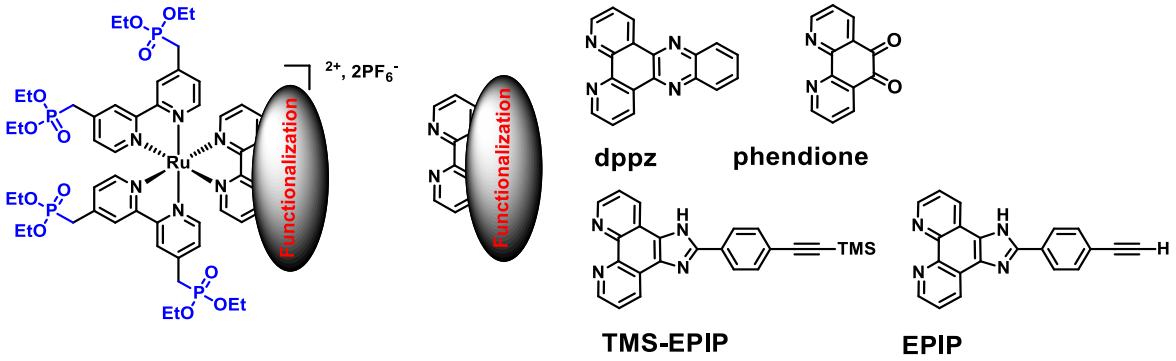

Chart II.2. Ruthenium complexes bearing four methyl phosphonate anchoring groups and functionalized by various diimine ligands.

The synthetic limitations encountered with the organometallic route forced us to re-examine the traditional approach and in particular the procedure reported by the group of S. Rau in order to prepare **RuP4^{OEt}-phendione**, starting from $Ru(DMSO)_4Cl_2$.[22] The intermediate product after the introduction of the methyl phosphonate groups ($[cis\text{-}Ru(4,4'\text{-}(CH_2PO_3Et_2)_2\text{-}bpy)_2Cl_{2-x}(DMSO)_x]Cl_x$) was not purified and used immediately to the next reaction to obtain the final complex in high yields (86% overall crude yield). We reproduced this synthesis with 78% yield, and we were able to isolate **RuP4^{OEt}-dppz** (55% yield). **RuP4^{OEt}-TMS-EPIP** and **RuP4^{OEt}-EPIP** were also synthesized with lower yields (20% and 30% accordingly) and protection of the terminal alkyne is not required anymore with this procedure. Hence, the traditional route is

a more efficient and straightforward way to prepare different ruthenium derivatives bearing four methyl phosphonate groups. The synthesis of the last two complexes will be presented in more details in the following part of this chapter.

II. Synthesis of RuP_4^{OEt}-Co

1) Preparation of RuP_4^{OEt}-EPIP

We synthesized **RuP_4^{OEt}-EPIP** through two different synthetic routes (**Scheme II.4**, **5**):

i) TMS-protected route

Starting from the commercially available compound, $Ru(dmso)_4Cl_2$,[148] we were able to obtain **RuP_4^{OEt}-EPIP** (**Scheme II.4**) in three steps.[145] The intermediate [*cis*-Ru(4,4′-$(CH_2PO_3Et_2)_2$-bpy)$_2Cl_{2-x}(DMSO)_x]Cl_x$ of the first reaction was not purified and could be stored under argon for days. We proceeded to the next reaction using an average molecular weight (1160 $g.mol^{-1}$) and the **TMS-EPIP** ligand,[146] which was already available in the lab, in a mixture of ethanol and water (3/1) under argon.

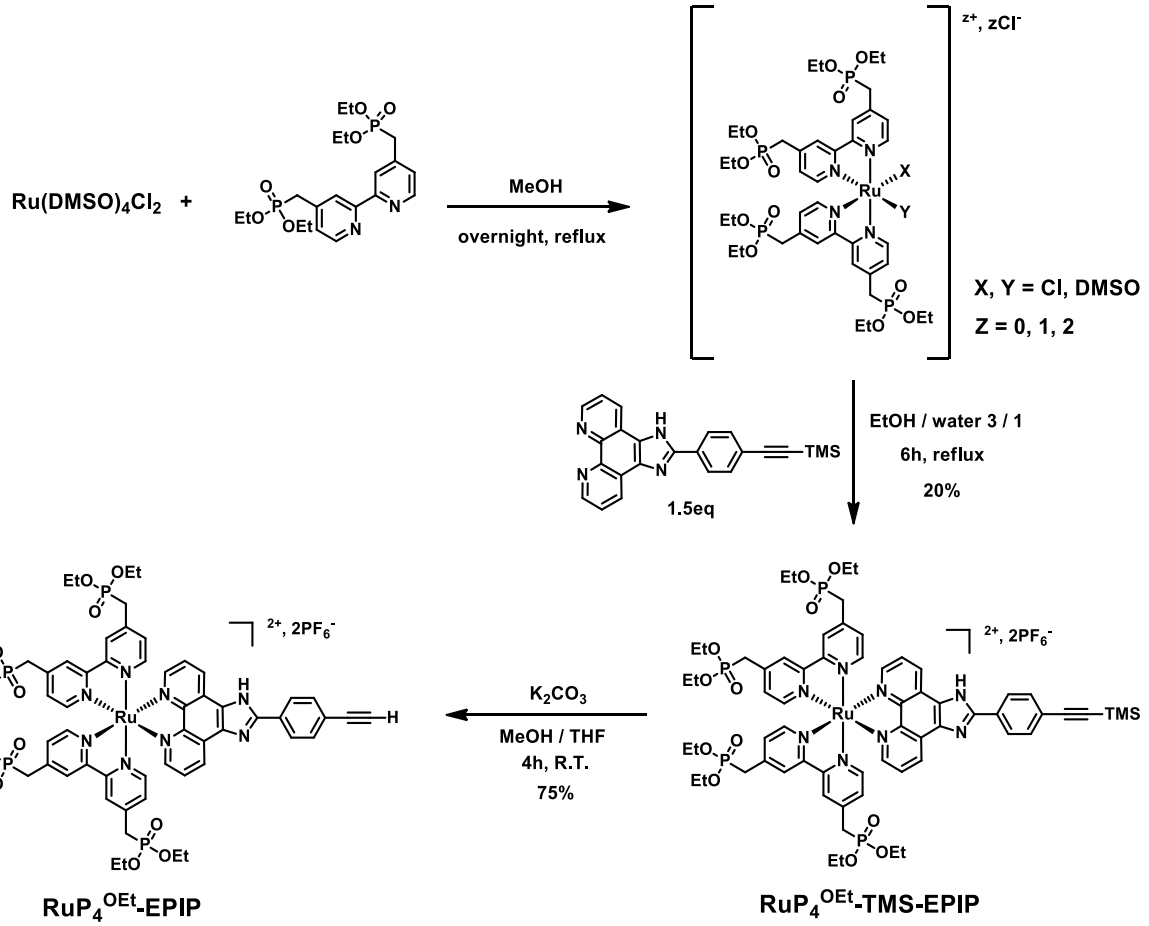

Scheme II.4. Synthetic procedure for the preparation of **RuP_4^{OEt}-EPIP** through the TMS-protected ligand**.**

A disappointing 10% yield was obtained during our first attempts. By increasing the amount of ligand to 1.5 eq, the yield was improved to 20%. Purification was achieved by column chromatography on silica gel with gradient elution (MeCN/aqueous 0.4 M KNO_3, from 98:2 to 90:10). Addition of saturated aqueous solution of KPF_6, did not precipitate the desired compound and further extraction with DCM was needed to isolate **RuP_4^{OEt}-TMS-EPIP**. The final compound has been characterized by ^1H and ^{13}C NMR, ESI-MS, HRMS and elemental analysis (see experimental part). The main peak from ESI-MS at m/z: 703.4 with the characteristic isotopic pattern for ruthenium is attributed to $[M-2PF_6]^{2+}$. Deprotection of the triple bond of **RuP_4^{OEt}-TMS-EPIP** in basic conditions (K_2CO_3) resulted the desired compound (**RuP_4^{OEt}-EPIP**) with hexafluorophosphate as counter ions after addition of KPF_6 and with the same purification protocol already presented.

ii) Direct route

We succeeded to prepare **RuP_4^{OEt}-EPIP** in 30% yield by directly reacting **EPIP** ligand with [*cis*-Ru(4,4′-$(CH_2PO_3Et_2)_2$-bpy)$_2Cl_{2-x}(DMSO)_x]Cl_x$ **(Scheme II.5)**. Maximum yield was 30%, after increasing the temperature and using 1.5 eq of the ligand. This procedure is more straightforward, as it contains one less reaction and purification step. Thus, we adopted this procedure for the synthesis of **RuP_4^{OEt}-EPIP**. The final compound was characterized by NMR (more details in the corresponding part) and mass spectrometry. The expected peak in ESI-MS at m/z: 667.3 for $[M-2PF_6]^{2+}$ is a proof for the isolation of the right complex. During the preparation of **RuP_4^{OEt}-EPIP**, we observed by-products with partly hydrolyzed phosphonate groups, which are retained on silica gel column and could give a possible explanation for the low final yields.[148]

EPIP ligand was prepared by Debus-Radziszewski condensation between the 4-ethynylbenzaldehyde and the phendione (**Scheme II.5**).[146] After neutralization with aqueous NH_4OH, the precipitate was filtered and we obtained the desired ligand with 90% yield (m/z: 321.3 for $[M+H]^+$).

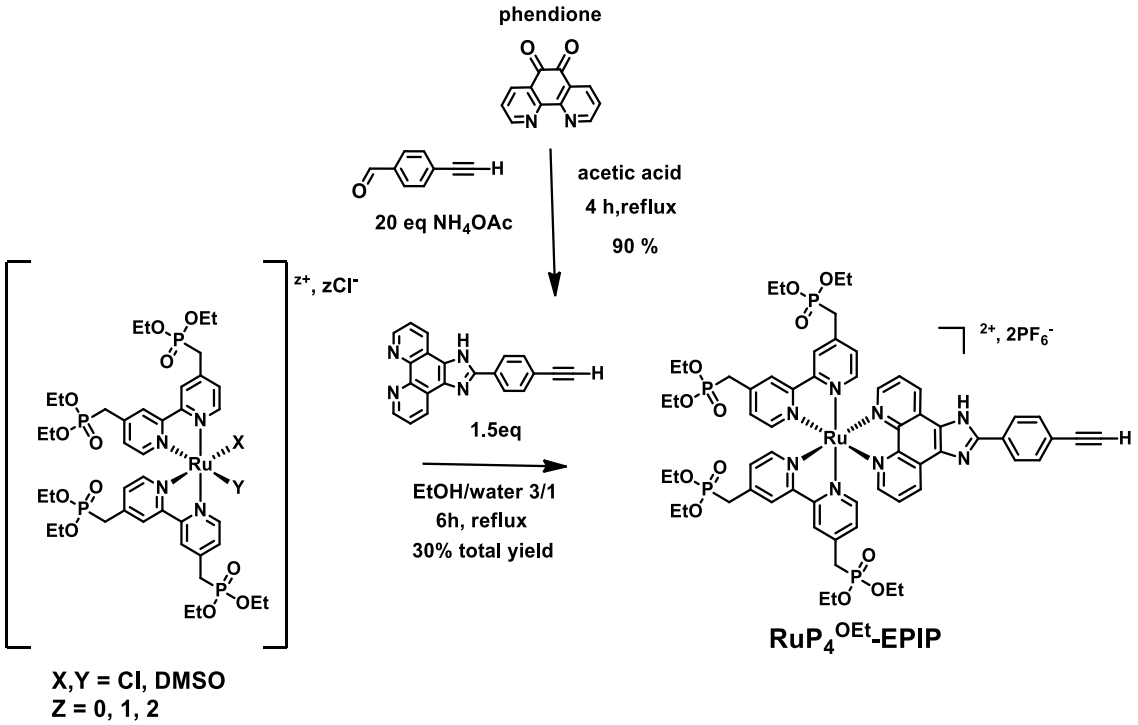

Scheme II.5. Synthetic procedure for the preparation of **RuP_4^{OEt}-EPIP** through the direct route.

2) Preparation of Cu-N_3

The *N2,N2'*-2-azidopropanediylbis(2,3-butadione-2-imine-3-oxime) ligand was custom-synthesized by the company "Provence Technologies" following a reported procedure.[68] A concentrated solution of $CuClO_4.6H_2O$ in acetone was added in a hot ligand solution (acetone) under stirring (**Scheme II.6**).[87,131,149] The reaction mixture was left standing at room temperature overnight and the precipitate was filtrated, yielding the paramagnetic **Cu-N_3**.

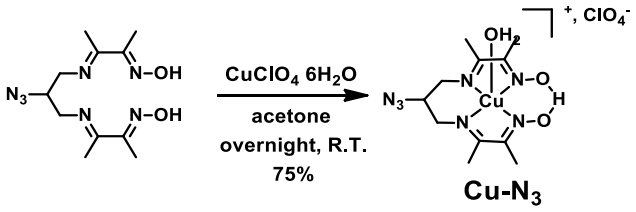

Scheme II.6. Synthesis of **Cu-N_3**.

3) CuAAC coupling

RuP_4^{OEt}-EPIP and **Cu-N_3** are ready to be coupled. The optimized synthetic procedure to obtain **Ru-Cu**[131] was successfully applied to yield the paramagnetic **RuP_4^{OEt}-Cu** dyad (**Scheme II.7**). $CuSO_4$ is reduced in situ to catalytic Cu(I) species by an excess of sodium ascorbate under inert atmosphere. A mixture of three solvents (DCM/MeOH/H_2O) is essential for a homogeneous solution. The reaction mixture is left under stirring for 2 days at room temperature and protected from light. Purification was accomplished on silica gel column chromatography with a gradient elution of MeCN/aqueous 0.4 M KNO_3 (from 95/5 to 80/20). The final dyad was isolated as a hexafluorophosphate salt after extraction with DCM with 55% yield. Due to its paramagnetic nature, NMR was not used for the characterization. The final structure was confirmed by ESI-MS with a main peak at m/z: 559.3 for $[M\text{-}H_2O\text{-}3PF_6]^{3+}$ with a characteristic isotopic pattern.

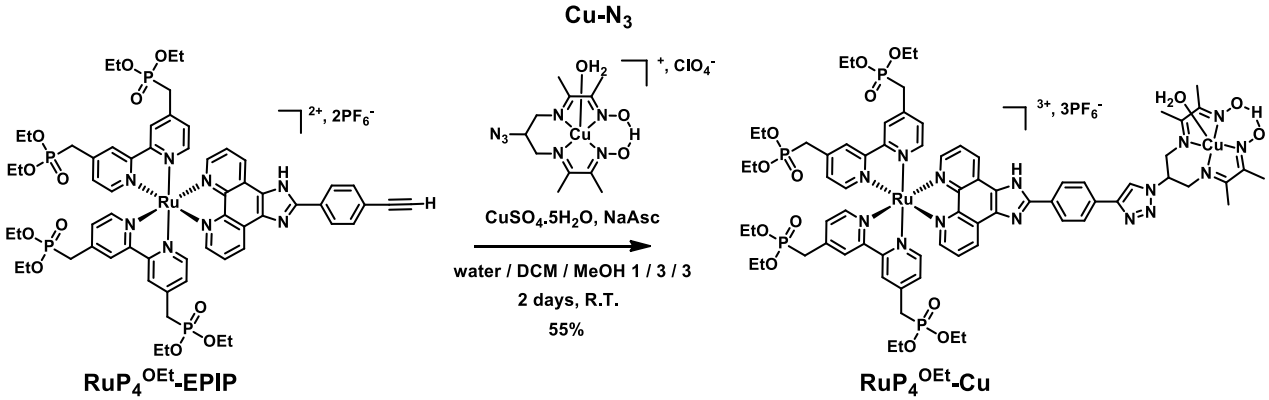

Scheme II.7. CuAAC to obtain the paramagnetic **RuP_4^{OEt}-Cu.**

4) Transmetallation from RuP_4^{OEt}-Cu to RuP_4^{OEt}-Co

A key step for the synthesis of the final dyad is the exchange from copper to cobalt (**Scheme II.8**).[87,98] Initially, we performed this reaction using **Ru-Cu**, after resynthesizing the complex (**Scheme II.2**).[131] We decided to work first with **Ru-Cu**, as the absence of phosphonate groups could be beneficial for the efficient transmetallation and isolation of the dyad. In addition, the final **Ru-Co** dyad could also serve as a reference system for photophysical studies. Metal exchange occurs by reacting the copper-derivative complex (**Ru-Cu**) with a Co(II)-salt (in our case $CoBr_2$.hydrate) in acetone under air bubbling for the oxidation of Co(II) to Co(III) species, a more stable derivative. In contrast to previous dyads with organic dyes, ruthenium compounds exhibit poor solubility in acetone, affected by its charged nature, and addition of methanol was needed. After purification with column chromatography on silica gel using a mixture of acetone/H_2O/aqueous KBr 90/9/1, we obtained **Ru-Co** in 60% yield.

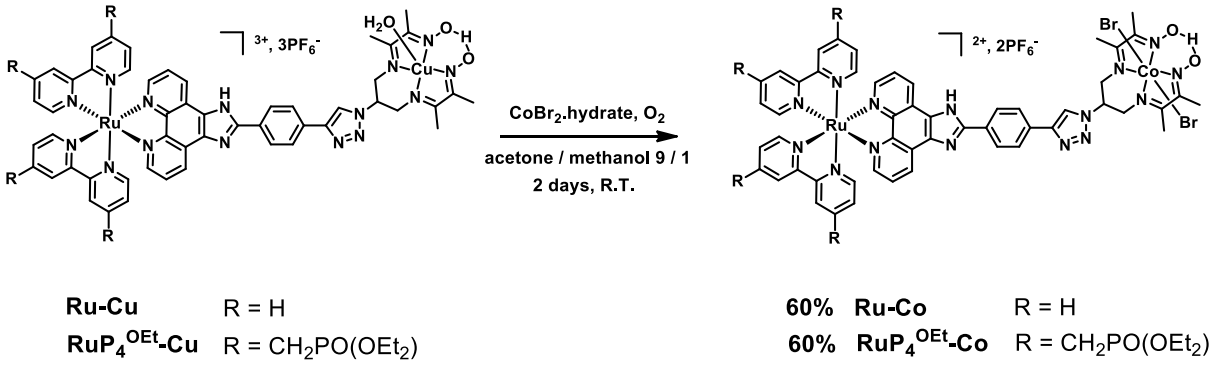

Scheme II.8. Transmetallation procedure to obtain the final ruthenium-cobalt assemblies.

RuP_4^{OEt}-Co was isolated (as a hexafluorophosphate salt) in 60% yield with the same synthetic and purification protocol. The main peak in HRMS and ESI-MS with a characteristic isotopic pattern at m/z: 916.6 for $[M-2PF_6]^{2+}$ is a good proof for the final dye-catalyst assembly. In addition, the diamagnetic dyad was confirmed by ^{1}H-NMR (see corresponding part below).

5) ^{1}H NMR characterization

^{1}H NMR spectra of the compounds were recorded in CD_3CN. The presence of 4 methyl phosphonate groups is undoubtedly with 8 protons for the methylene spacer, 16 and 24 protons for the ethyl part of the phosphonate groups (**Figure II.1**).

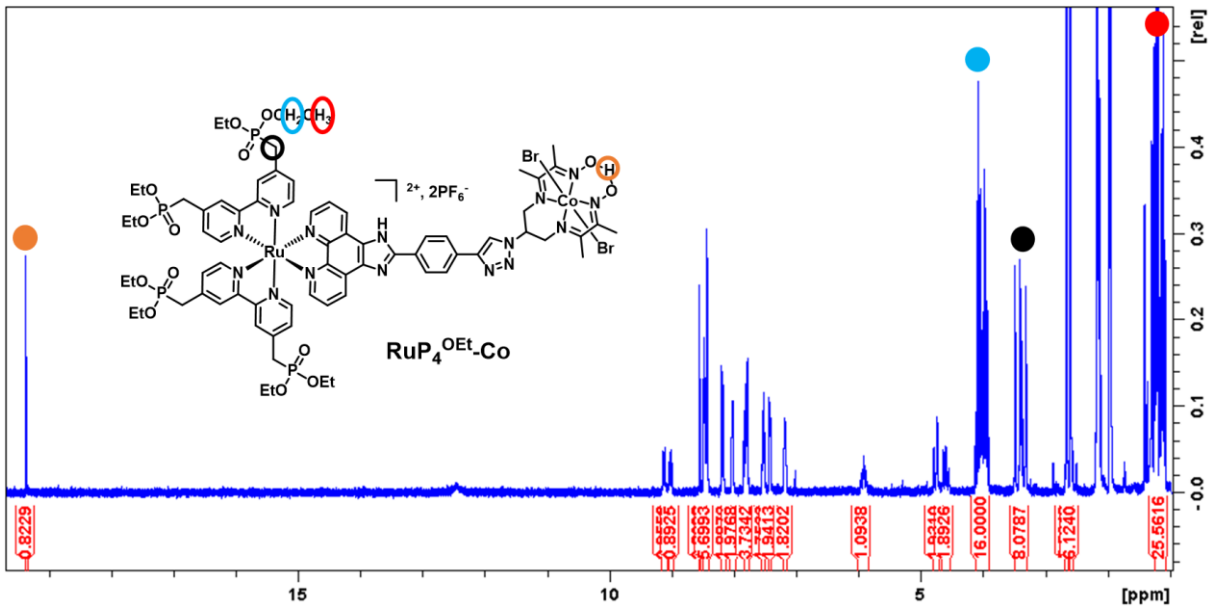

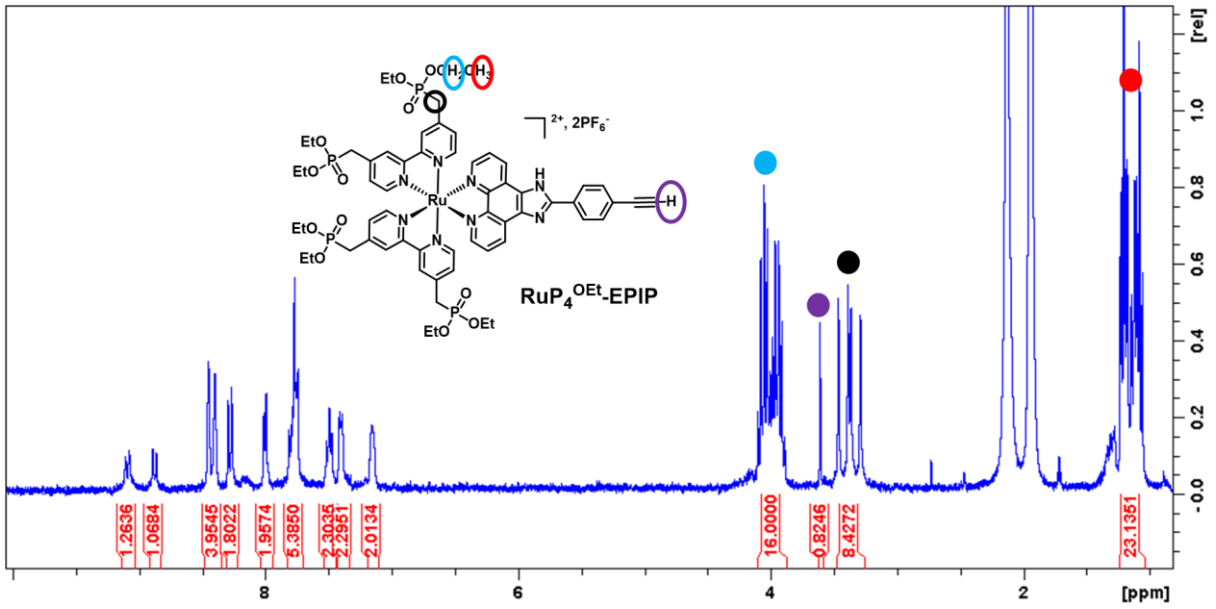

Figure II.1. ^{1}H NMR spectra of **RuP$_4^{OEt}$-Co** (top) and **RuP$_4^{OEt}$-EPIP** (bottom) recorded in CD_3CN.

Comparing the spectra of **RuP$_4^{OEt}$-EPIP** and **RuP$_4^{OEt}$-Co**, specific peaks are characteristic of the efficient isolation of the final dyad:

- A single peak at 19.35 ppm, assigned to the proton of the oxime bridge of the cobalt catalyst is the footprint of **RuP$_4^{OEt}$-Co** (**Figure II.1**).
- A single peak at 8.53 ppm, which corresponds to the proton of the triazole unit along with the disappearance of the peak for the alkyne at 3.60 ppm (**Figure II.2**). Thus, the CuAAC worked efficiently with 1,2,3-triazole ring formation.
- A triplet at 5.89 ppm, which corresponds to the proton α to the triazole unit.
- Multiple peaks in the region 4.78-4.57 ppm for the 4 methylene protons of the diimine-dioxime ligand and 2 singlets at 2.67 and 2.60 ppm integrating each for 6 protons are the 4 methyl groups of the cobalt complex (**Figure II.2**).

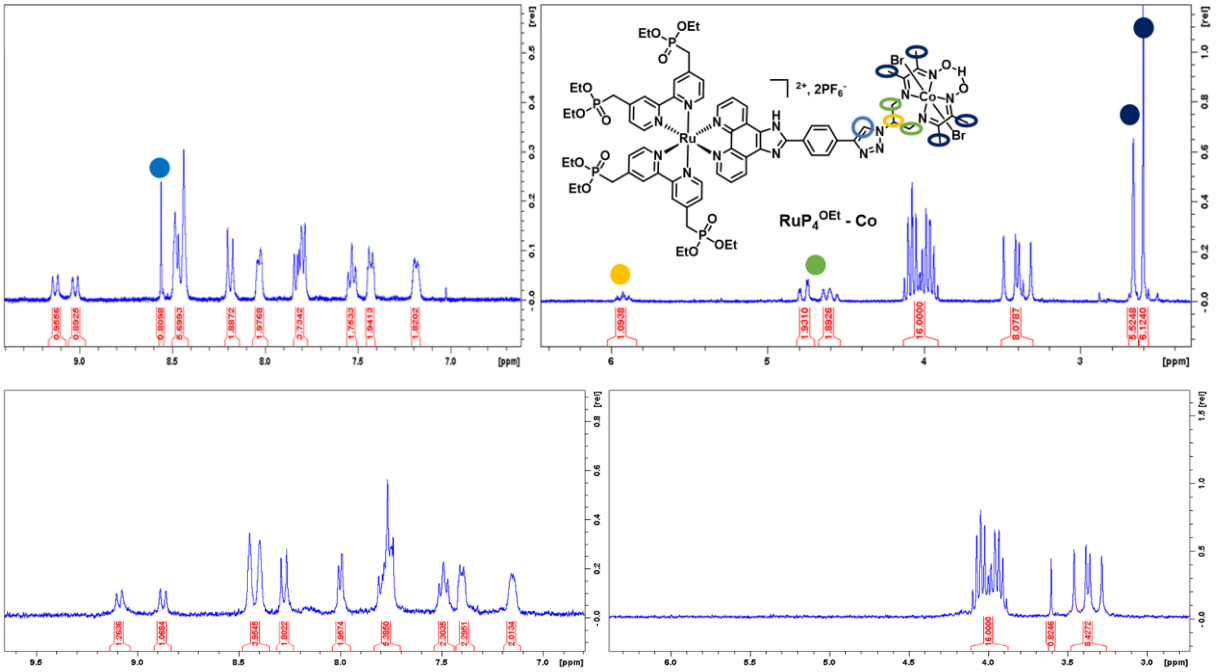

Figure II.2. Selected regions of ^{1}H NMR spectra of **RuP$_4^{OEt}$-Co** (top) and **RuP$_4^{OEt}$-EPIP** (bottom) recorded in CD_3CN.

III. Determination of the redox and spectroscopic properties of RuP$_4^{OEt}$-Co

1) Electrochemical characterization

i) Analysis of the redox couples

The electrochemical behavior of complexes **RuP$_4^{OEt}$-EPIP**, **RuP$_4^{OEt}$-Co** and **Co-N$_3$** (as a reference) were evaluated by cyclic voltammetry under inert conditions in acetonitrile (0.1 M *n*Bu$_4$NPF$_6$) at a glassy carbon working electrode at 100 mV·s^{-1} and referenced to the ferrocenium/ferrocene couple (Fc$^{+/0}$). The cyclic voltammograms are presented in **Figure II.3** and the potentials attributed to redox features are summarized in **Table II.1**.

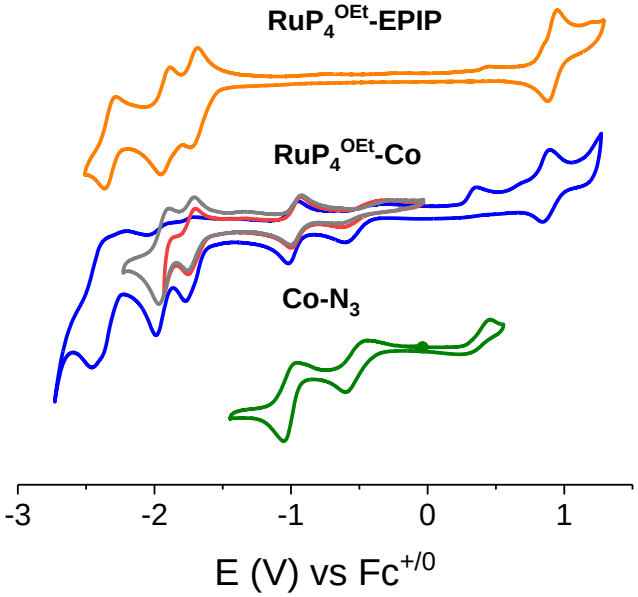

Figure II.3. Cyclic voltammograms of **RuP_4^{OEt}-EPIP**, **RuP_4^{OEt}-Co** and **Co-N_3** vs. $Fc^{+/0}$. Measurements were carried out at 100 $mV \cdot s^{-1}$ at a glassy carbon electrode in acetonitrile (0.1M nBu$_4$NPF$_6$) under inert atmosphere.

The cyclic voltammogram of **RuP_4^{OEt}-Co** displays several events. On the anodic part, a reversible oxidation peak at + 0.89 V vs $Fc^{+/0}$ associated to the metal-centered oxidation[55] of Ru(II) to Ru(III) correlates well with the oxidation wave of **RuP_4^{OEt}-EPIP at** + 0.92 V vs $Fc^{+/0}$. An additional irreversible oxidation peak is present at + 0.36 V vs $Fc^{+/0}$ for **RuP_4^{OEt}-Co**. This was initially attributed to the oxidation of the imidazole ring based on a study from A. Aukauloo and coworkers.[150] Comparing with the CV of **Co-N_3**, we could also postulate oxidation of the bromide axial ligands of the cobalt center.

Complexes	E_{ox1} $Ru^{II/III}$	E_{ox2}	E_{red1} $Co^{III/II}$	E_{red2} $Co^{II/I}$	E_{red3} Ru^{II}/Ru^{II}-$L^{\cdot-}$	E_{red4} Ru^{II}/Ru^{II}-$L^{\cdot-}$	E_{red5} Ru^{II}/Ru^{II}-$L^{\cdot-}$
RuP_4^{OEt}-Co	+ 0,89	+ 0,36	- 0,60	- 0,98	- 1,73	- 1,93	- 2,45
RuP_4^{OEt}-EPIP	+ 0,92				- 1,71	- 1,92	- 2,32
Co-N_3		+ 0,45	- 0,52	- 1,01			

Table II.1. Electrochemical properties of complexes **RuP_4^{OEt}-Co, RuP_4^{OEt}-EPIP** and **Co-N_3** (in V vs $Fc^{+/0}$).

On the cathodic part, two peaks were assigned to the reduction of the Co(III) center to Co(II) at - 0.60 V vs $Fc^{+/0}$ and then reduction of Co(II) to Co(I) at - 0.98 V vs $Fc^{+/0}$, by analogy with the **Co-N_3**. Three quasi-reversible electrochemical processes are monitored for **RuP_4^{OEt}-Co** at

-1.73 V, -1.93 V and -2.45 V vs $Fc^{+/0}$. These processes are ascribed to the reduction of the three polypyridine ligands and are in good agreement with the reduction waves of **RuP_4^{OEt}-EPIP**.

The electrochemical properties of the two separate components are present and quite unmodified in the final dye-catalyst assembly. This observation indicates that there is no electronic coupling between the two metallic centers at the ground state of the dyad.

ii) Spectro-electrochemical measurements

Following the analysis of the redox couples of the dyad, electrolysis of **RuP_4^{OEt}-Co** and UV-Vis monitoring will enable us to identify the spectroscopic signature of Co(II), Co(I) and Ru(I) species and subsequently perform transient absorption measurements. UV-Visible spectroelectrochemistry measurements were carried out in the glovebox in acetonitrile with a patterned "Honeycomb" Spectroelectrochemical Cell Kit (AKSTCKIT3) purchased by Pine Instrument Company (**Figure II.4**). A silver wire was used as the reference electrode and a gold as the working electrode. Prior to every measurement, a cyclic voltammogram was recorded in order to find the correct potential to apply for reduction to Co(II), Co(I) and Ru(I). At – 0.15 V applied potential, reduction to Co(II) state takes place and a positive absorption band with a maximum at around 500 nm arises (**blue line**).[151] Further reduction to Co(I) state at more negative potentials (-0.55 V), a double band with maxima at 600 and 720 nm appears (**orange line**). These results are in accordance with the previously reported Co(I) signature, obtained during the course of an electrolysis experiment with Co-diimine-dioxime complex.[98] Upon further reduction, we could observe the reduced species of the dye with a broad absorption at 369 and 534 nm, typical for Ru(I) species (**green line**).[152]

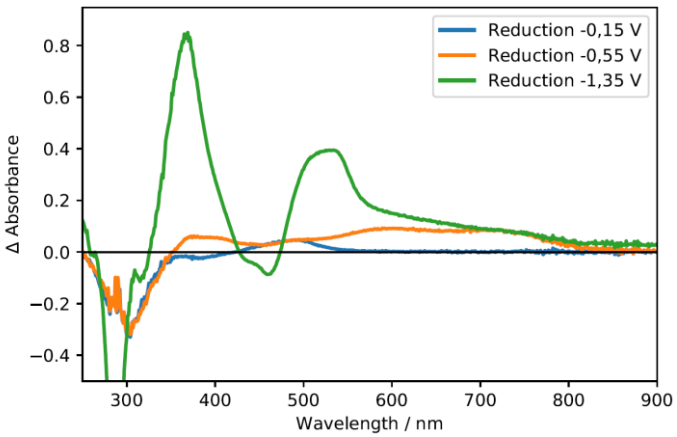

Figure II.4. Differential steady-state UV-Vis-SEC spectra of a 0.1 mM solution of **RuP_4^{OEt}-Co** in acetonitrile using 0.1 M $TBABF_4$ as electrolyte at different oxidation states of the catalyst and dye. All potentials were measured vs. Ag wire.

2) UV-Visible spectroscopy

i) Determination of molar extinction coefficients

The UV-Vis spectra of **RuP$_4^{OEt}$-EPIP**, **RuP$_4^{OEt}$-Co** and **Co-N$_3$** were recorded in acetonitrile (**Figure II.5**). The visible part of the spectra is dominated by the classical MLCT transition (double humped band)[135] with maxima for **RuP$_4^{OEt}$-Co** and **RuP$_4^{OEt}$-EPIP** at 462 nm (ε = 19700 $M^{-1}cm^{-1}$ and 19100 $M^{-1}cm^{-1}$ accordingly) and with a shoulder at 430 nm for both complexes. A small bathochromic shift on this region (5 to 7 nm), was previously observed for methyl phosphonate-functionalized complexes due to the weak electron donating character of the phosphonate groups, which can stabilize the bpy-based π^* orbital.[55,145] In the UV part, an intense band displayed at 291 nm (ε = 115000 $M^{-1}cm^{-1}$) for the dyad and at 290 nm (ε = 110000 $M^{-1}cm^{-1}$) for the ruthenium dye, is attributed to a π-π^* transition based on the polypyridine ligands. For both ruthenium-based complexes, the shoulder at around 350 nm and the tail at 500 nm can be attributed to transitions involving the imidazole ligand.[150] Moreover, a contribution from the Co-catalytic center in the near UV region is ascribed to ligand-centered transitions.

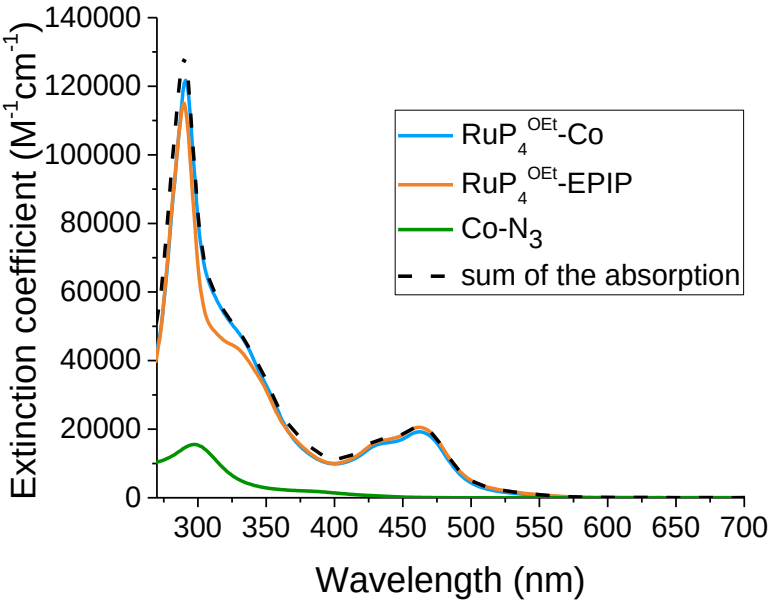

Figure II.5. UV-Visible absorption spectra of **RuP$_4^{OEt}$-Co** (blue line), **RuP$_4^{OEt}$-EPIP** (orange line), **Co-N$_3$** (green line) and sum of the absorption **Co-N$_3$** and **RuP$_4^{OEt}$-EPIP** (dashed line) recorded in acetonitrile.

The absorption spectra of the dyad correlates well with the sum of the absorption of the two separate components in **Figure II.5** (black dotted line). The fact that the spectroscopic properties remain almost unmodified between the precursor complexes and the dyad is again

an indication of an electron decoupling between the dye and the catalyst at the ground state of the dyad. An important feature, implying no significant modification of the properties of the two subunits in the final assembly.

ii) Protonation state of the imidazole bridge

The imidazole ring is part of the bridge connecting our chromophore with the cobalt complex. From the literature, it is known that the protonation state of this unit can modify the photophysical properties of similar ruthenium-polypyridine complexes.[150,153,154,155] In order to elucidate the protonation state of **RuP$_4^{OEt}$-Co**, titration measurements were performed using aliquots of TFA and TEA solutions (**Figure II.6**) in acetonitrile (1.1×10^{-5} M). No spectral changes were observed even when 2 eq. of TFA were added (**Figure II.6a**).

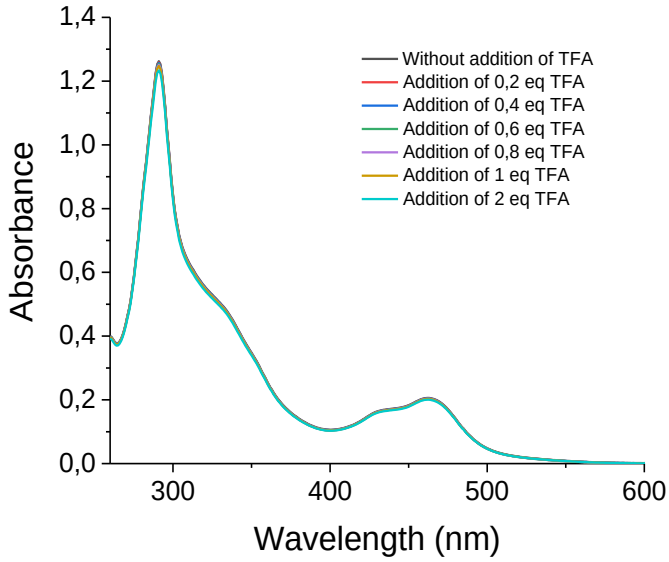

Figure II.6a. UV-Vis titration at the ground state of **RuP$_4^{OEt}$-Co** in acetonitrile (1.1×10^{-5} M) using aliquots of TFA solutions.

On the contrary, addition of TEA influenced the shape of the spectra (**Figure II.6b**). The main bands slightly decreased in intensity and the secondary ones (the two shoulders at 350 and 500 nm) increased. In addition, the formation of isosbestic points at 336, 420 and 475 nm indicates the formation of a new species.

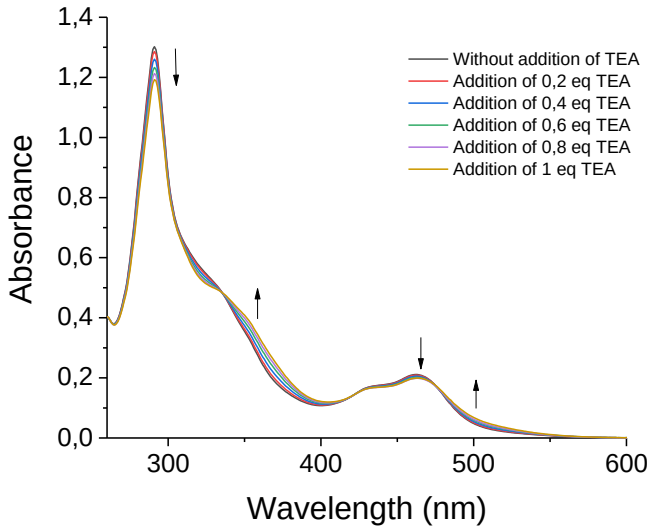

Figure II.6b. UV-Vis titration at the ground state of **RuP$_4^{OEt}$-Co** in acetonitrile (1.1×10^{-5} M) using aliquots of TEA solutions.

In agreement with A. Aukauloo's work,[150] this behavior is attributed to the protonated form of the imidazole ring for **RuP$_4^{OEt}$-Co** (**Chart II.3**). Similar spectra were obtained after titration measurements for **RuP$_4^{OEt}$-EPIP**, suggesting that at the end of the synthetic procedure, we isolated the complexes with a protonated imidazole ring. We should mention that the reaction yields and the ε values in **Figure II.5** have been calculated taking into consideration the protonated imidazole derivatives.

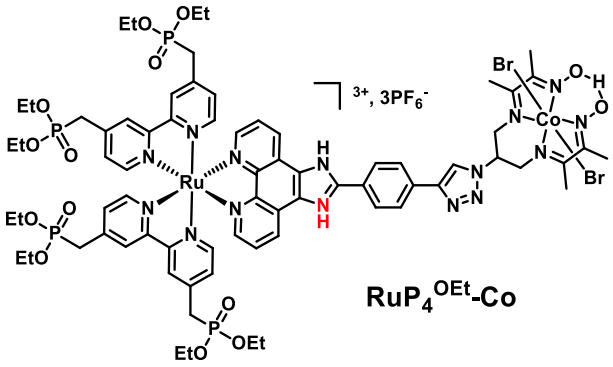

Chart II.3. Structure of **RuP$_4^{OEt}$-Co** eventually synthesized and confirmed after titration experiments.

It is worth noting that under our experimental conditions during the photoelectrochemical tests in Chapter III (aqueous solution at pH 5.5), **RuP$_4^{OEt}$-Co** is in its neutral form (**Chart II.1)**, based on the pKa for the imidazole ring calculated by Aukauloo and his group for similar ruthenium complexes (**Chart II.4**).[150] Values of 3.1 for the deprotonation of the iminium

fragment and 8.7 for the deprotonation of the secondary amine were estimated after titration experiments.

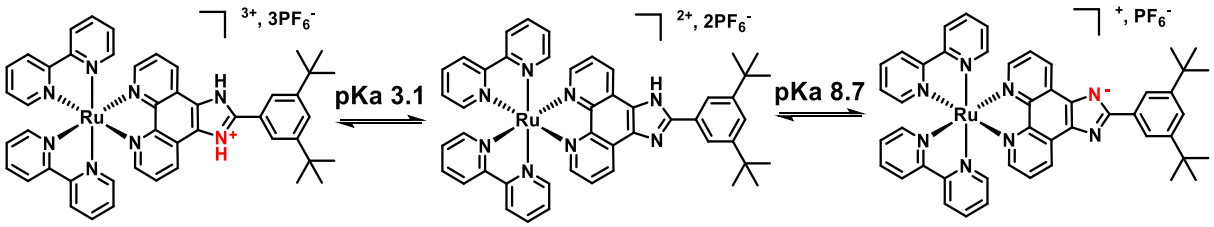

Chart II.4. Ruthenium polypyridine complexes issued from the three different protonation states of the imidazole ring and estimated pKa values by titration measurements under aqueous conditions.

The protonic state of the imidazole ring affects part of the photophysical properties of the compounds. Thus, some photophysical studies will be also carried out with the presence of 1 eq of base for efficient deprotonation of the imidazole unit. In addition, molar extinction coefficient was determined after addition of 1 eq of TEA and a lower value of 17700 $M^{-1}cm^{-1}$ was obtained for the MLCT transition at 463 nm for **RuP_4^{OEt}-Co**, in agreement with our titration experiments that the protonated complex exhibit higher MLCT band.

IV) Thermodynamic considerations

1) Feasibility of working mechanism on NiO electrodes

After synthesis and characterization of the final dye-catalyst assembly and before proceeding to the photoelectrochemical tests, it is crucial to check if thermodynamically our dyad is able to perform proton reduction. To be catalytically active, the Co(I) state (**Figure I.3**)[66] needs to be generated under light-driven conditions, in the presence of a source of electrons (a sacrificial electron donor in the solution or a semiconductor like NiO in the case of the photocathode). Two mechanisms can account for this Co(I) formation, either an oxidative or a reductive one (**Figure II.7**). In the latter, the excited PS can be quenched reductively by the supplier of electrons (NiO or SED), generating PS^-. Then, thermal intramolecular electron transfer from PS^- to the hydrogen evolution catalyst (HEC) will reduce Co(III) to Co(II). One more electron transfer to the cobalt center is needed to result a Co(I) species. The other path is a photoinduced intramolecular electron transfer from the excited dye to the catalyst (oxidative quenching) to obtain Co(II) with formation of PS^+. Regeneration of the oxidized PS occurs by the SED or NiO. Subsequently, a second photo-driven intramolecular electron transfer will reduce the

catalyst to Co(I). The relative viability of each of these two mechanisms is determined by the rates of the respective electron transfers.

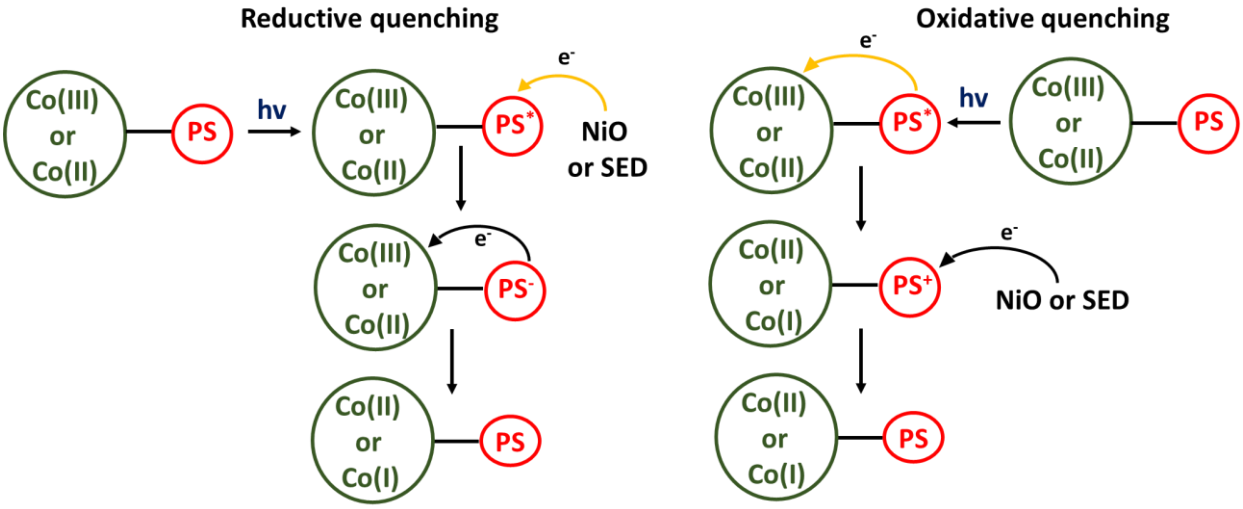

Figure II.7. Two possible mechanisms for the formation of Co(I) in a dye-catalyst assembly.

Previous transient absorption measurements in solution without the presence of any electron supplier excluded the photo-driven intramolecular electron transfer between the dye and the cobalt catalyst,[151] something that also proved in our system based on the first results with transient absorption spectroscopy from our collaborators in Germany in the group of Pr. B. Dietzek. Thus, oxidative quenching cannot occur and only the reductive one can account for the formation of Co(I).

In the next chapter, the PEC tests will be carried out at pH 5.5 with NiO as electron source and the basic principles of a NiO photocathode have been already presented in the first chapter. The NiO valence band edge potential at pH 5.5 was previously estimated to be + 0.46 V vs NHE[87] from the + 0.37 V vs NHE value determined at pH 7 by Wu and coworkers.[156] The energy of the excited state (E_{00}) for **RuP_4^{OEt}-Co** was estimated 2.01 eV from the maximum emission wavelength at 618 nm at room temperature in acetonitrile (recoded in Germany). From this value and the data in **Table II.2**, we could estimate a redox potential of + 0.81 V vs NHE for Ru^*/Ru^- with the following equation:

$$E(Ru^*/Ru^-) = E(Ru^{II}/Ru^{II}\text{-}L^{\bullet-}) + E_{00} \qquad \textbf{Eq. II.1}$$

where $E(Ru^{II}/Ru^{II}\text{-}L^{\bullet-})$ is E_{red3} = - 1.20 V vs NHE for **RuP_4^{OEt}-Co** (**Table II.2**).

Hole injection from the excited dye to the valence band of NiO is thermodynamically possible with ΔG_{inj} = - 0.35 eV using **Eq. II.2**. Generation of Co(II) and Co(I) from the reduced dye can occur with driving forces of ΔG_1 = - 1.13 eV and ΔG_2 = - 0.75 eV respectively (**Eq. II.3** and **4**).

$\Delta G_{inj} = e[E_{VB}(NiO) - E(Ru^{*}/Ru^{-})]$ **Eq. II.2**

$\Delta G_1 = e[E(Ru^{II}/Ru^{II}\text{-}L^{\bullet-}) - E(Co^{III/II})]$ **Eq. II.3**

$\Delta G_2 = e[E(Ru^{II}/Ru^{II}\text{-}L^{\bullet-}) - E(Co^{II/I})]$ **Eq. II.4**

where $E(Co^{III/II})$ and $E(Co^{II/I})$ are E_{red1} = - 0.07 V and E_{red2} = - 0.45 V vs NHE from **Table II.2**.

	E_{red1}[a] (Co^{III}/Co^{II})	E_{red2}[a] (Co^{II}/Co^{I})	E_{red3}[a] ($Ru^{II}/Ru^{II}\text{-}L^{\bullet-}$)	ΔG_{inj}[b]	ΔG_1[b]	ΔG_2[b]
Co-N_3	+ 0,01	- 0,48	-	-	-	-
RuP_4^{OEt}-EPIP	-	-	- 1,18	- 0,37	-	-
RuP_4^{OEt}-Co	- 0,07	- 0,45	- 1,20	- 0,35	- 1,13	- 0,75

Table II.2. Redox properties of **Co-N_3**, **RuP_4^{OEt}-EPIP** and **RuP_4^{OEt}-Co**.

a- In V vs NHE. The redox potentials were converted from $Fc^{+/0}$ (**Table II.1**) to NHE, considering $E°(Fc^{+/0})$ = + 0.53 V vs. NHE in acetonitrile.[157]

b- In eV.

From the estimated driving forces, hole injection from the excited dye to NiO and thermal intramolecular electron transfer from the reduced dye to the catalyst can thermodynamically take place. As far as the first reduction of the cobalt center concerns, spectroelectrochemical measurements implemented by the group on NiO electrodes with the cobalt diimine-dioxime complex, showed that the catalyst is at its Co(II) state without irradiation and further electron transfer is needed to be activated to Co(I).[98]

2) Photolysis experiment

Light irradiation and monitoring of the evolution of the UV-Visible spectra may give us experimental proof for the ability of our dyad to generate under homogeneous conditions the Co(I) reduced state of the catalyst, which is the entry point of the mechanism.[66] Photolysis experiments of **RuP_4^{OEt}-Co** (4.5×10^{-5} M) in degassed acetonitrile using TEOA as SED (10% v/v) with a Xe-lamp under visible light irradiation were performed, following already reported procedures from the group. [75,87] The time-dependent differential spectra of **RuP_4^{OEt}-Co** are presented in **Figure II.8**.

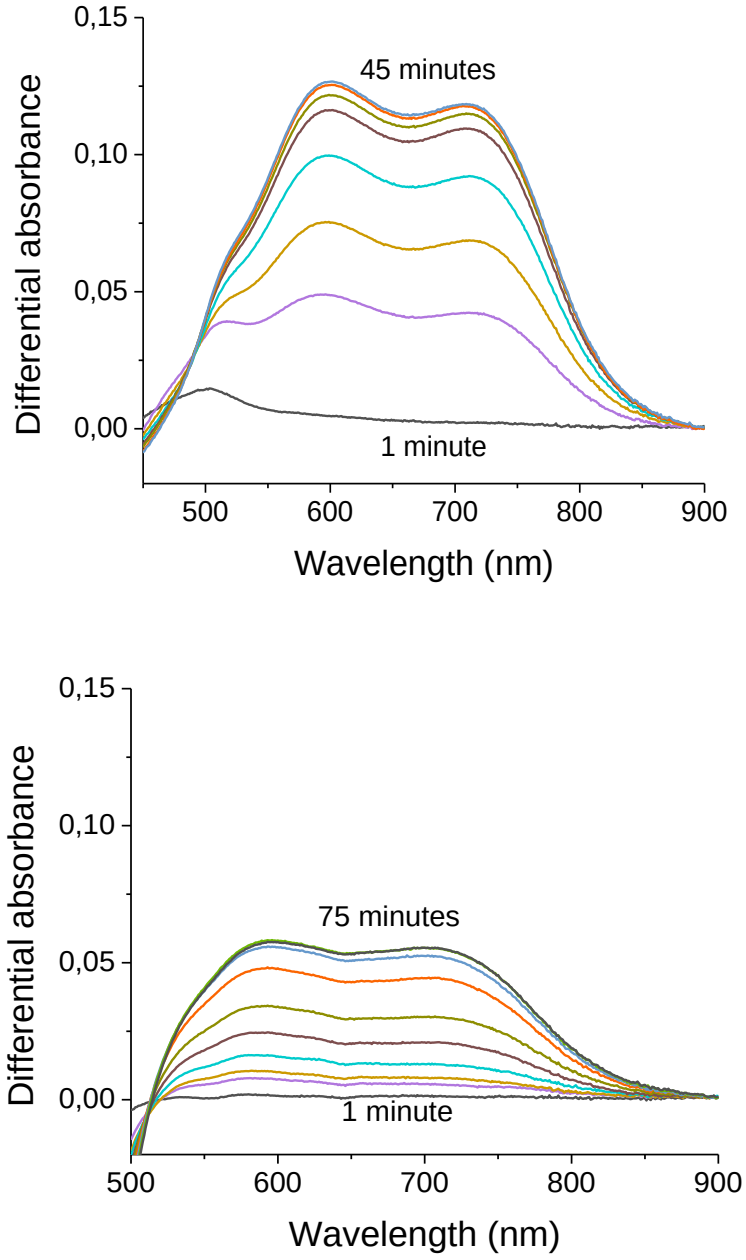

Figure II.8. Differential spectra of UV-Vis monitored photolysis experiment following the formation of Co(I) species for **RuP_4^{OEt}-Co** (top) and **Dyad 2** (bottom) (4.5×10^{-5} M) in CH_3CN/TEOA (90:10 v/v) under visible light illumination.

After 1 minute of irradiation, a new band arising at 510 nm can be attributed either to Co(II) species or Ru(I), as previously observed during an electrolysis experiment (**Figure II.4**). Afterwards and within some minutes a double band with maxima at 600 and 709 nm is generated and increases in intensity for 30 minutes, when a plateau is reached. Based on previous reports,[87] this band is typical for the formation of Co(I). The absence of broad and more pronounced peaks for Ru(I) around 500 nm (**Figure II.4**), hints that accumulation of

reduced species does not occur. This could be a result of regeneration of the reduced dye by the catalyst and formation of Co(I). Since the SED is in high excess compared to the catalyst, reductive quenching is more possible to occur under homogeneous conditions and the clear evolution of Co(I) implies that our dyad is able to accumulate Co(I).

A direct comparison (**Figure II.8**) under strictly identical experimental conditions for **Dyad 2** with the same catalyst and an organic dye[87] showed that Co(I) is formed after 60 minutes of irradiation and with lower intensity. Faster and more efficient electron transfer from ruthenium to the cobalt complex is indicated for **RuP_4^{OEt}-Co**. However, this is not conclusive as the efficiency of the reductive quenching of the dye from the SED should be also taken into consideration for both cases. Nevertheless, the build-up of Co(I) species for our dyad under homogenous conditions is a first promising sign for the photoelectrochemical tests that will follow.

V. Conclusions and perspectives

A new dye-catalyst assembly was synthesized and characterized for further use in a NiO photocathode for proton reduction. The light harvester is a ruthenium polypyridine complex and the hydrogen-evolving catalyst a cobalt diimine-dioxime. The traditional route proved a straightforward procedure for the preparation of ruthenium polypyridine complexes with four methyl phosphonate groups, even though the yields were moderate. The choice of the two components (PS, HEC) is crucial, along with the nature of the bridging ligand, as its structural and electronic properties affect the kinetics and the catalytic activity of the dyad.[158] Copper-catalyzed azide-alkyne cycloaddition was employed to couple the two moieties under mild conditions and with satisfying yields. This procedure can be a useful tool for the preparation of more sophisticated architectures. Transmetalation from copper to cobalt yielded the final dye-catalyst assembly. Full characterization was made for the dyad, which was isolated under the protonated form of the imidazole ring. Electronic decoupling at the ground state of the architecture between the two components is an important feature. This means that pairing the two subunits does not affect their initial redox and spectroscopic properties. Controlled electrochemical reduction of **RuP_4^{OEt}-Co** revealed the characteristic signatures for the reduced species of ruthenium and cobalt center.

All the thermodynamic requirements are met to have an active NiO photocathode (at pH 5.5) through a reductive mechanism. Previous TAS measurements and some initial results for our system excluded the oxidative quenching. Photolysis experiments under the presence of a SED

with UV-Visible monitoring indicated accumulation of Co(I) under homogeneous conditions. Thus, it can be assumed that reduction of the catalytic moiety should occur through two successive thermal electron transfers from the reduced dye. Direct comparison with the first reported dyad of the group (**Dyad 2**) showed more efficient and faster evolution of Co(I), when ruthenium was employed as PS. Hence, assessment of the photoelectrocatalytic activity for hydrogen production of our novel dye-catalyst assembly seems promising.

Chapter III

Characterization and H_2-evolving activity assessment of a novel RuP_4^{OH}-Co-based NiO photocathode

State-of-the-art photocathodes for proton reduction started to develop within the last 10 years and represent a continuously growing field with intensive research interest. In this chapter, we will prepare **RuP_4^{OH}-Co** sensitized NiO electrodes and assess their photoelectrocatalytic activity for proton reduction in fully aqueous medium. For comparison purposes, we will work under experimental conditions identical to the previously reported ones from the group for organic dye-based photocathodes.[87] This will enable us to correlate the performance with the nature of the photosensitizer, as the other parameters will remain unmodified. The influence of the light irradiation will be also emphasized. Post-operando characterization of the photocathodes using XPS, MALDI-ToF, ToF-SIMS and UV-Vis spectroscopy will be performed in order to shed light on the fate of our molecular dye-catalyst assembly after the activity tests.

I. Preparation of the sensitized NiO films

In this part, preparation of NiO films will be presented, as well as SEM characterization. Then, the synthetic protocol for the deprotection of the phosphonate ester groups will be demonstrated to obtain the corresponding acid anchoring groups. Finally, the procedure to sensitize the homemade NiO films will be explained.

1) F108-templated homemade NiO films

i) Preparation

NiO is the main p-type SC for the construction of p-type DSSCs[28,29,30] and DSPECs.[9,10,11,12,13] Their low-cost synthesis and good transparency make this material attractive for photoelectrocatalytic applications and a variety of protocols[41] to prepare mesoporous films are available. In this work, homemade nanostructured mesoporous NiO films were obtained according to the procedure previously reported by E. Suzuki[37] and later by our group.[87] Anhydrous $NiCl_2$ and F108 triblock co-polymer were dissolved into a mixture of water and ethanol. After centrifugation, the supernatant solution was deposited on 12 FTO glass substrates by spin-coating. The group of E. Suzuki used a doctor blade method. However, we could obtain more reproducible films with spin-coating. Finally, the films were annealed in air at 450 ºC for 30 minutes to remove organic impurities and sinter the particles together. The procedure was repeated four times to obtain four-layered films.

ii) SEM characterization

A small piece of 1 cm^2 of NiO films was cut and sent for scanning electron microscopy. Adina Morozan, a research engineer in our group, performed these measurements and some SEM images are depicted below. Porosity of 15 to 20 nm were calculated (**Figure III.1**), indicating that our films are mesoporous based on IUPAC nomenclature (2-50 nm). Thickness of up to 1 µm (**Figure III.1**) were measured for the nanostructured mesoporous four-layered NiO films.[87] This value is in the optimal range of 1-2 µm, based on a benchmarking analysis trying to correlate the preparation methods of NiO electrodes with the activity in DSSCs and DSPECs applications.[41]

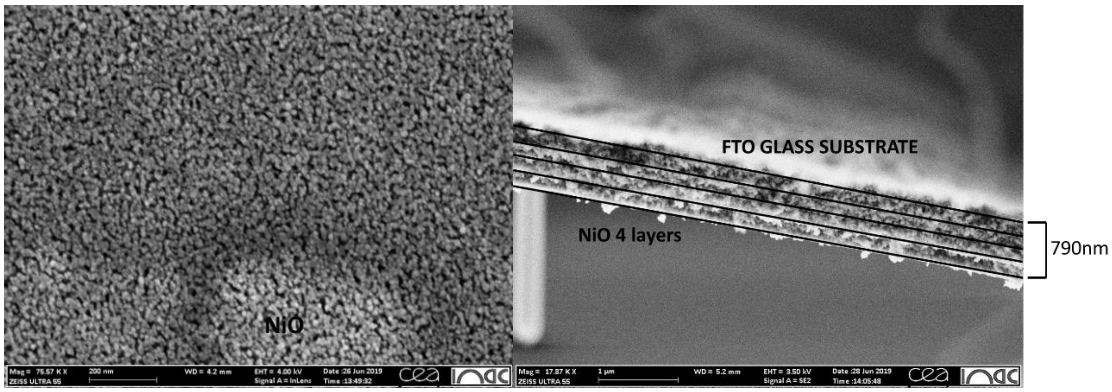

Figure III.1. Scanning electron microscopy (SEM) images of a mesoporous NiO film with porous size of 18 nm (left) and the four spin-coated layers onto FTO glass substrate with thickness of 790 nm (right).

2) Immobilization on NiO films

i) Hydrolysis of the phosphonate ester groups

In order to graft the dyad onto NiO films, hydrolysis of the phosphonates esters to the corresponding acids is needed. Two synthetic procedures exist. Strong acids like HCl or H_2SO_4 under reflux conditions are able to perform this deprotection.[51,139] However, this harsh environment could be detrimental for our dye-catalyst assembly and most specifically for the cobalt complex. Alternatively, the McKenna reaction based on the use of bromo-trimethylsilane (TMSBr) is a more convenient way for our dyad, as milder conditions are employed.[51,144]

RuP_4^{OEt}-Co was solubilized in dry DCM, TMSBr was added dropwise under an argon atmosphere and the reaction mixture was stirred at room temperature for 3 days. During this first step, silyl dealkylation takes place. After hydrolysis of the silyl ester in methanol, the deprotected compound was obtained (**Chart III.1**). **RuP_4^{OEt}-EPIP** was also deprotected (**RuP_4^{OH}-EPIP**) following the same synthetic protocol in order to use it as a reference compound for control tests.

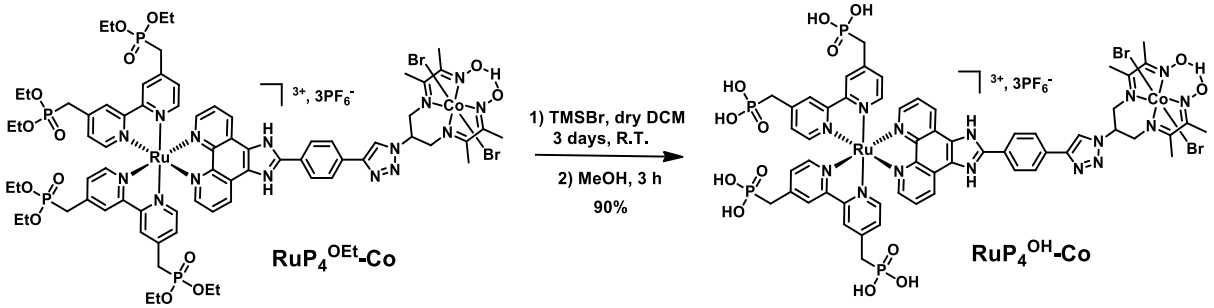

Chart III.1. Synthetic procedure to obtain **RuP_4^{OH}-Co**.

RuP$_4^{OH}$-Co exhibits moderate solubility in most common solvents due to the presence of four phosphonic acid groups. Nevertheless, MALDI-ToF was used for its characterization in methanol (**Figure III.2**) and in our hands it proved to be an important tool for the identification of complexes after grafting onto the electrodes and post-operando analysis. MALDI-ToF measurements were carried out in the SyMMES lab (C. Saint-Pierre and Dr D. Gasparutto) in CEA Grenoble. The main peak at m/z: 1448.2 corresponds to our dyad with the loss of 2 bromo axial ligands and the isotopic pattern is in good accordance with the theoretical one. In addition, different fragmentation peaks are observed, which are favored during this technique, with the main one ascribed to the loss of one oxygen atom (m/z: 1432). Less pronounced peaks are attributed to the loss of the cobalt center (small peak at m/z: 1391) and then the loss of one oxygen atom (m/z: 1375). Fragments with loss of the catalyst are also present at m/z: 1225 and 1152. It should be noted that all peaks are detected under their single charged form, as previously observed for similar ruthenium complexes, probably due to fully reduced metal complexes obtained during the experiment.[159,160,161]

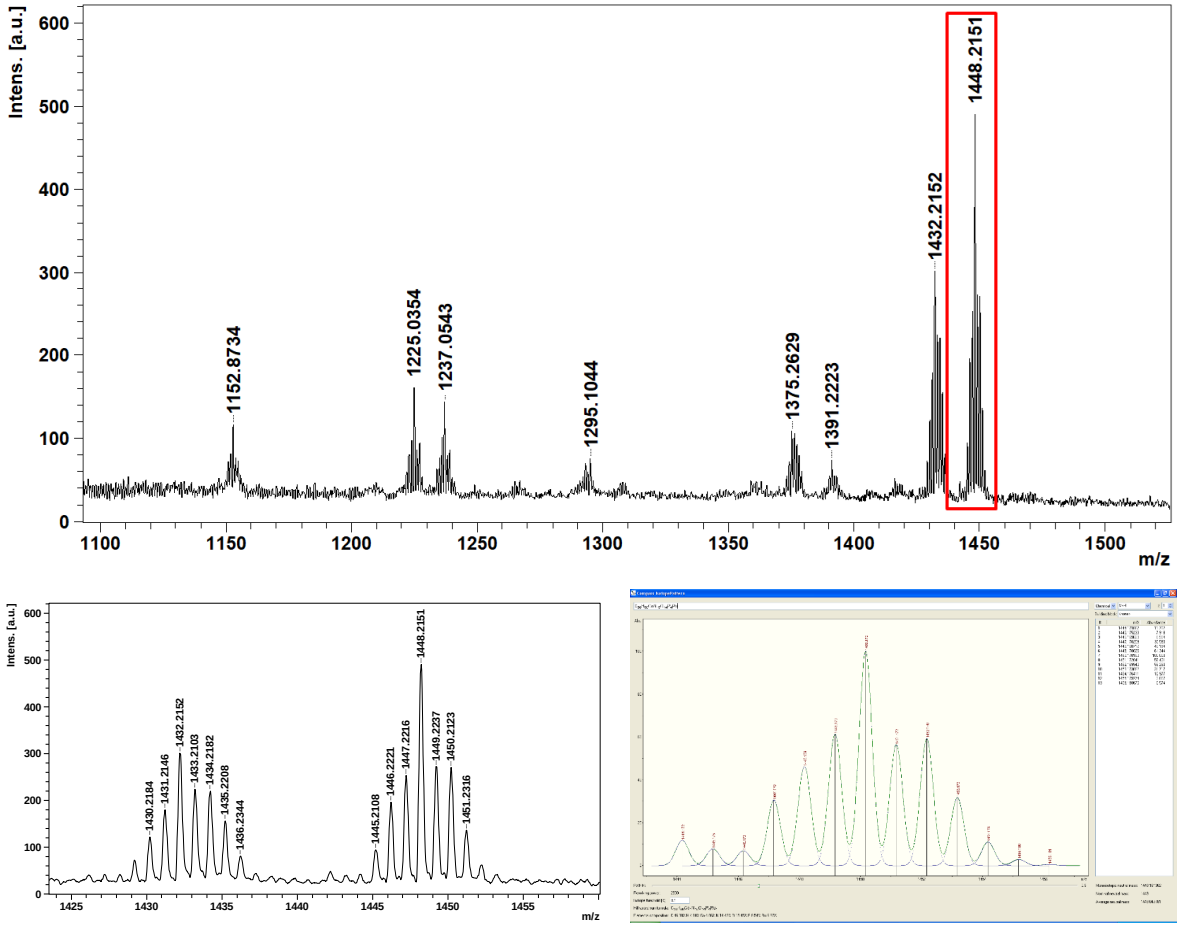

Figure III.2. MALDI-ToF spectra of **RuP$_4^{OH}$-Co** recorded in methanol (top). Left bottom is zoom in the region m/z: 1424-1460 of the spectrum where the main peak at 1448 is displayed and right bottom is depicted the theoretical isotopic pattern for **RuP$_4^{OH}$-Co** without the two bromo axial ligands.

ii) Film sensitization

Sensitization of the films was achieved by soaking them in 0.1 mM deprotected complexes (**RuP_4^{OH}-Co**, **RuP_4^{OH}-EPIP**) solutions in MeOH for 24h. Finally, the films were placed in pure methanol to remove physisorbed compounds from the surface and dried under air flow. The sensitized films were kept protected from light. This procedure has been previously optimized in the group.[79,87] It was observed that soaking for 24 hours is sufficient to achieve maximum grafting of the molecular components onto NiO films.

II. Characterization of RuP_4^{OH}-Co sensitized NiO films

Here, we will first determine the amount of dyad immobilized on the films. Subsequently, the sensitized NiO films will be characterized by various techniques in order to prove the integrity of the molecular assembly after grafting and before starting the photoelectrocatalytic tests for proton reduction.

1) Dyad loading determination

The dyad loading was estimated by UV-Vis spectroscopy after the desorption of the dyad from the surface of the film. This was achieved by dipping the sensitized NiO films in methanolic solution of 1 M phenyl phosphonic acid.[93,162] The phenyl phosphonic acid, an ideal competitive colorless adsorbent with strong affinity to NiO, can displace the compounds from the surface and release them in the solution. It should be noted that molar extinction coefficients were determined on the protected complexes (2.7×10^{-5} M) in methanolic solution of 1 M phenyl phosphonic acid (**Figure III.3**). For **RuP_4^{OEt}-Co**, the value was estimated 18700 $M^{-1}cm^{-1}$ and for **RuP_4^{OEt}-EPIP** 18400 $M^{-1}cm^{-1}$.

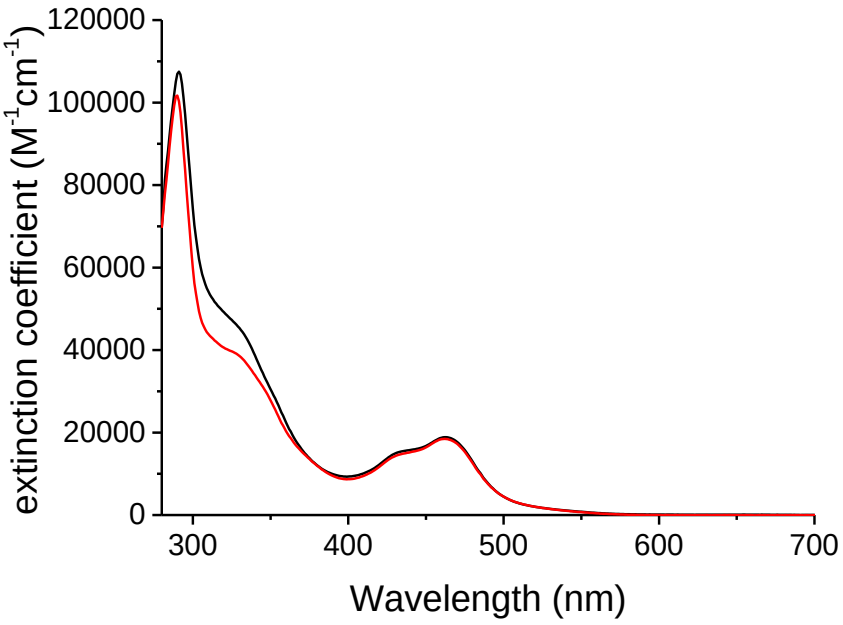

Figure III.3. UV-vis absorption spectra (epsilon curve) of **RuP_4^{OEt}-Co** (black line) and **RuP_4^{OEt}-EPIP** (red line) in a methanolic solution of 1 M phenylphosphonic acid.

The estimation of the immobilized compounds was previously made by measuring the UV-Vis absorption spectra of the sensitized NiO films.[79,55] However, scattering could complicate the interpretation of the spectra depending on the NiO film thickness. Thus, the methodology employed here is more accurate.

12 different samples gave us an average dyad loading of 5.2 ± 0.8 nmol.cm^{-2} (**Table III.1**). Increasing the sensitization time to 2, 3 or 5 days did not improve the grafting efficiency in agreement with the previous work of the group. The dyad loading will allow us to precisely compare one film to another and to calculate turn-over numbers (TON) based on the catalyst.

F1	F2	F3	F4	F5	F6	F7	F8	F9	F10	F11	F12
5.5	5.1	5.8	4.2	5.3	6.4	5.6	4.7	3.3	6.1	5.5	5.2

Table III.1. Surface concentration (nmol.cm^{-2}) of **RuP_4^{OH}-Co** determined by the desorption procedure for 12 freshly grafted films (F); this corresponds to an average surface concentration of 5.2 ± 0.8 nmol.cm^{-2}.

The obtained dyad loading value is slightly lower than for previous dye-catalyst assemblies with the same NiO preparation (6-8 nmol.cm^{-2}).[87,93] Lower solubility of the dyad and its bulky structure could be a possible explanation. Higher grafting efficiencies (> 13 nmol.cm^{-2}) were

determined previously in the group for ruthenium complexes bearing methyl phosphonate groups immobilized on NiO films.[55] Thicker films due to different NiO preparation and the less bulky nature of the complexes can justify the higher dye loadings.

2) MALDI-ToF analysis

The solutions containing **RuP_4^{OH}-Co** in 1 M phenyl phosphonic acid after detaching from the surface were sent for MALDI-ToF analysis. Identical fragmentation is observed (**Figure III.4**) with the non-grafted complex (**Figure III.2**), implying that integrity of the molecular assembly is retained after immobilization on NiO films. Hence, the higher in intensity peak at m/z: 1448 corresponds to the molecular weight of the dye-catalyst assembly after loss of the two bromo axial ligands.

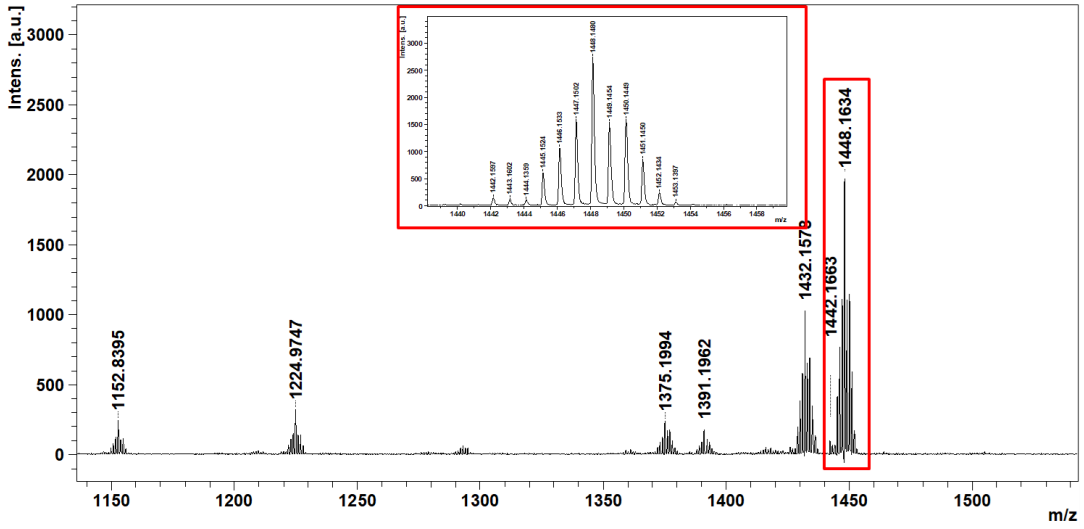

Figure III.4. MALDI-ToF spectrum of **RuP_4^{OH}-Co** dyad recorded in a methanolic solution of 1 M phenylphosphonic acid after detached from NiO films. Zoom in m/z: 1438-1460, where the isotopic pattern of the main peak at 1448.16 is presented.

3) XPS analysis

XPS analysis to screen the surface of the NiO films (ppm detection range) was used in collaboration with D. Aldakov from SyMMES lab in Grenoble. The survey high-resolution XPS spectrum of a typical FTO/NiO electrode (**Figure III.5** top) shows the core levels of Ni and O. A small peak at 285 eV represents the 1s core level of carbon. Its presence is either an artifact of the experimental procedure or a residue from the NiO preparation. The presence of Ni(II)-species is confirmed with the peak at 855 eV for Ni $2p_{3/2}$, based on previous XPS studies.[87,163]

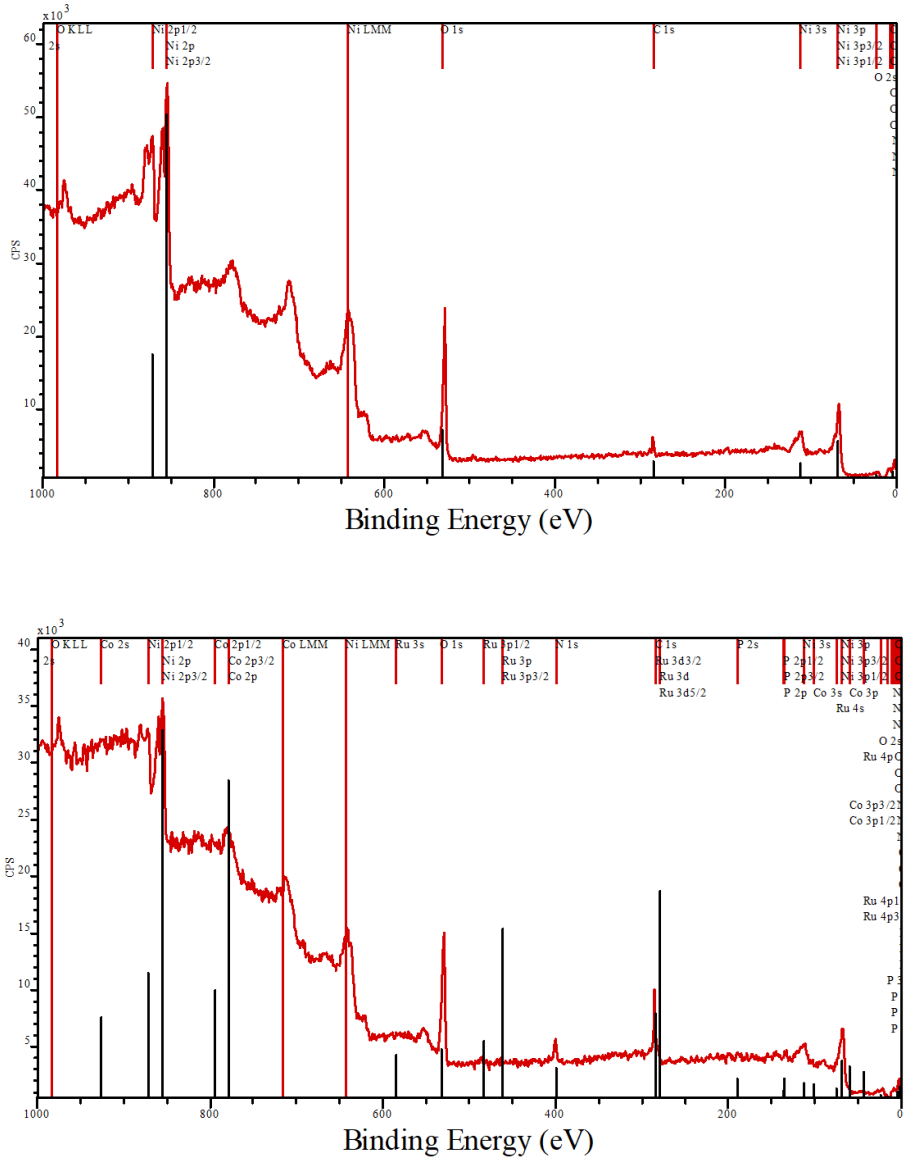

Figure III.5. XPS spectra of glass/FTO/NiO electrode pristine (top) and sensitized by **RuP_4^{OH}-Co** (bottom).

XPS spectrum of the sensitized NiO films by **RuP_4^{OH}-Co** is depicted in Figure **III.5** (bottom). Upon sensitization, the features attributed to the pristine NiO film remained unmodified. In addition, new peaks are observed at 132 for P 2p, at 280 for Ru 3d, at 400 for N 1s and at 460 eV for Ru $3p_{3/2}$.[55] Increase in intensity of the peak at 285 eV for the C 1s compared to the pristine NiO film is clear due to the presence of carbon atoms in our dyad.

The existence of the prominent Co 2p over the Ni LMM background (Ni Auger line)[164] was also recognized (**Figure III.6**). The position of the peaks (blue and turquois lines) and its satellites (red line) in the region of 780-790 eV confirm the presence of the Co(III) state in

accordance with previous XPS measurements of the group for the same Co-diimine-dioxime catalyst.[98,68]

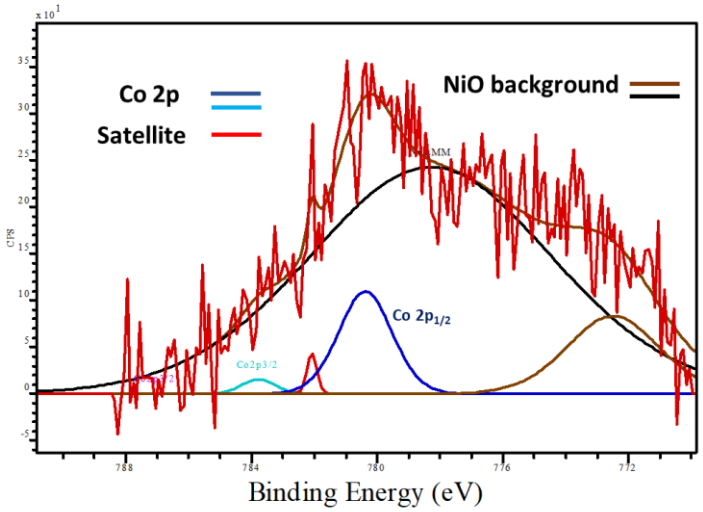

Figure III.6. XPS core-level spectra of Co 2p peak over the Ni LMM background in **RuP_4^{OH}-Co** sensitized NiO films.

4) ToF-SIMS analysis

The surface-sensitive analytical method of ToF-SIMS was also employed in the frame of a collaboration with the team of Dr. D. Leonard at the Institut des Sciences Analytiques in Villeurbanne. This is a technique of analyzing the extreme surface bringing deep chemical, atomic and molecular information.

i) Positive mode

In the positive mode (**Figure III.7**), the most useful fragments are at m/z: 738 (a) and 659 (b), indicating the coupling of the third diimine ligand containing the imidazo-phenathroline group with the cobalt catalyst through a triazole unit with one bromo axial ligand and without accordingly. Ruthenium-containing ions were identified thanks to its specific isotopic pattern. Ions corresponding to the type $C_aH_bN_cO_dP_eRu^+$ are present with methyl phosphonate groups. The peak at m/z: 616 (c), corresponding to $[Ru(bpy)(CH_2^{\cdot})(bpy)(CH_2\text{-}PO_3H_2)_2]^+$ with the break of the C-P bond supports a chemisorption rather than physisorption process of grafting.[160] In the range of m/z: 300-400 (d), a fraction at 362 is ascribed to the third diimine ligand with the triazole ring. In addition, peaks corresponding to the loss of nitrogen or carbon atoms of the main fragment at m/z: 362 are observed.

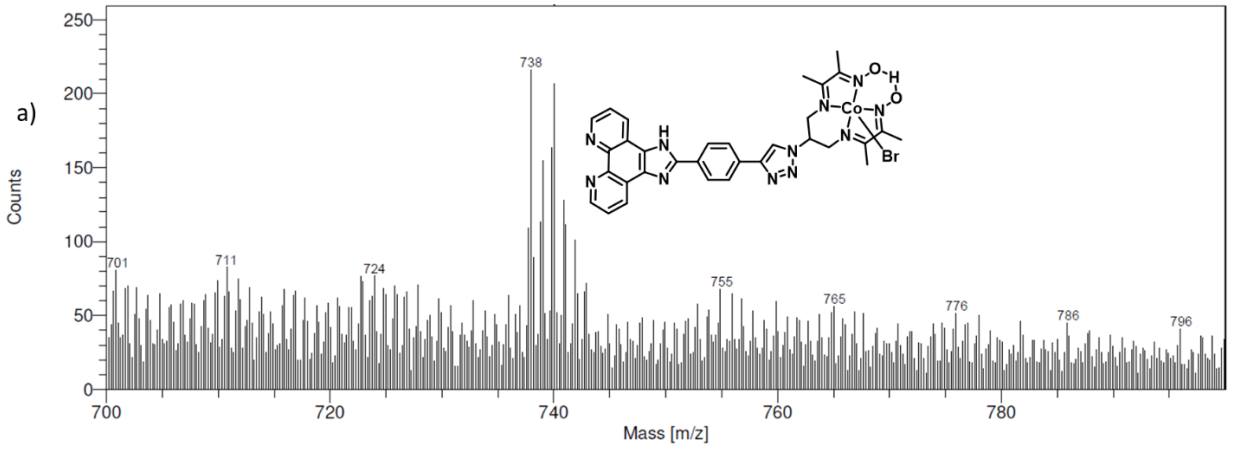
a)
Counts
Mass [m/z]
701
711
724
738
755
765
776
786
796
Br

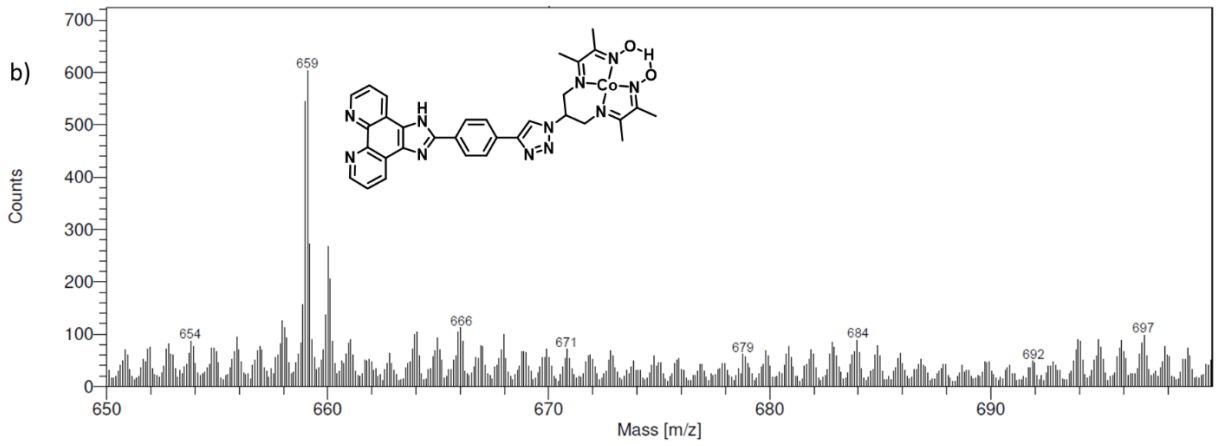
b)
Counts
Mass [m/z]
654
659
666
671
679
684
692
697

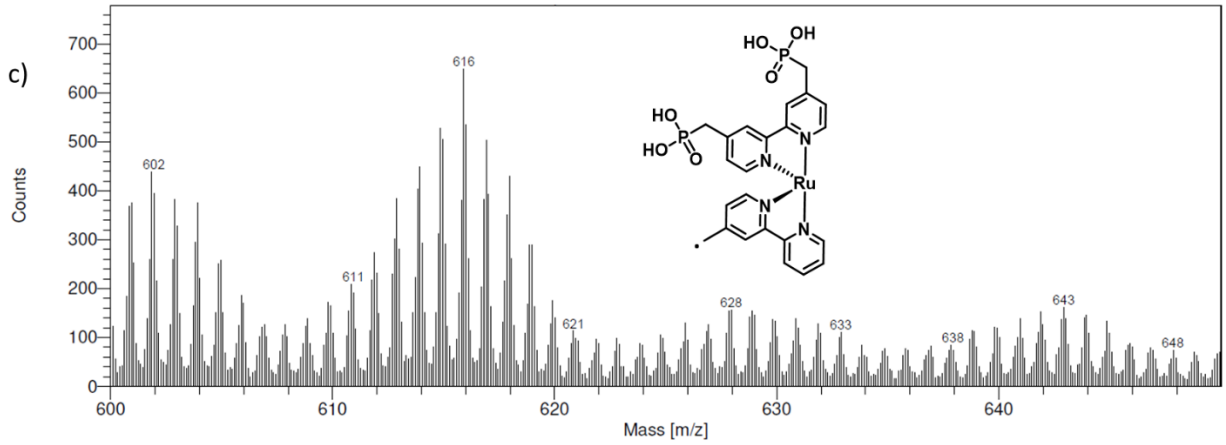
c)
Counts
Mass [m/z]
602
611
616
621
628
633
638
643
648
Ru

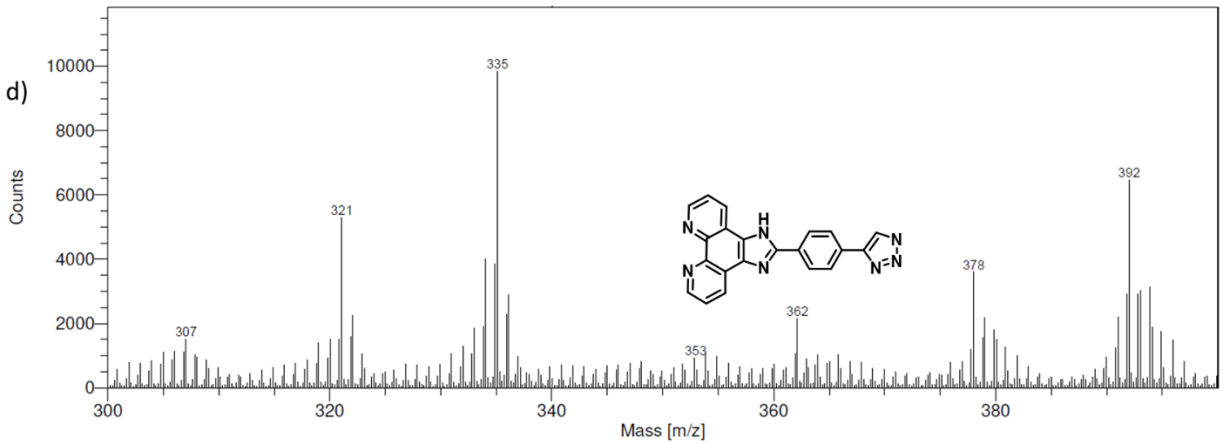

Figure III.7. Positive mode ToF-SIMS spectra of NiO films freshly sensitized by **RuP_4^{OH}-Co** in the m/z range a) 700-800, b) 650-700, c) 600-650, d) 300-400. Some proposed fragments are also depicted.

ii) Negative mode

In the negative mode, the recorded spectra (**Figure III.8**) provided again evidence for the efficient coupling of the two subunits, as well as the covalent nature of grafting. The peak at m/z: 817 (a) further supports the efficient CuAAC coupling between the two subunits with the presence of two bromo axial ligands. Furthermore, the peak at m/z: 737 corresponds to the loss of 1 bromo axial ligand. Various $Ni_aP_bO_cH_d^-$ fragments were detected (c), such as at m/z: 138 ($NiPO_3H^-$), 154 ($NiPO_4H^-$), 171 ($NiPO_5H_2^-$), 200 ($NiP_2O_5^-$) and 216 ($NiP_2O_6^-$). This clearly proves the formation of P-O-Ni bonds between the dyad and NiO, as already shown for phosphonic acids onto TiO_2 (P-O-Ti)[165,166] and NiO films.[98,55]

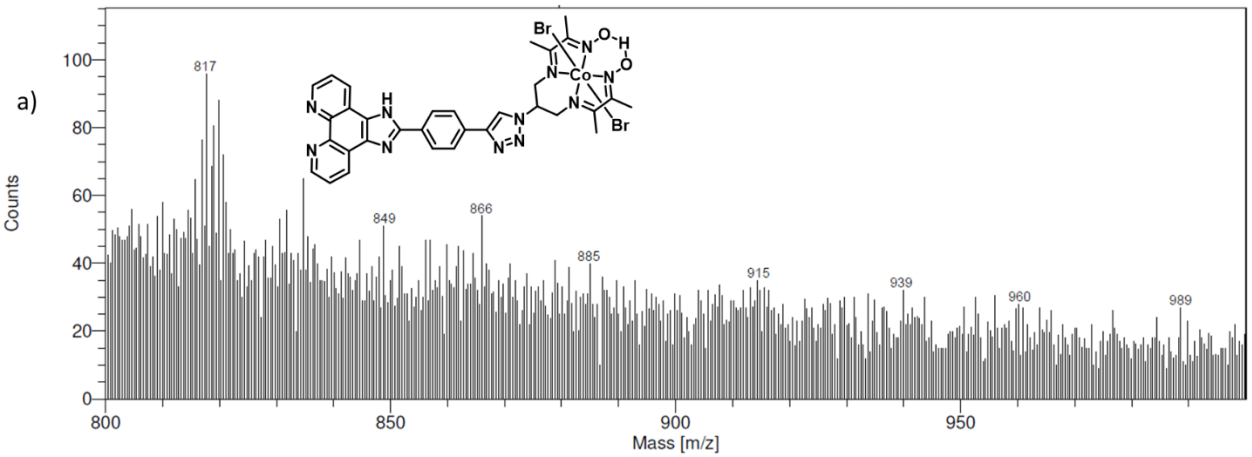

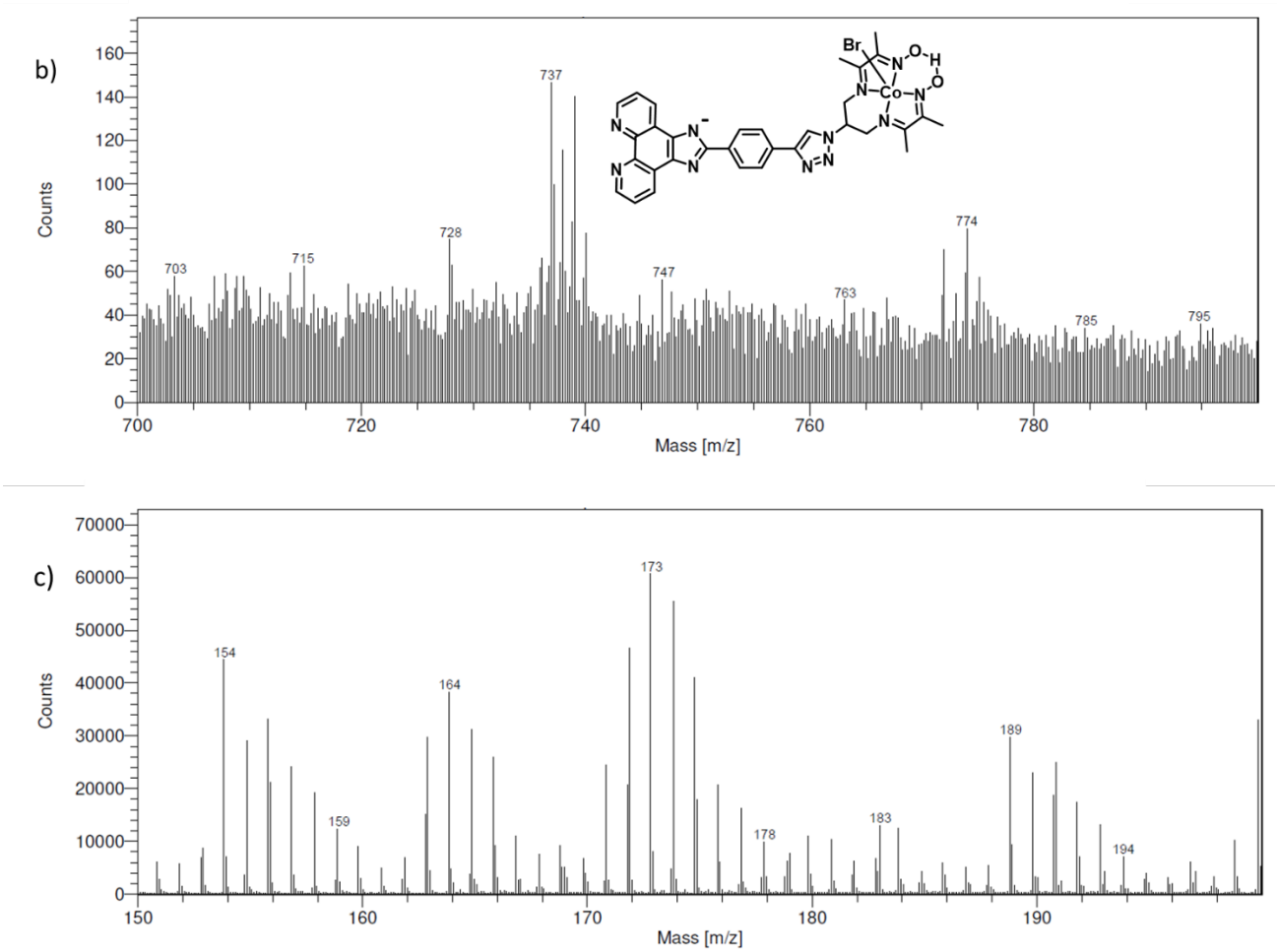

Figure III.8. Negative mode ToF-SIMS spectra of NiO films freshly sensitized by **RuP$_4^{OH}$-Co** in the m/z range a) 800-1000, b) 700-800, c) 150-200. Some proposed fragments are also depicted.

ToF-SIMS analysis gave us signatures of ruthenium-cobalt containing ions. However, the intact molecular peak was not detected probably due to the harsh nature of the technique, which facilitates fragmentation. Nevertheless, several secondary ions for the different parts of **RuP$_4^{OH}$-Co** gave reliable evidence that the whole dyad is grafted onto NiO films.

III. Photoelectrocatalytic activity of RuP_4^{OH}-Co sensitized films

The PEC activity for proton reduction of the dyad will be evaluated in a 3-electrode set-up configuration with the sensitized NiO film as the working electrode.

1) Experimental set-up

In order to accurately compare all the dye-sensitized photocathodes prepared in the group, a standardized procedure was defined in collaboration with S. Bold (PhD student), based on the previous studies from the group.[87,90]

1) Every NiO film was cut in half after sensitization. One half was used to determine the grafting density and the other half was used for the assessment of the PEC activity and for post-operando analysis. For the preparation of the working electrode, a silver wire was deposited on the FTO substrate of the film using silver conducting paste to increase the contact and it was isolated with a tape.

2) The experiments were carried out in a three-electrode cell with quartz windows (**Figure III.9**), using the NiO-sensitized film as the working electrode (3 to 3.4 cm^2), Ag/AgCl (KCl 3M) as the reference electrode and a titanium wire as the counter electrode. As supporting electrolyte we used a non-coordinating 0.1 M 2-(N-morpholino)ethanesulfonic acid (MES)/0.1 M NaCl buffer at pH 5.5.[87] The counter electrode was separated with a frit to avoid the influence of the oxidation reaction taking place. Then, the electrolyte in the two-compartment cell was degassed with nitrogen for 30 minutes. The volume of the solution was around 5 ml and the headspace approximately 2 ml.

3) Irradiation was carried out with a Xe lamp operated at 280 W. A water-filled filter for elimination of IR irradiation ($\lambda < 800$ nm) and a UV cut-off filter ($\lambda > 400$ nm) or an AM 1.5 G filter, as a mimicking for natural sunlight, were employed. The irradiation was calibrated at the equivalent of 1 sun. In the following part and in Chapter V, these two types of irradiation will be referred as visible light irradiation (400-800 nm), when the UV cut-off filter will be used and AM 1.5G irradiation when the AM 1.5G filter will be employed. The cell was placed at a fixed distance from the lamp and the light power was calibrated prior to every experiment.

4) Prior to the long-term chronoamperometric experiments, linear sweep voltammograms were recorded for each sensitized NiO film under dark conditions (lamp off), continuous irradiation (lamp on) and then chopped light irradiation (lamp on-off), screening from + 0.5 V to - 0.5 V vs Ag/AgCl with a scan rate of 10 $mV.s^{-1}$. For all the experiments, the potential is

reported vs Ag/AgCl and vs RHE. The potential against a reversible hydrogen electrode (RHE) was calculated using the equation below (**Eq.III.1**):

$$E\ (V)\ vs\ RHE = E\ (V)\ vs\ Ag/AgCl + 0.199 + 0.059 \times pH \qquad \textbf{Eq.III.1}$$

5) The amounts of evolved hydrogen were determined after chronoamperometry runs by gas chromatography in the headspace (50 µl sampling) and in the electrolyte, using a sensitive micro clark-type electrode (polarized at + 1000 mV), as an important fraction of hydrogen might remain in the solution for hours.[90] Calibration curves enabled us to correlate the response of the GC and of the electrode to the amount of produced hydrogen.

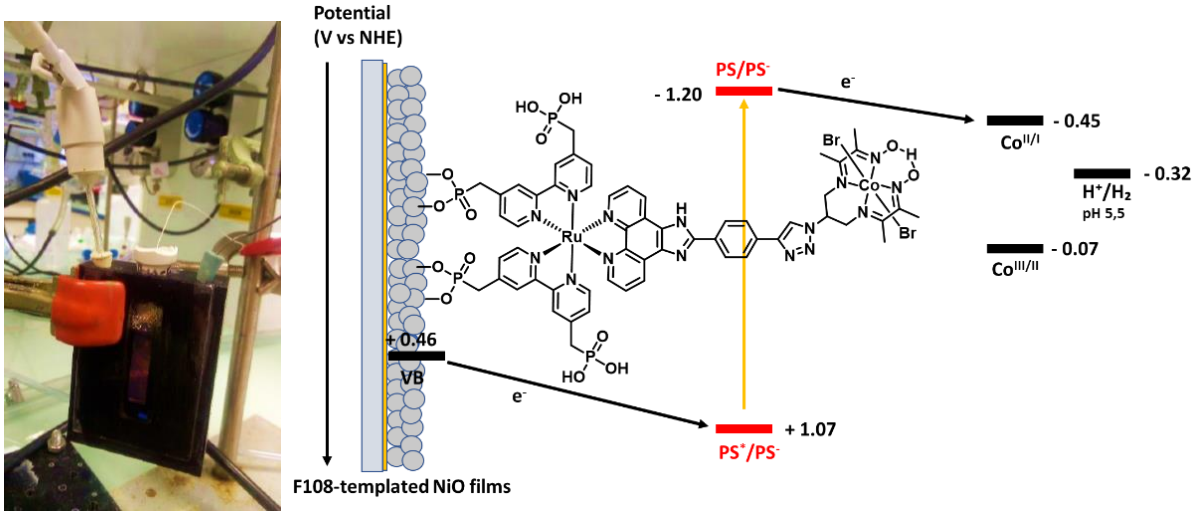

Figure III.9. Typical cell used for the PEC experiments (left) and NiO photocathode assessed for PEC proton reduction sensitized by **RuP_4^{OH}-Co** (right) at pH 5.5.

2) Assessment of the photoelectrochemical activity

i) Under visible light irradiation

In a three-electrode setup, the dyad-sensitized NiO electrodes were illuminated with visible light (400-800 nm) using the UV cut-off and the water-filled filter at the equivalent of 1 sun (65 $mW.cm^{-2}$) in a MES buffer solution at pH 5.5. First, functional characterization was performed by potential sweep techniques. Indication of an active photocathode is the appearance of cathodic photocurrents in a linear sweep voltammogram. In **Figure III.10** top, our system develops cathodic photocurrents after continuous light irradiation (red line) starting from + 0.42 V vs Ag/AgCl (+ 0.94 V vs RHE) and maintaining throughout the scanned potential range. Chopped light irradiation (blue line) allows to confirm that the observed current increase is indeed light induced. Broad processes observed in the dark at ca. + 0.4 V vs Ag/AgCl can be

assigned to capacitive charging of NiO films[36,87] and background current under dark conditions and chopped light irradiation is due to NiO itself.

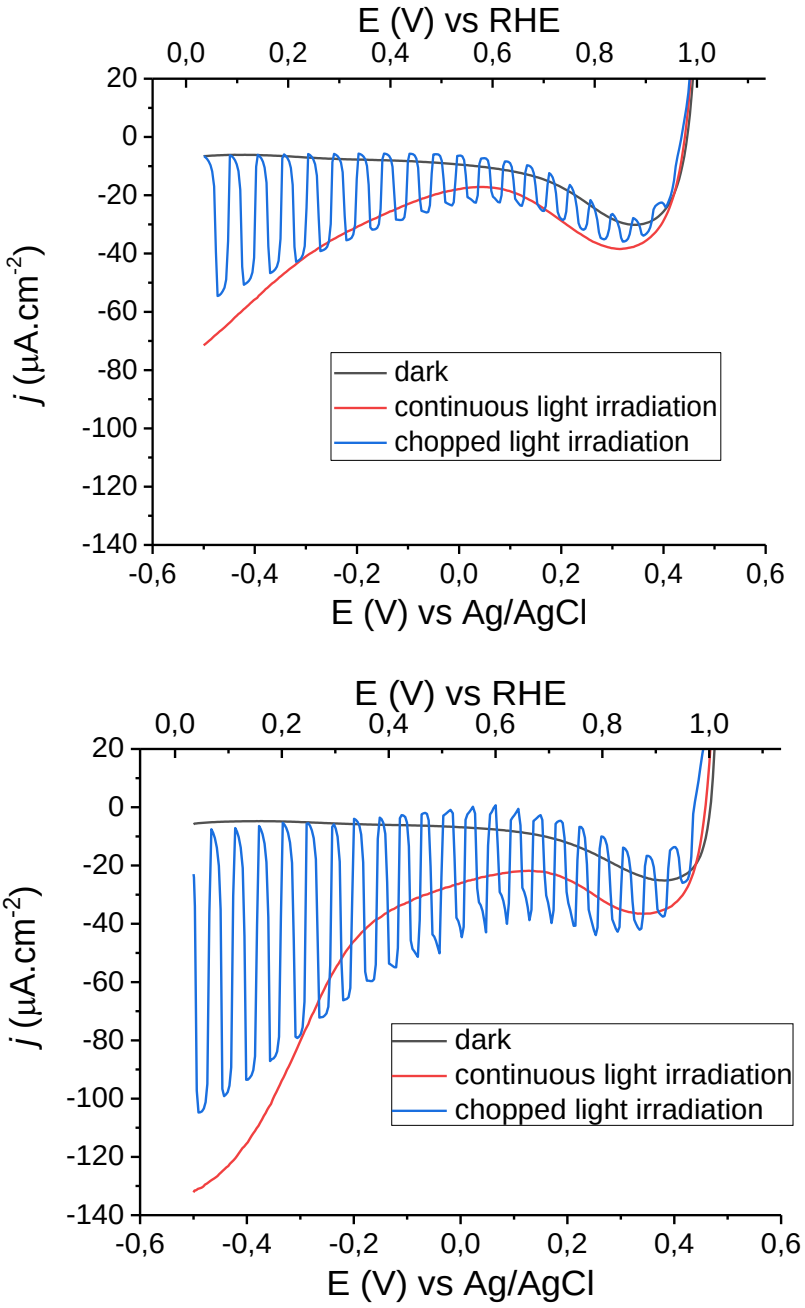

Figure III.10. Linear sweep voltammogram of NiO electrodes sensitized by **RuP_4^{OH}-Co** in pH 5.5 using MES 0.1 M/NaCl 0.1M as supporting electrolyte with a scan rate of 10 $mV.s^{-1}$. Top, irradiation was carried out with visible-light (400–800 nm, 65 $mW.cm^{-2}$, sun, red line) and bottom under AM 1.5G solar irradiation (70 $mW.cm^{-2}$, red line).

Highest photocurrent densities were observed at increasingly negative potentials. This is a result of slowing down the recombination processes, as proposed by L. Hammarström and

coworkers for DSSCs.[117] Recently, Papanikolas and his group also proved that at more negative potentials, the intragap states of NiO acting as hole traps are populated with electrons and the unwanted recombination processes can be decreased.[121]

Under visible light irradiation, photocurrent densities of - 58 ± 11 $\mu A.cm^{-2}$ (3 independent samples) after subtraction of the dark current at – 0.4 V vs Ag/AgCl were determined. A 4-fold increase (- 15 $\mu A.cm^{-2}$) in comparison with the previous dyad with the same cobalt catalyst (**Dyad 2**) is estimated.[87] If we take into consideration the dyad loading of our system, electron transfer efficiency of 11 ± 3 $\mu A.nmol_{\mathbf{dyad}}^{-1}$ can be determined. For **Dyad 2**, this efficiency was low, 2 $\mu A.nmol_{\mathbf{dyad}}^{-1}$. In agreement with the photolysis experiment (**Figure II.8**), more efficient electron transfer from the reduced ruthenium dye to the cobalt catalyst, could explain these differences.

ii) Under simulated AM 1.5G solar irradiation

Our dyad exhibits a broad absorption band at 300 nm due to π-π^* transitions based on the diimine ligands (**Figure II.5**). It was previously observed that photocatalytic systems with multicomponent or supramolecular ruthenium-cobalt assemblies displayed lower activity when a UV cut-off filter was employed.[23,58] Using an AM 1.5 G filter could enable us to take advantage of this strong absorption of ruthenium polypyridine complexes in the near-UV region. In addition, the air mass filter is a mimic of natural sunlight and it is used as a standardized filter for DSSCs.

LSV were recorded using the AM 1.5 G filter instead of the cut-off filter (> 400nm) and the IR filter (calibrated at 70 $mW.cm^{-2}$), leading to the generation of higher cathodic photocurrents (**Figure III.10** bottom). Photocurrent densities of – 84 ± 7 $\mu A.cm^{-2}$ (5 independent samples) after subtraction of the dark current at – 0.4 V vs Ag/AgCl were determined, 1.4 times higher than the photocurrents under visible-light irradiation. Taking into consideration the dyad loading, electron transfer efficiencies of 18 ± 3 $\mu A.nmol_{\mathbf{dyad}}^{-1}$ can be calculated. The increased efficiency (11 ± 3 $\mu A.nmol_{\mathbf{dyad}}^{-1}$ under visible light irradiation) when we applied the AM 1.5 G filter could be due to more efficient light harvesting.

To get more insights into the role of the cobalt center on the observed photocurrents, steady state chronoamperometric measurements were conducted on pristine NiO films, films sensitized by **RuP_4^{OH}-EPIP** and by **RuP_4^{OH}-Co** at - 0.4 V vs Ag/AgCl (**Figure III.11**).

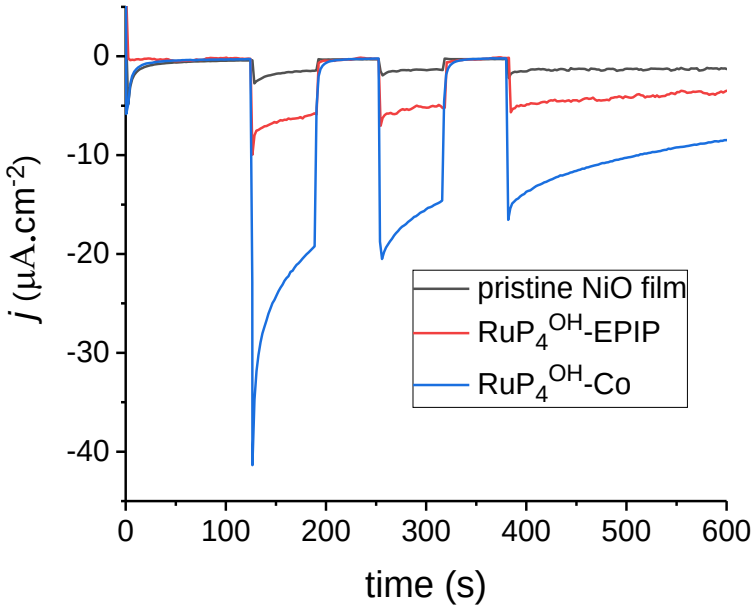

Figure III.11. Steady-state photocurrents recorded in a pH 5.5 MES 0.1 M/NaCl 0.1 M supporting electrolyte under AM 1.5 G irradiation (70 mW.cm^{-2}), at an applied potential of – 0.4 V vs Ag/AgCl, for NiO electrodes of pristine (black line), **RuP$_4^{OH}$-EPIP** (red line) and **RuP$_4^{OH}$-Co** (blue line).

Compared to **RuP$_4^{OH}$-Co**-sensitized films, pristine NiO and **RuP$_4^{OH}$-EPIP**-sensitized films, display significantly lower photocurrent densities. These results clearly confirmed the important role played by the cobalt complex for the enhancement of the photocurrents. We therefore ascribe this performance to electron transfer from the p-type NiO to the cobalt diimine-dioxime catalyst through the excitation of the dye, suggesting that catalysis is at the origin of the photocurrents. We can also notice that after an initial spike due to the accumulation of charge carriers at the electrode/electrolyte interface,[93] the cathodic photocurrent of the film sensitized by **RuP$_4^{OH}$-Co**, gradually decreases with time. The reasons behind this decay will be analyzed in the post-operando characterization section.

Preliminary tests with lower (0.5 sun) or higher (1.5 sun) light intensities were carried out with no significant differences in the photocurrent densities. Thus, subsequent longer-term irradiation experiments were performed under 1 sun illumination.

3) Assessment of the H_2-evolving activity

Chronoamperometric measurements were carried out under continuous irradiation for 2 hours at - 0.4 V vs. Ag/AgCl (+ 0.13 V vs RHE) for direct comparison with the previous dye-sensitized photocathode from the group.[87] These tests will allow us to correlate the cathodic photocurrents with catalytic hydrogen production. In **Figure III.12**, the photocurrent densities and charges are depicted for light illumination using the AM 1.5G filter for pristine NiO films and sensitized by **RuP_4^{OH}-EPIP** and by **RuP_4^{OH}-Co**. For **RuP_4^{OH}-Co**, fast photocurrent decay is observed, stabilizing after around 30 minutes. After 120 minutes, the lamp was switched off and the presence of low cathodic photocurrent was confirmed (< - 2 $\mu A.cm^{-2}$) with almost 98% drop of the initial photocurrent density. A second series of experiments were undertaken under visible light irradiation (data not presented), leading to similar observations.

Comparing these photocurrents and charges with the ones recorded for pristine NiO films and sensitized by **RuP_4^{OH}-EPIP**, clearly establish that the photo response is significantly enhanced by the presence of the catalyst in accordance with the steady-state photocurrents measurements (**Figure III.11**).

At the end of the two hours experiments, we measured for hydrogen in the headspace with gas chromatography and in the electrolyte with a micro clark-type electrode probe, following a reported protocol from the group.[90] In **Table III.2**, the PEC experiments with the two different light sources are presented, along with control tests. Under visible light irradiation and after triplicating the measurements, the average amount of evolved hydrogen was 28 ± 2 $nmol.cm^{-2}$. TON of 5 ± 1 were estimated based on the dyad loading, showing catalytic hydrogen production. Under AM 1.5 G light irradiation and identical experimental conditions, 50% growth of the amount of hydrogen and the TON were obtained, reaching 57 ± 21 $nmol.cm^{-2}$ and 12 ± 3 accordingly. Thus, the higher photocurrent densities (**Figure III.10**) are translated into higher catalytic activity.

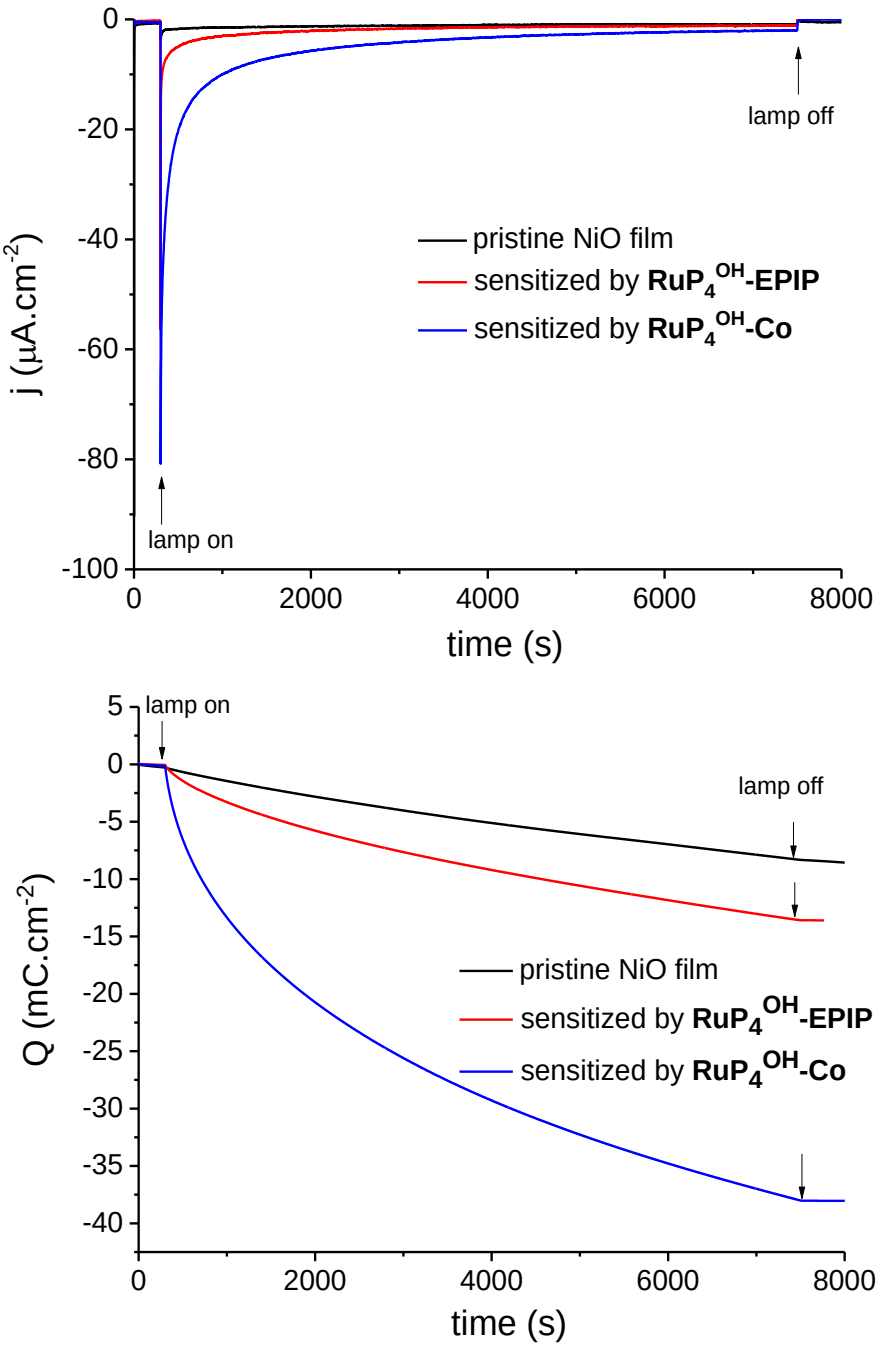

Figure III.12. Representative photocurrent densities (top) and corresponding charges (bottom) recorded during the course of two-hour PEC measurements under continuous light irradiation (AM 1.5G filter) at an applied potential of – 0.4 V vs Ag/AgCl for NiO electrodes of pristine (black line), **RuP_4^{OH}-EPIP** (red line) and **RuP_4^{OH}-Co** dyad (blue line).

6 times less hydrogen was produced with NiO films sensitized by **RuP_4^{OH}-EPIP** (< 10 nmol.cm^{-2}) under irradiation with the two different light sources. The production of low amounts of hydrogen without the presence of a catalyst was previously observed in the literature for p-type dye-sensitized photocathodes[84,93,167] and was attributed to the formation of Ni(0)

nanoparticles, which are active for proton reduction.[168] Decomposition of ruthenium, as evidenced in homogeneous photocatalytic systems, cannot be excluded for the evolution of H_2.[169,170,171] Traces of hydrogen was produced when pristine NiO films were illuminated with visible light (less than 1 nmol.cm^{-2}). The production of higher amounts of H_2 for pristine NiO films when AM 1.5G filter was employed (5 nmol.cm^{-2}) can be ascribed to the excitation of the semiconductor, as it can absorb in the UV region (band gap of 3.6 eV). Nevertheless, the increased photocurrents and hydrogen evolution for **RuP$_4^{OH}$-Co**-sensitized films could be ascribed to the electron transfer from the valence band of NiO to the cobalt diimine-dioxime catalyst through the excited state of the photosensitizer, which can then efficiently drive proton reduction.

An average faradaic efficiency of 24 ± 5 % and 26 ± 7 % was determined under visible light and AM 1.5 G irradiation accordingly, implying that the electrons are consumed for other reactions and not just for proton reduction. Although these values are still low, they are more than twice higher than all the other reported dye-sensitized photocathodes based on the cobalt diimine-dioxime catalyst (around 10%).[87,90,98] Main reasons for the modest F.E. could be the reduction of trapped oxygen, as well as partial reduction of NiO,[87] recently confirmed by Simonov and his group.[168]

Based on the fast decay of the photocurrents after some minutes of irradiation (**Figure III.12**), we decided to carry out CA experiments for 30 minutes instead of 2 hours. The amount of evolved H_2 and the TON were in the same range than the previous one (**Table III.2 c**). However, a lower charge passed during the course of this experiment leading to a faradaic efficiency of 72%. This experiment is important because it shows that, during the first 30 minutes of activity, our system displays a high selectivity for hydrogen production. Restarting the measurement for 2 hours, the amount of hydrogen produced was not further increased. Hence, it seems that our system is deactivated during the course of the experiment. Post-operando analysis may shed light on the origin of this deactivation and will be analyzed in detail in the corresponding section.

Irradiation	Film	Surface Area (cm^2)	Dye and dyad loading ($nmol.cm^{-2}$)	H_2 in the headspace[a] (nmol)	H_2 in solution[b] (nmol)	Total H_2 (nmol)	Total H_2 ($nmol.cm^{-2}$)	Charge passed ($mC.cm^{-2}$)	F.E. (%)	TON	Ref. exp.
400-800 nm	NiO	3.3	—	0	3	3	1	2	7	—	SB117
		3.0	—	0	1	1	< 1	3	3	—	SB120
	average						**1 ± 1**	**3 ± 1**	5 ± **2**		
	NiO|**RuP_4^{OH}-EPIP**	3.2	3.7	2	13	15	5	9	10	—	EG323
		3.3	1.9	0	11	11	3	8	8	—	EG324
	average						**4 ± 1**	**9 ± 1**	**9 ± 1**		
	NiO|**RuP_4^{OH}-Co**	3.3	6.4	70	33	102	31	32	19	5	EG273
		3	5.6	57	21	78	26	22	23	4	EG304
		3.1	4.7	30	56	85	28	18	31	6	EG314
	average						**28 ± 2**	**24 ± 6**	**24 ± 5**	**5 ± 1**	
AM 1.5 irradiation (IR filtered)	NiO	2.8	—	6	6	13	5	7	13	—	EG266
		2.6	—	4	9	13	5	8	12	—	EG311
	average						**5 ± 0**	**8 ± 1**	**13 ± 1**		
	NiO| **RuP_4^{OH}-EPIP**	2.6	4.2	6	30	36	14	13	20	—	EG264
		3.2	2.1	3	16	19	6	6	23	—	EG325
	average						**10 ± 4**	**10 ± 4**	**22 ± 2**		
	NiO| **RuP_4^{OH}-Co**	3.2	5.5	78	154	232	72	38	37	13	EG257
		2.9	4.2	115	70	185	64	46	27	15	EG270
		3.2	5.3	102	60	162	51	54	18	10	EG272
		2.5	3.3	74.1	53	127	51	42	23	15	EG342
		3.0	5.2[c]	25[c]	153[c]	178[c]	59	16[c]	72[c]	11[c]	EG418
	average[d]						**60 ± 9**	**45 ± 6**	**26 ± 7**	**13 ± 2**	

Table III.2. Photoelectrochemical experiments assessing hydrogen production activity on NiO electrodes. Conditions are as follows: MES buffer at pH = 5,5, -0.4 V vs. Ag/AgCl applied potential, 2 h runtime.

a- Measured by gas chromatography.
b- Measured with a micro-Clark electrode.
c- After half an hour instead of two hours.
d- Fifth measurement (half-an-hour instead of two hours) not included

IV. Transient absorption-spectroelectrochemistry (TA-SEC) on the sensitized films

To investigate the light-induced processes occurring in the photocathode under quasi-operando conditions, transient absorption spectroelectrochemistry (TA-SEC) on NiO films was carried out at different applied potentials. This technique was previously developed by Sebastian Bold in collaboration with our group to study **Dyad 2** in solution, combining the advantages of electrochemistry with transient absorption spectroscopy.[151] TA-SEC enabled to study the excited state dynamics and the intramolecular electron transfer in the dye-catalyst assembly. This technique will be employed here to characterize the films with the potential applied during the PEC tests. Thus, the influence of this potential on the charge-separated state lifetime can be identified, as it has already been done for ruthenium-sensitized NiO photocathodes.[117,121] The experiments below were performed by S. Bold in the group of Pr. B. Dietzek in Germany and some key information will be presented.

Using femtosecond laser pulse, TA spectra were recorded without applied potential (open-circuit potential, OCP), at - 0.74 V $Fc^{+/0}$, equivalent to the - 0.4 V vs. Ag/AgCl applied in the photoelectrochemical tests, and - 1.15 V vs. $Fc^{+/0}$. At - 0.74 V vs. $Fc^{+/0}$, the cobalt catalyst is under its Co(II) state,[98] while at - 1.15 V vs. $Fc^{+/0}$ it is reduced to the Co(I) state. Thus, the measurement at -1.15 V vs. $Fc^{+/0}$ serves as a reference measurement where any electron transfer to the cobalt catalyst is not thermodynamically possible.

TA spectra of NiO films sensitized by **RuP_4^{OH}-Co** (**Figure III.13**) show the following general shape: at early times, a spectrum with ground state bleach (GSB) at 480 nm and excited stimulated emission (ESA) at around 590 nm, corresponding to the ^{3}MLCT state. At OCP, this spectrum decays almost completely after 7 ns. However, at more negative potentials it develops into a long-lived spectrum with positive bands at 540 and 480 nm with a complete loss of the GSB. The band at 540 nm is characteristic for the one-electron reduced dye (**Figure II.4**), while the band at 480 nm is tentatively ascribed to oxidized Ni species.[32] This observation thus confirms the formation of a charge-separated state, produced by hole injection from the excited dye into the NiO film. Similar TA spectra with **RuP_4^{OH}-EPIP**-sensitized NiO films were obtained.

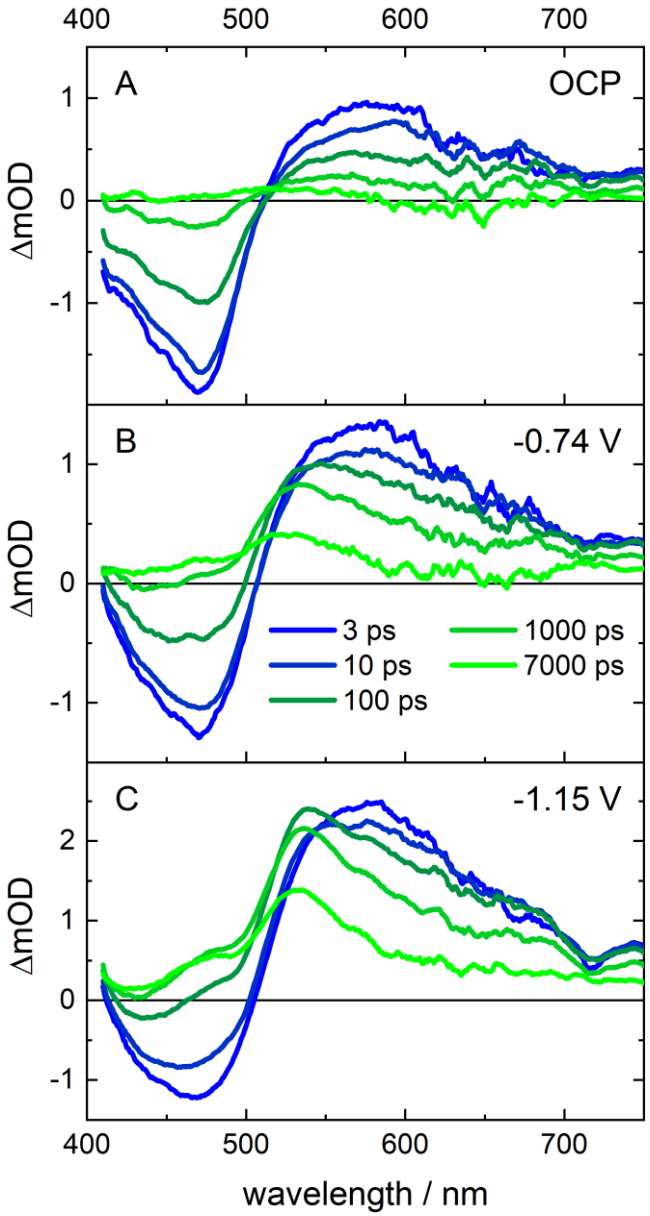

Figure III.13. TA-SEC spectra of **RuP$_4^{OH}$-Co**-sensitized NiO films at early delays up to 7 ns at (A) OCP, (B) - 0.74 V and (C) - 1.15 V vs. $Fc^{+/0}$ applied potential.

From exponential fit of the experimental data, there are two fast hole injection processes with time constants of < 2 ps (τ_0) and 45-70 ps (τ_1) (**Figure III.14**) which both become faster and more pronounced at more negative applied potentials. For **RuP$_4^{OH}$-Co**, the faster hole injection process is more efficient than for **RuP$_4^{OH}$-EPIP**, which could be explained by different electron density distributions in their excited states. In the case of the dyad, the electron density may be localized on the extended ligand due to the modification caused by the triazole unit and the hole injection can be more efficient.[172] Hole injection is followed by charge recombination, which is drastically affected by the applied potential, increasing from a time

constant of tens of picoseconds at OCP to > 7 ns (τ_3) at negative applied potentials, leading to a long-lived charge-separated state. In parallel, remaining ^{3}MLCT decays directly back to the ground state in ≈ 1 ns (τ_2).

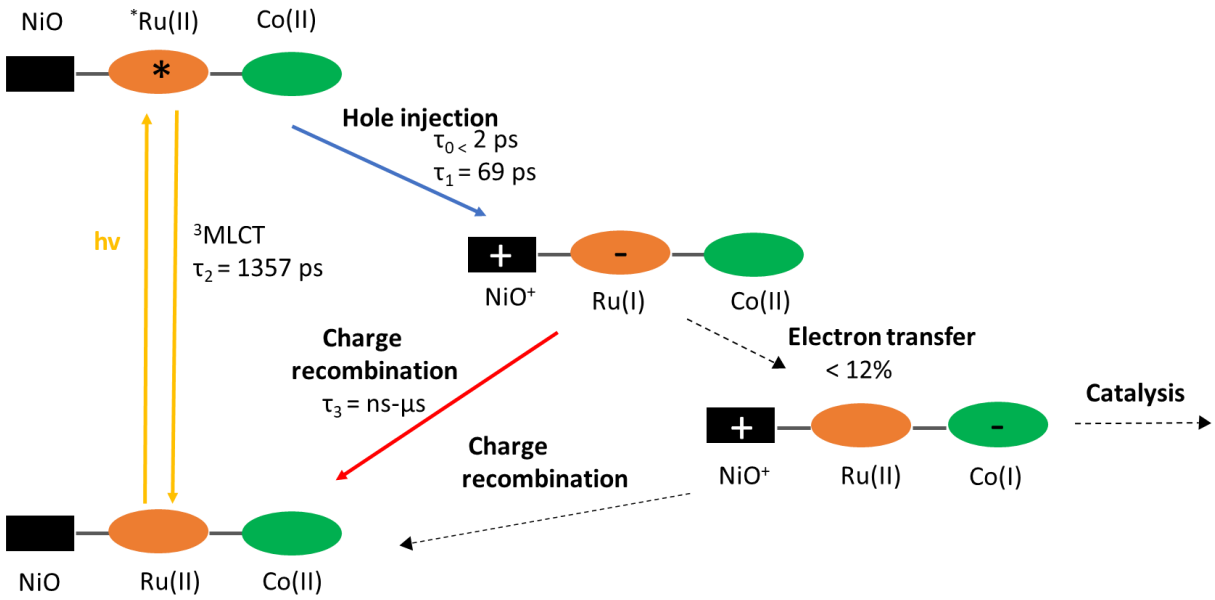

Figure III.14. Jablonski diagram summarizing the light-induced processes occurring for **RuP$_4^{OH}$-Co**-sensitized NiO films at - 0.74 V vs. $Fc^{+/0}$ (equivalent to - 0.4 V vs Ag/AgCl used in the photoelectrochemical tests).

The TA spectra of **RuP$_4^{OH}$-Co** in the time window up to 7 ns do not show any spectral indication of electron transfer to the cobalt catalyst unit. Such a charge transfer would be observable as an absorption band between 550 and 750 nm (**Figure II.4**) produced by the Co(I) state in the case of **RuP$_4^{OH}$-Co**, which is not present in our spectra. From the femto-second TA-SEC measurements, the most important observation is a long-lived separated state.

Since thermal electron transfer in triazole-bridged dyads has been shown to occur on the ns-µs time scale,[173,174,175,176,177] TA experiments were performed up to 15 µs. However, the TA spectra in this time range are spectrally identical to the last spectra and decay without any spectral changes. In particular, the signature of the Co(I) state did not appear on the TA spectra of **RuP$_4^{OH}$-Co** -sensitized NiO films at - 0.74 V vs. $Fc^{+/0}$, and the decay kinetics of the reduced Ru complex were not accelerated in comparison to **RuP$_4^{OH}$-EPIP**-sensitized films.

Overall, by applying a reductive potential, the lifetime of the charge-separated state was increased from hundreds of picoseconds to up to 15 µs, an increase of up to 5 orders of magnitude compared to OCP measurements. However, the formation of Co(I) species could not be detected. Therefore, the electron transfer from the reduced dye to Co(II) appears to be quite

inefficient. On the basis of the extinction coefficients of the reduced dye and Co(I) from the UV-Vis SEC experiment and the experimental noise of the TA-SEC measurement, we could estimate that less than 12% of the reduced dyes can undergo electron transfer to the catalyst. Thus, this inefficient thermal electron transfer to the catalyst is in agreement with the low activity of our photocathode.

V. Post-operando analysis of RuP_4^{OH}-Co-sensitized NiO films

The PEC activity of our photocathode in fully aqueous conditions was promising. However, after 30 minutes of continuous irradiation at – 0,4 V vs Ag/AgCl, most of the initial photocurrent is lost and the hydrogen production reaches a plateau. Post-operando analysis is of significant importance for finding out what is the destiny of the molecular dyad and may provide answers for the photocurrent decay. After completing the PEC tests, the surface of the NiO films were characterized by XPS and TOF-SIMS or they were placed in 1 M methanolic solution of phenyl phosphonic acid and the corresponding desorption solutions were analyzed by UV-Vis and MALDI-ToF.

1) XPS analysis

Post-operando XPS analysis of the sensitized NiO films was carried out, providing important information. In **Figure III.15**, the XPS spectra for Co 2p after catalysis (right) can be fitted with the same components as bare NiO films (left). Thus, partial or complete loss of Co is indicated. Previous high resolution HAXPES measurements, showed decreased amount of cobalt after 1000 s of photoelectrolysis, using a dye-catalyst assembly based on the same cobalt diimine-dioxime complex.[91] In addition, in our case, desorption of more than 40% was estimated for N 1s, which was higher than for ruthenium or phosphorus. This can further support the degradation of the catalyst, containing nitrogen atoms.

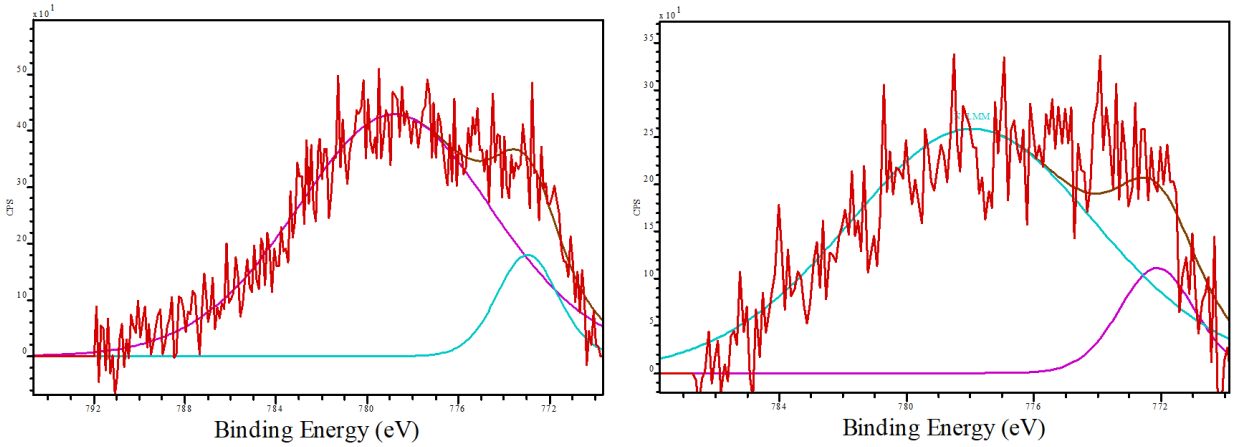

Figure III.15. Left XPS core-level spectrum of pristine NiO films and right XPS core-level spectrum after catalysis in the region where cobalt was expected to appear.

XPS spectra of P 2p at 132 eV (**Figure III.16** left) confirm the presence of phosphorus on the surface before (blue line) and after the PEC experiments (green line). Comparing their relative concentration versus nickel as reference, more than 30% of desorption is estimated. One interesting feature is that the desorption of ruthenium was almost 10% higher (about 40%). This can support the chemisorption nature of the phosphonic acids onto NiO films with cleavage of the P-C bond. In **Figure III.16 (**right), the XPS spectra of Ru 3d and C 1s (red line), overlapping at 284.5 eV, are presented. The existence of Ru 3d on the sensitized samples before (blue line) and after (green line) the proton reduction experiments are confirmed with no shape modification, neither an obvious shift.

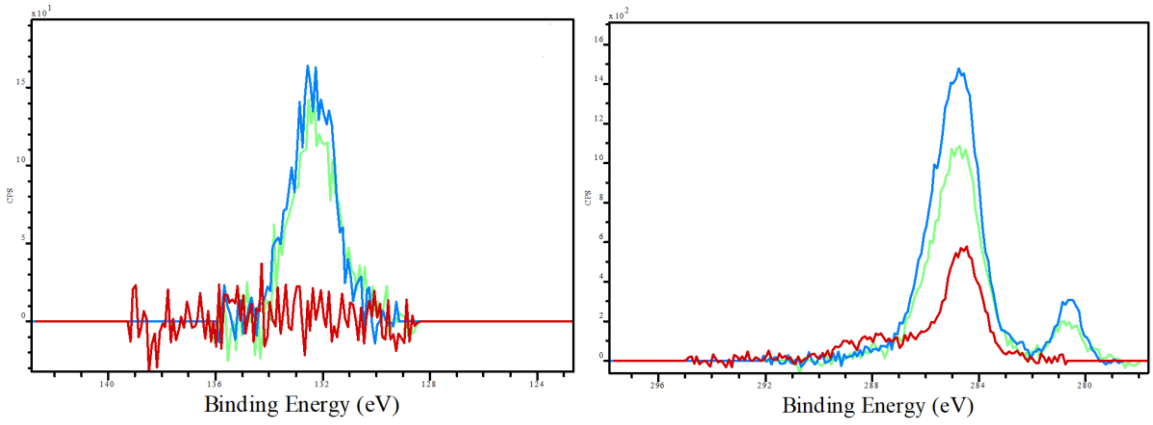

Figure III.16. Left, XPS core-level spectrum of P 2p of pristine NiO films (red line), NiO films sensitized by **RuP_4^{OH}-Co** before catalysis (blue line) and after 2 hours of PEC test (green line). Right XPS core-level spectrum of C 1s of pristine NiO films (red line) and Ru 3d of NiO films sensitized by **RuP_4^{OH}-Co** before (blue line) and after (green line) PEC test. Overlap between ruthenium and carbon is present in this region.

Finally, no significant changes were observed for Ni 2p concerning the shape of the main peaks from 852 to 868 eV (**Figure III.17** left) after catalysis (blue line). However, a small shift of the peak at 853 eV, indicating evolution of Ni(0) cannot be excluded.[87] This is in agreement with the production of traces of H_2 ascribed to Ni nanoparticles, obtained during our PEC tests.

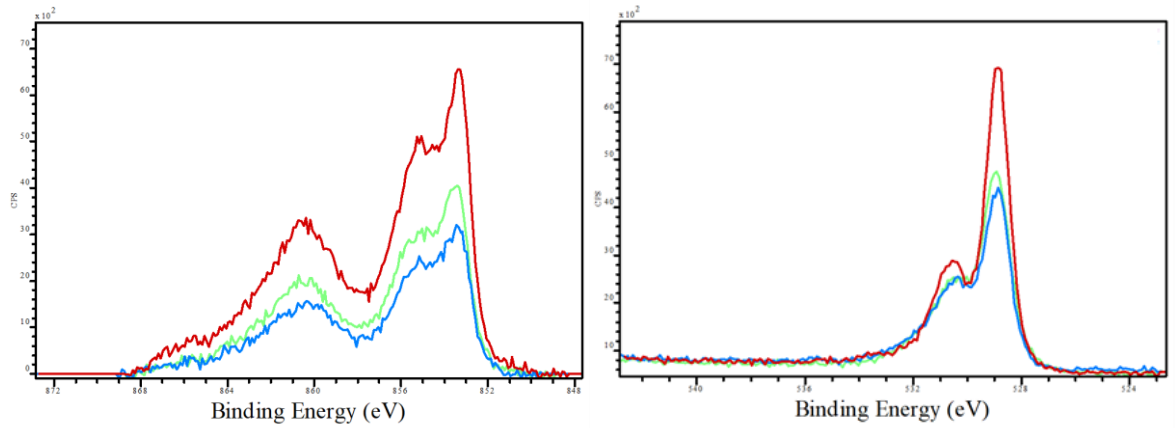

Figure III.17.XPS core-level spectrum of pristine NiO films (red line), NiO films sensitized by **RuP_4^{OH}-Co** before catalysis (green line) and after 2 hours of PEC test. Left spectrum depicts Ni 2p and right O 1s.

The absence of considerable changes in the O 1s spectra (**Figure III.17** right) for the bare NiO films (red line) and the NiO films before (green line) and after (blue line) the PEC experiments, indicates that oxidation processes do not occur after immobilization of the dyad and during catalysis.

2) TOF-SIMS analysis

Post-operando TOF-SIMS analysis for the sensitized NiO films was carried out in positive and negative mode.

i) Positive mode

In the positive mode (**Figure III.18**), the most important differences between the spectra before and after the PEC tests is that Co-containing fragments are limited and with lower intensity, in particular those at m/z: 738 and 659. In addition, peaks containing ruthenium corresponding to a type of $C_aH_bN_cO_dP_eRu^+$ similar to what observed before catalysis are still present, but anew in lower intensity. These observations imply that desorption and/or decomposition pathways based on the catalyst is a limiting factor for the efficiency of the photocathode. Peaks that can be ascribed to the triazole unit with the imidazole group of the

third diimine ligand are also observed in the region between m/z: 321 and 392 (d), identical with the ones before catalysis. This is an indication that the triazole bridge is stable during a photoelectrocatalytic test.

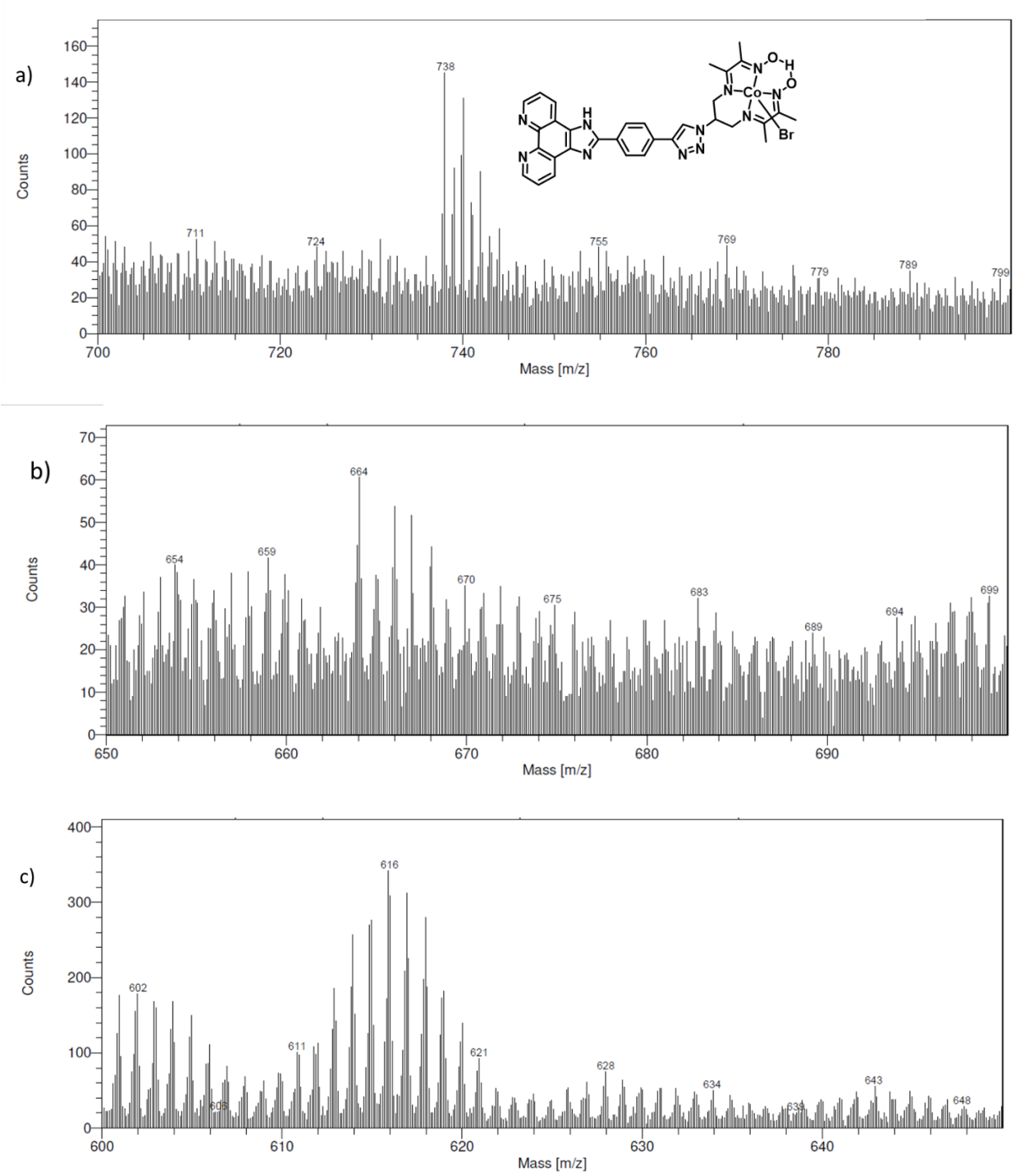

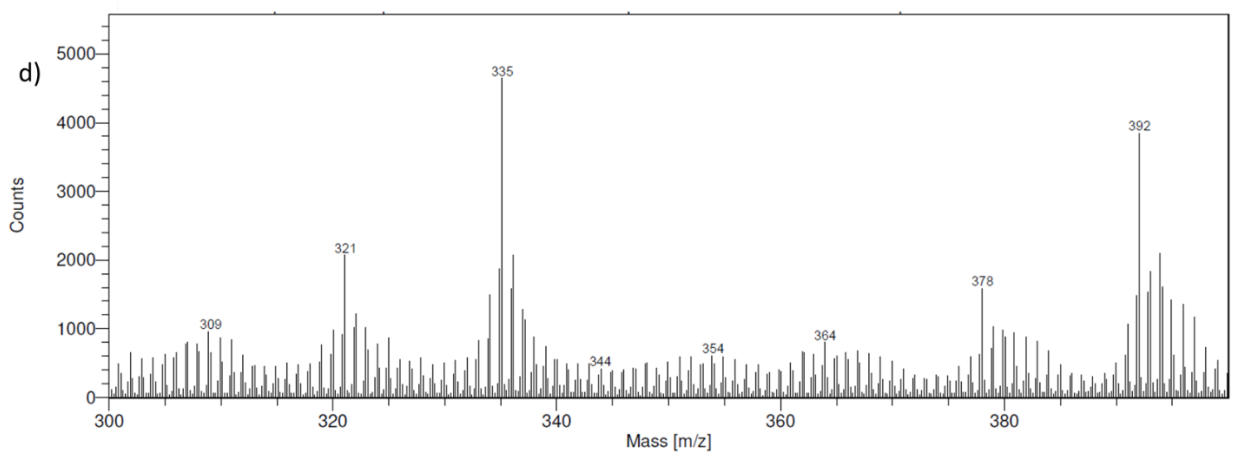

Figure III.18. Positive mode ToF-SIMS spectra of NiO electrodes sensitized by **RuP_4^{OH}-Co** after 2 hours of PEC tests in the m/z range a) 700-800, b) 650-700, c) 600-650, d) 300-400. Inset show proposed fragments.

Triazole has been reported to be resistant to hydrolysis, oxidation and reduction.[88] However, the group after performing post-operando TOF-SIMS measurements has found fragments due to reductive hydrogenation of the triazole unit for the co-grafted cobalt catalyst onto NiO films.[98] The loss of active immobilized Co complexes was ascribed to the instability of the triazole unit. Under our experimental conditions, similar decomposition pathways cannot be identified. The covalent grafting of the dye and the HER catalyst may control the electron transfer to the catalyst through the triazole bridge in a way that reductive bleach cannot occur.

ii) Negative mode

In the negative mode (**Figure III.19**), peaks containing Co have been disappeared at m/z: 817 and 738. Same $Ni_aP_bO_cH_d^-$ fragments were detected in the range of m/z: 150-200 with the spectra before catalysis, proving that the phosphonate linkage is present even after two hours of catalysis (c).

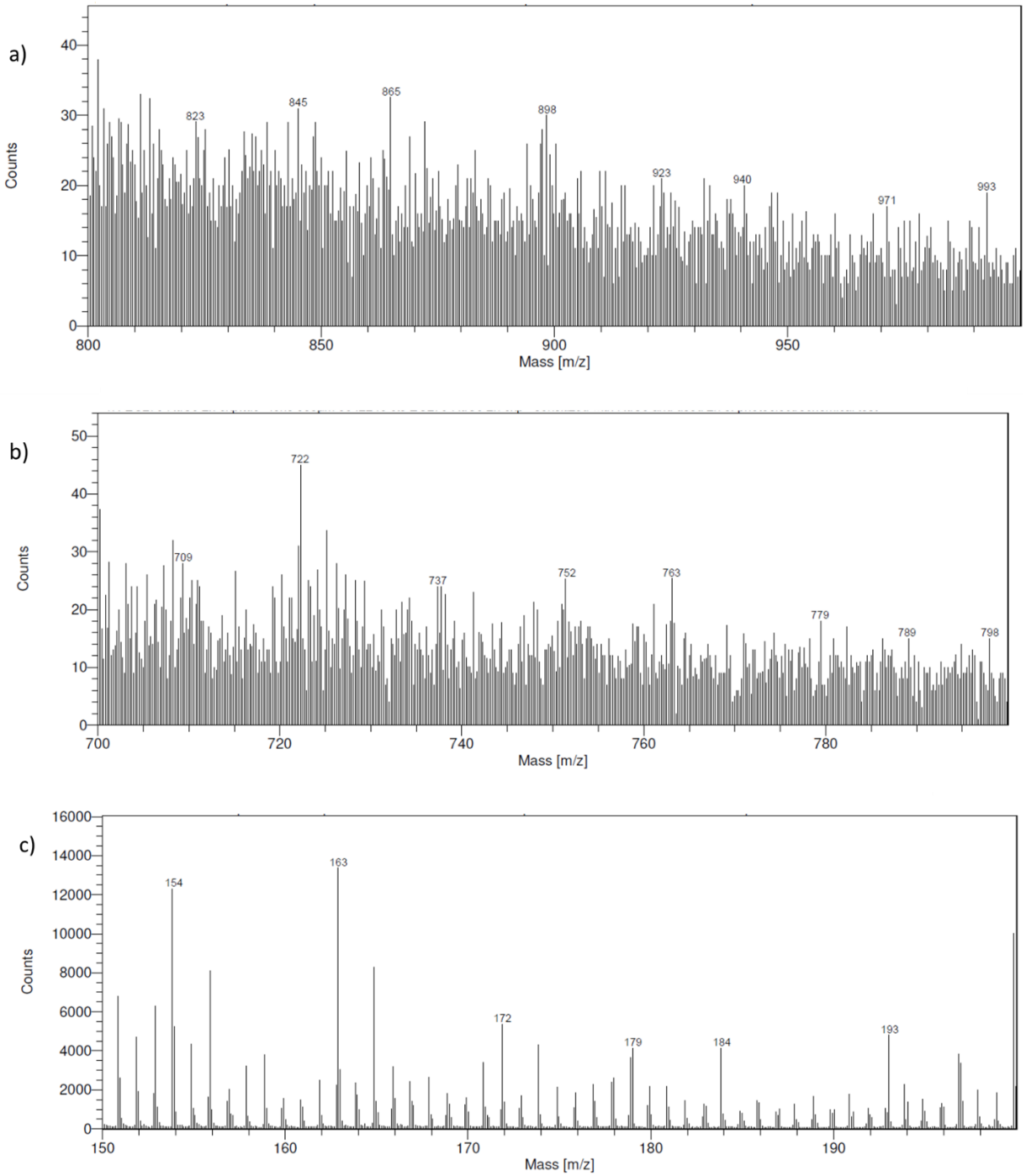

Figure III.19. Negative mode ToF-SIMS spectra of NiO electrodes sensitized by **RuP_4^{OH}-Co** after 2 hours of PEC tests in the m/z range a) 800-1000, b) 700-800, c) 150-200.

3) UV-Vis characterization

The desorption solutions were characterized first by UV-Vis spectroscopy. Comparing the spectra of the desorption solutions for the freshly sensitized films and the other half of the film after 2 hours of PEC tests (**Figure III.20**), extensive desorption is obvious regardless the irradiation (visible or AM 1.5 G).

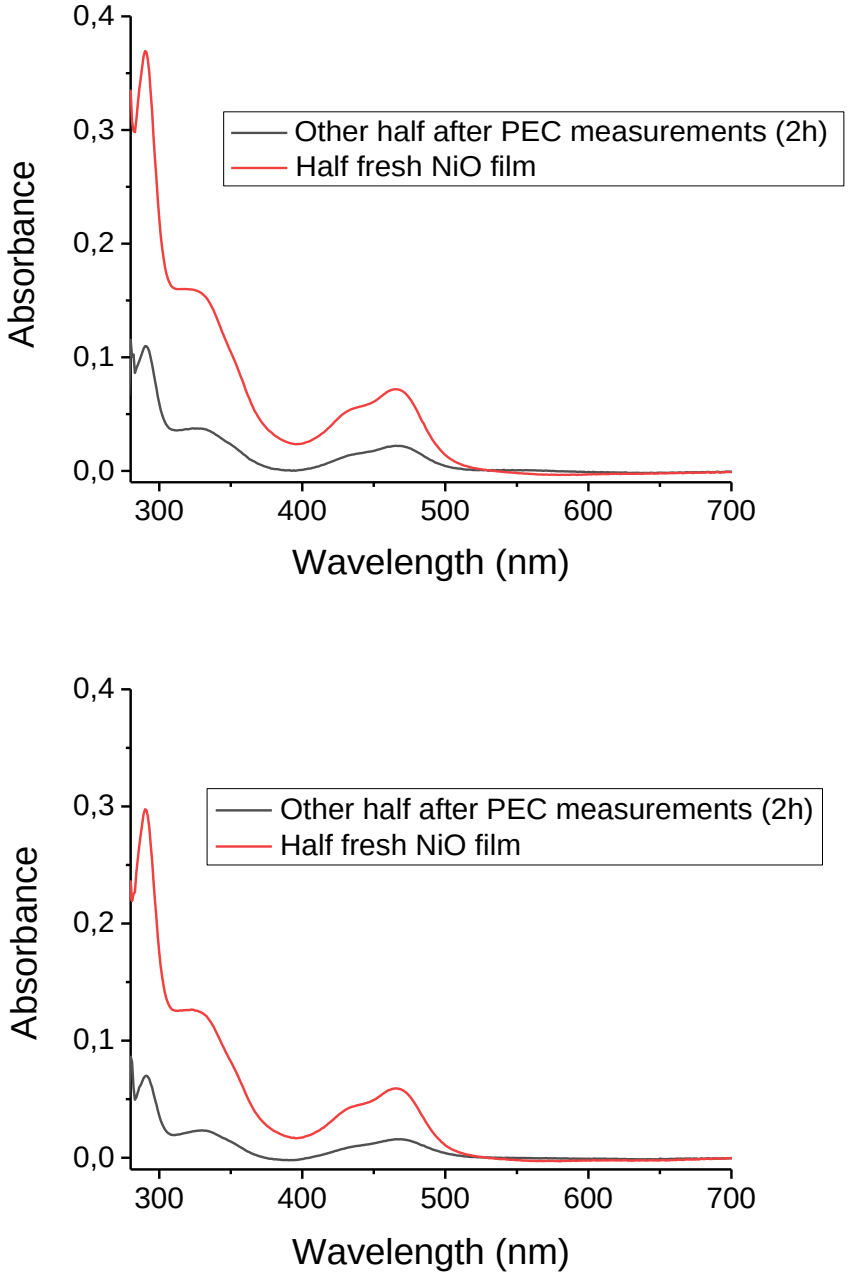

Figure III.20. UV-Visible spectra for **RuP_4^{OH}-Co** in methanolic solution of 1 M phenylphosphonic acid, where half of a fresh NiO film was dipped (red line) and the other half was dipped after 2 hours of PEC experiment (black line) with visible irradiation (left) or with AM 1.5 G illumination (right).

Desorption was estimated to be 76 ± 8 % (3 independent samples) for films irradiated with visible light and 80 ± 7 % (4 independent samples) when AM 1.5 G illumination was employed. Hence, the light source does not affect the desorption of the molecular components from the surface. The fact that most of the initial dyad is detached from the NiO surface after 2 hours is one limiting point for long-term activity. Hence, under our experimental conditions, desorption is a main issue to consider.

Desorption with similar ruthenium complexes have been already reported in the literature. Ruthenium-polypyridine dyes with two methyl phosphonic acid groups [$(Ru(bpy)_2(4,4'\text{-}(PO_3H_2)_2bpy)]^{2+}$ immobilized onto TiO_2 showed increased detachment in aqueous media after light irradiation in a range of pH from 1 to 7, reaching bare films after 15 hours.[52] In another study, the same complex grafted onto TiO_2 completely desorbed after 3 hours of continuous irradiation at pH 7.8 under open circuit conditions.[178] Furthermore, 20% desorption was previously observed from the group with ruthenium complexes bearing 4 methyl phosphonate groups after 10 minutes of photoelectrochemical tests in acetate buffer at pH 4.5.[55] Detachment of the molecular components from the surface is often acknowledged in the field of photoelectrocatalysis driving to low performances of p-type dye-sensitized photocathodes.[91,96,98,104]

About 40% desorption of ruthenium from the film was determined after performing XPS analysis, half from the estimation based on UV-Vis spectra. Decomposition of ruthenium could be the answer to this difference, even though XPS spectra do not support this assumption. $[Ru(bpy)_3]^{2+}$ is known to undergo bipyridine substitution during photogeneration of hydrogen in acidic water[128,179] with appearance of visible bands assigned to new coordination species with solvent molecules or anions. Furthermore, partial photochemical decomposition pathways under irradiation of ruthenium polypyridine complexes grafted onto metal oxides were reported in methanol, but not in water, with new bands at 500 nm for ligand substitution.[52] Another issue, is that for the XPS analysis we used a small piece of the lower part of a NiO film that could be irradiated less and decrease the desorption rate. Finally, a last issue might be linked to a lack of solubility of the dyad (or its derivatives) in the phenyl phosphonic acid methanolic solution employed for the desorption. Indeed, substitution of the halide ligands on the cobalt center occurs in aqueous medium leading to highly charged (5+) dyads.

4) MALDI-ToF analysis

The desorption solutions of the NiO films after 2 hours of PEC tests were sent for MALDI-TOF analysis. The peak at m/z: 1448, characteristic of the dyad, was absent from the spectrum (**Figure III.21**). One peak is observed at m/z: 1224, tentatively attributed to the complete decoordination of the cobalt center. Hydrolytic cleavage of the C-N bonds of the diimine-dioxime ligand seems the most probable explanation. The experimental isotopic pattern for the proposed molecular structure, ascribed to the degraded product, correlates well with the theoretical one.

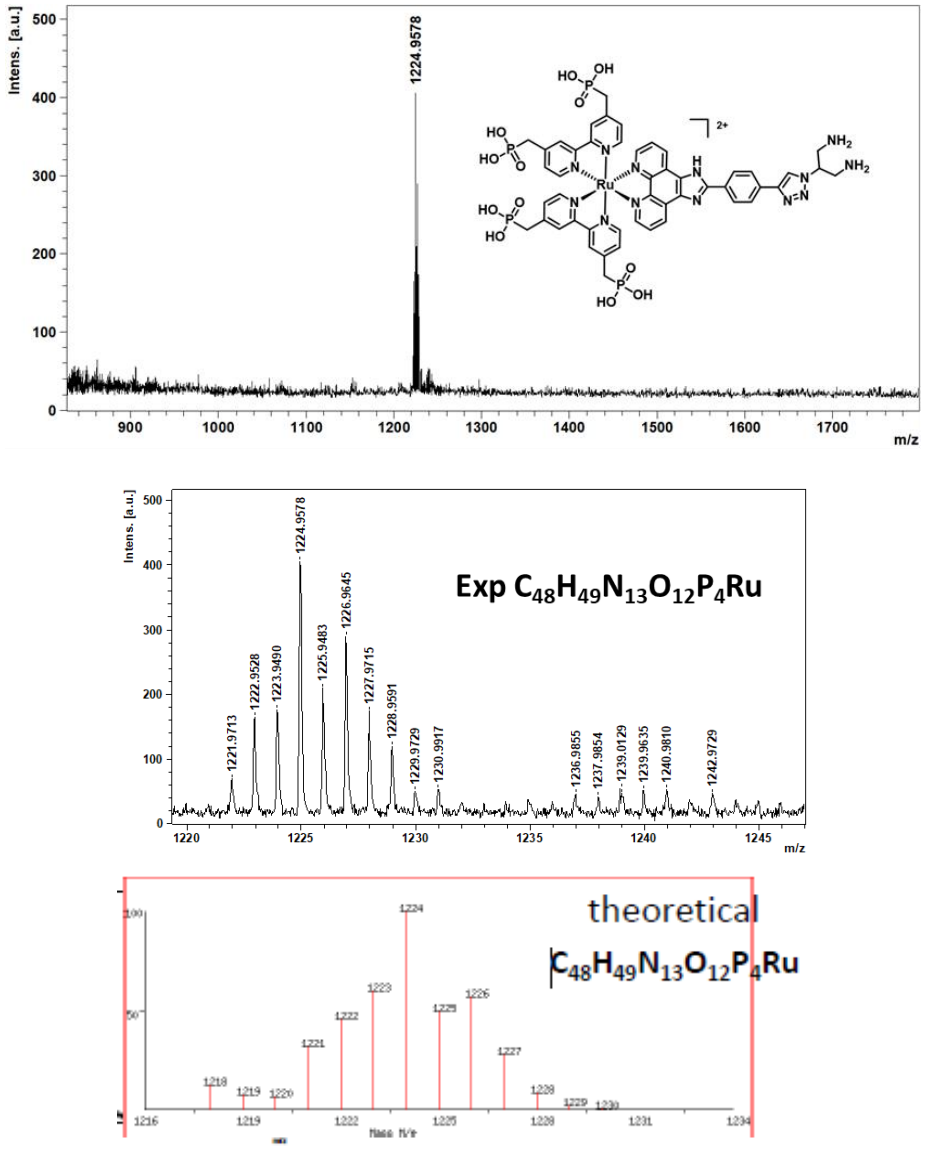

Figure III.21. Top, MALDI-TOF spectrum recorded in a methanolic solution of 1 M phenylphosphonic acid after 2 hours of PEC test, middle, the experimental isotopic pattern of the main peak at 1224 and bottom, the theoretical isotopic pattern are depicted.

In some cases, a peak at m/z: 1152 ascribed to the complete loss of the catalyst due to detachment from the triazole unit was also present. Supplementary post-operando techniques are needed to further elucidate the destiny of the dyad, as MALDI-ToF favors fragmentation, arising doubts for the speculated decomposition products. Here again, the fact that this analysis only provides information on the compounds soluble in the desorption solution has to be taken into consideration. Nevertheless, the fact that the signature of the intact dyad was not found after catalysis, is a good explanation for the deactivation of our photocathode due to the loss of the catalytic center.

VI. Conclusions and perspectives

The novel ruthenium-cobalt dyad was grafted onto nanostructured mesoporous NiO films, with dyad loading of 5.2 ± 0.8 nmol.cm$^{-2.}$ Even though this value is lower compared to the previous grafting efficiencies from the group, similar dyad loadings (4-5 nmol.cm^{-2}) have been reported for ruthenium based dyads on NiO electrodes.[180] Efficient sensitization and the integrity of the immobilized assembly were confirmed by XPS, ToF-SIMS and MALDI-ToF.

Photoelectrochemical characterization was carried out in fully aqueous conditions (pH 5.5) at - 0.4 V vs Ag/AgCl (+ 0.13 RHE) under standardized conditions. When visible light was employed, cathodic photocurrents were developed, reaching - 58 ± 11 μA.cm^{-2}. Long-term photoelectrolysis was performed and 28 ± 2 nmol.cm^{-2} of H_2 was evolved with 5 ± 1 TON. This new photocathode displayed superior activity compared to the previous system of the group based on a dyad with an organic dye[87] or with a porphyrin (see Annexes), highlighting the role of ruthenium, as all the other parameters were identical (setup, catalyst, triazole unit). More efficient and faster electron transfer from the dye to the catalyst, in agreement with our photolysis experiments (**Figure II.8**) could be a possible explanation.

Higher photocurrents were obtained when the activity was implemented with AM 1.5G illumination. Two times higher amount of H_2 and TON were estimated, reaching 60 ± 9 nmol.cm^{-2} and 13 ± 2 TON accordingly. More efficient light harvesting due to the strong absorption at 300 nm of ruthenium polypyridine complexes could be the main reason for this improvement. However, the performance is still low compared to homogeneous multicomponent photocatalytic systems employing the same cobalt catalyst (300 TON after 2 hours of continuous irradiation), where the electron transfer is controlled by diffusion.[75] In addition, it is even lower if we compare it with electrocatalytic systems (55000 TON),[68] where

the electron supply is sufficient. Thus, in our case the electron supply to the catalyst is limited, leading to moderate activity.

In order to investigate the electron transfer dynamics in our system, TA-SEC measurements were carried out. We could observe a fast hole injection, a long-lived primary charge separated state (one-electron reduced dye and oxidized Ni species) and charge recombination processes for our NiO/dyad system at quasi-operando conditions. The main kinetic issue does not seem to be the charge recombination, as it has been mainly proposed in the literature, but rather the efficiency of the electron transfer to the catalyst. No spectral feature could be identified for the formation of Co(I), the entry point of the mechanism for proton reduction,[66] suggesting that this electron transfer is not efficient and below the detection limit of the TA spectroscopy. This can explain the low activity of our photocathode. Different molecular design should be envisaged to enhance this thermal intramolecular electron transfer to the catalyst.

Although higher faradaic efficiencies were obtained compared to the previous dye-sensitized photocathodes of the group, the values are still low. After 2 hours of PEC experiments the estimated F.E. did not exceed 25%. However, almost 70% F.E. were determined during the first 30 minutes. This means that the catalyst works properly at the beginning of the tests. The lower F.E. after 2 hours raise questions about the stability of the system. Post-operando characterization was crucial to explain this behavior and to understand what happens at the end of the catalytic experiments.

Almost 80% desorption from the surface occurs during the course of the PEC tests. The group has addressed the instability of the cobalt diimine-dioxime catalyst under photochemical conditions[75] and Alberto and his coworkers assumed its decomposition under light irradiation.[74] Our group proposed that its immobilization onto carbon nanotubes increased the stability under electrochemical conditions.[68] However, in the work presented here XPS, MALDI-ToF and ToF-SIMS showed partial or complete disappearance of cobalt after catalysis. Decomposition pathways based on the catalytic part were identified.

To conclude, the main factors limiting the H_2-evolving performances of the ***RuP_4^{OH}-Co****-based photocathode are:*

- *an inefficient electron supply to the catalyst,*
- *a high percentage of desorption in the electrolyte*
- *a hydrolysis of the catalytic center.*

The inefficient supply of electrons to the catalyst implies that a new molecular design, favoring thermal electron transfer from the reduced dye, is needed.

Stronger attachment of the molecular architecture on the electrodes is crucial for long-term operation. This can be achieved either by functionalization of the dye with different anchoring groups or by protecting the interface of the anchorage from water (ALD).

More robust and noble metal-free catalysts should be used to enhance the performance of the photocathodes and this will be the subject of the next chapter.[129]

Chapter IV

Synthesis and characterization in solution of a novel dyad based on a cobalt tetraazomacrocyclic catalyst

In this chapter, we will present the synthesis and characterization of a new dye-catalyst assembly relying on the same ruthenium polypyridine photosensitizer functionalized with four methyl phosphonate groups (**RuP_4^{OEt}-EPIP**) and a cobalt tetraazomacrocyclic complex, referred below as **Cat1** (**Scheme IV.1**). Its redox and spectroscopic properties will be evaluated along with some thermodynamic considerations for the feasibility of the electron transfer from the NiO electrode to the catalyst.

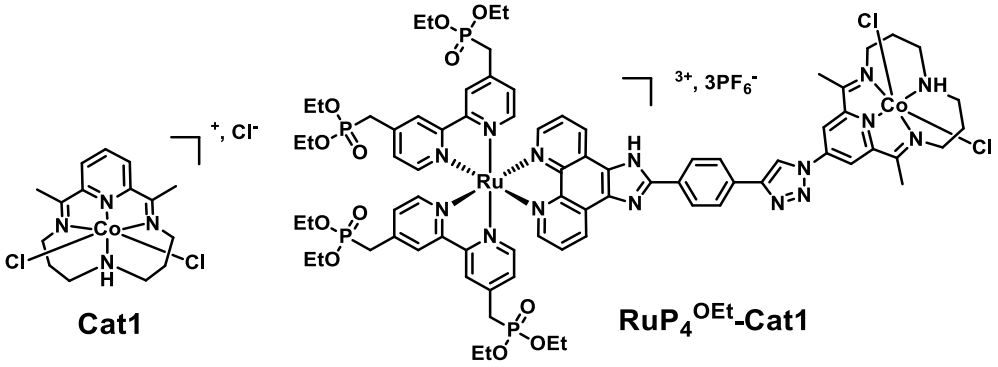

Chart IV.1. Structure of **Cat1** and the final dye-catalyst assembly, **RuP_4^{OEt}-Cat1**.

The motivation to introduce a novel catalyst arises by the increased activity and stability of polypyridinic and aminopyridinic cobalt complexes under reductive aqueous conditions reported over the last 10 years.[128,129,181] In addition, a comparative study by our group testing different molecular HER catalysts and employing a Clark-type microsensor, proved the superior activity of **Cat1** for proton reduction under homogeneous conditions compared to the cobalt diimine-dioxime catalyst.[182] In particular, at pH 4.5 with [$Ru(bpy)_3^{2+}$] as light absorber, **Cat1** exhibited a 5-fold increase in TON (102 vs 20.8).

I. Cat1 for H_2 evolution under homogeneous conditions

Cat1 is a cobalt(III) complex based on a tetradentate macrocyclic ligand, which is a 14-membered core (2,12-dimethyl-3,7,11,17 - tetraazabicyclo[11.3.1]heptadeca-1 (17),2,11,13,15-pentaene).[183,184] Cyclic voltammogram in 0.1 M $N^nBu_4PF_6$ in acetonitrile at a glassy carbon electrode revealed three reversible reduction potentials, ascribed to two metal reduction processes (Co(III)/Co(II), Co(II)/Co(I)) and one ligand based reduction, already reported for similar nickel complexes.[185] X-ray crystallography determined a six-coordinate complex with a distorted octahedral geometry and two trans to each other chloro ligands, under its Co(III) state.[186] **Cat1** was first reported as a catalyst for the reduction of CO_2.[187] A quick literature screening of **Cat1** for photo- and electro-catalytic proton reduction will be presented in the following part along with some recent results, by our group and others, to further assemble it with a light-harvesting unit.

1) Electrocatalytic hydrogen evolution

Electrocatalytic hydrogen evolution was first studied in acetonitrile by the group of T. Lau.[186] Addition of *p*-cyanoanilium tetrafluoroborate as proton source in acetonitrile generated a catalytic wave close to Co(II)/Co(I) redox couple. Bulk electrolysis at - 0.65 V vs SCE evolved hydrogen with 90% F.E., more than 50 TON and 200 mV overpotential. Electrolysis experiments were also carried out in mix organic/aqueous media. Addition of acetic acid caused again a catalytic wave close to Co(II)/Co(I) redox couple and bulk electrolysis at - 0.95 V vs SCE verified hydrogen production with similar F.E. and TON as in acetonitrile.

Recently, similar electrochemical behavior was obtained for **Cat1** in fully aqueous conditions with an irreversibly catalytic wave close to the Co(II)/Co(I) redox couple, increasing in intensity at more acidic pH.[188] Peters's group used also **Cat1** derivatives and other cobalt complexes for electrocatalytic hydrogen evolution in acidic water at pH 2.2.[189] Controlled-potential electrolysis at - 0.93 V vs SCE for 2 hours confirmed its catalytic activity towards proton reduction by gas chromatography. **Cat1** displayed the highest F.E. reaching 92% with roughly 20 TON.

2) Photocatalytic hydrogen evolution

Photo-driven hydrogen evolution using **Cat1** was first examined in an acetonitrile/water mixture (3/2) with Ir-PS, TEOA as SED and acetic acid as proton source, attaining 180 TON after 7 hours of continuous irradiation.[186] Maximal TON were achieved at pH 7.1. **Cat1**

exhibited higher activity with $[Ru(bpy)_3^{2+}]$ as light harvester. Ascorbate and ascorbic acid were used as SED and proton source respectively in fully aqueous conditions.[169] The highest TON_{cat} were 1000 and obtained with 10 times higher concentration of dye compared to the catalyst at pH 4. 12 ml of hydrogen was produced and the photocatalytic system was active for more than 20 hours. In a recent study, **Cat1** under similar conditions at pH 4.1, reached 680 TON after 4 hours of continuous illumination.[188]

Cat1 seems to be stable over time. One of the limiting factors for long-term operation was suggested to be the photosensitizer due to decomposition. Higher TON_{cat} (more than 4000) were obtained after substitution of ruthenium photosensitizer with an organic dye at pH 4.5 after 24 hours of irradiation.[170] Decreasing the amount of catalyst, increased the observed TON_{cat} to 8952. 75% of the initial concentration of the dye remains after 22 hours of irradiation. Thus, increased stability of the light harvester under reduced conditions can explain the increased TON compared to the previous systems. Comparing with other cobalt catalysts, among them Co-diimine-dioxime and noble metal complexes, **Cat1** showed superior activity, probably due to the macrocyclic nature of the ligand.[169] Resistance to hydrolysis and stabilization of low oxidation states of cobalt are the possible reasons leading to enhanced activity.

Trying to shed light on the mechanism for proton reduction,[190] electrochemical generation of Co(I) revealed its absorption spectrum with two intense peaks at 325 and 432 nm and a broad absorption above 500 nm.[169] Co(I) species were stable under anaerobic conditions in acetonitrile and mechanistic studies with addition of acids speculated a similar catalytic pathway with Co-diimine-dioxime.[66] Protonation of Co(I) species leads to a Co(III)-hydride. Further reduction to Co(II)-hydride and an additional protonation are needed for hydrogen evolution. However, reduction to Co(0), and then further protonation to obtain a Co(II)-hydride species, seemed to be also feasible.[188] It is clear that the working mechanism for proton reduction with **Cat1** is not as well-described as in the case of cobalt diimine-dioxime and investigation is ongoing.

3) Functionalization of Cat1 for covalent assembly with light-harvesting units

Although **Cat1** has been employed for the photo- or electrocatalytic proton and carbon dioxide reduction the last 30 years, mainly multicomponent systems were studied and there are almost no examples of substituted **Cat1** derivatives. Only a single example of **Cat1** functionalized on the pyridyl moiety for grafting onto quantum dots (QDs) was reported.[191] Recently, in our group two dye-catalyst assemblies based on organic dyes (submitted for publication) were prepared.[192]

i) Covalent grafting onto semiconductors QDs

Mei Wang's group in China lately reported the first example of a functionalized **Cat1** derivative for covalent grafting onto $CuInS_2$/ZnS QDs (**Chart IV.2**).[191] A Pd-catalyzed cross-coupling reaction was used for the introduction of a pyridine dicarboxylate anchoring group on the pyridine moiety of the ligand. To prove the beneficial influence of grafting, a direct comparison with the unfunctionalized catalyst was realized. Under the same experimental conditions and light illumination, the non-bonded catalyst evolved two times less hydrogen. Long-term experiments showed that the immobilized catalyst was still active after 32 hours of irradiation, compared to 16 hours for the catalyst in solution. Photoluminescence and TAS revealed that for the hybrid system, electron transfer to the catalyst is faster and back electron is slower, in agreement with its enhanced photocatalytic activity. Diffusion-limited processes is the principal interpretation for the inferior activity of the non-grafted catalyst.

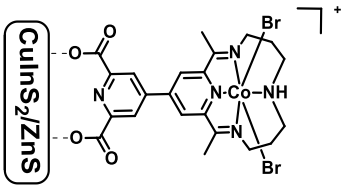

Chart IV.2. A covalently bonded hybrid assembly of **Cat1** on QDs.

ii) Covalent dye-catalyst assemblies prepared in our group

Before starting this thesis, our group synthesized the first covalent dye-catalyst assemblies with **Cat1** (manuscript submitted for publication).[192] Using our previously-reported CuAAC procedure,[87] J. Massin (post-doc) and Q. Vacher (master student) succeeded to couple **Cat1** with two different organic dyes, obtaining the two following dyads (**Chart IV.3**).

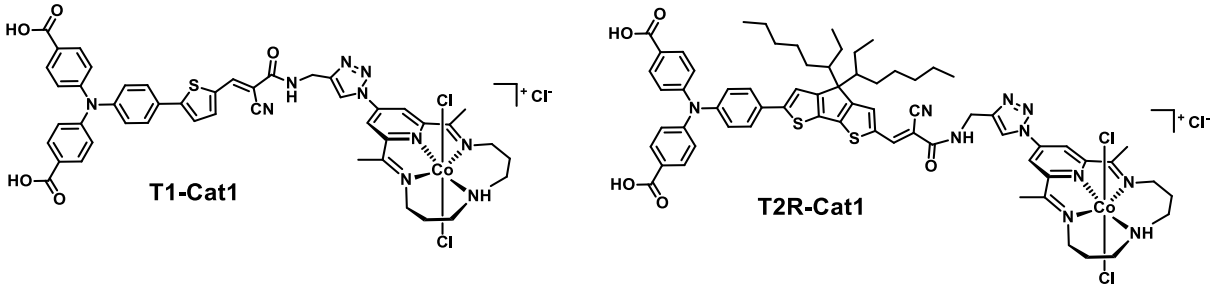

Chart IV.3. Structure of the two dyads prepared in our group.

Sebastian Bold, a PhD student in our team, assessed the photoelectrocatalytic activity of **T1-Cat1** and **T2R-Cat1** for hydrogen evolution with a promising outcome. Notably for **T2R-Cat1**, faradaic efficiencies higher than 65% and a 26-fold increase in TON were achieved compared

to similar photocathodes based on the cobalt diimine-dioxime catalyst, examined under strictly identical conditions (4 hours of continuous irradiation at – 0.4 V vs Ag/AgCl at pH 5.5).[87]

During my thesis, I participated to this project and optimized the synthesis and purification of **T1-Cat1**. Guided by these attractive results, I also tried to functionalize **T2R-Cat1** with methyl phosphonic acid anchoring groups instead of carboxylic acid ones in an attempt to examine in more details the role played by the nature of the anchoring groups on the grafting stability of the photocathode (**T2RP-Cat1**, more information in Annex). Following the superior hydrogen-evolving performance of these organic dyads with **Cat1**, coupling of this catalyst with **RuP$_4^{OEt}$-EPIP** was envisaged and will be presented in the following part.

II. Synthesis of RuP$_4^{OEt}$-Cat1

1) Synthetic strategies to couple RuP$_4^{OEt}$-EPIP and Cat1

The construction of the catalytic center and the coupling method can be challenging and here we will demonstrate our synthetic approaches to obtain the final dyad. Two synthetic routes (**Scheme IV.1**) were proposed to obtain **RuP$_4^{OEt}$-Cat1** (**Chart IV.1**). Source of inspiration of **Route 1** is the way we already isolated **RuP$_4^{OEt}$-Co**. It is based on a CuAAC coupling between **RuP$_4^{OEt}$-EPIP** and an azido functionalized derivative of **Cat1** (**N$_3$-Cat1**). The latter will be prepared using a cobalt-templated synthesis from a diacetylpyridine precursor functionalized by an azido group on the para-position of the pyridine moiety (**N$_3$-DAP**). The fact that exchanging from cobalt to copper occurs under normal Cu-driven cycloaddition[68] highlights the need to establish appropriate conditions to avoid this detrimental effect,[88,193] even though the more robust nature of **Cat1** might prevent this phenomenon by stabilizing the cobalt(III) center.

Following the efficient synthesis of the organic based-dyads with **Cat1** (**Chart IV.3**), **Route 2** is based on the CuAAC of **RuP$_4^{OEt}$-EPIP** with the catalyst precursor bearing an azido functional group (**N$_3$-DPA**). Then, cobalt-templated macrocyclization will take place for the ruthenium-based complex (**RuP$_4^{OEt}$-DAP**) to obtain the final dyad.

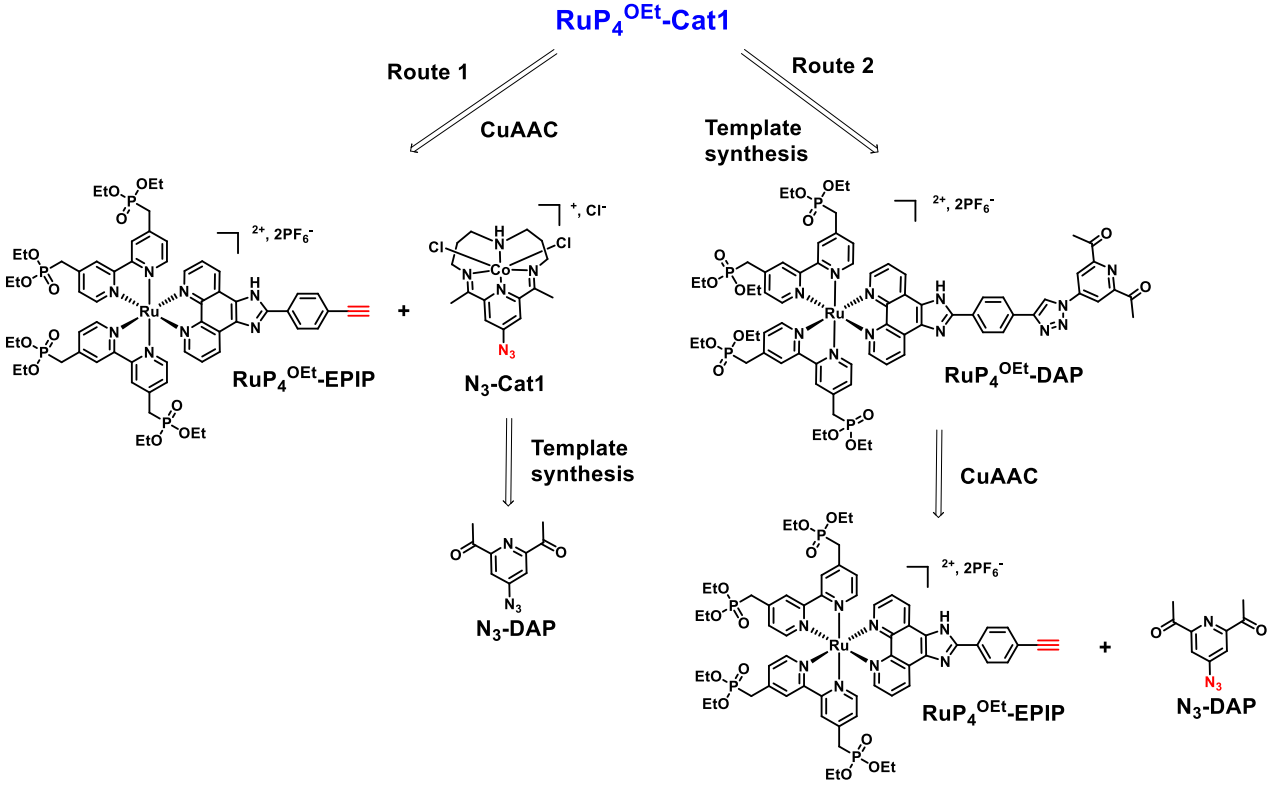

Scheme IV.1. Two retro-synthetic pathways to obtain **RuP_4^{OEt}-Cat1.**

Both routes use the same precursors. **RuP_4^{OEt}-EPIP**, whose synthesis is reported in chapter II and **N_3-DAP**, whose synthesis will be presented later. We should note that the anchoring groups were protected until the end of this chapter (like **RuP_4^{OEt}-Co**) and characterization in solution was carried out under the protected form due to low solubility of phosphonic acids in most common solvents.

2) Cobalt-templated synthesis of Cat1

Before testing the 2 routes, synthesis of a batch of **Cat1** was carried out in order to test the procedure of the cobalt-templated synthesis before applying it to a more complex system. Furthermore, a reference batch of **Cat1** is useful for comparison purposes. Synthesis of **Cat1** is well-described by different research groups and it is based on a metal-templated synthesis (**Scheme IV.2**). [169,184,186] 2,6 diacetylpyridine, 3,3'-diaminodipropylamine and a Co(II) salt in 1/1/1 ratio are heated at 75°C in a mixture of ethanol and water for 5 hours. Water is needed for avoiding the precipitation of the intermediate complex of 2,6 diacetylpyridine and Co(II). Some drops of acetic acid are added for buffering the amine solution and catalyzing the Schiff-base condensation. Addition of HCl (to provide an additional Cl anion) and oxidation to the more stable Co(III)-species with air-bubbling overnight yielded our final **Cat1** in 30% yield, after

precipitation with cold ethanol. Further crystallization as a perchlorate salt can also be undertaken.[169]

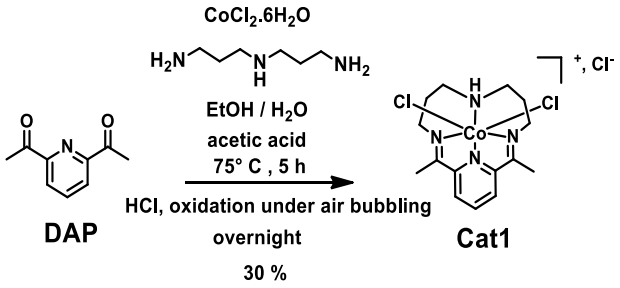

Scheme IV.2. General procedure for the preparation of **Cat1**.

3) Preparation of N_3-DAP

Starting from the commercially available chelidamic acid (**Scheme IV.3**), an aromatic nucleophilic substitution from hydroxyl to chloro groups takes place, as well as activation of the acid groups from thionyl chloride.[194] Subsequently, the chlorinated intermediate reacts with morpholine under inert atmosphere and a di-morpholino compound is obtained **(1)** with initial yields below 20%. Increase to 65% was achieved after addition of some drops of DMF, acting catalytically. NMR characterization and ESI-MS were used to identify the desired compound (more information in Experimental part). Then, a ketone-derivative (**2**)[195] was synthesized by replacing the two morpholine amides using a Grignard reagent (MeMgCl).[196] Purification was accomplished on silica gel column with DCM as eluent and ESI-MS and NMR proved its efficient synthesis. **N_3-DAP** was isolated by substitution of para-chloro group on pyridine using an excess of NaN_3 in a moderate 30% yield.[197] The same reaction was carried out with a commercially available bromo-derivative of (**2**) with similar yields. Column chromatography on silica gel with pentane/DCM (1/1) enabled us to purify our final compound. Reduction to amine-derivative under our experimental conditions is the limiting factor for the yield.[198] Absence of light or dry DMF did not seem to optimize the reaction. NMR spectroscopy and ESI-MS (m/z: 205.0 for $[M+H]^+$) confirmed the correct structure of **N_3-DAP**.

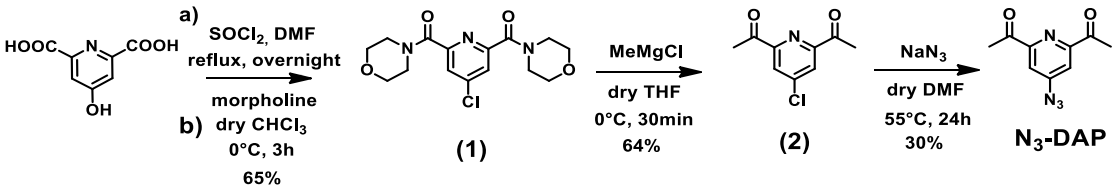

Scheme IV.3. Synthetic procedure to obtain **N_3-DAP**.

4) Route 1: attempts to prepare N_3-Cat1

We tried to synthesize **N_3-Cat1** by performing cobalt-templated synthesis on **N_3-DAP** using the previously presented procedure for the preparation of the non-substituted **Cat1**. $CoCl_2 \cdot 6H_2O$, **N_3-DAP** and 3,3'-diaminodipropylamine in equimolar amounts were heated at 75°C in a homogeneous mixture of EtOH/DCM/H_2O (3/1.5/1) for 5 hours (**Scheme IV.4**). Some drops of acetic acid were added for buffering the amine solution and catalyzing the Schiff-base condensation. After oxidation to Co(III) and precipitation with KCl, a green solid was collected. However, ESI-MS demonstrated that the final compound was amino-functionalized with three peaks at m/z: 402.1, 366.1 and 330.2 corresponding to $[M\text{-}Cl]^+$, $[M\text{-}2Cl\text{-}H]^+$ and $[M\text{-}3Cl\text{-}2H]^+$ accordingly. A previous attempt to isolate the same complex in the group was also unsuccessful. Hence, the reduction through hydrogenation from azido to amino due to the presence of water[198] is favorable under these conditions and in our hands subsequent CuAAC to obtain **RuP_4^{OEt}-Cat1** through **Route 1** was not possible.

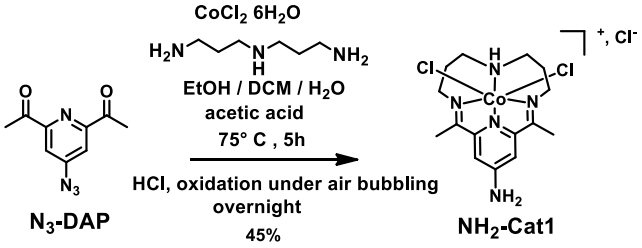

Scheme IV.4. **NH_2-Cat1** was obtained by performing Co-templated synthesis on **N_3-DAP**.

5) Route 2: CuAAC coupling for the preparation of RuP_4^{OEt}-DAP

We concentrated our efforts on the second route, previously employed for the synthesis of the organic dyes-based dyads (**Scheme IV.3**). Employing the previously optimized conditions,[131] **RuP_4^{OEt}-EPIP**, **N_3-DAP**, sodium ascorbate and copper sulfate were stirred for 2 days at room temperature in a homogeneous mixture of solvents (DCM/MeOH/H_2O). Purification on silica chromatography with a gradient eluent of MeCN/aqueous 0.4 M KNO_3 (from 98/2 to 85/15) followed by anion metathesis (hexafluorophosphate salt) resulted in the isolation of **RuP_4^{OEt}-DAP** (**Scheme IV.5**) with a yield of 60%. NMR spectroscopy (see corresponding part), ESI-MS and HRMS were used for the confirmation of the final structure. A single peak at m/z: 769.2 for $[M\text{-}2PF_6]^{2+}$ in ESI-MS and HRMS with an isotopic pattern in perfect agreement with the theoretical one indicates the efficient coupling of the subunits.

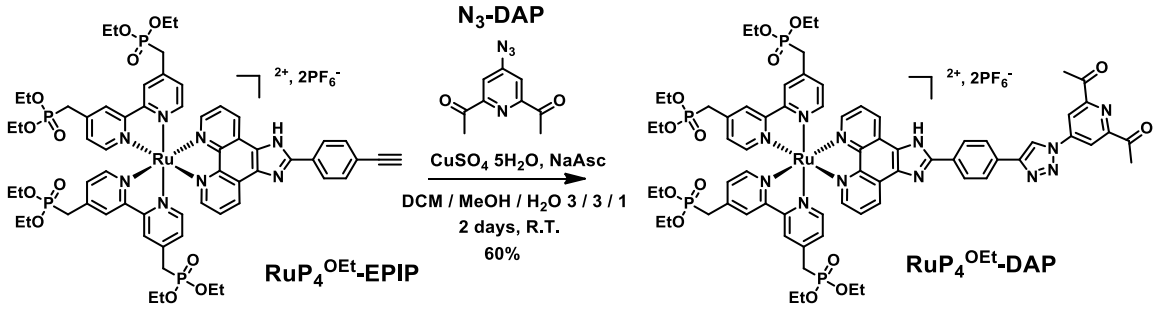

Scheme IV.5. CuAAC to obtain **RuP_4^{OEt}-DAP**.

6) Route 2: Cobalt-templated synthesis for the preparation of RuP_4^{OEt}-Cat1

The construction of the catalytic center on **RuP_4^{OEt}-DAP** was realized by a cobalt-templated synthesis based on the procedure employed to prepare **Cat1** (**Scheme IV.2**). $CoCl_2 \cdot 6H_2O$, **RuP_4^{OEt}-DAP** and 3,3'-diaminodipropylamine were heated at 75°C in a homogeneous mixture of EtOH/DCM/H_2O (3/1.5/1) overnight (**Scheme IV.6**). DCM was added for solubility reasons and the reaction was left overnight in order to try to increase the reaction yield (more details in **Table IV.1**). Some drops of acetic acid were also added.

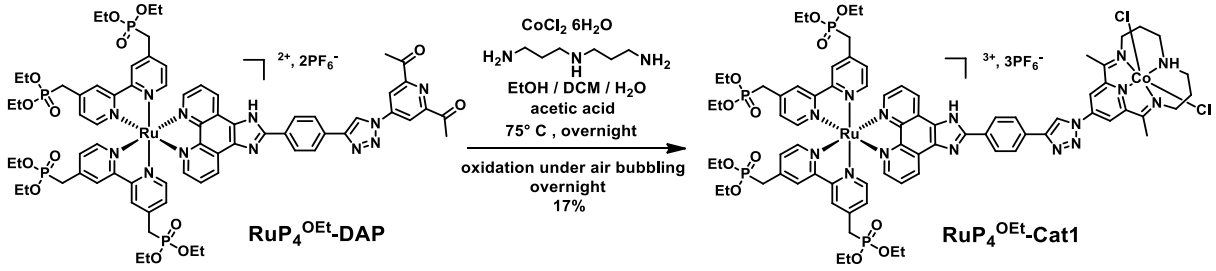

Scheme IV.6. Cobalt-templated synthesis to obtain **RuP_4^{OEt}-Cat1**.

After air bubbling overnight to oxidize to the more stable diamagnetic Co(III) species in the presence of HCl, column chromatography on silica was carried out. **RuP_4^{OEt}-Cat1** is highly charged and the purification was challenging. We found out that the best combination of solvents for good separation is to start with acetone/aq. 0.4 M KNO_3 (85/15) and some few mgs of starting material (**RuP_4^{OEt}-DAP**) could be removed. Then, we changed to acetone/H_2O/aq. saturated KCl (90/9/1) and the desired compound was desorbed from silica. After addition of KPF_6 and filtration, **RuP_4^{OEt}-Cat1** was obtained under its hexafluorophosphate salt, albeit with a yield not exceeding 20%.

Many efforts were devoted for synthesizing **RuP_4^{OEt}-Cat1** and to try to optimize the reaction conditions and the purification (**Table IV.1**):

- Leaving the reaction under stirring at 75°C for 6 hours, like the previous reports for the construction of the catalytic center for **Cat1** or overnight did not significantly affected the final yields. However, increasing the reaction time to 48 hours was detrimental for the synthetic procedure.

-Using acetonitrile instead of dichloromethane as co-solvent did not have any important impact.

- Two different cobalt salts were used ($CoCl_2.6H_2O$ and $CoBr_2$.hydrate). After adding $CoBr_2$.hydrate, we could not obtain the expected dyad. Its highly hygroscopic nature influences the accurate amount that we weighted, and this should affect the efficiency of the templated-synthesis.

Co(II) salt	Co-solvent	Reaction Time	Yield
$CoCl_2.6H_2O$	DCM	overnight	17
$CoCl_2.6H_2O$	DCM	6 hours	15
$CoBr_2$.hydrate	DCM	overnight	0
$CoCl_2.6H_2O$	CH_3CN	overnight	15
$CoCl_2.6H_2O$	DCM	48 hours	0

Table IV.1. Experimental conditions employed for the preparation of **RuP_4^{OEt}-Cat1**.

Our highest yield did not exceed 17%, which is lower than the one obtained for **Cat1** (30%). In addition, the yields for the dyads based on organic dyes were significantly higher, reaching 70% for **T1-Cat1** (Annexes). The presence of some starting material (**RuP_4^{OEt}-DAP**) was identified by ESI-MS analysis of the crude mixture, suggesting that a lack of efficiency of the cyclization might be an issue. In addition, the fact that the phosphonated derivative of **T2R-Cat1** (**T2RP-Cat1**, see Annexes) could not be isolated, suggests that the presence of phosphonate groups in **T2RP-Cat1** and **RuP_4^{OEt}-Cat1**, but not in **T1-Cat1** and **T2R-Cat1** could be an issue. Partial hydrolysis of the phosphonate esters might occur under the acidic conditions employed in the template synthesis procedure (acetic acid, HCl), rendering the complex more difficult to purify and isolate (different solubility, stronger adsorption onto silica gel).

7) ESI-MS analysis

ESI-MS was an important tool for us to confirm that we synthesized the desired dye-catalyst assembly. Before purifying the dyad, the crude mixture was checked by ESI-MS to confirm that the template synthesis was successful, and we could often detect mono-hydrolyzed derivatives, explaining the low final yields after column chromatography.

After purification, spectra acquired in the positive mode (**Figure IV.1**) exhibit different peaks attributed to the final dyad thanks to the specific isotopic pattern of ruthenium. The dominant peak detected at m/z: 588.1 is the signature of **RuP_4^{OEt}-Cat1** with a $Co(III)Cl_2$ center $[M-3PF_6]^{3+}$ and the peak at m/z: 954.4 corresponds to the same complex with a loss of $2PF_6$ $[M-2PF_6]^{2+}$. An additional peak at m/z: 881.5 is ascribed to **RuP_4^{OEt}-Cat1** with the loss of one proton $[M-H-2PF_6]^{2+}$.

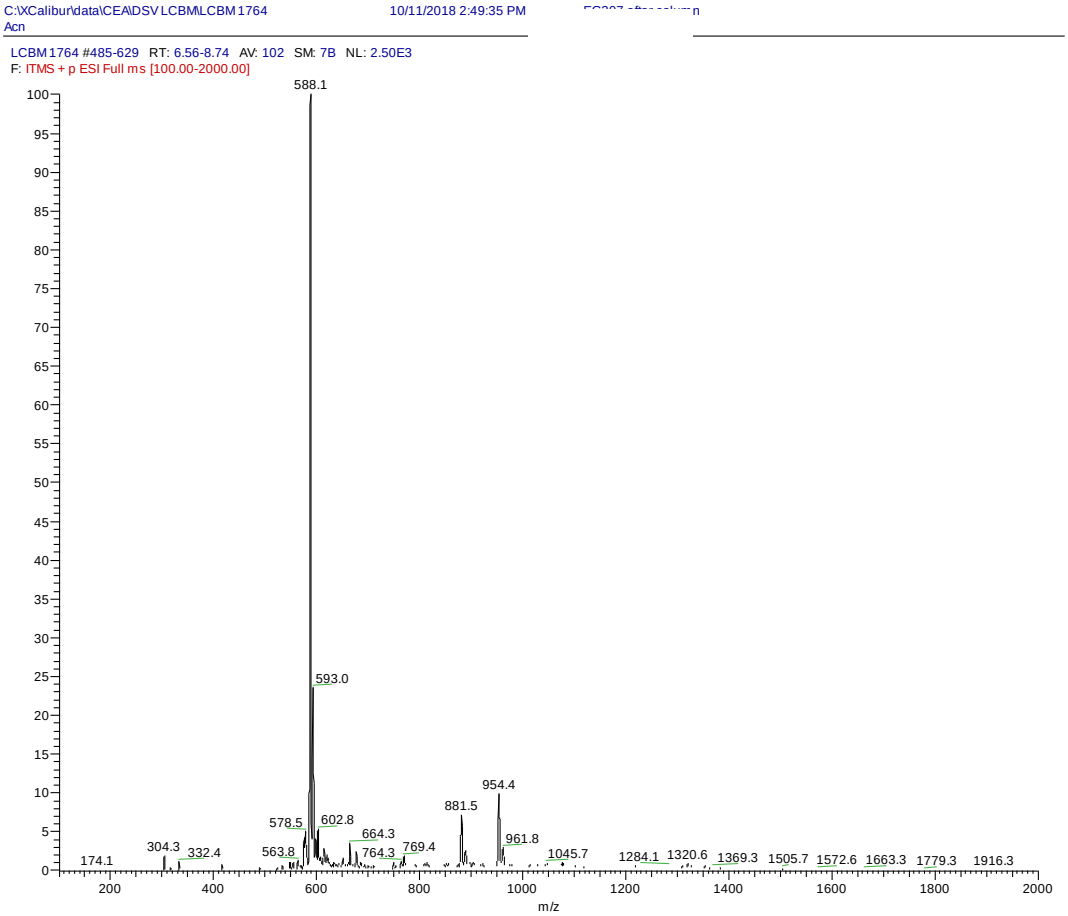

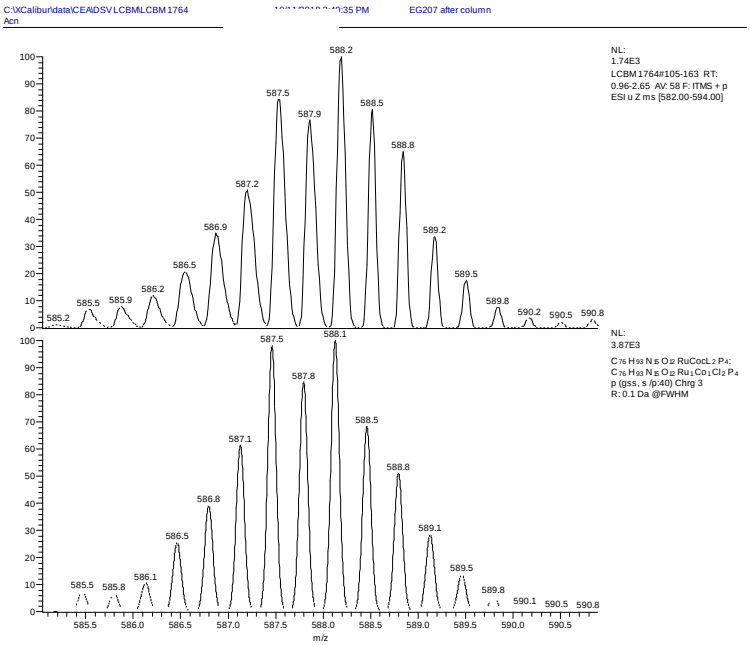

Figure. **IV.1**. Top, ESI-MS spectrum of purified **RuP$_4^{OEt}$-Cat1**, middle its experimental isotopic pattern and bottom its theoretical one.

8) ^{1}H-NMR characterization

i) RuP$_4^{OEt}$-DAP

NMR spectra were recorded in CD_3CN (300 MHz). In **Figure IV.2**, the ^{1}H-NMR spectra of **RuP$_4^{OEt}$-DAP** and **RuP$_4^{OEt}$-EPIP** are depicted for comparison. The presence of a singlet at 9.06 ppm for **RuP$_4^{OEt}$-DAP** corresponding to the proton of the triazole unit is characteristic of the efficient coupling, along with the disappearance of the singlet for the proton of the alkyne ligand (3.6 ppm top spectrum). The intact diacetylpyridine group coupled to the ruthenium complex with a triazole ring is confirmed by a singlet at 8.62 ppm, ascribed to the two protons of the pyridyl group. Furthermore, the appearance of a new singlet at 2.79 ppm for the two methyl groups of the diacetylpyridine unit is further proof for the integrity of **RuP$_4^{OEt}$-DAP**. The methyl phosphonate groups are observed unmodified with 8 protons for the methylene spacer (multiplet at 3.37 ppm) and 16 (multiplet at 3.99 ppm) and 24 (multiplet at 1.14 ppm) protons for the -CH_2 and -CH_3 groups of the phosphonate esters.

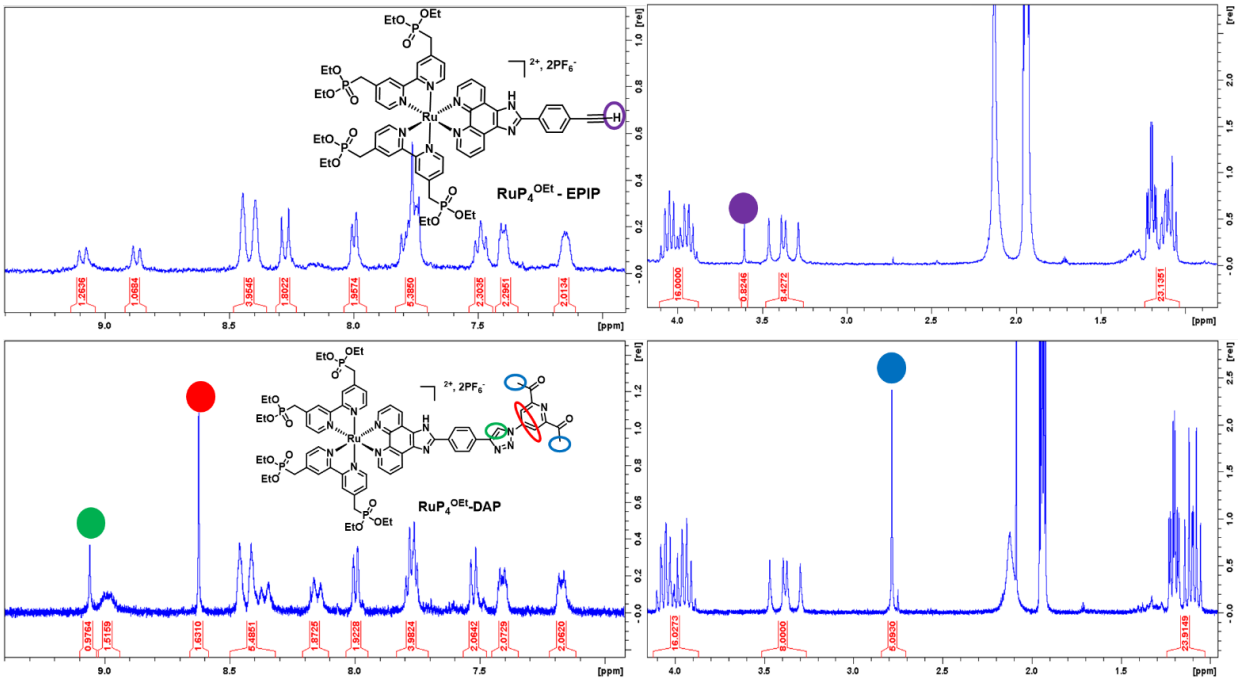

Figure IV.2.[1]H NMR spectra of **RuP_4^{OEt}-EPIP** (top) and **RuP_4^{OEt}-DAP** (bottom) recorded in CD_3CN at 300MHz.

ii) RuP_4^{OEt}-Cat1

The [1]H-NMR of **RuP_4^{OEt}-Cat1** recorded at 500MHz is depicted in **Figure IV.3**. We faced some problems with the interpretation of the spectrum and especially close to the catalytic center. Comparison with the spectrum of **RuP_4^{OEt}-DAP** (**Figure IV.2**) reveals that new peaks arise in the region of 6 ppm to 1.5 ppm; further comparison with the spectrum of **T2R-Cat1** allow to attribute them to the protons of the catalytic moiety. Interestingly, the peak at 5.95 ppm is the proton of Co-NH (one of the footprints of the complex) based on the detailed NMR analysis of **T2R-Cat1**. The interpretation of the latter proved also to be difficult due to some conformational restrictions in the dyad; various solvent mixtures were tested before being able to obtain a 500 MHz spectrum of correct quality. Efforts to improve the quality of [1]H NMR of **RuP_4^{OEt}-Cat1** are thus ongoing using different solvents, varying the experimental parameters and working with a 500MHz NMR spectrometer.

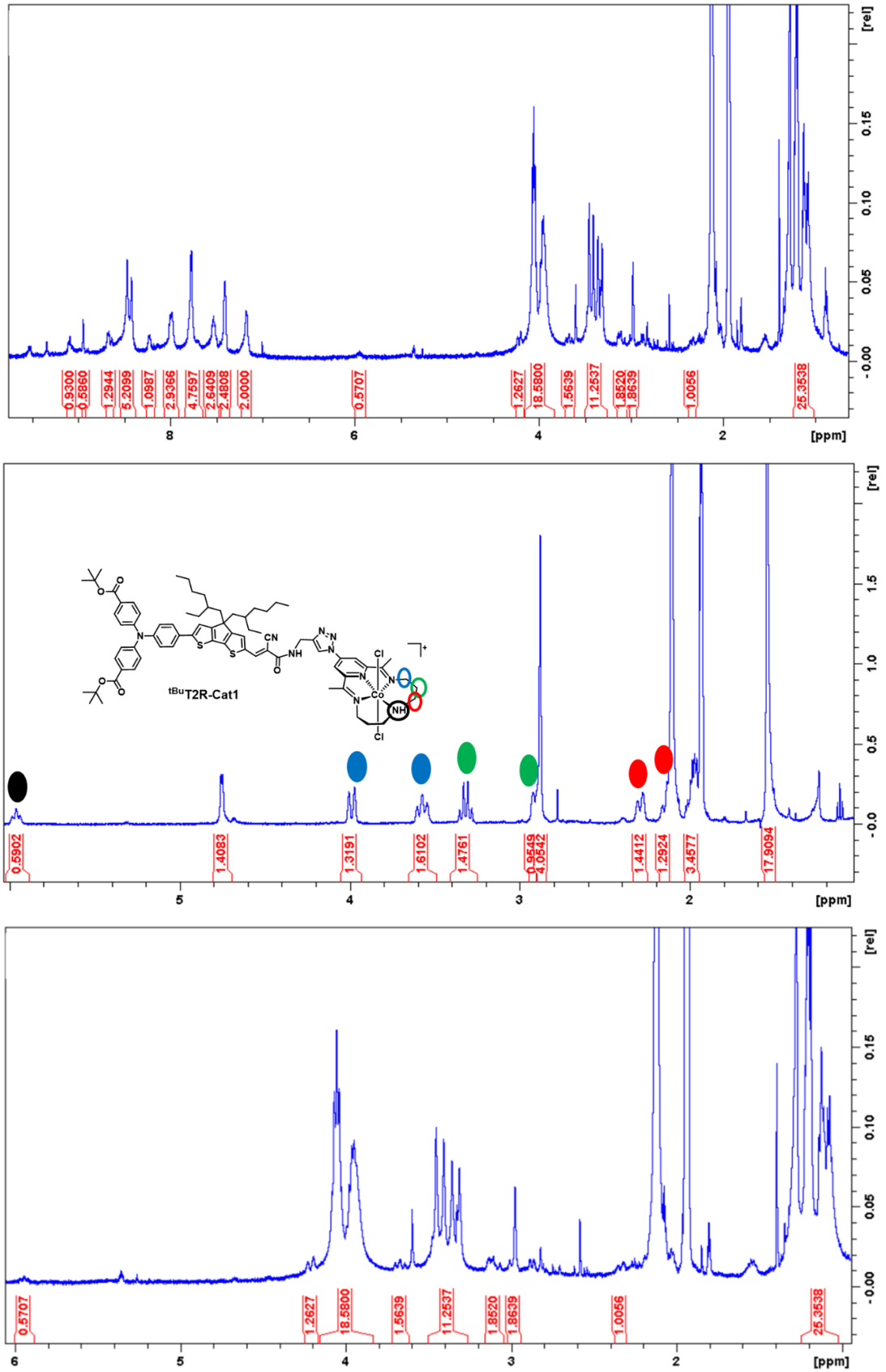

Figure IV.3. ^{1}H NMR spectra of **RuP$_4^{OEt}$-Cat1** (top) and selected regions (bottom) recorded in CH_3CN at 500MHz. Middle, selected region of ^{1}H NMR spectra of **T2R-Cat1** recorded in CH_3CN at 500MHz

III. Determination of the redox and spectroscopic properties of RuP_4^{OEt}-Cat1

1) Electrochemical characterization

The redox properties of **RuP_4^{OEt}-Cat1** were determined by cyclic voltammetry in degassed acetonitrile (0.1M *n*Bu_4NPF_6) at a glassy carbon working electrode at 100 $mV \cdot s^{-1}$ and referenced to the ferrocenium/ferrocene couple ($Fc^{+/0}$). The cyclic voltammograms are presented in **Figure IV.4** and the potentials attributed to the redox features for **RuP_4^{OEt}-Cat1**, **Cat1** and **RuP_4^{OEt}-EPIP** are summarized in **Table IV.2**.

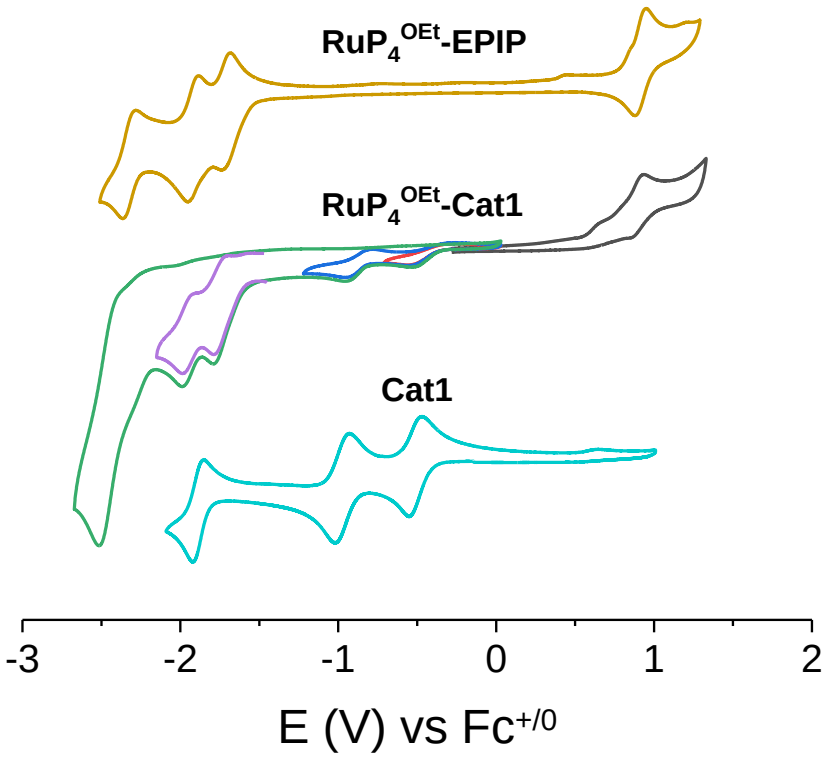

Figure IV.4. Cyclic voltammograms of **RuP_4^{OEt}-EPIP**, **RuP_4^{OEt}-Cat1** and **Cat1** vs. $Fc^{+/0}$. Measurements were carried out at 100 $mV \cdot s^{-1}$ at a glassy carbon electrode in acetonitrile (0.1 M *n*Bu_4NPF_6) under inert atmosphere.

On the anodic scan of the voltammogram, at + 0.90 V vs $Fc^{+/0}$ the reversible redox couple is associated to the metal-centered oxidation of Ru(II) to Ru(III).[55] On the cathodic part, two peaks for the redox couples of the cobalt center Co(III)/(II) at - 0.41 V vs $Fc^{+/0}$ and Co(II)/Co(I) at - 0.87 V vs $Fc^{+/0}$ are recognized, in comparison with the corresponding values of – 0.51 V and – 0.98 V $Fc^{+/0}$ for **Cat1**. The third ligand-based reduction of **Cat1** is not detectable in the dyad

due to overlap with the ligand-based reductions of ruthenium. Three quasi-reversible electrochemical processes are monitored for **RuP_4^{OEt}-Cat1** at -1.74 V, -1.95 V and -2.50 V vs $Fc^{+/0}$, attributed to the reduction of the three polypyridine ligands.

Complexes	E_{ox} $Ru^{II/III}$	E_{red1} $Co^{III/II}$	E_{red2} $Co^{II/I}$	E_{red3} Ru^{II}/Ru^{II}-$L^{\cdot-}$	E_{red4} Ru^{II}/Ru^{II}-$L^{\cdot-}$	E_{red5} Ru^{II}/Ru^{II}-$L^{\cdot-}$
RuP_4^{OEt}-Cat1	+ 0,90	- 0,41	- 0,87	- 1,74	- 1,95	- 2,50
RuP_4^{OEt}-EPIP	+ 0,92			- 1,71	- 1,92	- 2,32
Cat1		- 0,51	- 0,98			

Table IV.2. Electrochemical properties of complexes **RuP_4^{OEt}-Cat1**, **RuP_4^{OEt}-EPIP** and **Cat1** vs $Fc^{+/0}$.

As previously observed for **RuP_4^{OEt}-Co**, the individual redox properties of the photosensitizer (**RuP_4^{OEt}-EPIP**) and the catalyst (**Cat1**) are not modified after their efficient coupling, in agreement with their electronic decoupling at the ground state of the dyad **RuP_4^{OEt}-Cat1**.

2) UV-Visible spectroscopy

i) Protonation state of the imidazole bridge

The absorption spectrum of **RuP_4^{OEt}-Cat1** displays the dominant MLCT transition in the visible region and the π-π^* ligand-based one at 300nm. We previously showed by UV-vis titration that for the isolated **RuP_4^{OEt}-Co**, the imidazole ring of the bridging ligand is protonated. In this sense, similar titration measurements were performed for **RuP_4^{OEt}-Cat1** using aliquots of TFA (**Figure IV.5** top) and TEA solutions (**Figure IV.5** bottom) in acetonitrile (1.4×10^{-5} M). The UV-Vis spectra do not exhibit any modifications even after the addition of 2 eq of TFA as previously observed with **RuP_4^{OEt}-Co**. On the contrary, the shoulder at 450 nm and the tail exceeding to 550 nm increase in intensity after addition of TEA, indicating that these transitions involve the imidazole-based ligand. Appearance of isosbestic points at 336, 446 and 472 nm prove the evolution of new formed species.

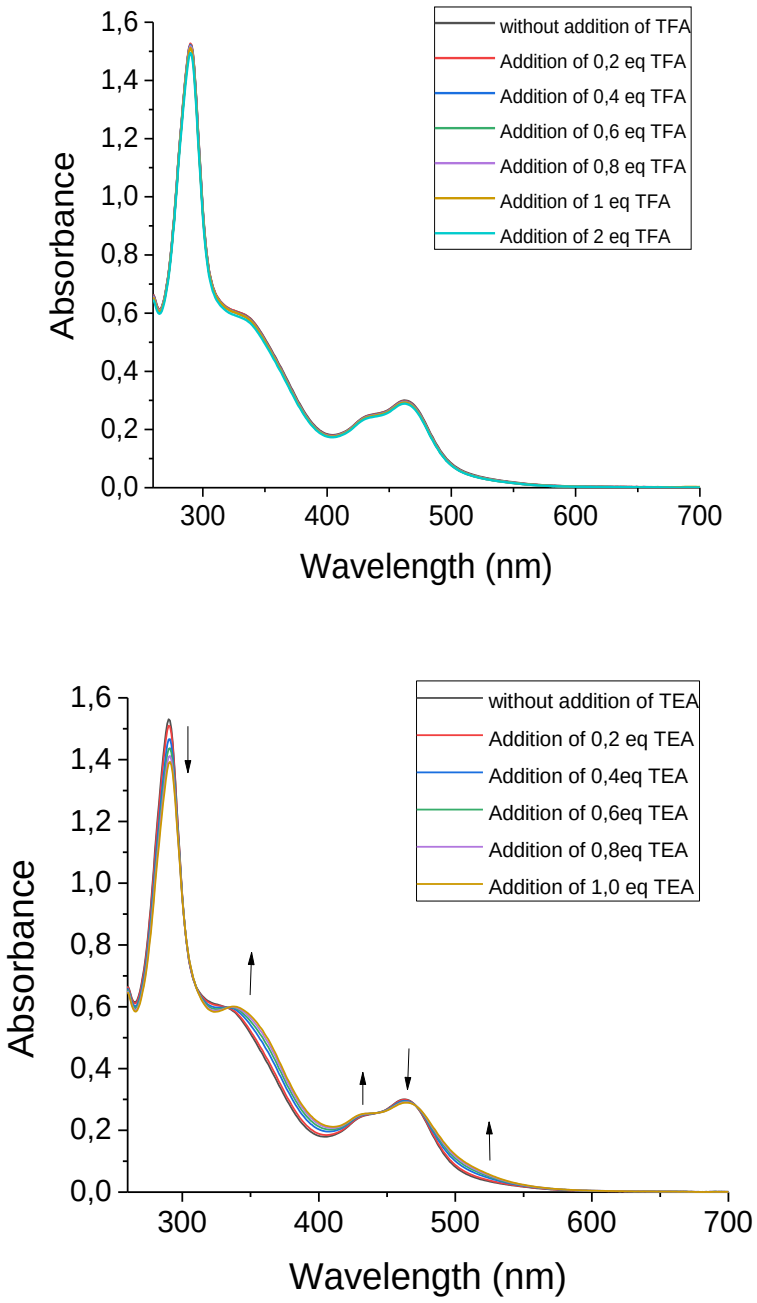

Figure IV.5. UV-Vis titration at the ground state of **RuP$_4^{OEt}$-Ca1** in acetonitrile using aliquots of TFA (top) or TEA (bottom) solutions.

These observations are in agreement with previous titration measurements on **RuP$_4^{OEt}$-Co** and based on Aukauloo's work,[150] the dyad is isolated under the protonated form of the imidazole ring at the end of the synthetic procedure (**Chart IV.4**). The usage of HCl and acetic acid during the construction of the macrocyclic cobalt center further justifies this statement. Similarly to the previous dyad, under the experimental conditions employed for the PEC tests (aqueous solution in pH 5.5), **RuP$_4^{OEt}$-Cat1** will be in its neutral form (**Chart IV.1)**, according

to the pKa for the imidazole ring calculated by A. Aukauloo and his group for similar ruthenium complexes.[150]

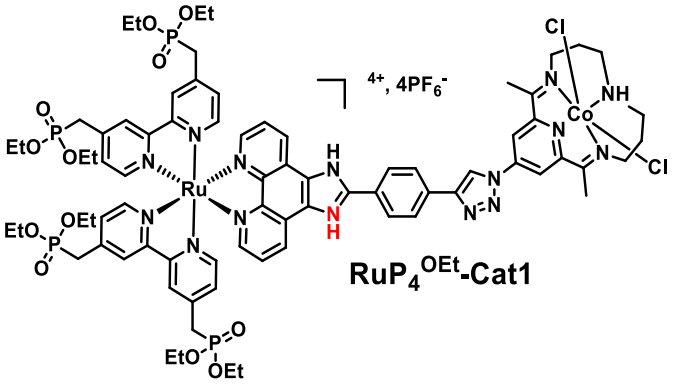

Chart IV.4. Structure of **RuP_4^{OEt}-Cat1** eventually synthesized and confirmed after titration experiments.

We should mention that the reaction yields and the ε values have been calculated taking into consideration the protonated imidazole derivatives.

ii) Determination of molar extinction coefficients

UV-Visible spectra of **RuP_4^{OEt}-Cat1** (**Figure IV.6**) were recorded in acetonitrile solutions (2.9×10^{-5} M). For **RuP_4^{OEt}-Cat1** the MLCT transition is observed in the visible region with maxima at 463 nm ($\varepsilon = 21400\ M^{-1}cm^{-1}$). The intense band displayed at 290 nm is a π-π* ligand-based transition and the shoulder at 350 nm and the tail exceeding to 550 nm are imidazole-based transitions. **Cat1** slightly absorbs in the near UV region and concerns ligand-centered transitions.[169]

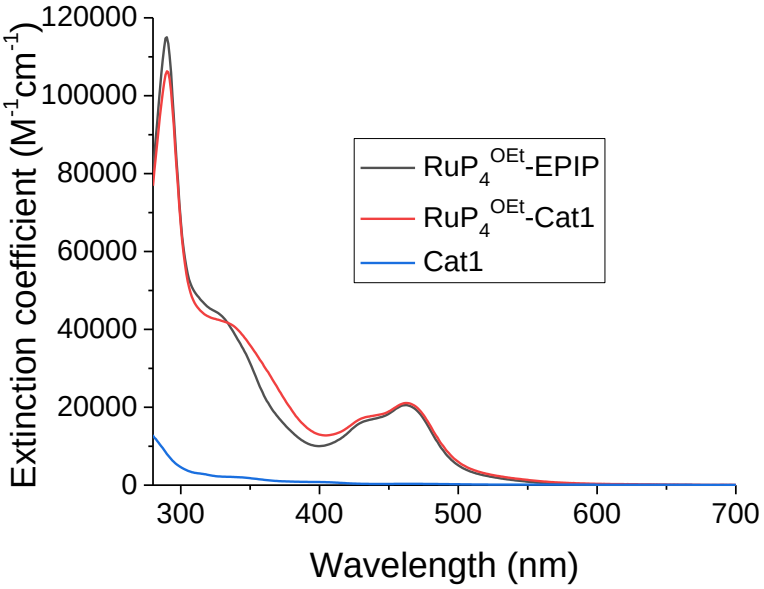

Figure IV.6. UV-Visible absorption spectra of **RuP_4^{OEt}-Cat1** (red line), **RuP_4^{OEt}-EPIP** (black line) and **Cat1** (blue line) recorded in acetonitrile.

IV. Thermodynamic considerations

1) Feasibility of working mechanism on NiO electrodes

Before carrying out the PEC tests onto NiO electrodes in fully aqueous conditions at pH 5.5, it is necessary to examine if all the thermodynamic criteria are met. Although the two mechanisms presented in **Figure II.7** (reductive quenching and oxidative quenching) could be taken into account here, we will focus on the reductive quenching one, considering that hole injection is occurring very fast (some ps) for ruthenium polypyridine dyes grafted onto NiO.[55] Fast hole injection was also proved for **RuP_4^{OEt}-Co** after performing TA-SEC measurements. In addition, for **T2R-Cat1** generation of the reduced dye occurred before electron transfer to **Cat1**, showing that reductive quenching will most likely take place.[192]

We will determine if electron transfer to the catalytic center to generate Co(I) species is possible. Emission spectra for **RuP_4^{OEt}-Cat1** have not been measured yet by our collaborators in Germany, but we can use the estimated value of 2.01 eV for **RuP_4^{OEt}-Co**, as this number does not remarkably vary among different ruthenium complexes. From the estimated energy of the excited state (2.01 eV) and using **Eq.II.1** and E_{red3} in **Table IV.3**, we can determine oxidizing power of + 0.80 V vs NHE for Ru^*/Ru^-. Hole injection from the excited dye to the valence band of NiO (+ 0.46 V vs NHE valence band edge potential) is thermodynamically feasible with ΔG_{inj} = - 0.34 eV using **Eq. II.2**. Generation of Co(II) and Co(I) from the reduced

light harvester can take place with driving forces of ΔG_{red1} = - 1.33 eV and ΔG_{red2} = - 0.87 eV respectively (**Eq. II.3** and **4**). Thus, hole injection and thermal intramolecular electron transfer from the reduced dye to the catalyst can thermodynamically occur.

	E_{red1}[a] (Co^{III}/Co^{II})	E_{red2}[a] (Co^{II}/Co^{I})	E_{red3}[a] (Ru^{II}/Ru^{II}-$L^{\cdot-}$)	ΔG_{inj}[b]	ΔG_1[b]	ΔG_2[b]
Cat1	+ 0,02	- 0,45	-	-	-	-
RuP_4^{OEt}-EPIP	-	-	- 1,18	- 0,37	-	-
RuP_4^{OEt}-Cat1	+ 0,12	- 0,34	- 1,21	- 0,34	- 1,33	- 0,87

Table IV.3. Redox properties of **Cat1**, **RuP_4^{OEt}-EPIP** and **RuP_4^{OEt}-Cat1**.

a. In V vs NHE. The redox potentials were converted from $Fc^{+/0}$ (**Table IV.1**) to NHE, considering $E°(Fc^{+/0})$ = + 0.53 V vs. NHE in acetonitrile.[157]

b. In eV.

From **Table IV.3** it is clear that generation of Co(I) is feasible from a thermodynamic point of view. Thus, all criteria are met to prepare functional photocathodes with **RuP_4^{OEt}-Cat1**. We should note that the redox potentials of the dyad were determined in organic media. Even though for **Cat1** chloro axial ligands are substituted by water in aqueous conditions and the redox couples can be slightly shifted,[66,188] we can have a good estimation of what happens in aqueous media.

2) Photolysis experiment

To further study the ability of the dye-catalyst assembly to generate and accumulate a Co(I) state under irradiation, a photolysis experiment was performed in degassed acetonitrile using TEOA as SED (10 % v/v). The time-dependent differential spectra of **RuP_4^{OEt}-Cat1** recorded in the range of 400 to 850 nm are presented in **Figure IV.7**.

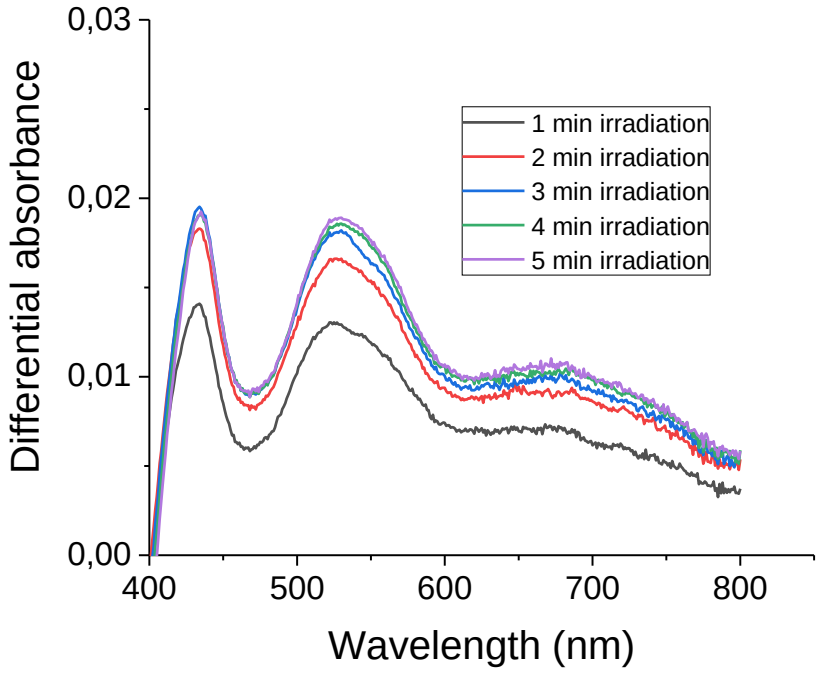

Figure IV.7. Differential spectra of UV-Vis monitored photolysis experiment of **RuP_4^{OEt}-Cat1** (3.6×10^{-5} M) in CH_3CN/TEOA (90:10 v/v) under visible light illumination.

After 1 minute of irradiation, new bands arise. A band with a maximum at 435 nm and one broad starting from 600 nm and exceeding until 800 nm. These transitions are characteristic of Co(I) for **Cat1** obtained during the course of extensive electrolysis experiments.[169] One more broad transition is obvious at around 550 nm and can be attributed either to the Co(II) derivative[169] or the reduced species of ruthenium (**Figure II.4**). Further irradiation generated more pronounced peaks, reaching maximum absorbance after 3 minutes.

The clear formation of Co(I) implies that **RuP_4^{OEt}-Cat1** can accumulate the reduced species of cobalt, the entry point of the proposed catalytic cycle.[169] Since TEOA is in high excess, reductive quenching is more likely to occur under these photochemical conditions, followed by thermal electron transfer from the reduced dye to the catalyst. Here, Co(I) is generated within the first minute of irradiation and reaches a plateau after 3 minutes. These features seem promising especially if we compare them with the photolysis experiment of **RuP_4^{OEt}-Co**, where accumulation of the Co(I)-species took more than 30 minutes (**Figure II.8**). This suggests that the overall process is faster in the case of **RuP_4^{OEt}-Cat1**.

V. Conclusions and perspectives

A second novel dye-catalyst assembly with a cobalt tetraazomacrocyclic complex was synthesized and characterized for further integration in a NiO hydrogen-evolving photocathode. Synthesis of the dyad was accomplished in two steps from **RuP$_4^{OEt}$-EPIP**: First, CuAAC was performed to couple the light harvester with a catalyst precursor bearing an azido group, followed by the cobalt-templated synthesis of the catalytic center. Full characterization of the final dye-catalyst assembly was performed and established that : *i*) the dyad was isolated under its protonated imidazole form at the end of the synthesis; *ii*) the redox and spectroscopic properties of the subunits remaining unmodified after the covalent coupling and iii) all the thermodynamic considerations for electron transfer to the catalyst can be met for an efficient NiO photocathode at pH 5.5 based on **RuP$_4^{OEt}$-Cat1**. Interestingly, a photolysis experiment revealed that the Co(I) state is formed within the first minutes of irradiation, suggesting that the electron transfer processes are faster for **RuP$_4^{OEt}$-Cat1** than **RuP$_4^{OEt}$-Co**.

This dyad thus seems very promising for PEC applications. However, its synthesis and purification were really low yielding (< 20%) and demanding. Comparison with the other **Cat1**-based dyads prepared in the group suggests that hydrolysis of the phosphonate groups during the course of the reaction could be an issue. A solution could be to fully hydrolyze the phosphonate esters to the corresponding acids before purification of the final dyad assembly by size-exclusion chromatography.[144]

In the retrosynthetic scheme below (**Scheme IV.7**), an alternative procedure is envisaged. The idea is to perform first the click coupling between **N$_3$-DAP** and the **EPIP** ligand. Then, cobalt-templated synthesis will follow to obtain the catalyst with the third diimine ligand (**EPIP-Cat1**) and finally coordination of this ligand to ruthenium for isolating the desiring **RuP$_4^{OEt}$-Cat1**. The main advantage is that possible hydrolysis of the phosphonate groups due to the presence of HCl and acetic acid could not anymore happen. Synthetic difficulties for this route might be the unwanted coordination of cobalt from both sides of the ligand (**EPIP-DAP**).

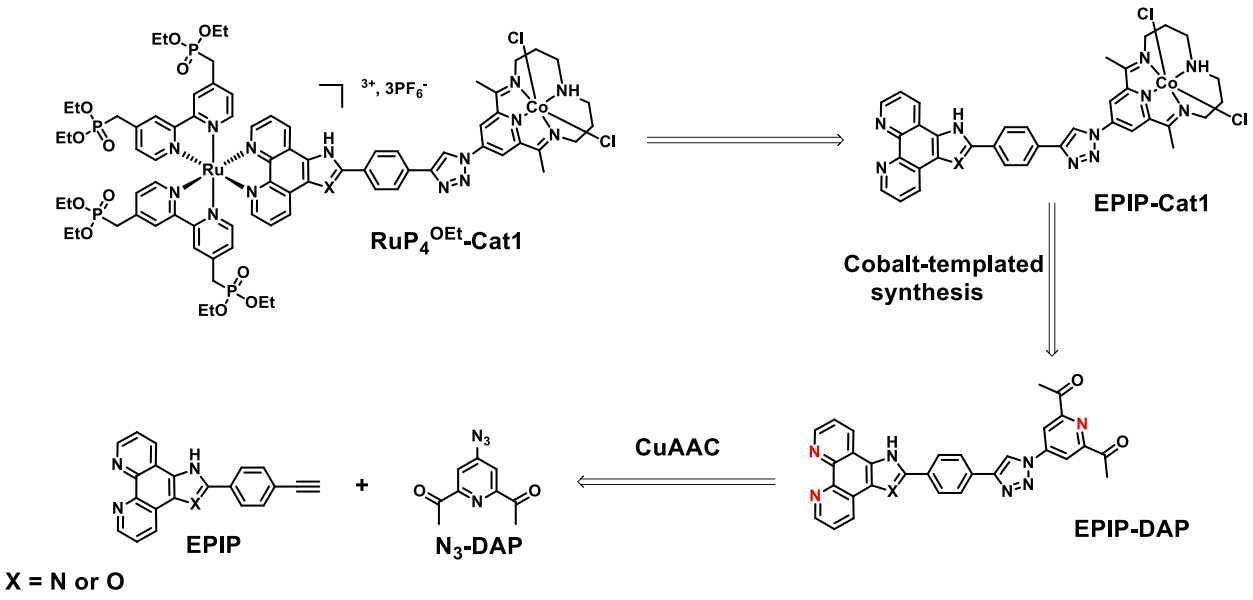

Scheme IV.7. Alternative synthetic route to prepare **RuP_4^{OEt}-Cat1**.

Finally, the issue of the protonation state of the imidazole ring that can affect the solubility and the photophysical properties can be avoided by preparing an oxazole derivative. Attempts to optimize the synthesis and the purification are ongoing by Dr. Tania Straistari (post-doc in our group).

Chapter V

Photoelectrochemical activity for proton and carbon dioxide reduction of a novel RuP_4^{OH}-Cat1 based NiO photocathode

In the last chapter, the novel **RuP_4^{OH}-Cat1**-sensitized NiO photocathode will be assessed for proton reduction under strictly identical conditions with **RuP_4^{OH}-Co**. This will give us the opportunity to expand our research and correlate the photoelectrocatalytic activity with the choice of the catalyst. In addition, we hope that we will be able to minimize the desorption rate from the surface, which was observed for our previous photocathode.

Cat1 has found few applications in the field of carbon dioxide reduction under photo- or electro-chemical conditions. In this frame, some preliminary results utilizing our dyad on NiO electrodes for PEC carbon dioxide reduction will be displayed in the second half of this chapter. A literature screening on p-type photocathodes for CO_2 reduction inspired us to work in fully aqueous media. Finally, comparison with the already existing molecular dye-sensitized photocathodes for proton and carbon dioxide reduction will be made in order to understand the future potentials of our photocathodes.

I. Preparation and characterization of the sensitized NiO films

Following the synthesis of **RuP$_4^{OEt}$-Cat1**, grafting onto homemade mesoporous nanostructured NiO electrodes was undertaken and the resulting sensitized films were characterized before assessing their photoelectrocatalytic activity.

1) Film sensitization and dyad loading determination

i) Classical sensitization procedure with RuP$_4^{OH}$-Cat1

Hydrolysis of the phosphonate esters to the corresponding acids was carried out by following the experimental procedure previously employed for **RuP$_4^{OEt}$-Co**. Acetonitrile was added to increase the solubility of **RuP$_4^{OEt}$-Cat1** and the reaction mixture was left under stirring at room temperature for 3 days after dropwise addition of TMSBr (**Scheme V.1**). Removal of the solvents followed by addition of MeOH to hydrolyze the silyl esters yielded in the deprotected **RuP$_4^{OH}$-Cat1**.

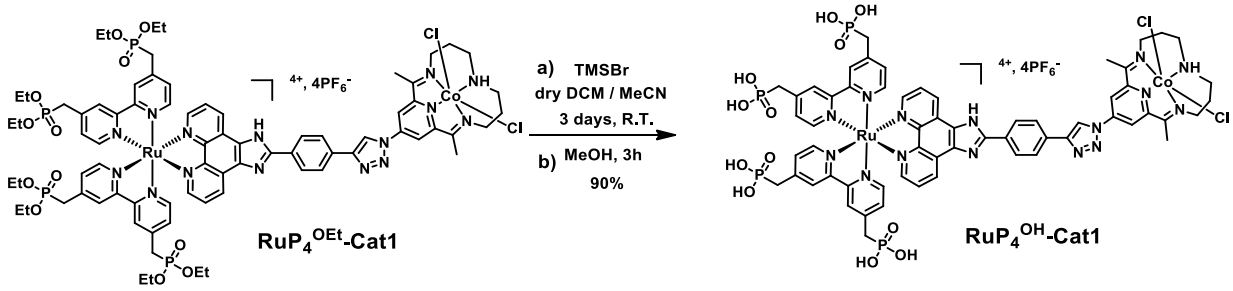

Scheme V.1. Hydrolysis of the phosphonate ester groups to obtain **RuP$_4^{OH}$-Cat1**.

We then sensitized homemade NiO films by soaking them into 0.1 mM solution of **RuP$_4^{OH}$-Cat1** in MeOH for 24h. Keeping the same experimental protocol already explained in Chapter III, the freshly sensitized NiO films were dipped for 4 hours in a methanolic solution of 1 M phenylphosphonic acid before recording the UV-Vis spectra of the solutions. It should be noted that molar extinction coefficients were determined to be 18800 $M^{-1}cm^{-1}$ at 463 nm in methanolic solution of 1 M phenyl phosphonic acid (5.2×10^{-5} M), again on the protected complexes due to solubility issues for the final dye-catalyst assembly (**Figure V.1**).

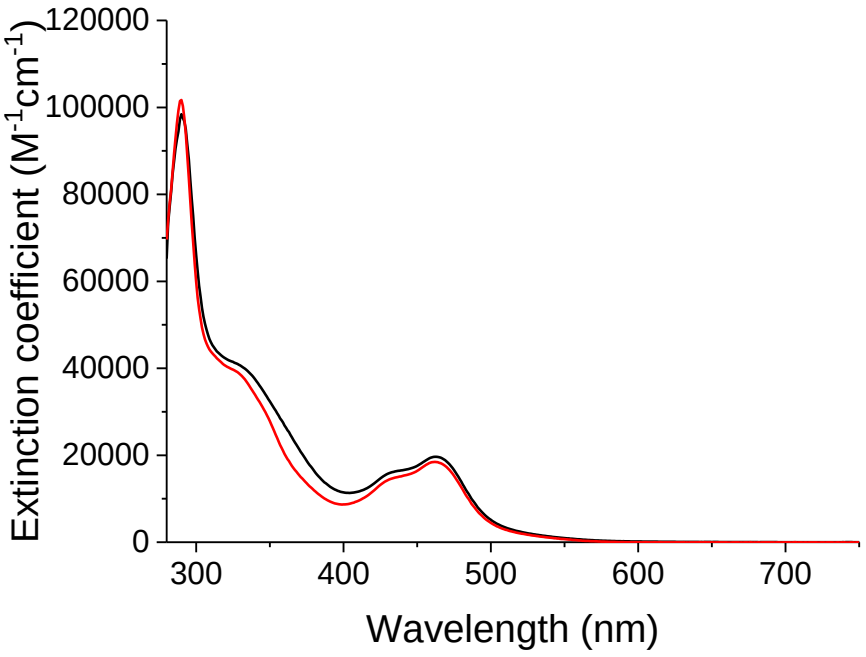

Figure V.1. UV-vis absorption spectra (epsilon curve) of **RuP$_4^{OEt}$-Cat1** (black line) and **RuP$_4^{OEt}$-EPIP** (red line) in a methanolic solution of 1 M phenylphosphonic acid.

The first sensitized film had a dyad loading of 4.2 nmol.cm^{-2} (**F1** in **Table V.1**), thus in the range of the 5.2 ± 0.8 nmol.cm^{-2} previously obtained with **RuP$_4^{OH}$-Co**. However, this result could not be reproduced (**F2-F11** in **Table V.1**). Using different batches of NiO films, in addition to the low solubility of the complex, resulted in lower grafting densities, varying from 0.5 to 2.3 nmol.cm^{-2}.

F1	F2	F3	F4	F5	F6	F7	F8	F9	F10	F11
4.3	2.0	1.0	0.9	0.5	1.3	2.3	1.3	1.4	0.5	1.1

Table V.1. Surface concentration (nmol.cm^{-2}) of **RuP$_4^{OH}$-Cat1** determined by the desorption procedure for 11 freshly grafted films (**F**).

ii) Alternative sensitization procedure using RuP$_4^{OTMS}$-Cat1

The low grafting densities obtained with **RuP$_4^{OH}$-Cat1** compared to our previous system, motivated us to search for ways to face this issue. A recent paper from S. Rau and T. Jacob described the immobilization of ruthenium polypyridine complexes onto NiO using trimethyl-silylated (TMS) substituted phosphonate anchoring groups instead of the acidic form of the latter.[199] Sensitization was realized in the glovebox, as TMS-groups are prone to hydrolysis under non-inert atmosphere, leading to higher initial kinetic adsorption rates and slightly higher

grafting densities compared to classical sensitization with phosphonic acid groups. They ascribed this behavior to the presence of a good leaving group, like TMS, which can accelerate grafting during the hetero condensation reaction with the reactive hydroxyl groups, taking place on the surface of the NiO film. In addition, lower desorption and better performances for DSSCs in organic media compared to the deprotected complexes were obtained due to a higher binding strength to the surface.

Driven by this study, we performed the McKenna reaction in the glovebox using dry acetonitrile and an excess of TMSBr, to obtain the corresponding protected dyad **RuP$_4^{OTMS}$-Cat1** (**Scheme V.2**).

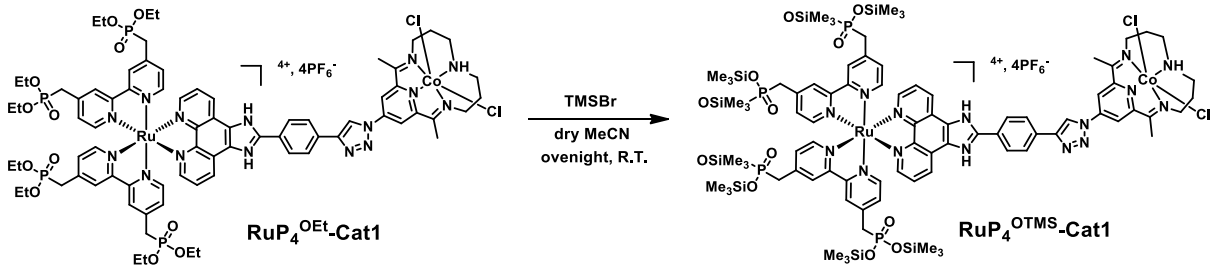

Scheme V.2. Synthetic procedure to obtain **RuP$_4^{OTMS}$-Cat1**.

Grafting onto NiO films was also undertaken in the glovebox, using dry acetonitrile as solvent, and after rinsing and drying, the sensitized films were kept protected from light. Using different batches of NiO, an average grafting density of 1.9 ± 0.5 nmol.cm^{-2} was determined.

F1	F2	F3	F4	F5
1.8	2.4	1.1	2.2	2.0

Table V.2. Surface concentration (nmol.cm^{-2}) of **RuP$_4^{OTMS}$-Cat1** determined by the desorption procedure for 5 freshly grafted films (**F**).

Although the dye loading was not enhanced, this procedure seemed to result in more reproducible values. Electrodes sensitized by the two different experimental procedures were assessed for photoelectrochemical H_2 production, for comparison purposes.

2) MALDI-ToF analysis

The desorption solutions were analyzed by MALDI-ToF with two different methods in order to prove that the integral dye-catalyst assembly (**RuP$_4^{OH}$-Cat1**) has been grafted onto NiO films. Similarly to **RuP$_4^{OH}$-Co**, all peaks are detected under their single charged form.

i) Linear positive mode

In linear positive mode, with which the resolution for the isotopic pattern is not possible, we could observe a signal at 1465.6 corresponding to our dyad with the loss of the two Cl^- axial ligands and the PF_6^- counter ions (**Figure V.2**). The peak at 1439.7 is ascribed to the loss of two nitrogen atoms due to fragmentation and the one at 1313.8 to some hydrolyzed starting material (**RuP_4^{OH}-DAP**). This can be linked to the desorption conditions or fragmentation during the experiment. **Cat1** was tentatively analyzed to better understand the fragmentation patterns, but its low molecular weight did not enable us to observe its spectroscopic signature in MALDI-ToF.

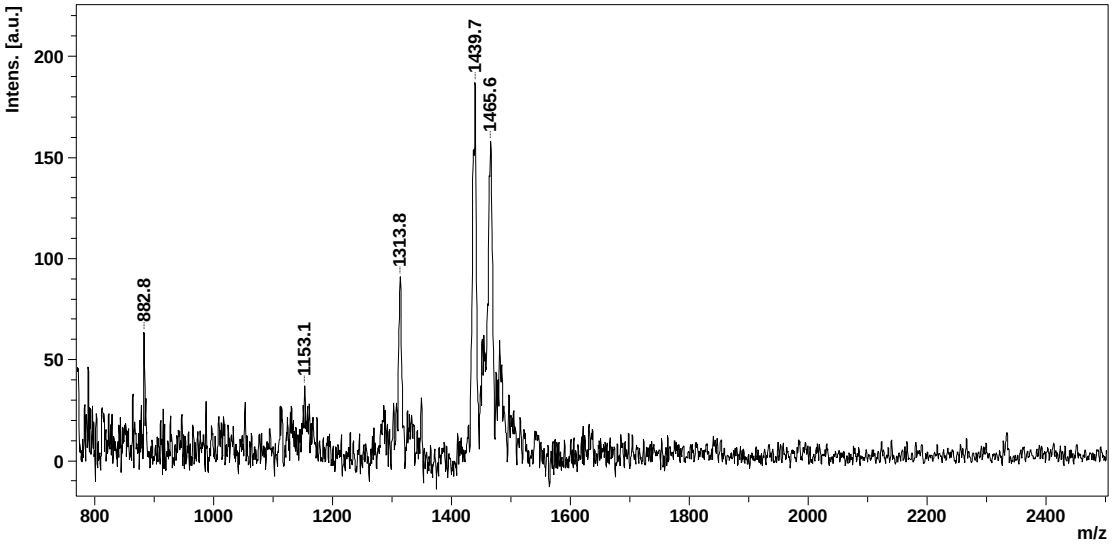

Figure V.2. MALDI-TOF spectrum of **RuP_4^{OH}-Cat1** dyad recorded with linear positive mode in a methanolic solution of 1 M phenylphosphonic acid.

ii) Reflecting positive mode

The spectra were also recorded using a reflecting positive mode to provide the isotopic pattern of the peaks (**Figure V.3**). The signal at m/z 1465.9 is still present with a characteristic isotopic pattern for ruthenium, but in lower intensity, as this method favors fragmentation. Thus, the main peak is at 1438, corresponding to our dye-catalyst assembly with the loss of two nitrogen atoms.

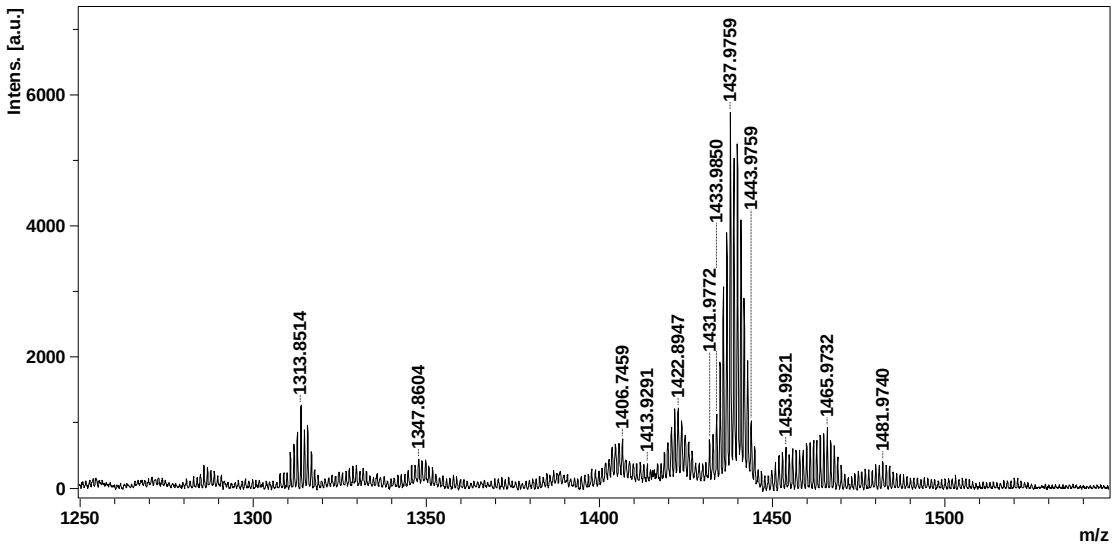

Figure V.3. MALDI-TOF spectrum of **RuP$_4^{OH}$-Cat1** dyad recorded with reflecting positive mode in a methanolic solution of 1 M phenylphosphonic acid.

II. Photoelectrocatalytic activity for H_2 evolution

The photocathode in **Figure V.4** was assessed for photoelectrocatalytic hydrogen evolution in fully aqueous media at pH 5.5 in MES buffer using AM 1.5G solar irradiation in order to provide a direct comparison with the **RuP$_4^{OH}$-Co**-based photocathode. NiO films sensitized by the two grafting procedures were tested. In addition, some preliminary experiments were carried out at more acidic pH to test the stability of the anchorage.

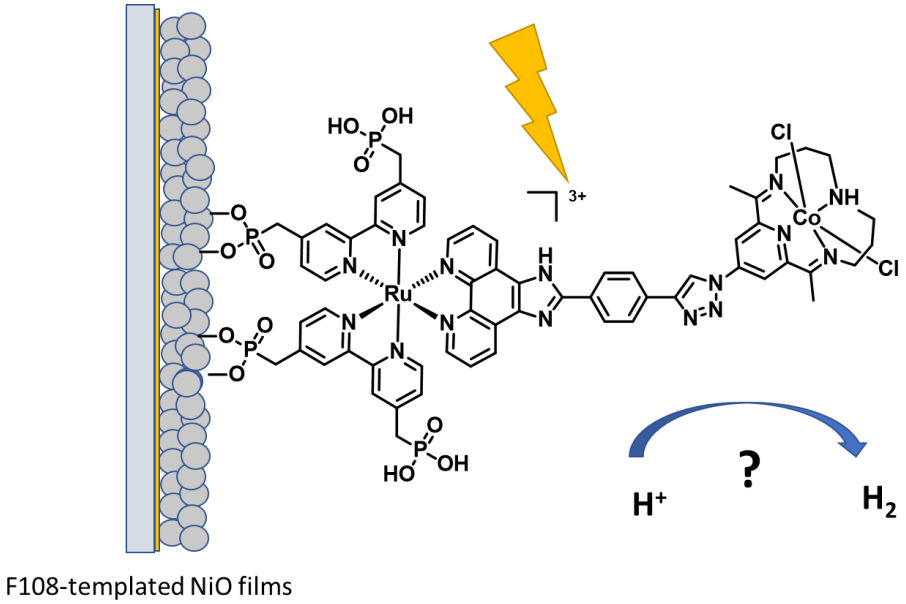

Figure V.4. Photocathode assessed for PEC H_2 evolution based on **RuP$_4^{OH}$-Cat1**.

1) Photoelectrochemical characterization

In the three-electrode cell (**Figure III.9**), the NiO photocathode was illuminated with filtered light (AM 1.5G irradiation and IR filter) at the equivalent of 1 sun (70 $mW.cm^{-2}$) with an applied potential of – 0.4 V vs Ag/AgCl (+ 0.13 V vs RHE). Linear sweep voltammograms were first recorded for each NiO film under dark conditions screening from + 0.5 V to - 0.5 V vs Ag/AgCl with a scan rate of 10 $mV.s^{-1}$. Then, LSV were carried out under light illumination (lamp on), followed by chopped-light irradiation on the same voltage range (**Figure V.5** top). The photocathode develops cathodic photocurrents after continuous light irradiation (red line) with onset potential at + 0.41 V vs Ag/AgCl (+ 0.94 V vs RHE). Furthermore, chopped light irradiation (blue line) implies that the generated current is photo-induced.

Higher photocurrent densities were recorded at increasingly negative potentials.[117,121] This is in agreement with the TA-SEC measurements for the **RuP_4^{OH}-Co** based photocathode (presented in Chapter III), where at more negative applied potentials a long-lived charged separated state is present along with increasing time constants for charge recombination, leading to enhanced activity. At - 0.4 V vs Ag/AgCl we reached an average of 67 ± 36 $\mu A.cm^{-2}$ (3 independent samples) after subtraction of the dark current. Taking into consideration the grafting density for a more accurate comparison, the photocurrent per grafted dyad is 59 ± 22 $\mu A.nmol_{\mathbf{dyad}}^{-1}$, an impressive three times increase compared to the previous photocathode. This photoelectrochemical characterization is in agreement with the photolysis experiments (**Figure IV.7**) where the evolution of Co(I) for **RuP_4^{OEt}-Cat1** was suggested to be faster than for **RuP_4^{OEt}-Co** (**Figure II.8**).

Photoelectrochemical tests were also carried out using the alternative sensitization procedure with **RuP_4^{OTMS}-Cat1** under strictly identical conditions. From the LSV (**Figure V.5** bottom), the photocurrents are higher (134 ± 57 $\mu A.cm^{-2}$ determined for 3 different samples) compared to the ones obtained with the classical immobilization procedure. This mainly arises from the higher grafting densities, as the electron transfer efficiency is only slightly enhanced (75 ± 8 compared to 59 ± 22 $\mu A.nmol_{\mathbf{dyad}}^{-1}$). Nevertheless, investigating the photoelectrocatalytic activity under continuous irradiation will indicate if this grafting procedure could have a positive impact in a long-term scale.

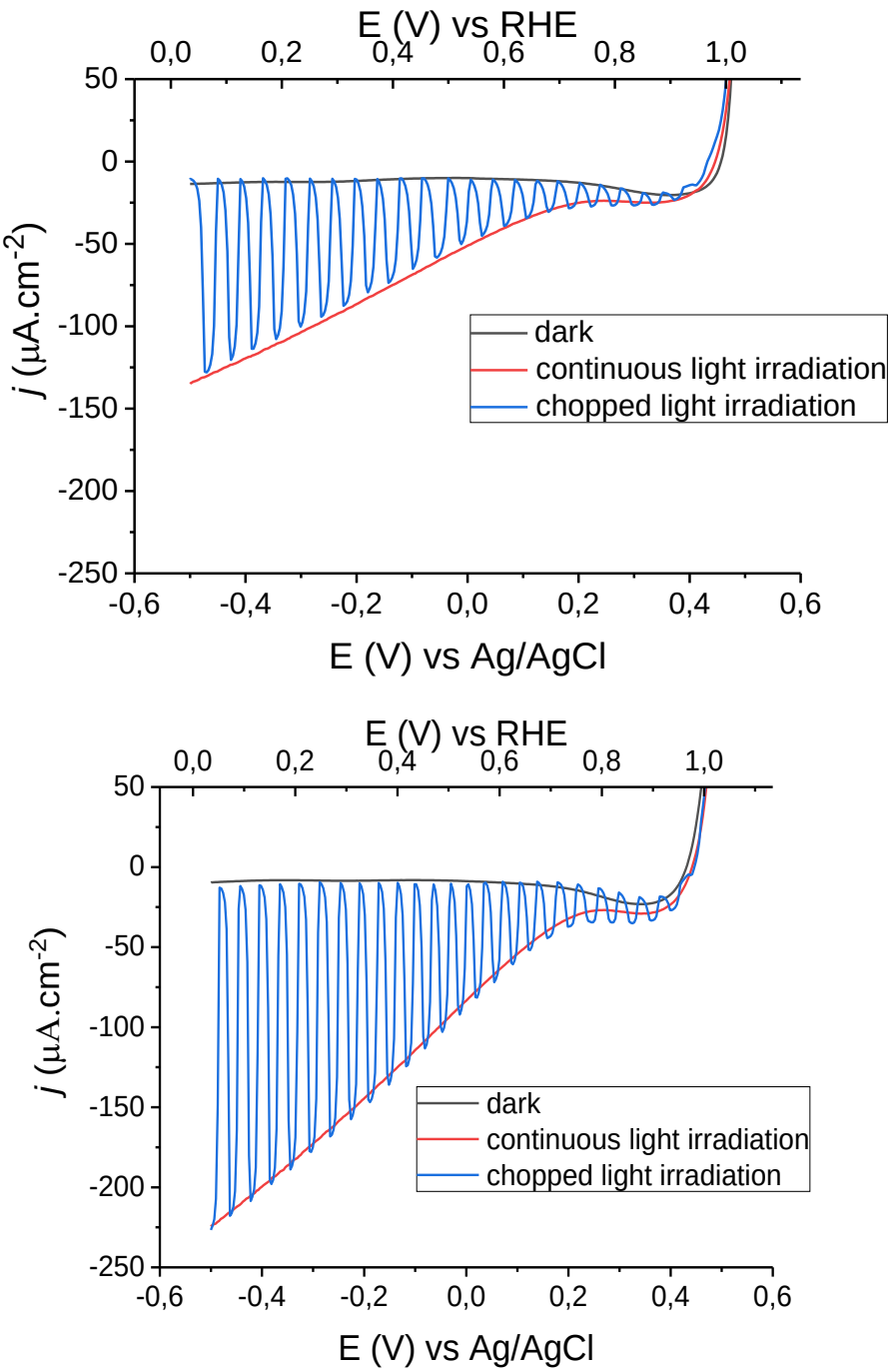

Figure V.5. Linear sweep voltammograms of NiO electrodes sensitized by **RuP_4^{OH}-Cat1** (top) and **RuP_4^{OTMS}-Cat1** (bottom) in pH 5.5 using 0.1 M MES 0.1 M/NaCl as supporting electrolyte under AM 1.5 G solar irradiation (70 mW.cm^{-2}, red line), dark conditions (black line) and chopped light irradiation (blue line).

For the dye-sensitized photocathodes using cobalt diimine-dioxime as catalyst, pH 5.5 was initially chosen as the optimal pH. Preliminary results obtained with organic dyes coupled with **Cat1** (**Chart IV.3**) indicated that the chemical nature of the buffer solution does not affect the activity, as similar values were obtained using MES or Britton-Robinson (B.R.) buffer at pH

5.5. In this work, we started to examine more acidic pH values, as **Cat1** was mostly employed at lower pH in homogeneous photocatalytic systems. Hence, we tested B.R. buffer, a wide range pH buffer system,[200] at pH 3 (**Figure V.6**), as a representative value.

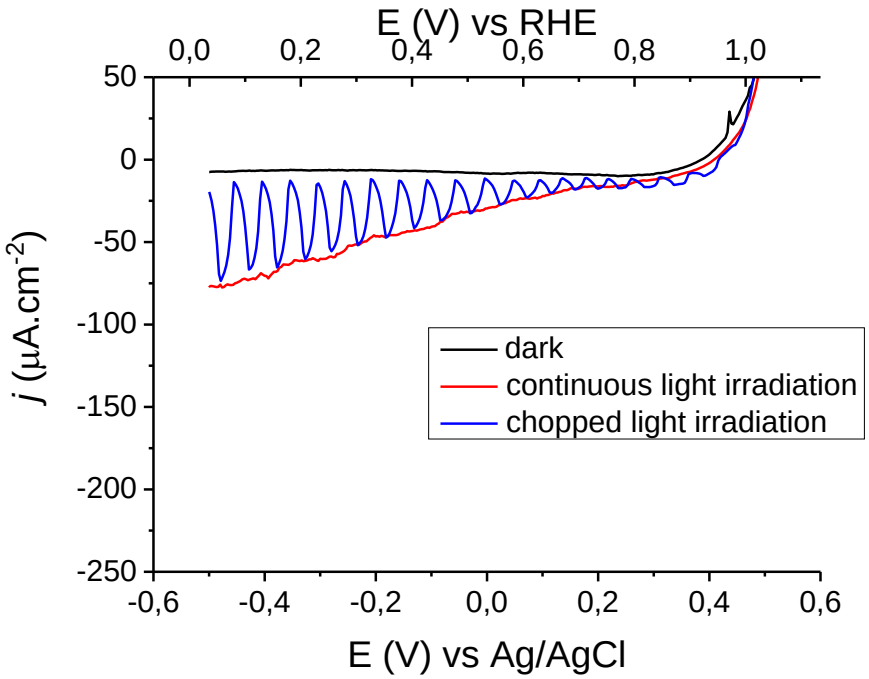

Figure V.6. Linear sweep voltammograms of NiO electrodes sensitized by **RuP_4^{OH}-Cat1** dyad in pH 3 using Britton-Robinson as supporting electrolyte under AM 1.5 G solar irradiation (70 $mW.cm^{-2}$, red line), dark conditions (black line) and chopped light irradiation (blue line).

After recording LSVs under dark and light irradiation at pH 3, the cathodic photocurrents were significantly decreased compared to the photocathodes at pH 5.5 (**Figure V.5**) as well as the electron transfer efficiency (43 ± 8 $\mu A.nmol^{-1}_{\mathbf{dyad}}$ for 2 different samples). This could be a result of different kinetics of the electron transfer at lower pH. Furthermore, at this value, our dye-catalyst assembly might be protonated on the imidazole ring (**Chart II.4**)[150] affecting the possible intramolecular electron transfer to the catalyst through the bridging ligand. Nevertheless, a more detailed study is needed to conclude about the influence of the pH on the performance.

2) H_2-evolving activity assessment

Long-term chronoamperometric measurements were performed under continuous irradiation and coupled to hydrogen detection in order to correlate the cathodic photocurrents observed in the previous LSV experiments with photoelectrocatalytic hydrogen evolution. For a direct

comparison with our previous photocathode, strictly identical conditions were employed, i.e. the same applied potential (– 0.4 V vs Ag/AgCl) with AM 1.5 G irradiation for 2 hours. The initial photocurrent density of 110 µA.cm^{-2} (**Figure V.7**) is in good accordance with the values obtained during the LSV (**Figure. V.5**) for the NiO films sensitized by **RuP$_4^{OH}$-Cat1.** A decay of the photocurrent is observed over the 2 hours experiment, with only 3.5 µA.cm^{-2} remaining when the lamp was switched off at the end of the experiment. Gas chromatographic analysis in the headspace of the cell and using the micro-clark electrode in the solution confirmed the evolution of hydrogen. The overall faradaic yield was determined to be 50 ± 3 % and hydrogen is produced with an impressive average TON value of 237 ± 14 (**Table V.3**), the highest values reported until today for NiO dye-sensitized photocathodes (**Table I.1**).

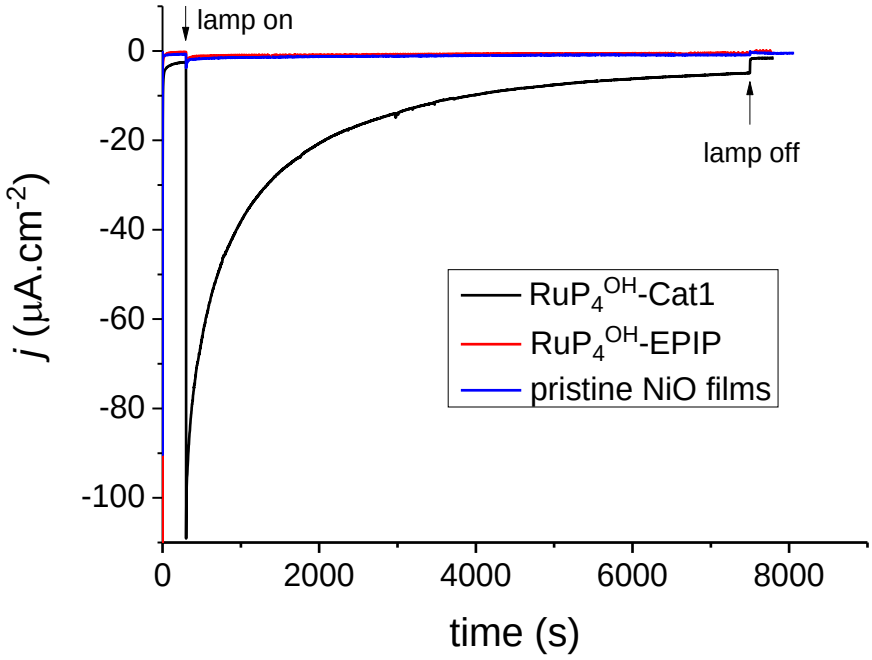

Figure V.7. 2 hours chronoamperometry measurements of pristine NiO films (blue line), NiO films sensitized by **RuP$_4^{OH}$-Cat1** dyad (black line) and **RuP$_4^{OH}$-EPIP** (red line) in pH 5.5 using 0.1 M MES 0.1 M/NaCl as supporting electrolyte under AM 1.5G light irradiation (70 mW.cm^{-2}).

Chronoamperometric measurements were also performed with NiO films sensitized by **RuP$_4^{OH}$-EPIP** or pristine NiO films (**Figure IV.7**); both systems exhibit drastically lower cathodic photocurrent densities, compared to **RuP$_4^{OH}$-Cat1**. In addition, few hydrogen is produced during the course of these experiments, clearly highlighting the primordial role played by the catalytic center for the photocurrent generation and hydrogen evolving activity of the system.

2 hours chronoamperometric measurements at pH 3, showed again photocurrent decay and the total amount of hydrogen produced was low (EG 331 and EG437). In addition, F.E. and TON were estimated 30 ± 8% and 60 ± 13 accordingly. Hence, the moderate photoelectrochemical behavior is followed by a moderate photoelectrocatalytic activity.

The photoelectrocatalytic activity of the sensitized NiO-films with **RuP_4^{OTMS}-Cat1** were also tested for hydrogen evolution. After 2 hours of CA (**Figure V.8** top), 8% of the initial photocurrent (178 $\mu A.cm^{-2}$) remains compared to less than 3% for the dyads grafted with the phosphonic acid groups, implying slightly higher stability in agreement with the original publication.[199]

If we compare the photocurrent per grafted dyad (**Figure V.8** bottom), the initial values are similar for both **Cat1**-based systems regardless of the grafting technique. However, the **RuP_4^{OTMS}-Cat1**-based photocathode displays less pronounced photocurrent decay, suggesting higher stability. The different nature of anchorage could also influence the organization of the dyads on the surface, affecting the subsequent electron transfer from the valence band of NiO to the light harvester. Nevertheless, we cannot be conclusive, as this decay is significant for both photocathodes and at this level it is not clear if the remaining response is due to the grafted dyad. Post-operando analysis may give us more accurate answers to our questions. In **Figure V.8** there is also a comparison of the chronoamperometry experiments among the three different photocathodes under identical conditions. The increased performance of the photocathodes based on **Cat1** is clear. If we take into consideration the low grafting density for **Cat1**-based systems, their superior activity is undoubtful (**Figure V.8 bottom**).

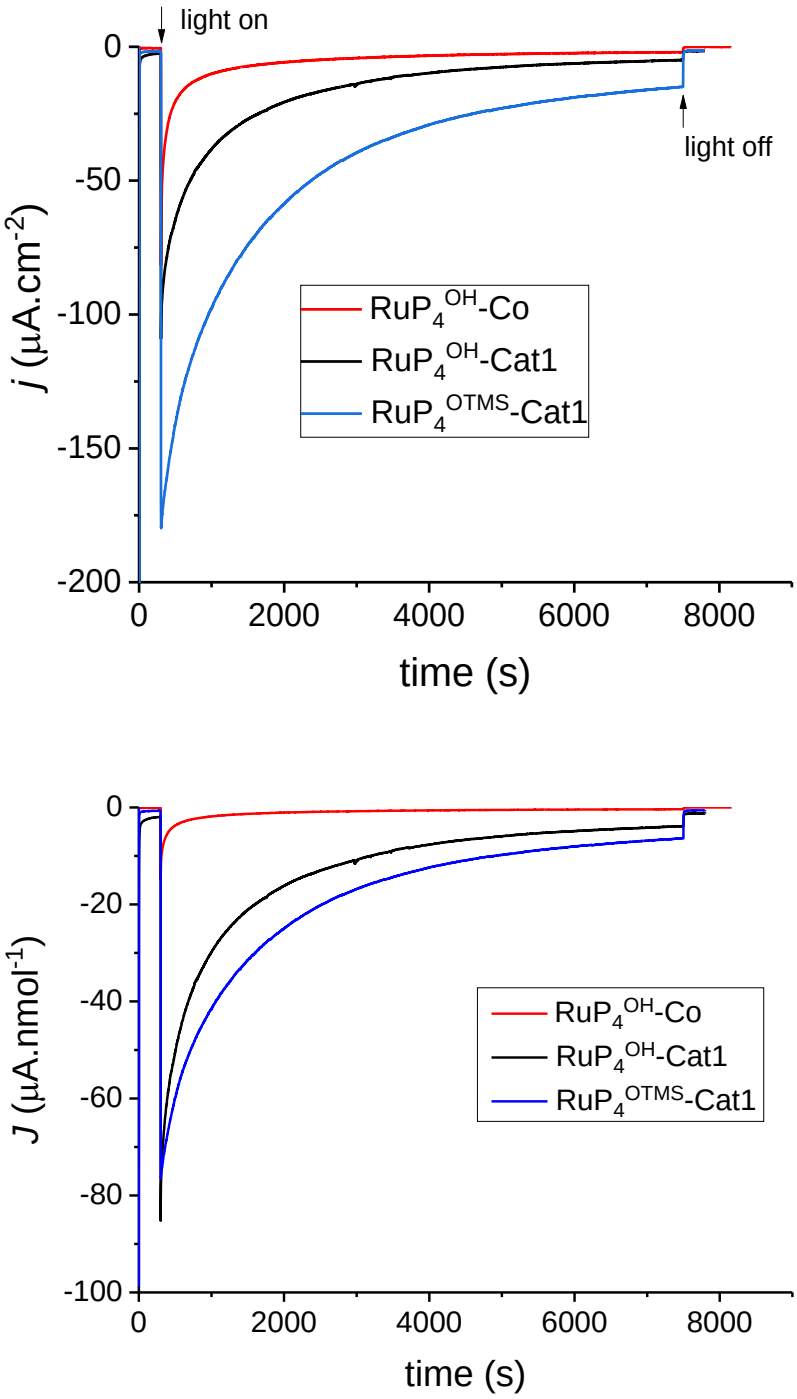

Figure V.8. 2 hours chronoamperometry measurements expressed in photocurrent densities (top) and photocurrent per nmol of dyad (bottom) of NiO films sensitized by **RuP_4^{OH}-Co** (black line), **RuP_4^{OH}-Cat1** (red line) and **RuP_4^{OTMS}-Cat1** (blue line) in pH 5.5 using MES 0.1 M/NaCl 0.1M as supporting electrolyte under AM 1.5G light irradiation (1 sun).

Measuring hydrogen after 2 hours of PEC tests for the photocathodes sensitized by **RuP_4^{OTMS}-Cat1**, F.E. of 64 ± 2% were estimated, indicating that the selectivity for proton reduction is a little bit increased. TON of 371 ± 128 TON were determined, showing anew an

enhancement. The data tend to indicate that the grafting procedure influences the photoelectrocatalytic activity with slightly better F.E and TON in the case of **RuP_4^{OTMS}-Cat1**-sensitized films. More experiments are needed in order to confirm the superior performance of the photocathodes prepared with the protected silylated derivatives of the dyad, as different batches of NiO films may also be responsible for the activity.

pH	Film	Surface Area (cm^2)	Surface concentration ($nmol.cm^{-2}$)	Total H_2 ($nmol.cm^{-2}$)	Charge passed ($mC.cm^{-2}$)	F.E. (%)	TON	Ref. exp.
5.5	NiO	2.8	—	5	7	13	—	EG266
		2.6	—	5	8	12	—	EG311
	average			**5 ± 0**	**8 ± 1**	**13 ± 1**		
	NiO|**RuP_4^{OH}-EPIP**	2.6	4.2	14	13	20	—	EG264
		3.3	2.1	6	6	23	—	EG325
	average			**10 ± 4**	**10 ± 4**	**22 ± 2**		
	NiO|**RuP_4^{OH}-Cat1**	3.0	1.0	218	79	53	227	EG328
		2.9	0.9	214	86	49	227	EG330
		3.1	1.3	302	120	49	235	EG425
		3.1	4.3	1098	407	52	258	EG261
	average					**50 ± 3**	**237 ± 14**	
	NiO|**RuP_4^{OTMS}-Cat1**	3.1	1.8	767	230	64	431	EG414
		3.0	2.4	1078	318	65	459	EG426
		3.2	1.1	263	83	61	224	EG447
	average					**64 ± 2**	**371 ± 128**	
3.0	NiO|**RuP_4^{OH}-Cat1**	3.2	0.5	36	20	36	69	EG331
		3.0	2.3	131	74	24	51	EG437
	average					**30 ± 8**	**60 ± 13**	

Table V.3. Photoelectrochemical experiments assessing hydrogen production activity of the **RuP_4^{OH}-Cat1** or **RuP_4^{OTMS}-Cat1** on NiO electrodes. Conditions are as follows: MES buffer at pH = 5,5 or B.R. buffer at pH 3, AM 1.5 G solar irradiation, - 0.4 V vs. Ag/AgCl applied potential, 2 h runtime.

The increase in performance for the **RuP_4^{OH}-Cat1**-based photocathode compared to **RuP_4^{OH}-Co** is undeniable with two times higher F.E. and 18-fold increase in TON. The more efficient and faster electron uptake (catalysis) by the catalyst, as the same harvesting unit and bridging ligand are used, and its different nature (robust macrocyclic complex) could be hidden behind this behavior. It should be noted that the first example to integrate **Cat1** into a photocathode was made in 2015.[201] In this work, a ruthenium complex grafted onto mesoporous NiO films, produced negligible photocurrents in organic media, probably due to diffusion-limited electron-transfer to the free in solution catalyst. Thus, coupling **Cat1** with the dye and

immobilizing on the electrode could face the problem of diffusion and directionality of the electron transfer and enhance the activity.

3) Preliminary post-operando analysis

The PEC activity of **RuP$_4^{OH}$-Cat1** and **RuP$_4^{OTMS}$-Cat1** after 2 hours in fully aqueous conditions is clearly superior to the one previously recorded with **RuP$_4^{OH}$-Co**. Nevertheless, 92 to 97% drop of the initial current density is observed under continuous light irradiation, implying stability problems. Post-operando analysis is crucial for understanding the source of this photocurrent decay. After the 2 hours PEC tests, the NiO films were dipped in the methanolic solution of 1 M phenylphosphonic acid and the solutions were characterized by UV-Vis spectroscopy and MALDI ToF.

i) UV-Vis characterization

Analyzing the desorption solutions for the fresh half of sensitized NiO films and the other half after 2 hours of PEC test gave us evidence for significant detachment of the dyad from the NiO during the experiment (**Figure V.9**). We could estimate desorption of 69 ± 1% (3 independent experiments) for the normal grafting and 74 ± 6% (2 independent experiments) for the alternative grafting using the TMS-protected derivative. Thus, a stronger binding onto NiO when the TMS-protected dyad is employed could not be confirmed in contrast to the study from the group of S. Rau.[199] In addition, these values are similar to the one obtained for **RuP$_4^{OH}$-Co** dyad.

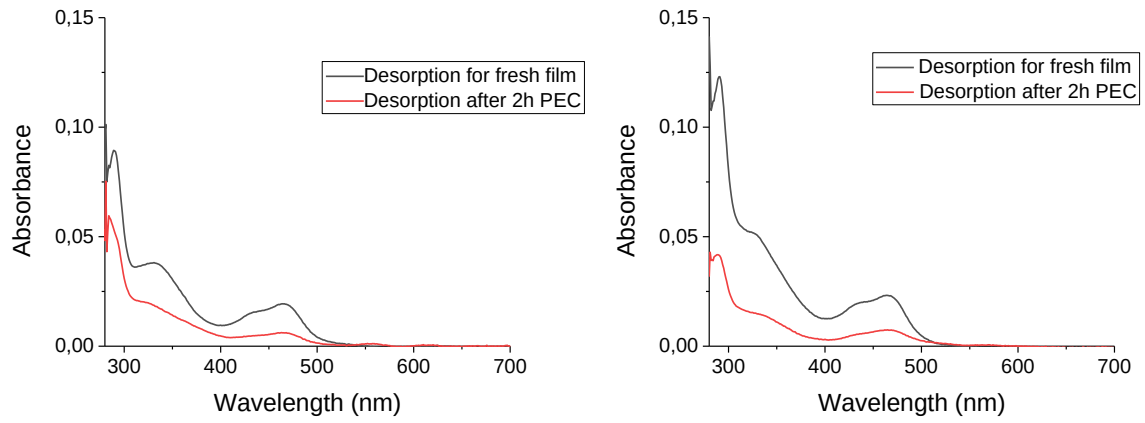

Figure V.9. UV-Visible spectra for **RuP_4^{OH}-Cat1** using normal grafting procedure (left) or grafting using **RuP_4^{OTMS}-Cat1** (right) in methanolic solution of 1 M phenylphosphonic acid, where half of a fresh NiO film was dipped (black line) and the other half was dipped after 2 hours of PEC experiment (red line).

50% desorption of the initial dyad is also determined after carrying out PEC tests at pH 3. T. J. Meyer's group highlighted that desorption of $[Ru(bpy)_2(4,4'-(PO_3H_2)_2bpy)]^{2+}$ from metal oxides (TiO_2 and ZrO_2) is pH-dependent in aqueous conditions.[52] Notably, at pH higher than 5, desorption took place even without light irradiation. Based on this work and our study here, phosphonates could offer more stable linkage at more acidic pH, but this stabilization is not enough, as inferior performance for hydrogen evolution was obtained.

ii) MALDI-ToF analysis

The desorption solutions were sent for MALDI-ToF analysis. The peak at m/z 1465 characteristic for **RuP_4^{OH}-Cat1** (**Figure V.2** and **3**) is completely absent from the spectra regardless the grafting procedure (**Figure V.10**). One main peak is observed at m/z: 1152, tentatively attributed to the cleavage of C-N bond between the triazole unit and the cobalt complex with a characteristic isotopic pattern for ruthenium.

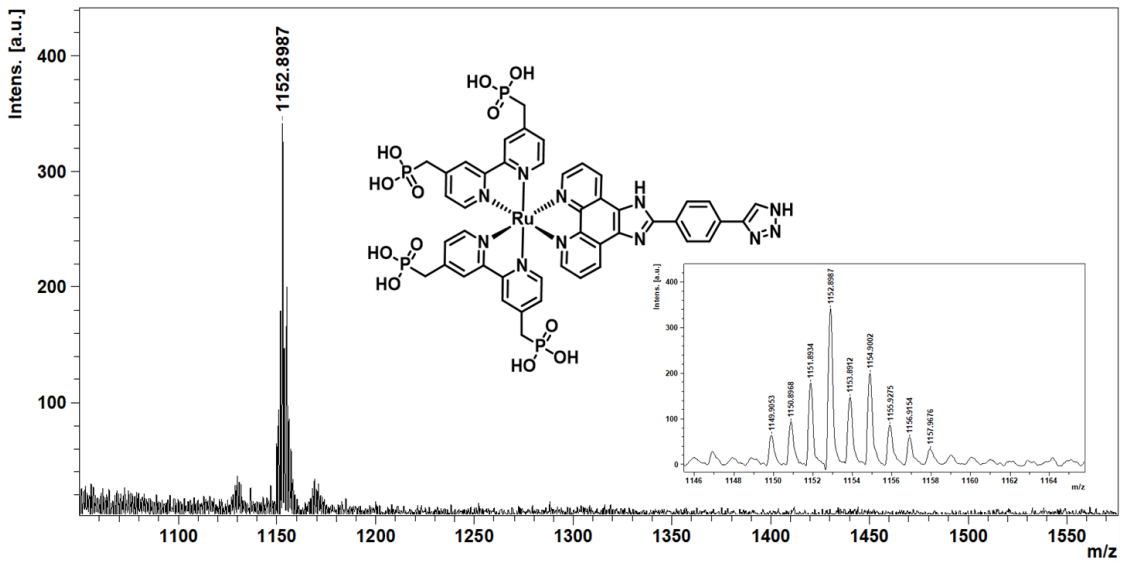

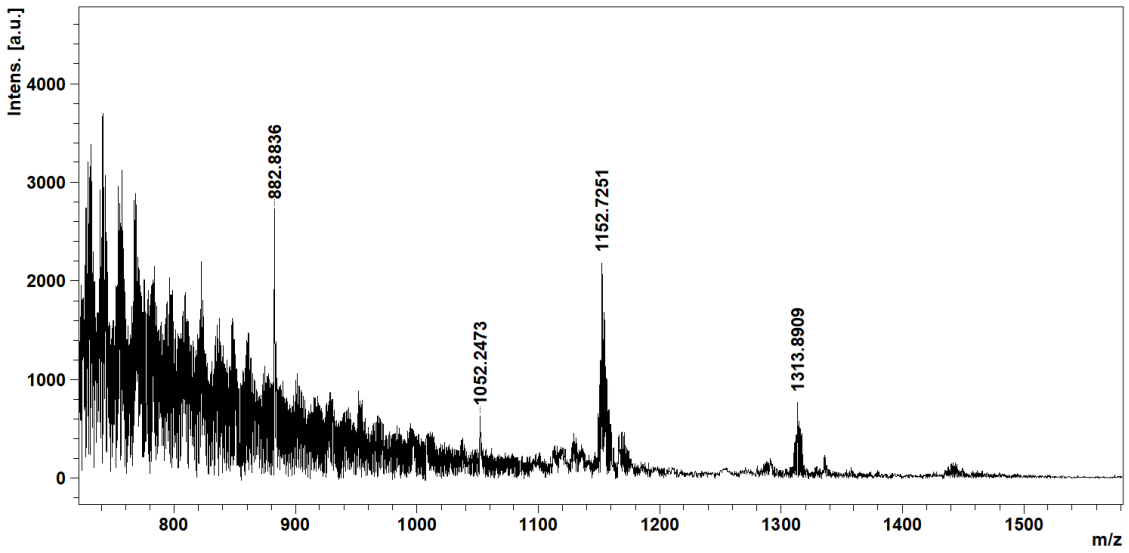

Figure V.10. MALDI-TOF spectra recorded in a methanolic solution of 1 M phenylphosphonic acid after 2 hours of PEC test with normal grafting procedure (top) and with grafting using TMS-protected phosphonate groups (middle).

These results tend to indicate that the catalyst is completely lost after 2 hours of PEC activity. However, it should be noted that this peak is also present for the fresh NiO films (**Figure V.2** and **3**). Thus, additional measurements are needed to accurately identify possible decomposition pathways. Furthermore, quantifying cobalt by ICP-AES may help to clarify if some cobalt is still present or not at the end of the PEC experiments.

III. Photoelectrochemical activity for CO_2 reduction

1) General introduction

The worldwide consumption of fossil fuels increased the levels of carbon dioxide in the atmosphere with negative impacts on the environment.[202] A solution to decrease the accumulation of CO_2 lies in the development of selective and efficient methods to reduce it into carbon-based fuels using solar or other renewable energy sources.[203] Plants are able to harness the solar energy in order to convert CO_2 into carbohydrates, the fuels of the cells (photosynthesis) and this is the inspiration for molecular chemists to develop sunlight-driven devices for CO_2 reduction (artificial photosynthetic systems).

Carbon dioxide can be reduced to a mixture of products (**Eq.V.1**) due to close thermodynamics such as CO, HCOOH, CH_3OH, CH_4, CH_2CH_2, C_2H_5OH, CH_3COOH and oxalate. CO_2 is an inert substrate and reduction to a variety of products at reasonable rates demands the use of potentials more negative than those corresponding to the thermodynamic equilibrium. Thus, efficient, stable and selective catalysts are needed to decrease the reaction barriers due to multiple electron-proton reduction processes and to target specific compounds.

$CO_2 + e^- \rightarrow CO_2^{\cdot -}$ $E^0 = - 1.9$ V

$CO_2 + 2H^+ + 2e^- \rightarrow HCOOH$ $E^0 = - 0.61$ V

$CO_2 + 2H^+ + 2e^- \rightarrow CO + H_2O$ $E^0 = - 0.53$

$CO_2 + 4H^+ + 4e^- \rightarrow HCHO + H_2O$ $E^0 = - 0.48$ V

$CO_2 + 6H^+ + 6e^- \rightarrow CH_3OH + H_2O$ $E^0 = - 0.38$ V

$CO_2 + 8H^+ + 8e^- \rightarrow CH_4 + 2H_2O$ $E^0 = - 0.24$ V

Eqn.V.1. Two-electron reduction reactions of CO_2. Standard potentials vs NHE a pH 7.

Electro- and/or photochemical reduction of carbon dioxide has gained scientific interest from 1980s.[204,205] The following years, various molecular complexes based on noble metals (Re and Ru mostly) but also on first-row transition metals like Cu, Co, Ni, Mn and Fe have been reported as carbon dioxide reduction catalysts.[13,206,207,208,209,210,211] As photosensitizers, organic dyes, ruthenium, iridium polypyridine complexes and porphyrins have been employed. In addition, dyads with ruthenium and rhenium play a central role in the field.[212,213] Although a fine tuning of the catalyst structure can lead to good selectivity, few of these systems can work in fully aqueous conditions, where competition with proton reduction can take place, and even less can reduce CO_2 beyond the two-electron reduction products, CO and HCOOH (**Eqn. V.1**).

Photochemical systems need sacrificial electron donors to function. Immobilization onto surfaces are important for construction of functional devices that can achieve carbon dioxide reduction with water as reductant. A few examples of molecular photocathodes for CO_2 reduction were reported up to date and will be presented below, along with the use of **Cat1** for photo- or electro-chemical CO_2 reduction.

2) Dye-sensitized photocathodes for CO_2 reduction

The field of dye-sensitized photocathodes for CO_2 reduction was emerged the last years[13,214] with the first functional systems appearing in 2014.[215,216] In this field, two main approaches exist for the construction of the photocathodes, the covalent dye-catalyst assemblies and the "layer-by-layer" approach and the main breakthroughs will be presented in the following

section. Alternatively, examples of molecular photocathodes based on narrow band-gap semiconductors combined with molecular catalysts are presented in a third part.

i) Covalent dye-catalyst assemblies

The first example of a p-type dye-sensitized photocathode with a molecular catalyst adopted the covalent dye-catalyst assembly architecture.[216] A dyad composed of a zinc porphyrin as photosensitizer and a rhenium bipyridyl complex (**Dyad a**) as catalyst proved to be active for CO_2 reduction under photochemical conditions in DMF/TEA (4/1) solution producing CO with 10 TON. After immobilization onto NiO films, the fluorescence lifetime of the dyad was diminished, indicating hole injection from the excited dye to the valence band of the semiconductor. Irradiating the cell at 430 nm in organic media saturated with CO_2, cathodic photocurrents of around - 20 $\mu A.cm^{-2}$ were obtained and CO was evolved with 6% F.E. and 10 TON. Co-absorption of the dyad and the dye increased the TON to 122, as the light harvester plays the role of the electron reservoir to the system.

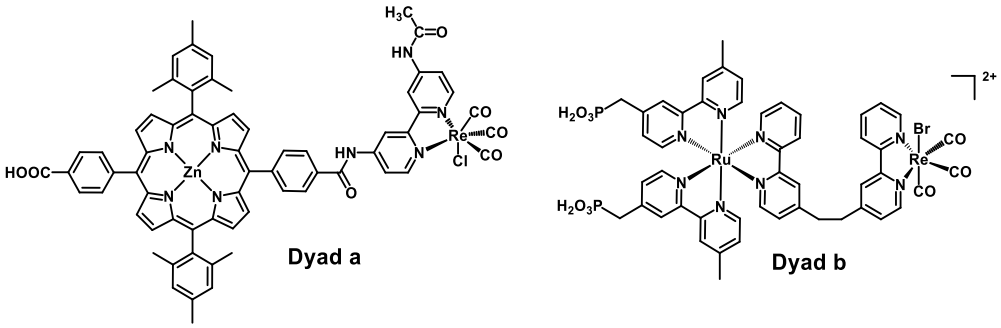

Chart V.1. Dye-catalyst assemblies used in photocathodes for carbon dioxide reduction.

The group of O. Ishitani has significantly contributed to the field of CO_2 reduction. A ruthenium-rhenium photocatalyst coupled with an ethylene chain and bearing methyl phosphonic acid groups (**Dyad b**) was grafted onto NiO films.[217] The photocathode was irradiated in a DMF/TEOA (5/1 v/v) solution saturated with CO_2. After 5 hours of continuous irradiation at - 1.2 V vs $Ag/AgNO_3$, only CO was produced (255 nmol) with 32 TON and 71% F.E. The carbon source for CO was CO_2, confirmed with $^{13}CO_2$ labelling experiments. Control tests showed that the photocathode is active only after illuminating the whole photocatalyst under CO_2-saturated conditions.

Subsequently, in collaboration with the team of R. Abe and our group, this photocathode was assessed under fully aqueous conditions.[180] LSV with intermittent light irradiation (λ = 460 nm) of the grafted **Dyad b** onto NiO films in aqueous electrolyte (50 mM $NaHCO_3$) at pH 6.6,

showed photocathodic currents starting at - 0.1 V vs Ag/AgCl. Long-term photoelectrolysis at - 0.7 V vs Ag/AgCl evolved 361 nmol of CO with 32 TON and 64% F.E. Hydrogen was also detected but not formate, as the capillary electrophoresis analyzer had a detection limit of 2 μmol. Proving the efficiency of the photocathode separately, the first photoelectrochemical cell for CO_2 reduction with water as reductant was constructed relying on a CoO_X/TaON photoanode separated by a Nafion membrane (**Figure V.11**). The cell was irradiated from the backside of the NiO electrode and - 0.3 V vs Ag/AgCl was applied (plus an additional chemical bias of 0.1 V due to pH difference). After 1 hour of PEC experiment, 79 nmol of CO were produced in the photocathode compartment, reaching 17 TON and 37% F.E.

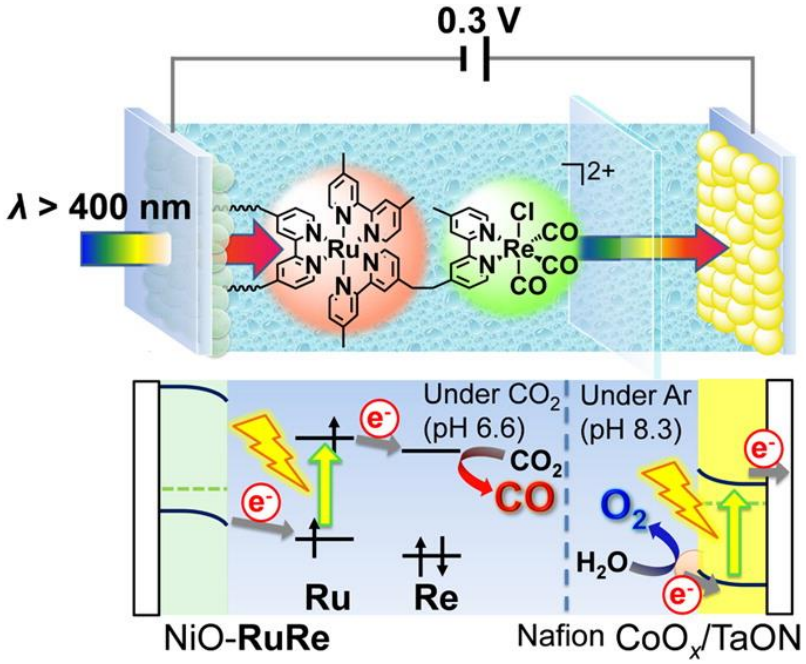

Figure V.11. A schematic representation of the hybrid photoelectrochemical cell, taken from reference [180].

In these studies, the amount of grafted dyad was relatively low (not more than 4 nmol.cm^{-2}) and more importantly the detachment from the surface limits the efficiency of the photocathodes.[217,180] In order to improve both the surface concentration in active compound and the stability of the grafting, a loading method using reductive electropolymerization was employed by Ishitani's group.[218] First, a ruthenium complex with methyl phosphonic acid groups and two 4-methyl-4′-vinyl-2,2′-bipyridine ligands (**Dye a**) were grafted onto NiO films. Then, the RuRe dyad with two 4-methyl-4′-vinyl-2,2′-bipyridine ligands (**Dyad c**) was electrodeposited in acetonitrile and three times more immobilized dyad compared to normal grafting was estimated from CV and ICP measurements. Desorption significantly decreased in aqueous $NaHCO_3$ solution, because of the hydrophobic nature of the vinyl polymer groups. Irradiation of the photocathode showed high cathodic photocurrents and long-term

photoelelectrolysis at - 0.7 V vs Ag/AgCl produced 500 nmol of CO as well as H_2 and HCOOH with a total of 85% F.E. Hydrogen and formate were products of the decomposition of ruthenium as evidenced by control tests. The higher amount of CO and F.E. compared to the non-polymerized dyad[180] can be explained by the higher loading and the lower desorption of the dyad as evidenced by XPS and UV-Vis at the end of the experiment. However, only 16 TON_{CO} were achieved, which represents a twice lower activity, suggesting that the electron transfer from the dye to the catalyst might be less efficient in this polymerized architecture.

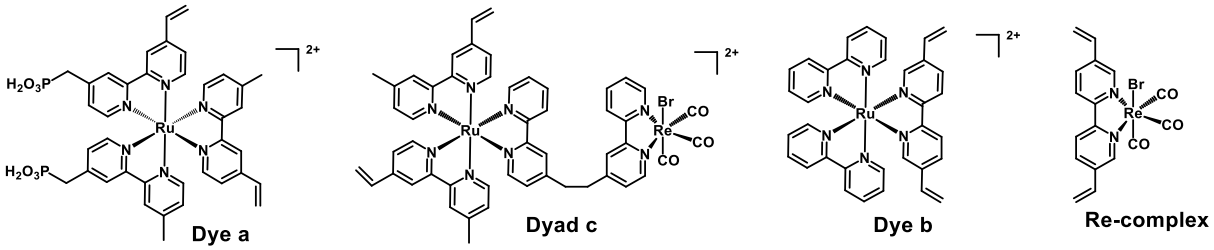

Chart V.2. Ruthenium and rhenium complexes used to build CO_2-reduction photocathodes by the electropolymerisation technique.

In a similar approach, NiO films were silanized with a vinyltrimethoxysilane bridge and ruthenium (**Dye b**) and rhenium complexes (**Chart V.2**) were stepwise reductively electropolymerized, forming carbon-carbon bonds, with 1/1 ratio.[219] Photocurrent densities of - 20 $\mu A.cm^{-2}$ were recorded under light irradiation at - 0.7 V vs Ag/AgCl in neutral aqueous conditions. CO and H_2 were the two products during the course of 10 hours photoelectrolysis with 65% F.E. and 58 TON for CO. Time-resolved spectroscopic measurements confirmed that fast hole injection occurs after dye excitation; In addition, relatively slow charge recombination enables electron transfer to the catalyst. Photocurrent decay was limited due to the stability of the assembly onto the surface, but rhenium decomposition or detachment was observed with post-operando XPS analysis.

$GuGaO_2$ semiconductors offer an alternative to NiO, because of its higher conductivity and more positive flat band potential.[103] O. Ishitani's group grafted **Dyad b** onto $GuGaO_2$ in order to compare the efficiency with NiO under similar experimental conditions.[220] The photocathode exhibited cathodic photocurrents with 0.4 V more positive potential than NiO in aqueous electrolyte (pH 6.6). The observed current is a result of photo-induced hole injection from the excited photosensitizer to the semiconductor. Under continuous light irradiation at - 0.3 V vs Ag/AgCl for 15 hours, the amount of CO was estimated 1 μmol with 122 TON and a total F.E. of 81% (including hydrogen). This is a clear improvement compared to the NiO-based photocathode.[180] The most significant achievement of this work is the preparation of the first

bias-free tandem cell active for CO_2 reduction under visible light illumination and using water as a reductant. The photocathode evolved CO (22 TON) and H_2 with a total F.E. of 72% and the CoO_X/TaON photoanode O_2 with 70% F.E.

ii) "Layer-by-layer" assembly

A "layer-by-layer" approach based on Zr(IV)-phosphonate bridges was used for the construction of dye-sensitized photocathodes for CO_2 reduction in 2019 by the group of T. J. Meyer (**Figure V.12**).[221] Ruthenium and catalytic rhenium complexes bearing two methyl phosphonic acid groups were used and a ratio of roughly 1/1 was determined by XPS. The initial part of the assembly is an electron donating dianiline coupled onto mesoporous NiO films. The corresponding photocathode was illuminated with visible light (1 sun) in a CO_2-saturated acetonitrile solution and photocurrent densities of - 65 $\mu A.cm^{-2}$ were obtained at -0.54 V vs NHE. 8 times lower responses were measured for the assembly without the dianiline, which acts as an electron donor and promotes the intramolecular electron transfer to the excited dye. After 20 minutes of continuous irradiation, CO was produced with 85% F.E. and 22 TON. Transient absorption measurements showed that hole injection takes place in sub-nanoseconds and that direct electron transfer to the catalyst is in competition with charge recombination on the microsecond scale.

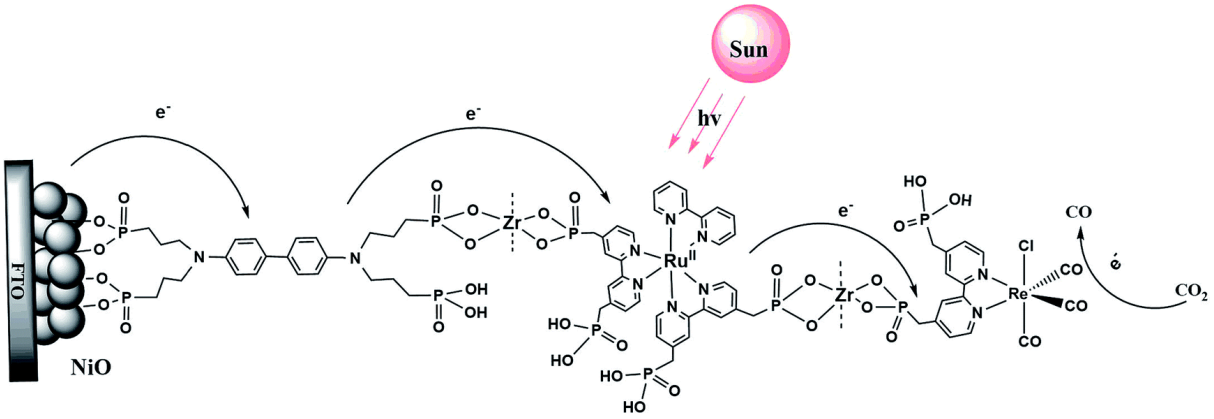

Figure V.12. Dye-sensitized photocathode for CO_2 reduction based on "layer-by-layer" assembly. The figure was taken by reference [221].

iii) Molecular photocathodes based on narrow band-gap semiconductors

Most of the constructed photocathodes for CO_2 fixation are based on noble metal catalysts, notably ruthenium and rhenium. Last year, a functional photocathode using a p-Si photoelectrode and an immobilized phosphonated cobalt bis(terpyridine) catalyst was prepared.[222] High grafting density (45 $nmol.cm^{-2}$) was determined due to a mesoporous TiO_2

scaffold on the electrode. The photocathode reduced CO_2 to mostly CO, formate and hydrogen in a mixture of organic/aqueous media, but also in fully aqueous conditions. In 6/4 MeCN/H_2O at – 1.0 V vs Fc^+/Fc, a total F.E. of 77% and 330 TON were estimated. Control experiments with a cobalt salt proved that the molecular catalyst is crucial for the activity, even though some H_2 and minimal amounts of CO were measured due to a heterogenous Co-deposit. Stability for more than 24 hours is an important characteristic of this system. In addition, the performance of the catalyst outperforms its previous activity in solution or grafted onto dark electrodes.[208,223] Most importantly, the corresponding photocathode is the most efficient reported for CO_2 reduction, highlighting the fact that precious metal free catalysts can compete the noble metal-based one.

The groups of M. Robert and F. Odobel reported a photocathode based on $Cu(In,Ga)Se_2$ (CIGS) as narrow band-gap SCs and a cobalt quaterpyridine.[224] The molecular catalyst was functionalized with phosphonic acid anchoring groups for the immobilization on a TiO_2 protective layer of the architecture. LSVs in fully aqueous media (pH 6.8) under intermittent irradiation showed impressive photocurrent densities higher than 3 $mA.cm^{-2}$ at potentials more negative than 0 V vs RHE. 2 hours PEC tests were carried out at - 0.06 V vs RHE and high selectivity for CO (97%, 3% H_2), activity (8000 TON) and stability were obtained.

Recently, T. J. Meyer's group reported a combination of molecular and semiconductor p-n junctions for efficient photoelectrocatalytic CO_2 reduction (**Figure V.13**).[225] For the semiconductor, one-dimensional n-GaN nanowire arrays were grown on n^+–p–p^+ silicon wafers. A NiO overlayer was deposited with ALD for binding the first monolayer of the molecular assembly, an electron relay (NPhN) with carboxylic acid anchoring groups and different structural variations. Then, a ruthenium dye and the common used rhenium catalyst with carboxyl groups were subsequently immobilized on the electrode by Zr(IV)-bridging units in a "layer-by-layer" assembly. Finally, a protective NiO layer was added by ALD for shielding the anchorage on the electrodes and the binding between the different layers. Complementary light absorption occurs due to the presence of silicon wafers and the molecular dye. Thus, the system takes advantage of the whole visible spectrum. Solar illumination (AM 1.5G) of the photocathode in aqueous electrolyte (pH 6.8) generates cathodic photocurrents from 0 V to -0.4V vs RHE. At – 0.25 V vs RHE, reduction of CO_2 to formate was accomplished with F.E. from 35 to 65% with quite stable photocurrent densities (-1.1 $mA.cm^{-2}$) for 20 hours.

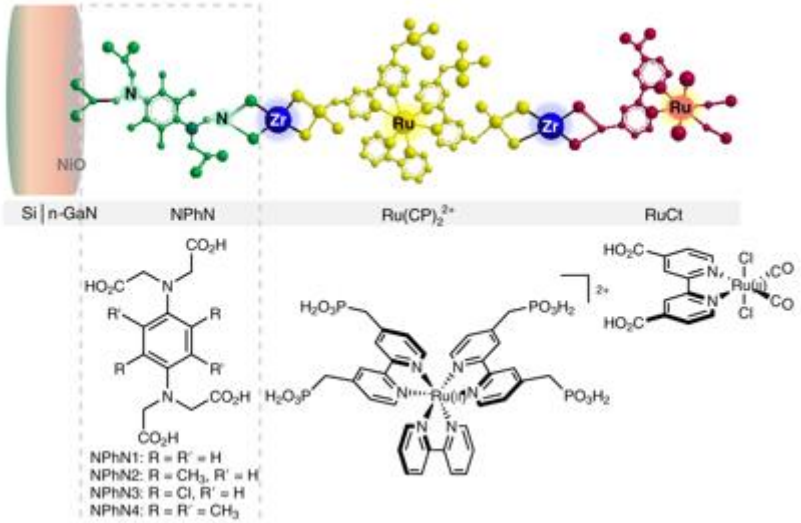

Figure V.13. "Layer-by-layer" molecular p–n-junction assembly formed by Zr(IV)-phosphonate bridging. The figure was taken by reference [225].

3) Cat1 as catalyst for CO_2 reduction

Cat1 has been first used as catalyst for CO_2 reduction in the eighties.[187] CO and H_2 were generated under irradiation of CO_2-saturated aqueous (pH 4) photocatalytic system containing **Cat1**, $[Ru(bpy)_3]^{2+}$ and ascorbate as SED. The selectivity for CO was low, as hydrogen was produced in higher yields. In addition, electrochemical reduction of CO_2 was carried out in fully aqueous media or in a mixture with DMF. From CVs, catalytic wave was observed at more negative potentials than the second reduction wave (Co(II)/Co(I)) in the presence of CO_2. CO and H_2 were produced, even though some oxalate and formate were also present after electrolysis (no exact quantification). Higher selectivity for CO was found in a mixture of H_2O/DMF (5/95) and the process is catalytic with TON values above unity (7). F.E. of 70% was estimated at – 1.3 V vs SCE.

Many years later, Peters and his team reexamined the electrocatalytic CO_2 reduction with **Cat1** in a mixture of organic/aqueous conditions.[226] Catalytic activity was observed close to the third reduction potential (ligand-based redox couple), increasing with the addition of water. Controlled potential electrolysis with a glassy carbon at – 2.0 V vs $Ag/AgNO_3$ for 40 minutes proved the reduction of CO_2 to CO. Higher performance (45% F.E. and 4 TON) and selectivity (CO/H_2 3/2) for CO evolution were obtained in an electrolyte containing 10 M H_2O. **Cat1** was also active for photocatalytic CO_2 in the same media with $Ir(ppy)_3$ light harvester and TEA as electron donor.[227,228] CO was detected in the solution and in the gas headspace with FT-IR and some intermediate species of the catalytic cycle could be characterized.

4) Assessment of the photoelectrocatalytic activity for CO_2 reduction of RuP_4^{OH}-Cat1-sensitized NiO films under fully aqueous conditions

Cat1 has been reported to be active for CO_2 reduction. In this context it appeared interesting to examine the activity of the novel **RuP_4^{OH}-Cat1**-sensitized photocathode for photoelectrocatalytic CO_2 reduction (**Figure V.14**). In the following part, some preliminary results with **RuP_4^{OH}-Cat1** grafted onto NiO electrodes in fully aqueous media will be presented. For the PEC tests, we decided to use the conditions from the study by O. Ishitani in collaboration with our group for the NiO photocathode based on **Dyad b** (aq. 50 mM $NaHCO_3$ pH 6.6).[180]

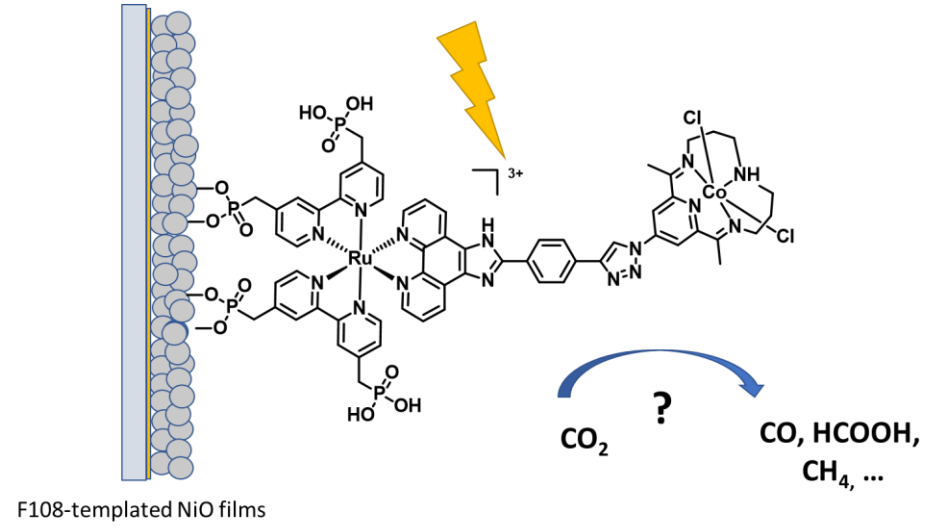

Figure V.14. NiO photocathode assessed for PEC CO_2 reduction based on **RuP_4^{OH}-Cat1**.

i) Experimental set-up and conditions

The set-up for the photoelectrochemical CO_2 reduction experiments is similar to the one previously employed for H_2 evolution. The photocathode performances were assessed in a three-electrode cell, using a 50 mM $NaHCO_3$ aqueous electrolyte[180,220] and two different applied potentials for comparison purposes. Irradiation was carried out with a 300W ozone-free Xe lamp operated at 280 W, equipped with a water-filled filter for elimination of IR irradiation and AM 1.5G filter. Pure CO_2 was bubbled for at least 40 minutes in the electrolyte in order to saturate the solution. CO and H_2 were quantified in the headspace by gas chromatography with FID and TCD detectors respectively. HCOOH in the solution was quantified by ion-exchanged chromatography at the end of the experiment. Prior to every chronoamperometric test, linear sweep voltammograms were recorded screening from + 0.6 V to - 0.8 V vs Ag/AgCl.

ii) Photoelectrochemical characterization

PEC measurements with the NiO/**RuP_4^{OH}-Cat1** photocathode were conducted to examine its ability for reducing CO_2 in water. **Figure V.15** shows the current-potential curve of the photocathode under dark conditions and illumination. Photocathodic current responses can be clearly observed starting at approximately + 0.4 V vs Ag/AgCl (+ 1.0 V vs RHE) and increasing at more negative potentials, reaching photocurrent densities of - 100 µA.cm^{-2}. Of note, the photocurrent density recorded with our films is significantly higher than the ones previously-reported for NiO-based photocathodes.[217,180]

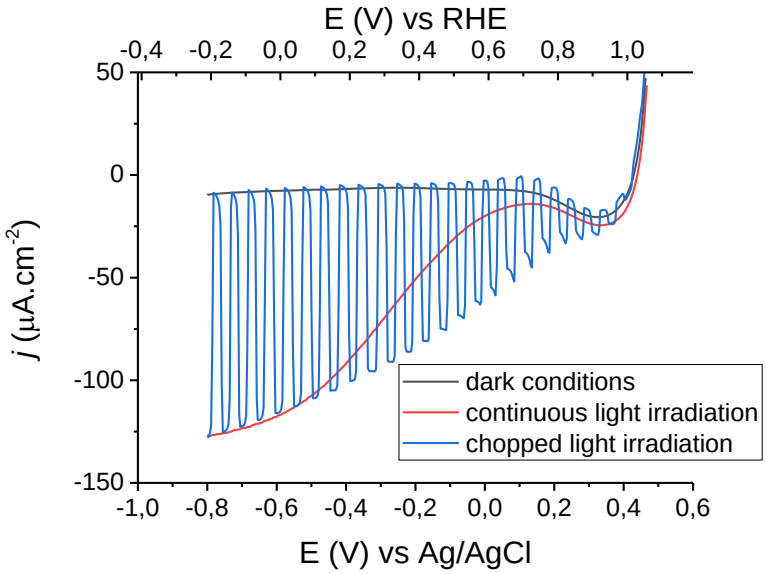

Figure V.15. Linear sweep voltammograms of NiO electrodes sensitized by **RuP_4^{OH}-Cat1** in a CO_2-saturated 50 mM $NaHCO_3$ aqueous solution at pH 6.6 under AM 1.5 G solar irradiation (1 sun, red line), dark conditions (black line) and chopped light irradiation (blue line).

iii) Assessment of the photoelectrocatalytic activity

3 hours chronoamperometric measurements were then carried out with NiO films sensitized by the dye-catalyst assembly, as well as with films sensitized by **RuP_4^{OH}-EPIP** and NiO pristine films for control (**Figure V.16**). These experiments were recorded at an applied potential of - 0.7 V vs Ag/AgCl in agreement with a previous study[180] and also at a less negative bias (- 0.4 V vs Ag/AgCl) for comparison purposes. CO_2-saturated conditions were used for the experiments, but a PEC test under N_2-saturated atmosphere with **RuP_4^{OH}-Cat1** was also performed as control.

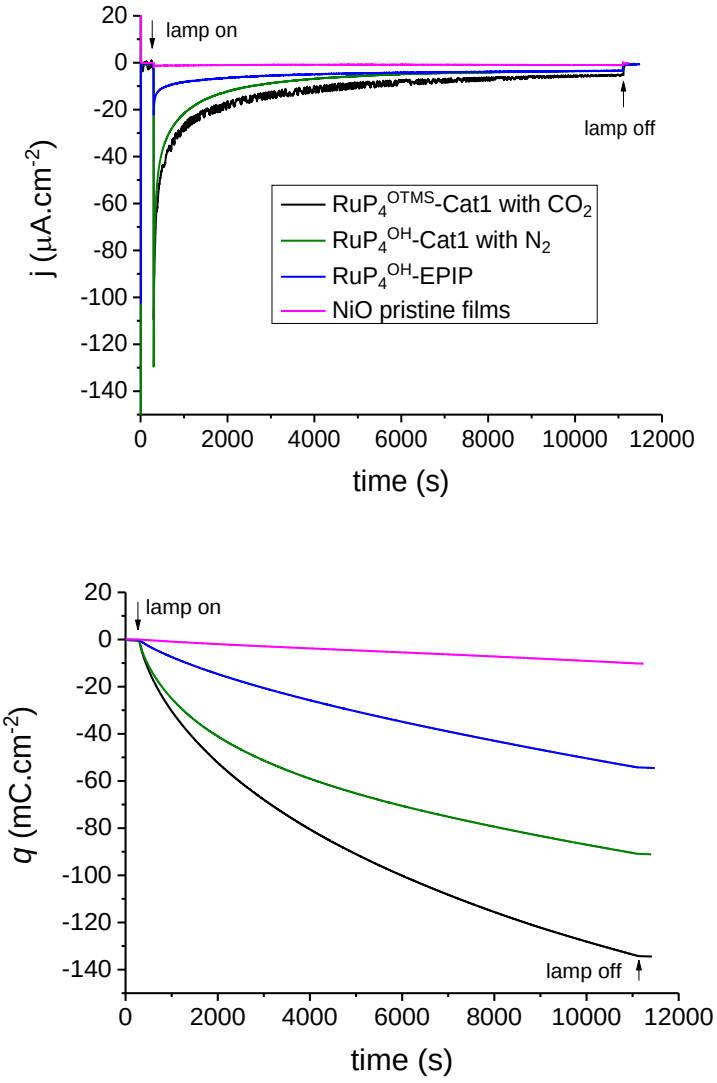

Figure V.16. 3 hours chronoamperometric (top), chronocoulometric measurements (bottom) of NiO films sensitized by **RuP_4^{OTMS}-Cat1** in CO_2-saturated conditions (black line), **RuP_4^{OH}-Cat1** in N_2-saturated conditions(red line), **RuP_4^{OH}-EPIP** (blue line) and NiO pristine films (pink line) in pH 6.6 aqueous 50 mm $NaHCO_3$ as supporting electrolyte under AM 1.5G light irradiation (IR-filterted) at –0.7 V vs Ag/AgCl.

From **Figure V.16**, where the photocurrent densities are depicted, the presence of the dyad significantly enhanced the photocurrent responses compared to **RuP_4^{OH}-EPIP**-sensitized films or NiO pristine films. High photocurrent densities were also obtained for the **RuP_4^{OH}-Cat1**-sensitized films under N_2-saturated atmosphere. Product identification and quantification in the headspace and in the solution was performed at the end of the experiments in order to understand the efficiency and the selectivity of the PEC CO_2 reduction.

Table V.4 gathers the figure of merits obtained for the different systems and experimental conditions tested. Under CO_2-saturated conditions, the **RuP_4-Cat1** sensitized photocathode is

active for CO_2 reduction to CO. Hydrogen was also produced, as expected due to the presence of water and the competitive proton reduction, but interestingly, the selectivity for CO is superior over H_2, with 230 ± 27 TON for CO (52 % F.E.) produced at – 0.4 V vs Ag/AgCl compared to 61 ± 18 TON for H_2 (13 % F.E.). Surprisingly, we observed that the activity is lower at – 0.7 V vs Ag/AgCl with 121 ± 11 TON (44 % F.E.) achieved to produce CO and 31 ± 2 TON for H_2 (11 % F.E.). Experiments under strictly identical conditions are now needed to understand if these differences really arise from the applied potential or if the grafting method plays a role here (classical sensitization employed for the set of experiments at – 0.4 V vs Ag/AgCl, whereas the alternative sensitization with TMS-protected dyads was used for the experiments at – 0.7 V vs Ag/AgCl). By contrast, when pristine NiO films were used, very low photocurrents were recorded, corresponding to the production of only traces of CO and H_2. The NiO photocathode sensitized by **RuP_4^{OH}-EPIP** produced slightly higher amount of H_2 but also traces of CO. The former can derive from some ruthenium-based activity through decomposition processes as previously reported under similar experimental conditions.[180,220] This first series of experiments thus clearly prove that the presence of **Cat1** is required for substantial CO_2 reduction activity. Of note, low amounts of formate are also produced in the electrolyte solution, but roughly the same amount is quantified whatever the system tested (with our without **Cat1**), including for pristine NiO films.

In addition, PEC tests were performed under N_2 atmosphere at – 0.7 V vs Ag/AgCl. In that case, only small quantities of CO were produced (9 $nmol.cm^{-2}$) and the main activity is the reduction of protons from the aqueous electrolyte. Interestingly, our photocathode is still active for PEC H_2 evolution under these quasi neutral conditions (pH 6.6) with an amount of evolved hydrogen (234 $nmol.cm^{-2}$) in the range of the ones previously obtained at pH 5.5 (**Table V.3**).

Finally, 2 experiments were run over a longer time (19 hours) and these preliminary results indicate that our photocathode is still active after 3 hours at both potentials: up to 291 TON for CO were indeed achieved under these conditions (- 0.4 V vs Ag/AgCl). However, additional experiments and post-operando analysis are required in order to fully understand this behavior.

sample	Potential (V vs Ag/AgCl)	Surface conc. ($nmol.cm^{-2}$)	Charge density ($mC.cm^{-2}$)	n(CO) / $nmol.cm^{-2}$ (TON)	n(H_2) / $nmol.cm^{-2}$ (TON)	n(HCOOH) / $nmol.cm^{-2}$ (TON)	FE_{CO}/ %	FE_{H2}/ %	FE_{HCOOH}/ %	Ref. exp.
NiO	- 0.4	-	11	1	1	22	2	2	38	EG400
	- 0.7	-	10	6	4	-[a]	11	8	-	EG450
RuP_4^{OH}-EPIP	- 0.4	5.1	68	5 (1)	120 (22)	-[a]	1	34	-	EG453
	- 0.7	5.4	54	9 (2)	91 (16)	46	3	32	16	EG444
RuP_4^{OH}-Cat1										
	-0.4	1.4	104 219[b]	298 (211) 410 (291)	60 (43) 86 (61)	-[a] 42 (30)	56 36	11 8	- 4	EG397
	-0.4	0.5	56	135 (249)	43 (79)	14 (26)	47	15	5	EG398
RuP_4^{OTMS}-Cat1	-0.7	2.2	134 282[c]	329 (129) 633 (249)	86 (34) 149 (59)	-[a] 62 (24)	47 43	12 10	- 4	EG441
	-0.7	2.0	116	240 (113)	61 (28)	28 (13)	40	10	5	EG446
RuP_4^{OH}-Cat1 (N_2 saturated)	-0.7	1.1	91 244[c]	11 (10) 34 (30)	234 (206) 361 (317)	-[a] -[a]	3 3	50 28	- -	EG454

Table V.4. Photoelectrochemical experiments assessing CO_2 reduction activity of the **RuP_4^{OH}-Cat1** dyad on NiO electrodes (surface area 3.0 ± 0.2 cm^2). Conditions are as follows: CO_2-saturated 50 mM aqueous $NaHCO_3$ at pH = 6.6, AM 1.5 G solar irradiation, 3 h runtime. a) HCOOH was not quantified, b) 21 h runtime, c) 19 h runtime.

IV. Conclusions and perspectives

In the first part of this chapter, a novel dye-catalyst assembly was grafted onto NiO films. Photoelectrocatalytic tests were carried out under strictly identical conditions for direct comparison with the previous H_2-evolving photocathode. Under fully aqueous conditions at pH 5.5 at an applied potential of – 0.4 V vs Ag/AgCl (+ 0.13 RHE) with AM 1.5 G solar irradiation, higher photocurrents and electron transfer efficiency were obtained, implying more efficient electron uptake (catalysis) by the cobalt tetraazomacrocyclic catalyst. The produced H_2 and F.E. were also enhanced, reaching F.E. higher than 50% compared to 25% for the previous system. Higher than 200 TON were determined, showing an 18-fold increase. The attractive activity of the new dyad is ascribed to the cobalt complex as the photosensitizer, the anchorage and the bridging ligand are the same. To the best of our knowledge, these TON values are the highest ever reported for a dye-sensitized NiO photocathode.

Low grafting densities were estimated due to the moderate solubility of the dyad and the different batches of NiO films. Slightly increase was accomplished after grafting the dye-catalyst assembly under its TMS-protected form and almost 400 TON were achieved after 2 hours of CA experiments. However, the results were not always reproducible, and more measurements are essential to identify a clear trend. Nevertheless, improving the grafting procedure either by electropolymerization or by introducing new anchoring groups could further improve the performance of the photocathode.

Post-operando analysis showed desorption after 2 hours of PEC test, in agreement with **RuP_4^{OH}-Co**, regardless the grafting method. ALD could be used in order to face this detrimental phenomenon. Preliminary MALDI-ToF spectra suggested that loss of the catalyst can occur during the long-term tests. Obviously, more post-mortem techniques like ToF-SIMS, XPS, ICP-AES are needed to obtain a more distinct view of the possible decomposition pathways and the destiny of the molecular dye-catalyst assembly. This will enable us to correlate the activity of the photocathode with the nature of the catalyst and in a following step to optimize the molecular architecture to further boost the long-term operation.

In the last part of this thesis, we showed that our new dyad is also promising for photoelectrocatalytic CO_2 reduction. To the best of our knowledge, this is the first example of functional dye-sensitized photocathode based on a cobalt catalyst, which produces CO with high efficiency and selectivity in fully CO_2-saturated aqueous media. The evolution of hydrogen due to the competitive proton reduction can produce the industrially useful syngas.[229] The TON values are higher than the previous NiO-photocathodes with the RuRe dyad in

aqueous media[180] and outperforms previous work with **Cat1** under electro or photo-chemical conditions. In addition, these preliminary results exhibit the highest TON with a dye-sensitized photocathode for CO_2 reduction to date. Further experiments, post-operando characterization and mechanistic investigations are under way in order to shed light on the activity and stability of the photocathode.

General conclusion and perspectives

This thesis falls within the field of bio-inspired chemistry and artificial photosynthesis for solar fuel production. Production of hydrogen or carbon-based fuels in a tandem DSPEC, where a photoanode for water oxidation is coupled to a photocathode performing the reduction processes of interest (proton, carbon dioxide) represents the ultimate goal. Unfortunately, up to now the performances of the p-type photocathode are a limiting factor to develop competent full devices and the construction of efficient dye-sensitized photocathodes is currently the subject of intensive research interest.

Here, we presented the synthesis and characterization of two covalent dye-catalyst assemblies functionalized with methyl phosphonate anchoring groups for grafting onto NiO. For both architectures, the same ruthenium tris-diimine complex as photosensitizer was employed coupled with two different cobalt complexes.

Our first dyad with a cobalt diimine-dioxime catalyst was active for hydrogen evolution in fully aqueous medium. Strictly identical experimental conditions were used for the photoelectrocatalytic tests in order to have a direct comparison with the previous photocathode from the group based on a push-pull organic dye-catalyst assembly. The superior performance of our photocathode could be ascribed to the ruthenium photosensitizer. We could further increase the activity when standardized AM 1.5G filter was used due to more efficient light harvesting by the ruthenium complex. The obtained activity lies in the range of the previously reported best performing dye-sensitized hydrogen-evolving photocathodes with photocurrents of some tens of μA and TONs (**Table I.1**).

Transient absorption spectroscopy and post operando experiments allowed us to identify the main factors limiting the performance of the photocathode. Firstly, the thermal electron transfer from the reduced dye to the catalyst is one of the kinetic bottlenecks. Secondly, desorption of the dyad from the surface of the electrode and degradation of the cobalt diimine-dioxime catalyst are two issues that should be taken into consideration for the overall efficiency and long-term stability of our system. We should mention that post-operando analysis in order to elucidate the fate of the molecular components in the literature is scarce.

We designed a second dye-catalyst assembly with a more robust cobalt tetraazomacrocyclic complex. Its preparation proved to be a big challenge as synthesis and purification are highly demanding and optimization is ongoing in the lab. Nevertheless, the corresponding

photocathode exhibits the highest TON reported until today for p-type dye-sensitized NiO photocathodes for proton reduction. The enhanced activity is clearly ascribed to the catalytic unit, as all the other parameters remained identical. Supplementary post-operando analysis is needed in order to understand the reasons behind this increase in performance. Our novel dyad was also used for CO_2 reduction and the preliminary results showed high TON and F.E. for CO.

Overall, this work now provides some guidance to build more performant dye-sensitized photocathodes:

- ***Cat1** opens the way to integrate more stable and robust aminopyridyl and polypyridyl cobalt complexes in these devices.*
- *Covalent dye-catalyst architectures achieving more efficient electron transfer need to be designed.*
- *To improve the stability of the molecular anchoring, different approaches can be followed. Deposition of a thin oxide layer by ALD, typically alumina, at the top of the sensitized film is well-known to decrease desorption from the surface of metal oxides. Formation of a hydrophobic monolayer and (electro)polymerized assemblies are other solutions in order to diminish the detachment of the molecular components. Finally, a detailed screening of the anchoring groups is crucial in order to obtain the most stable anchorage (not sensitive to pH).*
- *Improvements of the semiconductor is also necessary for future applications. New materials like $CuGaO_2$ or $CuCrO_2$ have been employed in the field and outperformed analogous NiO-based photocathodes. With these materials, the construction of more efficient systems could be accomplished.*

*Finally, the performance of the **RuP_4^{OH}-Cat1**-based photocathode and in particular its activity under neutral pH starts to pave the way for its integration in a tandem dye-sensitized photoelectrochemical cell.*

References

(1) Lewis, N. S.; Nocera, D. G. Powering the Planet: Chemical Challenges in Solar Energy Utilization. *PNAS* **2006**, *103* (43), 15729–15735. https://doi.org/10.1073/pnas.0603395103.

(2) Perez, R.; Perez, M. A Fundamental Look At Supply Side Energy Reser Ves For The Planet. *IEA-SHC* **2009**, 4–6.

(3) Lubitz, W.; Ogata, H.; Ru, O.; Reijerse, E. Hydrogenases. *Chem. Rev.* **2014**, *114* (8), 4081−4148. https://doi.org/10.1021/cr4005814.

(4) Andreiadis, E. S.; Chavarot-Kerlidou, M.; Fontecave, M.; Artero, V. Artificial Photosynthesis: From Molecular Catalysts for Light-Driven Water Splitting to Photoelectrochemical Cells. *Photochem. Photobiol.* **2011**, *87* (5), 946–964. https://doi.org/10.1111/j.1751-1097.2011.00966.x.

(5) Zhang, B.; Sun, L. Artificial Photosynthesis : Opportunities and Challenges of Molecular Catalysts. *Chem. Soc. Rev.* **2019**, *48*, 2216–2264. https://doi.org/10.1039/c8cs00897c.

(6) Mckone, J. R.; Lewis, N. S.; Gray, H. B. Will Solar-Driven Water-Splitting Devices See the Light of Day? *Chem. Mater.* **2014**, *26* (1), 407–414. https://doi.org/10.1021/cm4021518.

(7) Fujishima, A.; Honda, K. Electrochemical Photolysis of Water at a Semiconductor Electrode. *Nature* **1972**, *238*, 37–38. https://doi.org/doi.org/10.1038/238037a0.

(8) Swierk, J. R.; Mallouk, T. E. Design and Development of Photoanodes for Water-Splitting Dye-Sensitized Photoelectrochemical Cells. *Chem. Soc. Rev.* **2013**, *42* (6), 2357–2387. https://doi.org/10.1039/c2cs35246j.

(9) Walter, M. G.; Warren, E. L.; Mckone, J. R.; Boettcher, S. W.; Mi, Q.; Santori, E. A.; Lewis, N. S. Solar Water Splitting Cells. *Chem. Rev.* **2010**, *110* (11), 6446–6473. https://doi.org/10.1021/cr1002326.

(10) Queyriaux, N.; Kaeffer, N.; Morozan, A.; Chavarot-Kerlidou, M.; Artero, V. Molecular Cathode and Photocathode Materials for Hydrogen Evolution in Photoelectrochemical Devices. *J. Photochem. Photobiol. C Photochem. Rev.* **2015**, *25*, 90–105. https://doi.org/10.1016/j.jphotochemrev.2015.08.001.

(11) Xu, P.; Mccool, N. S.; Mallouk, T. E. Water Splitting Dye-Sensitized Solar Cells. *Nano Today* **2017**, *14*, 42–58. https://doi.org/10.1016/j.nantod.2017.04.009.

(12) Gibson, E. A. Dye-Sensitized Photocathodes for H2 Evolution. *Chem. Soc. Rev.* **2017**, *46*, 6194–6209. https://doi.org/10.1039/C7CS00322F.

(13) Dalle, K. E.; Warnan, J.; Leung, J. J.; Reuillard, B.; Karmel, I. S.; Reisner, E. Electro- and Solar-Driven Fuel Synthesis with First Row Transition Metal Complexes. *Chem. Rev.* **2019**, *119* (4), 2752–2875. https://doi.org/10.1021/acs.chemrev.8b00392.

(14) Li, F.; Yang, H.; Li, W.; Sun, L. Device Fabrication for Water Oxidation, Hydrogen Generation, and CO2 Reduction via Molecular Engineering. *Joule* **2018**, *2* (1), 36–60. https://doi.org/10.1016/j.joule.2017.10.012.

(15) Gordon, R. B.; Bertram, M.; Graedel, T. E. Metal Stocks and Sustainability. *PNAS* **2006**, *103* (5), 1209–1214. https://doi.org/10.1073/pnas.0509498103.

(16) Thoi, V. S.; Sun, Y.; Long, R.; Chang, C. J. Complexes of Earth-Abundant Metals for Catalytic Electrochemical Hydrogen Generation under Aqueous Conditions. *Chem. Soc. Rev.* **2013**, *42*, 2388–2400. https://doi.org/10.1039/c2cs35272a.

(17) Tong, L.; Duan, L.; Zhou, A.; Thummel, R. P. First-Row Transition Metal Polypyridine Complexes That Catalyze Proton to Hydrogen Reduction. *Coord. Chem. Rev.* **2020**, *402*, 213079–213100.

https://doi.org/10.1016/j.ccr.2019.213079.

(18) Artero, V.; Chavarot-kerlidou, M.; Fontecave, M. Splitting Water with Cobalt. *Angew. Chem. Int. Ed.* **2011**, *50* (32), 7238–7266. https://doi.org/10.1002/anie.201007987.

(19) Dempsey, J. L.; Brunschwig, B. S.; Winkler, J. A. Y. R.; Gray, H. B. Hydrogen Evolution Catalyzed by Cobaloximes. *Acc. Chem. Res.* **2009**, *42* (12), 1995–2004. https://doi.org/https://doi.org/10.1021/ar900253e.

(20) Eckenhoff, W. T.; Eisenberg, R.; Eisenberg, R. Molecular Systems for Light Driven Hydrogen Production †. *Dalt. Trans.* **2012**, *41*, 13004–13021. https://doi.org/10.1039/c2dt30823a.

(21) Kovacs, T.; Pan, Q.; Lang, P.; O'Reilly, L.; Rau, S.; Browne, W. R.; Pryce, M. T.; Huijser, A.; Vos, J. G. Supramolecular Bimetallic Assemblies for Photocatalytic Hydrogen Generation from Water. *Faraday Discuss.* **2015**, *185*, 143–170. https://doi.org/10.1039/C5FD00068H.

(22) Braumüller, M.; Schulz, M.; Sorsche, D.; Pfeffer, M.; Schaub, M.; Popp, J.; Park, B.-W.; Hagfeldt, A.; Dietzek, B.; Rau, S. Synthesis and Characterization of an Immobilizable Photochemical Molecular Device for H2-Generation. *Dalt. Trans.* **2015**, *44*, 5577–5586. https://doi.org/10.1039/c4dt03730h.

(23) Fihri, A.; Artero, V.; Razavet, M.; Baffert, C.; Leibl, W.; Fontecave, M. Cobaloxime-Based Photocatalytic Devices for Hydrogen Production. *Angew. Chem. Int. Ed.* **2008**, *47* (3), 564–567. https://doi.org/10.1002/anie.200702953.

(24) Fihri, A.; Artero, V.; Pereira, A.; Fontecave, M. Efficient H2 -Producing Photocatalytic Systems Based on Cyclometalated Iridium- and Tricarbonylrhenium-Diimine Photosensitizers and Cobaloxime Catalysts. *Dalt. Trans.* **2008**, 5567–5569. https://doi.org/10.1039/b812605b.

(25) O'Regan, B.; Grätzel, M. A Low-Cost, High-Efficiency Solar Cell Based on Dye-Sensitized Colloidal TiO2 Films. *Nature* **1991**, *353*, 737–740. https://doi.org/10.1038/353737a0.

(26) Kallmann, H.; Pope, M. Decomposition of Water by Light. *Nature* **1960**, *188* (4754), 935–936. https://doi.org/10.1038/188935a0.

(27) He, J. J.; Lindström, H.; Hagfeldt, A.; Lindquist, S. E. Dye-Sensitized Nanostructured p-Type Nickel Oxide Film as a Photocathode for a Solar Cell. *J. Phys. Chem. B* **1999**, *103* (42), 8940–8943. https://doi.org/10.1021/jp991681r.

(28) Hagfeldt, A.; Boschloo, G.; Sun, L.; Kloo, L.; Pettersson, H. Dye-Sensitized Solar Cells. *Chem. Rev.* **2010**, *110* (11), 6595–6663. https://doi.org/10.1021/cr900356p.

(29) Nikolaou, V.; Charisiadis, A.; Charalambidis, G.; Coutsolelos, A. G. . O. F. . Recent Advances and Insights in Dye-Sensitized NiO Photocathodes for Photovoltaic Devices. *J. Mater. Chem. A* **2017**, *5*, 21077–21113. https://doi.org/10.1039/C7TA06500K.

(30) Benazzi, E.; Mallowsa, J.; Summers, G. H.; Black, F. A.; Gibson, E. A. Developing Photocathode Materials for P-Type Dye-Sensitized Solar Cells. *J. Mater. Chem. A* **2019**, *7*, 10409–10445. https://doi.org/10.1039/C9TC01822K.

(31) Odobel, F.; Pellegrin, Y. Recent Advances in the Sensitization of Wide-Band-Gap Nanostructured p -Type Semiconductors. Photovoltaic and Photocatalytic Applications. *J. Phys. Chem. Lett.* **2013**, *4* (15), 2551–2564. https://doi.org/10.1021/jz400861v.

(32) Boschloo, G.; Hagfeldt, A. Spectroelectrochemistry of Nanostructured NiO. *J. Phys. Chem. B* **2001**, *105* (15), 3039–3044. https://doi.org/10.1021/jp003499s.

(33) Dare-Edwards, M. P.; Goodenough, J. B.; Hamnett, A.; Nicholson, N. D. Photoelectrochemistry of Nickel (II) Oxide. *J. Chem. Soc., Faraday Trans. 2* **1981**, *77*, 643–661. https://doi.org/10.1039/F29817700643.

(34) Nandy, S.; Saha, B.; Mitra, M. K.; Chattopadhyay, K. K. Effect of Oxygen Partial Pressure on the Electrical and Optical Properties of Highly (200) Oriented p-Type Ni 1 – x O Films by DC Sputtering. *J. Mater. Sci.* **2007**, *42*, 5766–5772. https://doi.org/10.1007/s10853-006-1153-x.

(35) Warnan, J.; Gardner, J.; Le Pleux, L.; Petersson, J.; Pellegrin, Y.; Blart, E.; Hammarström, L.; Odobel, F. Multichromophoric Sensitizers Based on Squaraine for NiO Based Dye-Sensitized Solar Cells. *J. Phys. Chem. C* **2014**, *118* (1), 103–113. https://doi.org/10.1021/jp408900x.

(36) Dini, D.; Halpin, Y.; Vos, J. G.; Gibson, E. A. The Influence of the Preparation Method of NiOx Photocathodes on the Efficiency of P-Type Dye-Sensitized Solar Cells. *Coord. Chem. Rev.* **2015**, *304–305*, 179–201. https://doi.org/10.1016/j.ccr.2015.03.020.

(37) Sumikura, S.; Mori, S.; Shimizu, S.; Usami, H.; Suzuki, E. Syntheses of NiO Nanoporous Films Using Nonionic Triblock Co-Polymer Templates and Their Application to Photo-Cathodes of p-Type Dye-Sensitized Solar Cells. *J. Photochem. Photobiol. A Chem.* **2008**, *199* (1), 1–7. https://doi.org/10.1016/j.jphotochem.2008.04.007.

(38) Li, B. L.; Gibson, E. A.; Qin, P.; Boschloo, G.; Gorlov, M.; Hagfeldt, A.; Sun, L. Double-Layered NiO Photocathodes for p-Type DSSCs with Record IPCE. *Adv. Mater.* **2010**, *22* (15), 1759–1762. https://doi.org/10.1002/adma.200903151.

(39) Vera, F.; Schrebler, R.; Muñoz, E.; Suarez, C.; Cury, P.; Gómez, H.; Córdova, R.; Marotti, R. E.; Dalchiele, E. A. Preparation and Characterization of Eosin B- and Erythrosin J-Sensitized Nanostructured NiO Thin Film Photocathodes. *Thin Solid Films* **2005**, *490* (2), 182–188. https://doi.org/10.1016/j.tsf.2005.04.052.

(40) Lepleux, L.; Chavillon, B.; Pellegrin, Y.; Blart, E.; Cario, L.; Jobic, S.; Odobel, F. Simple and Reproducible Procedure to Prepare Self-Nanostructured NiO Films for the Fabrication of P-Type Dye-Sensitized Solar Cells. *Inorg. Chem.* **2009**, *48* (17), 8245–8250. https://doi.org/10.1021/ic900866g.

(41) Wood, C. J.; Summers, G. H.; Clark, C. A.; Kaeffer, N.; Braeutigam, M.; Carbone, R.; Amario, L. D.; Fan, K.; Stevens, L. A.; Parmenter, C. D. J.; Fay, M. W.; La Torre, A. et al. A Comprehensive Comparison of Dye-Sensitized NiO Photocathodes for Solar Energy Conversion †. *Phys. Chem. Chem. Phys.* **2016**, *18*, 10727–10738. https://doi.org/10.1039/C5CP05326A.

(42) Pujari, S. P.; Scheres, L.; Marcelis, A. T. M.; Zuilhof, H. Covalent Surface Modification of Oxide Surfaces Angewandte. *Angew. Chemie - Int. Ed.* **2014**, *53* (25), 6322–6356. https://doi.org/10.1002/anie.201306709.

(43) Zhang, L.; Cole, J. M. Anchoring Groups for Dye-Sensitized Solar Cells. *ACS Appl. Mater. Interfaces* **2015**, *7* (6), 3427–3455. https://doi.org/10.1021/am507334m.

(44) Pellegrin, Y.; Le Pleux, L.; Blart, E.; Renaud, A.; Chavillon, B.; Szuwarski, N.; Boujtita, M.; Cario, L.; Jobic, S.; Jacquemin, D.; Odobel, F. Ruthenium Polypyridine Complexes as Sensitizers in NiO Based P-Type Dye-Sensitized Solar Cells : Effects of the Anchoring Groups. *J. Photochem. Photobiol. A Chem.* **2011**, *219* (2–3), 235–242. https://doi.org/10.1016/j.jphotochem.2011.02.025.

(45) Galoppini, E. Linkers for Anchoring Sensitizers to Semiconductor Nanoparticles. *Coord. Chem. Rev.* **2004**, *248* (13–14), 1283–1297. https://doi.org/10.1016/j.ccr.2004.03.016.

(46) Brennan, B. J.; Llansola Portolés, M. J.; Liddell, P. A.; Moore, T. A.; Moore, A. L.; Gust, D. Comparison

of Silatrane, Phosphonic Acid, and Carboxylic Acid Functional Groups for Attachment of Porphyrin Sensitizers to TiO2 in Photoelectrochemical Cells. *Phys. Chem. Chem. Phys.* **2013**, *15* (39), 16605–16614. https://doi.org/10.1039/c3cp52156g.

(47) Mutin, P. H.; Guerrero, G. . V. A. Hybrid Materials from Organophosphorus Coupling Molecules. *J. Mater. Chem.* **2005**, *15*, 3761–3768. https://doi.org/10.1039/b505422b.

(48) Queffélec, C.; Petit, M.; Janvier, P.; Knight, D. A.; Bujoli, B. Surface Modification Using Phosphonic Acids and Esters. *Chem. Rev.* **2012**, *112* (7), 3777−3807. https://doi.org/10.1021/cr2004212.

(49) Hotchkiss, P. J.; Jones, S. C.; Paniagua, S. A.; Sharma, A.; Kippelen, B.; Armstrong, N. R.; Marder, S. R. The Modification of Indium Tin Oxide with Phosphonic Acids: Mechanism Tuning of Surface Properties , and Potential for Use in Organic Electronic Applications. *Acc. Chem. Res.* **2012**, *45* (3), 337–346. https://doi.org/10.1021/ar200119g.

(50) Brodard-severac, F.; Guerrero, G.; Maquet, J.; Florian, P.; Gervais, C.; Mutin, P. H. High-Field 17-O MAS NMR Investigation of Phosphonic Acid Monolayers on Titania. *Chem. Mater.* **2008**, *20* (12), 5191–5196. https://doi.org/10.1021/cm8012683.

(51) Gillaizeau-Gauthier, I.; Odobel, F.; Alebbi, M.; Argazzi, R.; Costa, E.; Bignozzi, C. A.; Qu, P.; Meyer, G. J. Phosphonate-Based Bipyridine Dyes for Stable Photovoltaic Devices. *Inorg. Chem.* **2001**, *40* (23), 6073–6079. https://doi.org/10.1021/ic010192e.

(52) Hanson, K.; Brennaman, M. K.; Luo, H.; Glasson, C. R. K.; Concepcion, J. J.; Song, W.; Meyer, T. J. Photostability of Phosphonate-Derivatized, Ru(II) Polypyridyl Complexes on Metal Oxide Surfaces. *ACS Appl. Mater. Interfaces* **2012**, *4* (3), 1462−1469. https://doi.org/10.1021/am201717x.

(53) Farré, Y.; Maschietto, F.; Föhlinger, J.; Wykes, M.; Planchat, A.; Pellegrin, Y.; Blart, E.; Ciofini, I.; Hammarström, L.; Odobel, F. A Comparative Investigation of the Role of the Anchoring Group on Perylene Monoimide Dyes in NiO-Based Dye-Sensitized Solar Cells. *ChemSusChem* **2020**, *13* (7), 1844–1855. https://doi.org/10.1002/cssc.201903182.

(54) Ooyama, Y.; Harima, Y. Photophysical and Electrochemical Properties , and Molecular Structures of Organic Dyes for Dye-Sensitized Solar Cells. *ChemPhysChem* **2012**, *13* (18), 4032–4080. https://doi.org/10.1002/cphc.201200218.

(55) Queyriaux, N.; Wahyuono, R. A.; Fize, J.; Gablin, C.; Wächtler, M.; Martinez, E.; Léonard, D.; Dietzek, B.; Artero, V.; Chavarot-kerlidou, M. Aqueous Photocurrent Measurements Correlated to Ultrafast Electron Transfer Dynamics at Ruthenium Tris Diimine Sensitized NiO Photocathodes. *J. Phys. Chem. C* **2017**, *121* (11), 5891−5904. https://doi.org/10.1021/acs.jpcc.6b12536.

(56) Losse, S.; Vos, J. G.; Rau, S. Catalytic Hydrogen Production at Cobalt Centres. *Coord. Chem. Rev.* **2010**, *254* (21–22), 2492–2504. https://doi.org/10.1016/j.ccr.2010.06.004.

(57) Schrauzer, G. N. Organocobalt Chemistry of Vitamin B12 Model Compounds (Cobaloximes). *Acc. Chem. Res.* **1968**, *1* (4), 97–103. https://doi.org/10.1021/ar50004a001.

(58) Hawecker, J.; Lehn, J. M.; Ziessel, R. Efficient Homogeneous Photochemical Hydrogen Generation and Water Reduction Mediated by Cobaloxime or Macrocyclic Cobalt Complexes. *New J. Chem.* **1983**, *7*, 271–277.

(59) Eckenhoff, W. T.; Mcnamara, W. R.; Du, P.; Eisenberg, R. Cobalt Complexes as Artificial Hydrogenases for the Reductive Side of Water Splitting. *Biochim. Biophys. Acta* **2013**, *1827* (8–9), 958–973.

https://doi.org/10.1016/j.bbabio.2013.05.003.

(60) Razavet, M.; Artero, V.; Fontecave, M. Proton Electroreduction Catalyzed by Cobaloximes : Functional Models for Hydrogenases. *Inorg. Chem.* **2005**, *44* (13), 4786–4795. https://doi.org/10.1021/ic050167z.

(61) Baffert, C.; Artero, V.; Fontecave, M. Cobaloximes as Functional Models for Hydrogenases . 2 . Proton Electroreduction Catalyzed by Difluoroborylbis(Dimethylglyoximato)Cobalt (II) Complexes in Organic Media. *Inorg. Chem.* **2007**, *46* (5), 1817–1824. https://doi.org/10.1021/ic061625m.

(62) Hu, X.; Cossairt, B. M.; Brunschwig, B. S.; Lewis, N. S.; Peters, J. C. Electrocatalytic Hydrogen Evolution by Cobalt Difluoroboryl-Diglyoximate Complexes. *Chem. Commun.* **2005**, *45*, 4723–4725. https://doi.org/10.1039/b509188h.

(63) Hu, X.; Brunschwig, B. S.; Peters, J. C. Electrocatalytic Hydrogen Evolution at Low Overpotentials by Cobalt Macrocyclic Glyoxime and Tetraimine Complexes. *J. Am. Chem. Soc.* **2007**, *129* (29), 8988–8998. https://doi.org/10.1021/ja067876b.

(64) McCormick, T. M.; Han, Z.; Weinberg, D. J.; Brennessel, W. W.; Holland, P. L.; Eisenberg, R. Impact of Ligand Exchange in Hydrogen Production from Cobaloxime-Containing Photocatalytic Systems. *Inorg. Chem.* **2011**, *50* (21), 10660–10666. https://doi.org/10.1021/ic2010166.

(65) Seeber, R.; Parker, W.; Marzilli, P. A.; Marzilli, L. G. Electrochemical Synthesis of "Costa-Type" Cobalt Complexes. *Organometallics* **1989**, *8* (10), 2377–2381. https://doi.org/10.1021/om00112a018.

(66) Kaeffer, N.; Chavarot-kerlidou, M.; Artero, V. Hydrogen Evolution Catalyzed by Cobalt Diimine − Dioxime Complexes. *Acc. Chem. Res.* **2015**, *48* (5), 1286−1295. https://doi.org/10.1021/acs.accounts.5b00058.

(67) Jacques, P.- A.; Artero, V.; Pécaut, J.; Fontecave, M. Cobalt and Nickel Diimine-Dioxime Complexes as Molecular Electrocatalysts for Hydrogen Evolution with Low Overvoltages. *PNAS* **2009**, *106* (49), 20627–20632. https://doi.org/10.1073?pnas.0907775106.

(68) Andreiadis, E. S.; Jacques, P.-A.; Tran, P. D.; Leyris, A.; Chavarot-kerlidou, M.; Jousselme, B.; Matheron, M.; Pécaut, J.; Palacin, S.; Fontecave, M.; Artero, V. Molecular Engineering of a Cobalt-Based Electrocatalytic Nanomaterial for H2 Evolution under Fully Aqueous Conditions. *Nat. Chem.* **2013**, *5* (1), 48–53. https://doi.org/10.1038/nchem.1481.

(69) Sletten, E. M.; Bertozzi, C. R. From Mechanism to Mouse: A Tale of Two Bioorthogonal Reactions. *Acc. Chem. Res.* **2011**, *44* (9), 666–676. https://doi.org/10.1021/ar200148z.

(70) Cobo, S.; Heidkamp, J.; Jacques, P.; Fize, J.; Fourmond, V.; Guetaz, L.; Jousselme, B.; Ivanova, V.; Dau, H.; Palacin, S.; Fontecave, M.; Artero, V. A Janus Cobalt-Based Catalytic Material for Electro-Splitting of Water. *Nat. Mater.* **2012**, *11* (9), 802–807. https://doi.org/10.1038/nmat3385.

(71) Kaeffer, N.; Morozan, A.; Artero, V. Oxygen Tolerance of a Molecular Engineered Cathode for Hydrogen Evolution Based on a Cobalt Diimine-Dioxime Catalyst. *J. Phys. Chem. B* **2015**, *119* (43), 13707–13713. https://doi.org/10.1021/acs.jpcb.5b03136.

(72) Bhattacharjee, A.; Andreiadis, E. S.; Chavarot-Kerlidou, M.; Fontecave, M.; Field, M. J.; Artero, V. A Computational Study of the Mechanism of Hydrogen Evolution by Cobalt(Diimine-Dioxime) Catalysts. *Chem. - A Eur. J.* **2013**, *19* (45), 15166–15174. https://doi.org/10.1002/chem.201301860.

(73) Probst, B.; Guttentag, M.; Rodenberg, A.; Hamm, P.; Alberto, R. Photocatalytic H2 Production from Water with Rhenium and Cobalt Complexes. *Inorg. Chem.* **2011**, *50* (8), 3404–3412.

https://doi.org/10.1021/ic102317u.

(74) Guttentag, M.; Rodenberg, A.; Kopelent, R.; Probst, B.; Buchwalder, C.; Brandstätter, M.; Hamm, P.; Alberto, R. Photocatalytic H2 Production with a Rhenium / Cobalt System in Water under Acidic Conditions. *Eur. J. Inorg. Chem.* **2012**, *2012* (1), 59–64. https://doi.org/10.1002/ejic.201100883.

(75) Zhang, P.; Jacques, P.; Chavarot-kerlidou, M.; Wang, M.; Sun, L.; Fontecave, M.; Artero, V. Phosphine Coordination to a Cobalt Diimine − Dioxime Catalyst Increases Stability during Light-Driven H2 Production. *Inorg. Chem.* **2012**, *51* (4), 2115−2120. https://doi.org/10.1021/ic2019132.

(76) Hamd, W.; Chavarot-Kerlidou, M.; Fize, J.; Muller, G.; Leyris, A.; Matheron, M.; E. Courtin, E.; Fontecave, M.; Sanchez, C.; Artero, V.; Laberty-Robert, C. Dye-Sensitized Nanostructured Crystalline Mesoporous Tin-Doped Indium Oxide Films with Tunable Thickness for Photoelectrochemical Applications. *J. Mater. Chem. A* **2013**, *1*, 8217–8225. https://doi.org/10.1039/c3ta10728k.

(77) Gennari, M.; Legalite´, F.; Zhang, L.; Pellegrin, Y.; Blart, E.; Fortage, J.; Brown, A. M.; Deronzier, A.; Collomb, M.-N.; Boujtita, M.; Jacquemin, D.; Hammarström, L.; Odobel, F. Long-Lived Charge Separated State in NiO-Based P-Type Dye- Sensitized Solar Cells with Simple Cyclometalated Iridium Complexes. *J. Phys. Chem. Lett.* **2014**, *5* (13), 2254−2258. https://doi.org/10.1021/jz5009714.

(78) Han, Y.; Dillon, R. J.; Flynn, C. J.; Rountree, E. S.; Alibabaei, L.; Cahoon, J. F.; Papanikolas, J. M.; Dempsey, J. L. Interfacial Electron Transfer Yields in Dye-Sensitized NiO Photocathodes Correlated to Excited-State Dipole Orientation of Ruthenium Chromophores. *Can. J. Chem.* **2018**, *96* (9), 865–874. https://doi.org/10.1139/cjc-2017-0359.

(79) Massin, J.; Bräutigam, M.; Kaeffer, N.; Queyriaux, N.; Field, M. J.; Schacher, F. H.; Popp, J.; Chavarot-Kerlidou, M.; Dietzek, B.; Artero, V. Dye-Sensitized PS-b-P2VP-Templated Nickel Oxide Films for Photoelectrochemical Applications. *Interface Focus* **2015**, *5* (3), 20140083–20140092. https://doi.org/10.1098/rsfs.2014.0083.

(80) Massin, J.; Lyu, S.; Pavone, M.; Muñoz-García, A. B.; Kaumann, B.; Toupance, T.; Chavarot-kerlidou, M.; Artero, V. Design and Synthesis of Novel Organometallic Dyes for NiO Sensitization and Photo-Electrochemical Applications. *Dalt. Trans.* **2016**, *45*, 12539–12547. https://doi.org/10.1039/c6dt02177h.

(81) Li, L.; Duan, L.; Wen, F.; Li, C.; Wang, M.; Hagfeldt, A.; Sun, L. Visible Light Driven Hydrogen Production from a Photo-Active Cathode Based on a Molecular Catalyst and Organic Dye-Sensitized p-Type Nanostructured NiO. *Chem. Commun.* **2012**, *48*, 988–990. https://doi.org/10.1039/c2cc16101j.

(82) Click, K. A.; Beauchamp, D. R.; Huang, Z.; Chen, W.; Wu, Y. Membrane-Inspired Acidically Stable Dye-Sensitized Photocathode for Solar Fuel Production. *J. Am. Chem. Soc.* **2016**, *138* (4), 1174−1179. https://doi.org/10.1021/jacs.5b07723.

(83) Hinnemann, B.; Moses, P. G.; Bonde, J.; Jørgensen, K. P.; Nielsen, J. H.; Horch, S.; Chorkendorff, I.; Nørskov, J. K. Biomimetic Hydrogen Evolution : MoS2 Nanoparticles as Catalyst for Hydrogen Evolution. *J. Am. Chem. Soc.* **2005**, *127* (15), 5308–5309. https://doi.org/10.1021/ja0504690.

(84) Kamire, R. J.; Majewski, M. B.; Ho, W. L.; Phelan, B. T.; Farha, O. K.; Hupp, J. T.; Wasielewski, M. R. Photodriven Hydrogen Evolution by Molecular Catalysts Using Al2O3-Protected Perylene-3,4-Dicarboximide on NiO Electrodes. *Chem. Sci.* **2017**, *8*, 541–549. https://doi.org/10.1039/C6SC02477G.

(85) Massin, J.; Brautigam, M.; Bold, S.; Wächtler, M.; Pavone, M.; Muñoz-garcía, A. B.; Dietzek, B.; Artero, V.; Chavarot-kerlidou, M. Investigating Light-Driven Hole Injection and Hydrogen Evolution Catalysis at

Dye-Sensitized NiO Photocathodes : A Combined Experimental- Theoretical Study. *J. Phys. Chem. C* **2019**, *123* (28), 17176–17184. https://doi.org/10.1021/acs.jpcc.9b04715.

(86) Ji, Z.; He, M.; Huang, Z.; Ozkan, U.; Wu, Y. Photostable P-Type Dye-Sensitized Photoelectrochemical Cells for Water Reduction. *J. Am. Chem. Soc.* **2013**, *135* (32), 11696−11699. https://doi.org/10.1021/ja404525e.

(87) Kaeffer, N.; Massin, J.; Lebrun, C.; Renault, O.; Chavarot-kerlidou, M.; Artero, V. Covalent Design for Dye-Sensitized H2 - Evolving Photocathodes Based on a Cobalt Diimine − Dioxime Catalyst. *J. Am. Chem. Soc.* **2016**, *138* (38), 12308−12311. https://doi.org/10.1021/jacs.6b05865.

(88) Kolb, H. C.; Finn, M. G.; Sharpless, K. B. Click Chemistry : Diverse Chemical Function from a Few Good Reactions. *Angew. Chem. Int. Ed.* **2001**, *40* (11), 2004–2021. https://doi.org/10.1002/1521-3773(20010601)40:11<2004::AID-ANIE2004>3.0.CO;2-5.

(89) Kaeffer, N.; Morozan, A.; Fize, J.; Martinez, E.; Guetaz, L.; Artero, V. The Dark Side of Molecular Catalysis: Diimine − Dioxime Cobalt Complexes Are Not the Actual Hydrogen Evolution Electrocatalyst in Acidic Aqueous Solutions. *ACS Catal.* **2016**, *6* (6), 3727−3737. https://doi.org/10.1021/acscatal.6b00378.

(90) Windle, C. D.; Massin, J.; Chavarot-kerlidou, M.; Artero, V. A Protocol for Quantifying Hydrogen Evolution by Dye-Sensitized Molecular Photocathodes and Its Implementation for Evaluating a New Covalent Architecture Based on an Optimized Dye-Catalyst Dyad. *Dalt. Trans.* **2018**, *47*, 10509–10516. https://doi.org/10.1039/c8dt01210e.

(91) Pati, P. B.; Zhang, L.; Philippe, B.; Fernández-Terán, R.; Ahmadi, S.; Tian, L.; Rensmo, H.; Hammarström, L.; Tian, H. Insights into the Mechanism of a Covalently Linked Organic Dye – Cobaloxime Catalyst System for Dye- Sensitized Solar Fuel Devices. *ChemSusChem* **2017**, *10* (11), 2480–2495. https://doi.org/10.1002/cssc.201700285.

(92) Põldme, N.; Reilly, L. O.; Fletcher, I.; Portoles, J.; Sazanovich, I. V; Towrie, M.; Long, C.; Vos, J. G.; Pryce, M. T.; Gibson, E. A. Photoelectrocatalytic H2 Evolution from Integrated Photocatalysts Adsorbed on NiO. *Chem. Sci.* **2019**, *10*, 99–112. https://doi.org/10.1039/c8sc02575d.

(93) Lyu, S.; Massin, J.; Pavone, M.; Muñoz-García, A. B.; Labrugère, C.; Toupance, T.; Chavarot-kerlidou, M.; Artero, V.; Olivier, C. H2 -Evolving Dye-Sensitized Photocathode Based on a Ruthenium Diacetylide / Cobaloxime Supramolecular Assembly. *ACS Appl. Energy Mater.* **2019**, *2* (7), 4971–4980. https://doi.org/10.1021/acsaem.9b00652.

(94) Fan, K.; Li, F.; Wang, L.; Daniel, Q.; Gabrielsson, E.; Sun, L. Pt-Free Tandem Molecular Photoelectrochemical Cells for Water Splitting Driven by Visible Light. *Phys. Chem. Chem. Phys.* **2014**, *16*, 25234–25240. https://doi.org/10.1039/C4CP04489D.

(95) Li, F.; Fan, K.; Xu, B.; Gabrielsson, E.; Daniel, Q.; Li, L.; Sun, L. Organic Dye-Sensitized Tandem Photoelectrochemical Cell for Light Driven Total Water Splitting. *J. Am. Chem. Soc.* **2015**, *137* (28), 9153−9159. https://doi.org/10.1021/jacs.5b04856.

(96) Antila, L. J.; Ghamgosar, P.; Maji, S.; Tian, H.; Ott, S.; Hammarström, L. Dynamics and Photochemical H2 Evolution of Dye − NiO Photocathodes with a Biomimetic FeFe-Catalyst. *ACS Energy Lett.* **2016**, *1* (6), 1106−1111. https://doi.org/10.1021/acsenergylett.6b00506.

(97) Gardner, J. M.; Beyler, M.; Karnahl, M.; Tschierlei, S.; Ott, S.; Hammarström, L. Light-Driven Electron

Transfer between a Photosensitizer and a Proton-Reducing Catalyst Co-Adsorbed to NiO. *J. Am. Chem. Soc.* **2012**, *134* (47), 19322–19325. https://doi.org/10.1021/ja3082268.

(98) Kaeffer, N.; Windle, C. D.; Brisse, R.; Gablin, C.; Leonard, D.; Jousselme, B.; Chavarot-Kerlidou, M.; Artero, V. Insights into the Mechanism and Aging of a Noble-Metal Free H2-Evolving Dye-Sensitized Photocathode. *Chem. Sci.* **2018**, *9*, 6721–6738. https://doi.org/10.1039/C8SC00899J.

(99) Yu, M.; Draskovic, T. I.; Wu, Y. Cu(I)-Based Delafossite Compounds as Photocathodes in p-Type Dye-Sensitized Solar Cells. *Phys. Chem. Chem. Phys.* **2014**, *16*, 5026–5033. https://doi.org/10.1039/c3cp55457k.

(100) Creissen, C. E.; Warnan, J.; Reisner, E. Solar H2 Generation in Water with a CuCrO2 Photocathode Modified with an Organic Dye and Molecular Ni Catalyst. *Chem. Sci.* **2018**, *9* (6), 1439–1447. https://doi.org/10.1039/C7SC04476C.

(101) Creissen, C. E.; Warnan, J.; Anton-Garcia, D.; Farré, Y.; Odobel, F.; Reisner, E. Inverse Opal CuCrO2 Photocathodes for H2 Production Using Organic Dyes and a Molecular Ni Catalyst. *ACS Cat.* **2019**, *9* (10), 9530–9538. https://doi.org/10.1021/acscatal.9b02984.

(102) Windle, C. D.; Kumagai, H.; Higashi, M.; Brisse, R.; Bold, S.; Jousselme, B.; Chavarot-kerlidou, M.; Maeda, K.; Abe, R.; Ishitani, O.; Artero, V. Earth-Abundant Molecular Z-Scheme Photoelectrochemical Cell for Overall Water-Splitting. *J. Am. Chem. Soc.* **2019**, *141* (24), 9593−9602. https://doi.org/10.1021/jacs.9b02521.

(103) Renaud, A.; Chavillon, B.; Le Pleux, L.; Pellegrin, Y.; Blart, E.; Boujtita, M.; Pauporté, T.; Cario, L.; Jobic, S.; Odobel, F. CuGaO 2 a Promising Alternative for NiO in P-Type Dye Solar Cells. *J. Mater. Chem.* **2012**, *22*, 14353–14356. https://doi.org/10.1039/C2JM31908J.

(104) Gross, M. A.; Creissen, C. E.; Orchard, K. L.; Reisner, E. Photoelectrochemical Hydrogen Production in Water Using a Layer-by-Layer Assembly of a Ru Dye and Ni Catalyst on NiO. *Chem. Sci.* **2016**, *7*, 5537–5546. https://doi.org/10.1039/C6SC00715E.

(105) Shan, B.; Das, A. K.; Marquard, S.; Farnum, B. H.; Wang, D.; Bullock, R. M.; Meyer, T. J. Photogeneration of Hydrogen from Water by a Robust Dye-Sensitized Photocathode. *Energy Environ. Sci.* **2016**, *9*, 3693–3697. https://doi.org/10.1039/C6EE02903E.

(106) Wang, D.; Sheridan, M. V; Shan, B.; Farnum, B. H.; Marquard, S. L.; Sherman, B. D.; Eberhart, M. S.; Nayak, A.; Dares, C. J.; Das, A. K.; Bullock, R. M.; Meyer, T. J. Layer-by-Layer Molecular Assemblies for Dye-Sensitized Photoelectrosynthesis Cells Prepared by Atomic Layer Deposition. *J. Am. Chem. Soc.* **2017**, *139* (41), 14518–14525. https://doi.org/10.1021/jacs.7b07216.

(107) Shan, B.; Sherman, B. D.; Klug, C. M.; Nayak, A.; Marquard, S. L.; Liu, Q.; Bullock, R. M.; Meyer, T. J. Modulating Hole Transport in Multilayered Photocathodes with Derivatized P-Type Nickel Oxide and Molecular Assemblies for Solar-Driven Water Splitting. *J. Phys. Chem. Lett.* **2017**, *8* (18), 4374−4379. https://doi.org/10.1021/acs.jpclett.7b01911.

(108) Sun, K.; Shen, S.; Liang, Y.; Burrows, P. E.; Mao, S. S.; Wang, D. Enabling Silicon for Solar-Fuel Production. *Chem. Rev.* **2014**, *114* (17), 8662−8719. https://doi.org/10.1021/cr300459q.

(109) Leung, J. J.; Warnan, J.; Nam, D. H.; Zhang, J. Z.; Willkomm, J.; Reisner, E. Photoelectrocatalytic H2 Evolution in Water with Molecular Catalysts Immobilised on P-Si via a Stabilising Mesoporous TiO2 Interlayer. *Chem. Sci.* **2017**, *8*, 5172–5180. https://doi.org/10.1039/c7sc01277b.

(110) Shan, B.; Brennaman, M. K.; Troian-gautier, L.; Liu, Y.; Nayak, A.; Klug, C. M.; Li, T.; Bullock, R. M.; Meyer, T. J. A Silicon-Based Heterojunction Integrated with a Molecular Excited State in a Water-Splitting Tandem Cell. *J. Am. Chem. Soc.* **2019**, *141* (26), 10390−10398. https://doi.org/10.1021/jacs.9b04238.

(111) Díez-García, M. I.; Gómez, R. Metal Doping for Enhancing the Photoelectrochemical Behavior of LaFeO3 Photocathodes. *ChemSusChem* **2017**, *10* (11), 2457–2463. https://doi.org/10.1002/cssc.201700166.

(112) Li, F.; Xu, R.; Nie, C.; Wu, X.; Zhang, P.; Duan, L.; Sun, L. Dye-Sensitized LaFeO3 Photocathode for Solar-Driven H2 Generation. *Chem. Commun.* **2019**, *55*, 12940–12943. https://doi.org/10.1039/c9cc06781g.

(113) Kirner, J. T.; Finke, R. G. Water-Oxidation Photoanodes Using Organic Light-Harvesting Materials: A Review. *J. Mater. Chem. A* **2017**, *5* (37), 19560–19592. https://doi.org/10.1039/c7ta05709a.

(114) Gust, D.; Moore, T. A.; Moore, A. L. Mimicking Photosynthetic Solar Energy Transduction. *Acc. Chem. Res.* **2001**, *34* (1), 40–48. https://doi.org/10.1021/ar9801301.

(115) Harriman, A.; Sauvage, J. P. A Strategy for Constructing Photosynthetic Models: Porphyrin-Containing Modules Assembled around Transition Metals. *Chem. Soc. Rev.* **1996**, *25* (1), 41–48. https://doi.org/10.1039/cs9962500041.

(116) Dürr, H.; Bossmann, S. Ruthenium Polypyridine Complexes. On the Route to Biomimetic Assemblies as Models for the Photosynthetic Reaction Center. *Acc. Chem. Res.* **2001**, *34* (11), 905–917. https://doi.org/10.1021/ar9901220.

(117) D'Amario, L.; Antila, L. J.; Pettersson Rimgard, B.; Boschloo, G.; Hammarström, L. Kinetic Evidence of Two Pathways for Charge Recombination in NiO- Based Dye-Sensitized Solar Cells. *J. Phys. Chem. Lett.* **2015**, *6* (5), 779–783. https://doi.org/10.1021/acs.jpclett.5b00048.

(118) Nakade, S.; Kanzaki, T.; Wada, Y.; Yanagida, S. Stepped Light-Induced Transient Measurements of Photocurrent and Voltage in Dye-Sensitized Solar Cells : Application for Highly Viscous Electrolyte Systems. *Langmuir* **2005**, *21* (23), 10803–10807. https://doi.org/10.1021/la051257j.

(119) Mori, S.; Fukuda, S.; Sumikura, S.; Takeda, Y.; Tamaki, Y.; Suzuki, E.; Abe, T. Charge-Transfer Processes in Dye-Sensitized NiO Solar Cells. *J. Phys. Chem. C* **2008**, *112* (41), 16134–16139. https://doi.org/10.1021/jp803919b.

(120) D'Amario, L.; Föhlinger, J.; Boschloo, G.; Hammarström, L. Unveiling Hole Trapping and Surface Dynamics of NiO Nanoparticles. *Chem. Sci.* **2018**, *9*, 223–230. https://doi.org/10.1039/C7SC03442C.

(121) Dillon, R. J.; Alibabaei, L.; Meyer, T. J.; Papanikolas, J. M. Enabling Efficient Creation of Long-Lived Charge-Separation on Dye-Sensitized NiO Photocathodes. *ACS Appl. Mater. Interfaces* **2017**, *9* (32), 26786−26796. https://doi.org/10.1021/acsami.7b05856.

(122) Uehara, S.; Sumikura, S.; Suzuki, E.; Mori, S. Retardation of Electron Injection at NiO / Dye / Electrolyte Interface by Aluminium Alkoxide Treatment. *Energy Environ. Sci.* **2010**, *3*, 641–644. https://doi.org/10.1039/b920083e.

(123) Natu, G.; Huang, Z.; Ji, Z.; Wu, Y. The Effect of an Atomically Deposited Layer of Alumina on NiO in P-Type Dye-Sensitized Solar Cells. *Langmuir* **2012**, *28* (1), 950–956. https://doi.org/10.1021/la203534s.

(124) Hanson, K.; Losego, M. D.; Kalanyan, B.; Ashford, D. L.; Parsons, G. N.; Meyer, T. J. Stabilization of [Ru(Bpy)2(4,4′-(PO3H2)Bpy)]2+ on Mesoporous TiO2 with Atomic Layer Deposition of Al2O3. *Chem.*

Mater. **2013**, *25* (1), 3–5. https://doi.org/10.1021/cm303172w.

(125) Langmar, O.; Ganivet, C. R.; Lennert, A.; Costa, R. D.; Torre, G. De; Torres, T.; Guldi, D. M. Combining Electron-Accepting Phthalocyanines and Nanorod-like CuO Electrodes for p-Type Dye-Sensitized Solar Cells. *Angew. Chem. Int. Ed.* **2015**, *54* (309194), 7688–7692. https://doi.org/10.1002/anie.201501550.

(126) Orchard, K. L.; Hojo, D.; Sokol, K. P.; Chan, M.-J.; Asao, N.; Adschiri, T.; Reisner, E. Catechol–TiO2 Hybrids for Photocatalytic H2 Production and Photocathode Assembly. *Chem. Commun.* **2017**, *53*, 12638–12641. https://doi.org/10.1039/C7CC05094A.

(127) Lapides, A. M.; Sherman, B. D.; Brennaman, M. K.; Dares, C. J.; Skinner, K. R.; Templeton, J. L.; Meyer, T. J. Synthesis, Characterization, and Water Oxidation by a Molecular Chromophore-Catalyst Assembly Prepared by Atomic Layer Deposition. The "Mummy" Strategy. *Chem. Sci.* **2015**, *6*, 6398–6406. https://doi.org/10.1039/C5SC01752A.

(128) Khnayzer, R. S.; Thoi, V. S.; Nippe, M.; King, A. E.; Jurss, J. W.; El Roz, K. A.; Long, J. R.; Chang, C. J.; Castellano, F. N. Towards a Comprehensive Understanding of Visible- Light Photogeneration of Hydrogen from Water Using Cobalt (II) Polypyridyl Catalysts. *Energy Environ. Sci.* **2014**, *7*, 1477–1488. https://doi.org/10.1039/c3ee43982h.

(129) Queyriaux, N.; Jane, R. T.; Massin, J.; Artero, V.; Chavarot-Kerlidou, M. Recent Developments in Hydrogen Evolving Molecular Cobalt(II)–Polypyridyl Catalysts. *Coord. Chem. Rev.* **2015**, *304–305*, 3–19. https://doi.org/10.1016/j.ccr.2015.03.014.

(130) Queyriaux, N.; Giannoudis, E.; Windle, C. D.; Roy, S.; Pécaut, J.; Coutsolelos, A. G.; Artero, V.; Chavarot-Kerlidou, M. A Noble Metal-Free Photocatalytic System Based on a Novel Cobalt Tetrapyridyl Catalyst for Hydrogen Production in Fully Aqueous Medium. *Sustain. Energy Fuels* **2018**, *2* (3), 553–557. https://doi.org/10.1039/c7se00428a.

(131) Queyriaux, N.; Andreiadis, E. S.; Torelli, S.; Pecaut, J.; Veldkamp, B. S.; Margulies, E. A.; Wasielewski, M. R.; Chavarot-kerlidou, M.; Artero, V. CuAAC-Based Assembly and Characterization of a Ruthenium – Copper Dyad Containing a Diimine – Dioxime Ligand Framework. *Faraday Discuss.* **2017**, *198*, 251–261. https://doi.org/10.1039/c6fd00204h.

(132) Rostovtsev, V. V; Green, L. G.; Fokin, V. V; Sharpless, K. B. A Stepwise Huisgen Cycloaddition Process : Copper (I) -Catalyzed Regioselective "Ligation" of Azides and Terminal Alkynes. *Angew. Chem. Int. Ed.* **2002**, *41* (14), 2596–2599. https://doi.org/10.1002/1521-3773(20020715)41:14<2596::aid-anie2596>3.0.co;2-4.

(133) Baron, A.; Herrero, C.; Quaranta, A.; Charlot, M.-F.; Leibl, W.; Vauzeilles, B.; Aukauloo, A. Efficient Electron Transfer through a Triazole Link in Ruthenium (II) Polypyridine Type Complexes. *Chem. Commun.* **2011**, *2*, 11011–11013. https://doi.org/10.1039/c1cc13683f.

(134) Baron, A.; Herrero, C.; Quaranta, A.; Charlot, M.-F.; Leibl, W.; Vauzeilles, B.; Aukauloo, A. Click Chemistry on a Ruthenium Polypyridine Complex. An Efficient and Versatile Synthetic Route for the Synthesis of Photoactive Modular Assemblies. *Inorg. Chem.* **2012**, *51* (11), 5985–5987. https://doi.org/10.1021/ic300227.

(135) Campagna, S.; Puntoriero, F.; Nastasi, F.; Bergamini, G.; Balzani, V. Photochemistry and Photophysics of Coordination Compounds: Ruthenium. In *Topics in Current Chemistry;* 2007; pp 117–204.

(136) Mede, T.; Jäger, M.; Schubert, U. S. '"Chemistry-on-the-Complex"': Functional Ru (II) Polypyridyl-Type

Sensitizers as Divergent Building Blocks. *Chem. Soc. Rev.* **2018**, *47* (20), 7577–7627. https://doi.org/10.1039/c8cs00096d.

(137) Ziessel, R.; Grosshenny, V.; Hissler, M.; Stroh, C. Cis-[Ru(2,2′:6′,2″-Terpyridine)(DMSO)Cl2]: Useful Precursor for TheSynthesis of Heteroleptic Terpyridine Complexes under Mild Conditions. *Inorg. Chem.* **2004**, *43* (14), 4262–4271. https://doi.org/10.1021/ic049822d.

(138) Caramori, S.; Cristino, V.; Argazzi, R.; Meda, L.; Bignozzi, C. A. Photoelectrochemical Behavior of Sensitized TiO2 Photoanodes in an Aqueous Environment : Application to Hydrogen Production. *Inorg. Chem.* **2010**, *49* (7), 3320–3328. https://doi.org/10.1021/ic9023037.

(139) Zaban, A.; Ferrere, S.; Gregg, B. A. Relative Energetics at the Semiconductor/Sensitizing Dye/Electrolyte Interface. *J. Phys. Chem. B* **1998**, *102* (2), 452–460. https://doi.org/10.1021/jp972924n.

(140) Will, G.; Boschloo, G.; Rao, S. N.; Fitzmaurice, D. Potentiostatic Modulation of the Lifetime of Light-Induced Charge Separation in a Heterosupermolecule. *J. Phys. Chem. B* **1999**, *103* (38), 8067–8079. https://doi.org/10.1021/jp990414i.

(141) Sotomayor, J.; Will, G.; Fitzmaurice, D. Photoelectrochromic Heterosupramolecular Assemblies. *J. Mater. Chem.* **2000**, *10*, 685–692. https://doi.org/10.1039/A908064C.

(142) Braumüller, M.; Schulz, M.; Staniszewska, M.; Sorsche, D.; Wunderlin, M.; Popp, J.; Guthmuller, J.; Dietzek, B.; Rau, S. Synthesis and Characterization of Ruthenium and Rhenium Dyes with Phosphonate Anchoring Groups. *Dalt. Trans.* **2016**, *45*, 9216–9228. https://doi.org/10.1039/c6dt01047d.

(143) Ashford, D. L.; Song, W.; Concepcion, J. J.; Glasson, C. R. K.; Brennaman, M. K.; Norris, M. R.; Fang, Z.; Templeton, J. L.; Meyer, T. J. Photoinduced Electron Transfer in a Chromophore − Catalyst Assembly Anchored to TiO2. *J. Am. Chem. Soc.* **2012**, *134* (46), 19189−19198. https://doi.org/10.1021/ja3084362.

(144) Norris, M. R.; Concepcion, J. J.; Glasson, C. R. K.; Fang, Z.; Lapides, A. M.; Ashford, D. L.; Templeton, J. L.; Meyer, T. J. Synthesis of Phosphonic Acid Derivatized Bipyridine Ligands and Their Ruthenium Complexes. *Inorg. Chem.* **2013**, *52* (21), 12492–12501. https://doi.org/10.1021/ic4014976.

(145) Queyriaux, N.; Giannoudis, E.; Lefebvre, J.-F.; Artero, V.; Chavarot-Kerlidou, M. Synthesis of Ruthenium Tris-Diimine Photosensitizers Substituted by Four Methylphosphonate Anchoring Groups for Dye-Sensitized Photoelectrochemical Cell Applications. *Eur. J. Inorg. Chem.* **2019**, *2019* (15), 2154–2161. https://doi.org/10.1002/ejic.201900151.

(146) Ramachandra, S.; Schuermann, K. C.; Edafe, F.; Belser, P.; Nijhuis, C. A.; Reus, W. F.; Whitesides, G. M.; Cola, L. De. Luminescent Ruthenium Tripod Complexes : Properties in Solution and on Conductive Surfaces. *Inorg. Chem.* **2011**, *50* (5), 1581–1591. https://doi.org/10.1021/ic1002868.

(147) Cadierno, V.; Crochet, P.; Garcia-Garrido, S. E.; Gimeno, J. Water-Soluble Ruthenium(II) Catalysts [RuCl2(G6 -Arene)- {P(CH2OH)3}] for Isomerization of Allylic Alcohols and Alkyne Hydration. *Dalt. Trans.* **2004**, *2*, 3635–3641. https://doi.org/10.1039/B411177J.

(148) Zabri, H.; Gillaizeau, I.; Bignozzi, C. A.; Caramori, S.; Charlot, M.-F.; Cano-Boquera, J.; Odobel, F. Synthesis and Comprehensive Characterizations of New Cis -RuL2X2 Sensitizers for Nanocrystalline TiO2 Solar Cell Using Bis-Phosphonated Bipyridine Ligands (L). *Inorg. Chem.* **2003**, *42* (21), 6655−6666. https://doi.org/10.1021/ic034403m.

(149) Gagne, R. R. Models for Copper-Containing Proteins: Five-Coordinate Complexes of Copper(I). *J. Am. Chem. Soc.* **1976**, *98* (21), 6709–6710. https://doi.org/10.1021/ja00437a053.

(150) Quaranta, A.; Lachaud, F.; Herrero, C.; Guillot, R.; Charlot, M.-F; Leibl, W; Aukauloo, A. Influence of the Protonic State of an Imidazole-Containing Ligand on the Electrochemical and Photophysical Properties of a Ruthenium (II)–Polypyridine-Type Complex. *Chem. Eur. J.* **2007**, *13* (29), 8201–8211. https://doi.org/10.1002/chem.200700185.

(151) Bold, S.; Zedler, L.; Zhang, Y.; Massin, J.; Artero, V.; Chavarot-kerlidou, M.; Dietzek, B. Electron Transfer in a Covalent Dye–Cobalt Catalyst Assembly – a Transient Absorption Spectroelectrochemistry Perspective. *Chem. Commun.* **2018**, *54* (5), 10594–10597. https://doi.org/10.1039/C8CC05556D.

(152) Heath, G. A.; Yellowlees, L. J.; Braterman, P. S. Spectro-Electrochemical Studies on Tris-Bipyridyl Ruthenium Complexes ; Ultra-Violet, Visible, and Near -Infrared Spectra. *J.C.S. Chem. Comm.* **1981**, 287–289.

(153) Wächtler, M.; Kupfer, S.; Guthmuller, J.; Popp, J.; González, L.; Dietzek, B. Influence of Multiple Protonation on the Initial Excitation in a Black Dye. *J. Phys. Chem. C* **2011**, *115* (48), 24004–24012. https://doi.org/10.1021/jp2100717.

(154) Wächtler, M.; Kupfer, S.; Guthmuller, J.; Rau, S.; González, L.; Dietzek, B. Structural Control of Photoinduced Dynamics in 4H- Imidazole-Ruthenium Dyes. *J. Phys. Chem. C* **2012**, *116* (49), 25664−25676. https://doi.org/10.1021/jp309148u.

(155) Reichardt, C.; Sainuddin, T.; Wächtler, M.; Monro, S.; Kupfer, S.; Guthmuller, J.; Gräfe, S.; McFarland, S.; Dietzek, B. Influence of Protonation State on the Excited State Dynamics of a Photobiologically Active Ru (II) Dyad. *J. Phys. Chem. A* **2016**, *120* (32), 6379−6388. https://doi.org/10.1021/acs.jpca.6b05957.

(156) Natu, G.; Hasin, P.; Huang, Z.; Ji, Z.; He, M.; Wu, Y. Valence Band-Edge Engineering of Nickel Oxide Nanoparticles via Cobalt Doping for Application in P-Type Dye-Sensitized Solar Cells. *ACS Appl. Mater. Interfaces* **2012**, *4* (11), 5922−5929. https://doi.org/10.1021/am301565j.

(157) Isse, A. A.; Gennaro, A. Absolute Potential of the Standard Hydrogen Electrode and the Problem of Interconversion of Potentials in Different Solvents. *J. Phys. Chem. B* **2010**, *114* (23), 7894–7899. https://doi.org/10.1021/jp100402x.

(158) Schulz, M.; Karnahl, M.; Schwalbe, M.; Vos, J. G. The Role of the Bridging Ligand in Photocatalytic Supramolecular Assemblies for the Reduction of Protons and Carbon Dioxide. *Coord. Chem. Rev.* **2012**, *256* (15–16), 1682–1705. https://doi.org/10.1016/j.ccr.2012.02.016.

(159) Jahier, C.; Nlate, S. Dendritic Polyallyl and Polyferrocenyl Bipyridine Ligands : Synthesis , MALDI-TOF Characterization and Ruthenium (II) Complexation Studies. *J. Organomet. Chem.* **2009**, *694* (5), 637–642. https://doi.org/10.1016/j.jorganchem.2008.11.036.

(160) Hunsucker, S. W.; Watson, R. C.; Tissue, B. M. Characterization of Inorganic Coordination Complexes by Matrix-Assisted Laser Desorption/Ionization Mass Spectrometry. *Rapid Commun. Mass Spectrom.* **2001**, *15* (15), 1334–1340. https://doi.org/10.1002/rcm.377.

(161) Bodige, S.; Torres, A. S.; Maloney, D. J.; Tate, D.; Kinsel, G. R.; Walker, A. K.; MacDonnell, F. M. First-Generation Chiral Metallodendrimers: Stereoselective Synthesis of Rigid D 3-Symmetric Tetranuclear Ruthenium Complexes. *J. Am. Chem. Soc.* **1997**, *119* (43), 10364–10369. https://doi.org/10.1021/ja9720467.

(162) Ameline, D.; Diring, S; Farre, Y.; Pellegrin, Y.; Naponiello, G.; Blart, E.; Charrier, B.; Dini, D.; Jacquemin, D.; Odobel, F. Isoindigo Derivatives for Application in P-Type Dye Sensitized Solar Cells.

RSC Adv. **2015**, *8*, 85530–85539. https://doi.org/10.1039/C5RA11744E.

(163) Macdonald, T. J.; Mange, Y. J.; Dewi, M. R.; Islam, H. U.; Parkin, I. P.; Skinner, W. M.; Nann, T. CuInS2/ZnS Nanocrystals as Sensitisers for NiO Photocathodes. *J. Mater. Chem. A* **2015**, *3*, 13324–13331. https://doi.org/10.1039/C5TA01821H.

(164) Kim, K. S.; Winograd, N. X-RAY PHOTOELECTRON SPECTROSCOPIC STUDIES OF NICKEL-OXYGEN SURFACES USING OXYGEN AND ARGON ION-BOMBARDMENT. *Surf. Sci.* **1974**, *43* (2), 625–643. https://doi.org/10.1016/0039-6028(74)90281-7.

(165) Viornery, C.; Chevolot, Y.; Léonard, D.; Aronsson, B.-O.; Péchy, P.; Mathieu, H. J.; Descouts, P.; Grätzel, M. Surface Modification of Titanium with Phosphonic Acid To Improve Bone Bonding : Characterization by XPS and ToF-SIMS. *Langmuir* **2002**, *18* (7), 2582–2589. https://doi.org/10.1021/la010908i CCC:

(166) Adden, N.; Gamble, L. J.; Castner, D. G.; Hoffmann, A.; Gross, G.; Forschung, B. Phosphonic Acid Monolayers for Binding of Bioactive Molecules to Titanium Surfaces. *Langmuir* **2006**, *22* (19), 8197–8204. https://doi.org/10.1021/la060754c CCC:

(167) Tong, L.; Iwase, A.; Nattestad, A.; Bach, U.; Weidelener, M.; Götz, G.; Mishra, A.; Bäuerle, P.; Amal, R.; Wallace, G. G.; Mozer, A. Sustained Solar Hydrogen Generation Using a Dye-Sensitised NiO Photocathode/BiVO4 Tandem Photo-Electrochemical Device. *Energy Environ. Sci.* **2012**, *5*, 9472–9475. https://doi.org/10.1039/c2ee22866a.

(168) Hoogeveen, D. A.; Fournier, M.; Bonke, S. A.; Nattestad, A.; Mishra, A.; Bäuerle, P.; Spiccia, L.; Mozer, A. J.; Simonov, A. N. Origin of Photoelectrochemical Generation of Dihydrogen by a Dye- Sensitized Photocathode without an Intentionally Introduced Catalyst. *J. Phys. Chem. C* **2017**, *121* (46), 25836–25846. https://doi.org/10.1021/acs.jpcc.7b08067.

(169) Varma, S.; Castillo, C. E.; Stoll, T.; Fortage, J.; Blackman, A. G.; Molton, F.; Deronzier, A.; Collomb, M.-N. Efficient Photocatalytic Hydrogen Production in Water Using a Cobalt (III) Tetraaza-Macrocyclic Catalyst: Electrochemical Generation of the Low-Valent Co(I) Species and Its Reactivity toward Proton Reduction. *Phys. Chem. Chem. Phys.* **2013**, *15*, 17544–17552. https://doi.org/10.1039/c3cp52641k.

(170) Gueret, R.; Poulard, L.; Oshinowo, M.; Chauvin, J.; Dahmane, M.; Dupeyre, G.; Lainé, P. P.; Fortage, F.; Collomb, M.-N. Challenging the [Ru(Bpy)3]2+ Photosensitizer with a Triazatriangulenium Robust Organic Dye for Visible-Light-Driven Hydrogen Production in Water. *ACS Cat.* **2018**, *8* (5), 3792−3802. https://doi.org/10.1021/acscatal.7b04000.

(171) Krishnan, C. V.; Sutin, N. Homogeneous Catalysis of the Photoreduction of Water by Visible Light. 2. Mediation by a Tris(2,2'-Bipyridine)Ruthenium(II)-Cobalt(II) Bipyridine System. *J. Am. Chem. Soc.* **1981**, *103* (8), 2141–2142. https://doi.org/10.1021/ja00398a066.

(172) Föhlinger, J.; Maji, S.; Brown, A.; Mijangos, E.; Ott, S.; Hammarström, L. Self-Quenching and Slow Hole Injection May Limit the Efficiency in NiO-Based Dye-Sensitized Solar Cells. *J. Phys. Chem. C* **2018**, *122* (25), 13902–13910. https://doi.org/10.1021/acs.jpcc.8b01016.

(173) Tebo, A. G.; Quaranta, A.; Herrero, C.; Pecoraro, V. L.; Aukauloo, A. Intramolecular Photogeneration of a Tyrosine Radical in a Designed Protein. *ChemPhotoChem* **2017**, *1* (3), 89–92. https://doi.org/10.1002/cptc.201600044.

(174) Herrero, C.; Quaranta, A.; el Ghachtouli, S.; Vauzeilles, B.; Leibl, W.; Aukauloo, A. Carbon Dioxide Reduction via Light Activation of a Ruthenium–Ni(Cyclam) Complex. *Phys. Chem. Chem. Phys.* **2014**,

16 (24), 12067–12072. https://doi.org/10.1039/c3cp54946a.

(175) Herrero, C.; Quaranta, A.; Sircoglou, M.; Sénéchal-David, K.; Baron, A.; Marín, I. M.; Buron, C.; Baltaze, J.-P.; Leibl, W.; Aukauloo, A.; Banse, F. Successive Light Induced Two Electron Transfers in a Ru-Fe Supramolecular Assembly : From Ru-Fe(II)-OH2 to Ru-Fe(IV)-Oxo. *Chem. Sci.* **2015**, *6* (4), 2323–2327. https://doi.org/10.1039/C5SC00024F.

(176) Herrero, C.; Batchelor, L.; Baron, A.; Ghachtouli, S. El; Sheth, S.; Guillot, R.; Vauzeilles, B.; Sircoglou, M.; Mallah, T.; Leibl, W.; Aukauloo, A. Click Chemistry as a Convenient Tool for the Incorporation of a Ruthenium Chromophore and a Nickel – Salen Monomer into a Visible-Light-Active Assembly. *Eur. J. Inorg. Chem.* **2013**, *2013* (4), 494–499. https://doi.org/10.1002/ejic.201201161.

(177) Sheth, S.; Baron, A.; Herrero, C.; Vauzeilles, B.; Aukauloo, A.; Leibl, W. Light-Induced Tryptophan Radical Generation in a Click Modular Assembly of a Sensitiser-Tryptophan Residue. *Photochem. Photobiol. Sci.* **2013**, *12* (6), 1074–1078. https://doi.org/10.1039/c3pp50021g.

(178) Gray, C. L.; Xu, P.; Rothenberger, A. J.; Koehler, S. J.; Elacqua, E.; Milosavljevic, B. H.; Mallouk, T. E. Oligomeric Ruthenium Polypyridyl Dye for Improved Stability of Aqueous Photoelectrochemical Cells. *J. Phys. Chem. C* **2020**, *124* (6), 3542−3550. https://doi.org/10.1021/acs.jpcc.0c00493.

(179) Singh, W. M.; Baine, T.; Kudo, S.; Tian, S.; Ma, X. A. N.; Zhou, H.; Deyonker, N. J.; Pham, T. C.; Bollinger, J. C.; Baker, D. L.; Yan, B.; Webster, C. E.; Zhao, X. Electrocatalytic and Photocatalytic Hydrogen Production in Aqueous Solution by a Molecular Cobalt Complex. *Angew. Chem. Int. Ed.* **2012**, *51* (24), 1–5. https://doi.org/10.1002/anie.201200082.

(180) Sahara, G.; Kumagai, H.; Maeda, K.; Kaeffer, N.; Artero, V.; Higashi, M.; Abe, R.; Ishitani, O. Photoelectrochemical Reduction of CO2 Coupled to Water Oxidation Using a Photocathode with a Ru(II) − Re(I) Complex Photocatalyst and a CoOx/TaON Photoanode. *J. Am. Chem. Soc.* **2016**, *138* (42), 14152−14158. https://doi.org/10.1021/jacs.6b09212.

(181) Zee, D. Z.; Chantarojsiri, T.; Long, J. R.; Chang, C. J. Metal-Polypyridyl Catalysts for Electro- and Photochemical Reduction of Water to Hydrogen. *Acc. Chem. Res.* **2015**, *48* (7), 2027–2036. https://doi.org/10.1021/acs.accounts.5b00082.

(182) Roy, S.; Bacchi, M.; Berggren, G.; Artero, V. A Systematic Comparative Study of Hydrogen-Evolving Molecular Catalysts in Aqueous Solutions. *ChemSusChem* **2015**, *8* (21), 3632–3638. https://doi.org/10.1002/cssc.201501002.

(183) Karn, J. L.; Busch, D. H. Nickel (II) Complexes of the Tetradentate Macrocycle 2, 12-Dimethyl-3, 7, 11, 17-Tetraazabicyclo (11.3. 1) Heptadeca-1 (17), 2, 11, 13, 15-Pentaene. *Nature* **1966**, *211* (5045), 160–162. https://doi.org/doi.org/10.1038/211160a0.

(184) Long, K. M.; Busch, D. H. Cobalt (II) Complexes of the Quadridentate Macrocycle 2,12-Dimethyl-3,7,11,17-Tetraazabicyclo[11.3.1]Heptadeca-l(17),2,Ll,13,15-Pentaene. *Inorg. Chem.* **1970**, *9* (3), 505–512. https://doi.org/10.1021/ic50085a015.

(185) Ghosh, M.; Weyherm, T.; Wieghardt, K. Electronic Structure of the Members of the Electron Transfer Series [NiL] and [NiL(X)] Species Containing a Tetradentate, Redox-Noninnocent, Schiff Base Macrocyclic Ligand L : An Experimental and Density Functional Theoretical Study. *Dalt. Trans.* **2010**, *39*, 1996–2007. https://doi.org/10.1039/b916682c.

(186) Leung, C.; Chen, Y.; Yu, H.; Yiu, S.; Ko, C.; Lau, T. Electro and Photocatalytic Hydrogen Generation in

Acetonitrile and Aqueous Solutions by a Cobalt Macrocyclic Schiff-Base Complex. *Int. J. Hydrogen Energy* **2011**, *36* (18), 11640–11645. https://doi.org/10.1016/j.ijhydene.2011.06.062.

(187) Tinnemans, A. H. A.; Koster, T. P. M.; Thewissen, D. H. M. W.; Mackor, A. Tetraaza-Macrocyclic Cobalt(II) and Nickel(II) Complexes as Electron-Transfer Agents in the Photo(Electro)Chemical and Electrochemical Reduction of Carbon Dioxide. *Recl. Trav. Chim. Pays-Bas* **1984**, *103* (10), 288–295. https://doi.org/10.1002/recl.19841031004.

(188) Grau, S.; Schilling, M.; Moonshiram, D.; Benet-Buchholz, J.; Luber, S.; Llobet, A.; Gimbert-Suriñach, C. Electrochemically and Photochemically Induced Hydrogen Evolution Catalysis with Cobalt Tetraazamacrocycles Occurs Through Different Pathways. *ChemSusChem* **2020**, *13* (10), 2745–2752. https://doi.org/10.1002/cssc.202000283.

(189) Mccrory, C. C. L.; Uyeda, C.; Peters, J. C. Electrocatalytic Hydrogen Evolution in Acidic Water with Molecular Cobalt Tetraazamacrocycles. *J. Am. Chem. Soc.* **2012**, *134* (6), 3164−3170. https://doi.org/10.1021/ja210661k.

(190) Gueret, R.; Castillo, C. E.; Rebarz, M.; Thomas, F.; Hargrove, A.; Pécaut, J.; Sliwa, M.; Fortage, J.; Collomb, M. Cobalt (III) Tetraaza-Macrocyclic Complexes as Efficient Catalyst for Photoinduced Hydrogen Production in Water : Theoretical Investigation of the Electronic Structure of the Reduced Species and Mechanistic Insight. *J. Photochem. Photobiol. B Biol.* **2015**, *152*, 82–94. https://doi.org/10.1016/j.jphotobiol.2015.04.010.

(191) Nie, C.; Ni, W.; Gong, L.; Jiang, J.; Wang, J.; Wang, M. Charge Transfer Dynamics and Catalytic Performance of a Covalently Linked Hybrid Assembly Comprising a Functionalized Cobalt Tetraazamacrocyclic Catalyst and CuInS2/ZnS Quantum Dots for Photochemical Hydrogen Production. *J. Mater. Chem. A* **2019**, *7*, 27432–27440. https://doi.org/10.1039/c9ta10479h.

(192) Bold, S.; Massin, J.; Giannoudis, E.; Koepf, M.; Artero, V.; Dietzek, B.; Chavarot-Kerlidou, M. A Cobalt Tetraazamacrocyclic Catalyst as a Game Changer for Hydrogen Production at Dye- Sensitized NiO Photocathodes. *submitted* **2020**, 1–44.

(193) Zabarska, N.; Stumper, A.; Rau, S. CuAAC Click Reactions for the Design of Multifunctional Luminescent Ruthenium Complexes. **2016**, No. 3, 2338–2351. https://doi.org/10.1039/c5dt04599a.

(194) Müller, S.; Sanders, D. A.; Di Antonio, M.; Matsis, S.; Riou, J.-F.; Rodriguez, R.; Balasubramanian, S. Pyridostatin Analogues Promote Telomere Dysfunction and Long-Term Growth Inhibition in Human Cancer Cells. *Org. Biomol. Chem.* **2012**, *10* (32), 6537–6546. https://doi.org/10.1039/c2ob25830g.

(195) Dumont, A.; Jacques, V.; Desreux, J. F. New Synthons for the Synthesis of Lanthanide Containing Macrocyclic Schiff Bases Featuring Substituents Available for Tethering. *Tetrahedron* **2000**, *56* (14), 2043–2052. https://doi.org/10.1016/S0040-4020(00)00104-6.

(196) Martin, R.; Romea, P.; Tey, C.; Urpi, F. . V. J. Simple and Efficient Preparation of Ketones from Morpholine Amides. *Synlett. 12*, 1414–1416. https://doi.org/10.1055/s-1997-1050.

(197) Huang, B.; Prantil, M. A.; Gustafson, T. L.; Parquette, J. R. The Effect of Global Compaction on the Local Secondary Structure of Folded Dendrimers. *J. Am. Chem. Soc.* **2003**, *125* (47), 14518–14530. https://doi.org/10.1021/ja037895a CCC:

(198) Nyffeler, P. T.; Liang, C.; Koeller, K. M.; Wong, C. The Chemistry of Amine - Azide Interconversion : Catalytic Diazotransfer and Regioselective Azide Reduction. *J. Am. Chem. Soc.* **2002**, *124* (36), 10773–

10778. https://doi.org/10.1021/ja0264605.

(199) Amthor, S.; Braun, H.; Gröne, J.; Nauroozi, D.; Jacob, T.; Rau, S. Tailored Protective Groups for Surface Immobilization of Ruthenium Dyes. *Dalt. Trans.* **2020**, *49*, 3735–3742. https://doi.org/10.1039/c9dt03591e.

(200) Britton, T. S.; Robinson, R. A. CXCVIII.-Universal Buffer Solutions and the Dissociation Constant of Veronal. *J. Chem. Soc.* **1931**, 1456–1462. https://doi.org/10.1039/JR9310001456.

(201) Castillo, C. E.; Gennari, M.; Stoll, T.; Fortage, J.; Deronzier, A.; Collomb, M.-N.; Sandroni, M.; Légalité, F.; Blart, E.; Pellegrin, Y.; Delacote, C.; Boujtita, M.; Odobel, F.; Rannou, P.; Sadki, S. Visible Light-Driven Electron Transfer from a Dye-Sensitized p - Type NiO Photocathode to a Molecular Catalyst in Solution: Toward NiO- Based Photoelectrochemical Devices for Solar Hydrogen Production. *J. Phys. Chem. C* **2015**, *119* (11), 5806−5818. https://doi.org/10.1021/jp511469f.

(202) Davis, S. J.; Caldeira, K.; Matthews, H. D. Future CO2 Emissions and Climate Change from Existing Energy Infrastructure. *Science (80-.).* **2010**, *329* (5997), 1330–1333. https://doi.org/10.1126/science.1188566.

(203) Nielsen, D. U.; Hu, X.; Daasbjerg, K.; Skrydstrup, T. Chemically and Electrochemically Catalysed Conversion of CO2 to CO with Follow-up Utilization to Value-Added Chemicals. *Nat. Catal.* **2018**, *1*, 244–254. https://doi.org/10.1038/s41929-018-0051-3.

(204) Lehn, J.-M.; Ziessel, R. Photochemical Generation of Carbon Monoxide and Hydrogen by Reduction of Carbon Dioxide and Water under Visible Light Irradiation. *PNAS* **1982**, *79* (2), 701–704. https://doi.org/10.1073/pnas.79.2.701.

(205) Howecker, J.; Lehn, J. M.; Ziessel, R. Electrocatalytic Reduction of Carbon Dioxide Mediated by Re(Bipy)(CO)3I (Bipy = 2,2'-Bipyridine). *J. CHEM. SOC., CHEM. COMMUN.* **1984**, 328–330.

(206) Takeda, H.; Cometto, C.; Ishitani, O.; Robert, M. Electrons, Photons, Protons and Earth-Abundant Metal Complexes for Molecular Catalysis of CO2 Reduction. *ACS Catal.* **2017**, *7* (1), 70–88. https://doi.org/10.1021/acscatal.6b02181.

(207) Zhang, S.; Fan, Q.; Xia, R.; Meyer, T. J. CO2 Reduction : From Homogeneous to Heterogeneous Electrocatalysis. *Acc. Chem. Res.* **2020**, *53* (1), 255–264. https://doi.org/10.1021/acs.accounts.9b00496.

(208) Elgrishi, N.; Chambers, M. B.; Wang, X.; Fontecave, M. Molecular Polypyridine-Based Metal Complexes as Catalysts for the Reduction of CO2. *Chem. Soc. Rev.* **2017**, *46*, 761–796. https://doi.org/10.1039/c5cs00391a.

(209) Khadhraoui, A.; Gotico, P.; Boitrel, B.; Leibl, W.; Halime, Z.; Aukauloo, A. Local Ionic Liquid Environment at a Modified Iron Porphyrin Catalyst Enhances the Electrocatalytic Performance of CO2 to CO Reduction in Water. *Chem. Commun.* **2018**, *54* (82), 11630–11633. https://doi.org/10.1039/c8cc06475j.

(210) Gotico, P.; Halime, Z.; Aukauloo, A. Recent Advances in Metalloporphyrin-Based Catalyst Design towards Carbon Dioxide Reduction: From Bio-Inspired Second Coordination Sphere Modifications to Hierarchical Architectures. *Dalt. Trans.* **2020**, *49* (8), 2381–2396. https://doi.org/10.1039/c9dt04709c.

(211) Boutin, E.; Merakeb, L.; Ma, B.; Boudy, B.; Wang, M.; Bonin, J.; Anxolabéhère-Mallart, E.; Robert, M. Molecular Catalysis of CO2 Reduction: Recent Advances and Perspectives in Electrochemical and Light-Driven Processes with Selected Fe, Ni and Co Aza Macrocyclic and Polypyridine Complexes. *Chem. Soc.*

Rev. **2020**, *49* (16), 5772–5809. https://doi.org/10.1039/d0cs00218f.

(212) Takeda, H.; Ishitani, O. Development of Efficient Photocatalytic Systems for CO2 Reduction Using Mononuclear and Multinuclear Metal Complexes Based on Mechanistic Studies. *Coord. Chem. Rev.* **2010**, *254* (3–4), 346–354. https://doi.org/10.1016/j.ccr.2009.09.030.

(213) Windle, C. D.; Perutz, R. N. Advances in Molecular Photocatalytic and Electrocatalytic CO2 Reduction. *Coord. Chem. Rev.* **2012**, *256* (21–22), 2562–2570. https://doi.org/10.1016/j.ccr.2012.03.010.

(214) Tian, H. Molecular Catalyst Immobilized Photocathodes for Water / Proton and Carbon Dioxide Reduction. *ChemSusChem* **2015**, *8* (22), 3746–3759. https://doi.org/10.1002/cssc.201500983.

(215) Bachmeier, A.; Hall, S.; Ragsdale, S. W.; Armstrong, F. A. Selective Visible-Light-Driven CO2 Reduction on a P-Type Dye- Sensitized NiO Photocathode. *J. Am. Chem. Soc.* **2014**, *136* (39), 13518−13521. https://doi.org/10.1021/ja506998b.

(216) Kou, Y.; Nakatani, S.; Sunagawa, G.; Tachikawa, Y.; Masui, D.; Shimada, T.; Takagi, S.; Tryk, D. A.; Nabetani, Y.; Tachibana, H.; Inoue, H. Visible Light-Induced Reduction of Carbon Dioxide Sensitized by a Porphyrin – Rhenium Dyad Metal Complex on p -Type Semiconducting NiO as the Reduction Terminal End of an Artificial Photosynthetic System. *J. Catal.* **2014**, *310*, 57–66. https://doi.org/10.1016/j.jcat.2013.03.025.

(217) Sahara, G.; Abe, R.; Higashi, M.; Morikawa, T.; Maeda, K.; Ueda, Y.; Ishitani, O. Photoelectrochemical CO2 Reduction Using a Ru(II)– Re(I) Multinuclear Metal Complex on a p-Type Semiconducting NiO Electrode. *Chem. Commun.* **2015**, *51* (53), 10722–10725. https://doi.org/10.1039/C5CC02403J.

(218) Kamata, R.; Kumagai, H.; Yamazaki, Y.; Sahara, G.; Ishitani, O. Photoelectrochemical CO2 Reduction Using a Ru(II) − Re(I) Supramolecular Photocatalyst Connected to a Vinyl Polymer on a NiO Electrode. *ACS Appl. Mater. Interfaces* **2018**, *11* (6), 5632–5641. https://doi.org/10.1021/acsami.8b05495.

(219) Li, T.-T.; Shan, B.; Meyer, T. J. Stable Molecular Photocathode for Solar-Driven CO2 Reduction in Aqueous Solutions. *ACS Energy Lett.* **2019**, *4* (3), 629–636. https://doi.org/10.1021/acsenergylett.8b02512.

(220) Kumagai, H.; Sahara, G.; Maeda, K.; Higashi, M.; Abe, R.; Ishitani, O. Hybrid Photocathode Consisting of a CuGaO2 P-Type Semiconductor and a Ru(II)–Re(I) Supramolecular Photocatalyst: Non-Biased Visible-Light-Driven CO2 Reduction with Water Oxidation. *Chem. Sci.* **2017**, *8*, 4242–4249. https://doi.org/10.1039/C7SC00940B.

(221) Wang, D.; Wang, Y.; Brady, M. D.; Sheridan, M. V; Sherman, B. D.; Farnum, B. H.; Liu, Y.; Marquard, S. L.; Meyer, G. J.; Dares, J.; Meyer, T. J. A Donor-Chromophore-Catalyst Assembly for Solar CO2 Reduction. *Chem. Sci.* **2019**, *10* (4), 4436–4444. https://doi.org/10.1039/C8SC03316A.

(222) Leung, J. J.; Warnan, J.; Ly, K. H.; Heidary, N.; Nam, D. H.; Kuehnel, M. F.; Reisner, E. Solar-Driven Reduction of Aqueous CO2 with a Cobalt Bis(Terpyridine)-Based Photocathode. *Nat. Catal.* **2019**, *2*, 354–365. https://doi.org/10.1038/s41929-019-0254-2.

(223) Elgrishi, N.; Chambers, M. B.; Artero, V.; Fontecave, M. Terpyridine Complexes of First Row Transition Metals and Electrochemical Reduction of CO2 to CO. *Phys. Chem. Chem. Phys.* **2014**, *16*, 13635–13644. https://doi.org/10.1039/c4cp00451e.

(224) Pati, P. B.; Wang, R.; Boutin, E.; Diring, S.; Jobic, S.; Barreau, N.; Odobel, F.; Robert, M. Photocathode Functionalized with a Molecular Cobalt Catalyst for Selective Carbon Dioxide Reduction in Water. *Nat.*

Commun. **2020**, *11* (1), 1–9. https://doi.org/10.1038/s41467-020-17125-4.

(225) Shan, B.; Vanka, S.; Li, T.-T.; Troian-Gautier, L.; Brennaman, M. K.; Mi, Z.; Meyer, T. J. Binary Molecular-Semiconductor p–n Junctions for Photoelectrocatalytic CO2 Reduction. *Nat. Energy* **2019**, *4*, 290–299. https://doi.org/10.1038/s41560-019-0345-y.

(226) Lacy, D. C.; Mccrory, C. C. L.; Peters, J. C. Studies of Cobalt-Mediated Electrocatalytic CO2 Reduction Using a Redox-Active Ligand. *Inorg. Chem.* **2014**, *53* (10), 4980−4988. https://doi.org/10.1021/ic403122j.

(227) Zhang, M.; El-Roz, M.; Frei, H.; Mendoza-Cortes, J. L.; Head-Gordon, M.; Lacy, D. C.; Peters, J. C. Visible Light Sensitized CO2 Activation by the Tetraaza [Co(II)N4H(MeCN)]2+ Complex Investigated by FT-IR Spectroscopy and DFT Calculations. *J. Phys. Chem. B* **2015**, *119* (3), 4645−4654. https://doi.org/10.1021/jp5127738.

(228) Sheng, H.; Frei, H. Direct Observation by Rapid-Scan FT-IR Spectroscopy of Two- Electron-Reduced Intermediate of Tetraaza Catalyst [Co(II)N4H(MeCN)]2+ Converting CO2 to CO. *J. Am. Chem. Soc.* **2016**, *138* (31), 9959−9967. https://doi.org/10.1021/jacs.6b05248.

(229) Wang, Y.; Gonell, S.; Mathiyazhagan, U. R.; Liu, Y.; Wang, D.; Miller, A. J. M.; Meyer, T. J. Simultaneous Electrosynthesis of Syngas and an Aldehyde from CO2 and an Alcohol by Molecular Electrocatalysis. *ACS Appl. Energy Mater.* **2019**, *2* (1), 97–101. https://doi.org/10.1021/acsaem.8b01616.

Experimental part

I. Chemical products and solvents

All reagents were purchased from Sigma Aldrich or Strem and used as obtained unless otherwise stated. Solvents were dried from appropriate drying agents (sodium wire and benzophenone for THF, calcium hydride for CH_2Cl_2) and freshly distilled under argon before use. Reagent-grade solvents were used without further purification. The 4,4´-bis(diethylphosphonomethyl)-2,2´-bipyridine (4,4´-$(CH_2PO_3Et_2)_2$-bpy) and *N2,N2'*-2-azidopropanediylbis(2,3-butadione-2-imine-3-oxime) ligands were custom-synthesized by the companies Oribase Pharma and Provence Technologies, respectively.

II. Characterization methods and equipment

1) Column chromatography

Two techniques were chosen for carrying out separative chromatography. In a first case, these were performed manually on 60 M silica gel with a grain size of 0.04-0.063 nm (Macherey-Nagel). In a second case, the separative chromatography is assisted by a Puriflash 450 device (Interchim), with preconditioned silica cartridges (Interchim, Puriflash Silica HP 15 µm), after liquid deposition of the product.

2) UV-Vis absorption spectroscopy

UV–vis absorption spectra were recorded either on a Shimadzu UV-1800 spectrometer or on an Agilent Cary 60 UV–vis spectrometer in 1 cm optical light path quartz cuvettes**.**

3) Nuclear magnetic resonance spectroscopy (NMR)

^{1}H and ^{13}C NMR spectra were recorded at 298 K in 5 mm o.d. tubes either on a Bruker AC 300 spectrometer equipped with a QNP probehead operating at 300.0 MHz for ^{1}H and 75.5 MHz for ^{13}C or on a Bruker Avance III spectrometer equipped with a Prodigy cryoprobe and operating at 500.0 MHz for ^{1}H and 126 MHz for ^{13}C. The deuterated solvents are indicated in all cases and the chemical sifts are given in ppm and referenced to the solvent residual peak. The obtained spectra were treated using the software TOPSPIN (BRUKER). The multiplicity of the peaks is as follows: s (singlet), d (doublet), t (triplet), m (multiplet).

4) Electrospray ionization mass spectrometry (ESI-MS)

Electrospray ionization mass spectrometric measurements were carried out on a Thermoquest Finnigan LCQ spectrometer in positive and negative mode by Colette Lebrun and Jacques Pécaut at IRIG/SyMMES/CIBEST/CEA Grenoble.

5) High resolution mass spectrometry (HRMS)

Accurate mass measurements (HRMS) were performed on a Bruker maXis mass spectrometer by the "Fédération de Recherche" ICOA/CBM (FR 2708) platform.

6) Elemental analysis

Elemental analysis was carried out on a Thermofisher Scientific “Flash 2000” by the “Plateforme d’analyse pour la chimie” (GDS 3648, Strasbourg) for the analysis of C, H and N.

7) X-ray Photoelectron Spectroscopy (XPS)

XPS analysis was carried out with a Versa Probe II spectrometer (ULVAC-PHI) equipped with a monochromated Al Ka source (hn ¼ 1486.6 eV). The core level peaks were recorded with a constant pass energy of 23.3 eV. The XPS spectra were fitted with CasaXPS 2.3.15 software using Shirley background and a combination of Gaussian (70%) and Lorentzian (30%) distributions. Binding energies are referenced with respect to the adventitious carbon (C 1s BE ¼ 284.6 eV). The measurements were performed by Dr. Dmitry Aldakov at IRG/SyMMES/STEP/CEA Grenoble.

8) Time-of-flight secondary ion mass spectrometry (ToF-SIMS)

ToF-SIMS measurements were recorded on a TRIFT III ToF-SIMS instrument from Physical Electronics operated with a pulsed 22 keV Au+ ion gun (ion current of 2 nA) rastered over a 300 μm × 300 μm area. An electron gun was operated in pulsed mode at low electron energy for charge compensation. The ion dose was kept below the static conditions limit. Data were analyzed using the WinCadenceTM software. Mass calibration was performed on hydrocarbon secondary ions. All measurements were carried out by Corinne Gablin and Pr. Leonard Didier at the Institute of Analytical Science at the University of Lyon.

9) Matrix-assisted laser desorption/ionization time of flight mass spectrometry (MALDI-ToF)

MALDI-TOF spectra were obtained on a time-of-flight Microflex mass spectrometer (Bruker) equipped with a 337 nm nitrogen laser and pulsed delay source excitation by Christine Saint-Pierre and Pr. Didier Gasparutto at IRIG/SyMMES/CREAB/CEA Grenoble.

10) Photolysis experiments

A 3.6 10^{-5} M solution of the dye-catalyst assembly (either **RuP_4^{OH}-Co** or **Dyad 2**) in dry, degassed CH_3CN/TEOA (90:10 v/v) mixture was prepared in a H_2O/O_2-free glovebox and transferred in a quartz cuvette (1 mm optical light path). Irradiation was carried out outside the glovebox with a Newport 300 W ozone-free Xe lamp at 280 W equipped with a water-filled Spectra-Physics 6123NS liquid filter to eliminate infrared radiation ($\lambda > 800$ nm) and a 400 nm longpass filter (Spectra-Physics 59472). The power density was measured using a Newport PM1918-R power-meter and adjusted to 65 $mW.cm^{-2}$ (equivalent to one sun irradiation) using appropriate neutral density filters. The UV-Vis absorption spectra were recorded at time intervals.

11) Electrochemistry in solution

Electrochemical analysis was performed using a BioLogic SP300 potentiostat controlled via EC-Lab V10 software. Electrochemical experiments were recorded in a three-electrode cell combining a glassy carbon as working electrode, a platinum wire counter electrode, and a custom-made Ag/AgCl reference electrode (separated from the solution by a Vycor frit). Typical measurements were carried out in argon-purged acetonitrile solution (0.1 M n-Bu_4NBF_4 as supporting electrolyte) of 1 mM of each compound. Ferrocene was added at the end of every measurement as an internal reference.

12) Spectro-electrochemistry

UV-Vis-SEC measurements were performed in a three-electrode setup in a H_2O/O_2-free glovebox, using a patterned "Honeycomb" Spectroelectrochemical Cell Kit (AKSTCKIT3) purchased by Pine Instrument Company. The cell kit includes 1 mm quartz cuvette, a platinum honeycomb auxiliary electrode, a gold honeycomb working electrode and a Ag wire as reference electrode. A BioLogic VSP-300 potentiostat connected to the glovebox was used. The spectra were recorded with an optical fiber external-sampler connected to the UV-Vis

spectrometer. 0.1 M tetrabutylammonium tetrafluoroborate ($TBABF_4$) in dry acetonitrile was used as electrolyte solution. Initially, a cyclovoltammetry (CV) was carried out to determine the redox potentials. Then, potentials were applied in a chronoamperometry (CA) and UV-Vis spectra were recorded, until equilibrium was reached.

13) NiO film preparation

FTO glass substrates (Solems, TEC 7, 7Ω resistance) were used as TCO with dimensions of 40 × 20 × 3.1 mm. A cleaning protocol for the substrates including Gigapur, deionized water and ethanol was adopted. After drying with compressed-air, the glasses were treated with UV-Vis ozone cleaning to remove organic impurities. $NiCl_2$ (1.5 g) and F108 triblock co-polymer (1.5 g) were mixed in milli-Q water (4.5 ml) and ethanol (11.2 ml). The resulting viscous solution was sonicated overnight. The following day, the mixture was centrifuged for 30 minutes at 5000 rpm and filtrated. The supernatant solution was spin-coated for 60 seconds at 5000 rpm onto the conductive part of 12 FTO glasses. Sintering in the air in a flat oven was the last step (temperature increase within 30 minutes to 450°C, where stabilizes for 30 minutes). To increase the thickness, the procedure was repeated four times and light brown NiO films with 4 layers were prepared.

14) Photoelectrochemical measurements

The photoelectrochemical measurements were carried out in a home-made two compartement three-electrode cell with a sensitized NiO film as working electrode, a titanium wire as auxiliary electrode and a Ag/AgCl reference electrode. The reference electrode was made of a Ag wire dipped into a 3 M aqueous KCl solution and separated from the electrolyte by a Vycor frit. The auxiliary electrode was also separated from the main compartment of the cell by a Vycor frit. Irradiation was performed using a Newport 300 W ozone-free Xe lamp at 280 W equipped with a water-filled Spectra-Physics 6123NS liquid filter to eliminate infrared radiation ($\lambda > 800$ nm) and either a 400 nm longpass filter (Spectra-Physics 59472) or AM 1.5G filter (2×2 IN^2 81094 oriel instruments). The power density was measured at a specific distance from the lamp, using a Newport PM1918-R power-meter. When the 400 nm longpass filter was used, the irradiation power was adjusted to 65 $mW.cm^{-2}$ (equivalent to one sun irradiation) using appropriate neutral density filters. When the AM 1.5G filter was used, the irradiation power was adjusted to 1 sun without having fixed the water-filled liquid filter (this corresponds to 70 $mW.cm^{-2}$ when the water-filled liquid filter is present).

15) Desorption and dyad and dye loading quantification

Sensitized NiO films were soaked in 1 M methanolic solution of phenylphosphonic acid (5 ml) for 4 hours to desorb immobilized compounds. Afterwards, UV-Vis spectra of the desorption solutions were measured. From the maximum absorption at the MLCT band, the concentration of the dye or the dyad were determined using the molar extinction coefficient at the MLCT band (recorded in 1 M methanolic solution of phenylphosphonic acid) through the Beer-Lambert law ($A = \varepsilon \times d \times C$, where $d = 1$ cm). Then, the moles of the compounds in each solution were calculated. Finally, using the surface area of each film, the dye and dyad loadings were estimated.

16) Quantification of H_2 and CO

The amount of H_2 and CO were measured in the headspace by sampling aliquots (50 µl) in a Perkin Elmer Clarus 580 gas chromatograph equipped with a molecular sieve 5 Å column (30 m – 0.53 mm) and a TCD and FID detector respectively. Additionally, the amount of hydrogen dissolved in solution was determined by a Unisense H_2 microsensor. The zero value for the microsensor was measured in the assembled cell prior to irradiation. Calibration curves with known amounts of H_2 and CO enabled us to convert the signal of the GC and the probe in amount of produced H_2 and CO.

17) Quantification of HCOOH

A 883 Basic IC plus enabling chemical suppression was used for the determination of formate in the solution. The ion chromatograph is equipped with the Metrohm Suppressor Module Rotor A. The instrument contains a high-pressure pump, an inline filter, a pulsation absorber, an injection valve, a peristatic pump, a conductivity detector and a separation column. For the elution of anions, $NaHCO_3$ and Na_2CO_3 were used and for the suppression H_2SO_4. The instrument is operated with the MagIC Net Basic software. For the quantification of formate, we diluted 500 µl of the electrolyte in 5 ml milli-Q water before every injection. A calibration curve allowed us to convert the area of the peak to a concentration of formate.

III. Synthesis

2-(4-ethynylphenyl)-1H-imidazo[4,5-f][1,10]phénanthroline (EPIP)

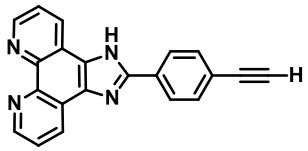

A solution of phendione (1.0 g, 4.7 mmol), 4-(ethynyl)benzaldehyde (611 mg, 4.7 mmol) and NH_4OAc (7.5 g, 94 mmol) in glacial acetic acid (100 ml) were refluxed (around 120 ºC) for 4 hours. After cooling down to room temperature, the reaction mixture was neutralized with an aqueous solution of NH_4OH (150 ml). The resulting yellow precipitate was filtered and thoroughly washed with water, diethyl ether and finally dried under vacuum. Yield 90% (1.35 g). ^{1}H-NMR (300 MHz, DMSO d6): δ (ppm) 9.03 (dd, J = 4.3, 1.6 Hz, 2H), 9.0 (br, 2H), 8.22 (d, J = 8.5 Hz, 2H), 7.80 (dd, J = 8.2, 4.4 Hz, 2H), 7.70 (d, J = 8.5 Hz, 2H), 3.71 (s, 1H). ^{13}C-NMR (75 MHz, DMSO d6): δ (ppm) 149.91, 143.71, 130.47, 122.45, 121.64, 117.96, 147.82, 132.34, 129.62, 126.27, 123.25, 83.22, 82.31. ESI-MS: m/z 321.3 $[M+H]^+$.

$[Ru(bpy)_2(TMS\text{-}EPIP)](PF6)_2$ (Ru-TMS-EPIP)

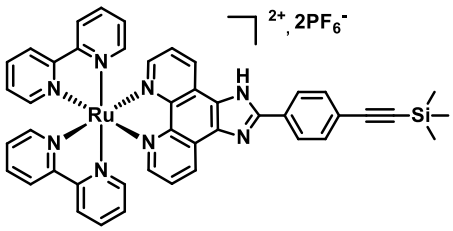

In a round bottom flask, $Ru(bpy)_2Cl_2 \cdot 2H_2O$ (146 mg, 0.28 mmol) and TMS-EPIP (122 mg, 0.31 mmol) were dissolved in a solvent mixture of EtOH and H_2O (1:1, 50 ml) under argon. The reaction mixture was refluxed (80°C) under argon protected from light for 6 hours. The organic solvents were evaporated and the desired compound was precipitated by dropwise addition of 5ml NH_4PF_6 -saturated aqueous solution. The orange precipitate was filtered, washed with water and dried under vacuum. The crude product was purified by column chromatography on silica gel (gradient elution MeCN/0.4 M aqueous KNO_3, from 98:2 to 90:10). The fractions were concentrated and the product was precipitated by dropwise addition of a saturated NH_4PF_6 aqueous solution. The orange precipitate was filtered, washed with water and dried under vacuum. Yield: 60% (180 mg). ^{1}H-NMR (300 MHz, CD_3CN): δ (ppm) 8.99 (d, J = 8.1 Hz, 1H), 8.78 (d, J = 8.1 Hz, 1H), 8.41 (dd, J = 8.2 Hz, 4H), 8.16 (d, J = 8.7 Hz, 2H), 8.00 (t, J = 8.2 Hz, 2H), 7.94 – 7.84 (m, 4H), 7.75 (d, J = 5.7 Hz, 2H), 7.68 (dd, J = 5.1, 5.0 Hz, 2H), 7.59 (d, J = 8.7 Hz, 2H), 7.49 (t, J = 6.2 Hz, 2H), 7.35 (t, J = 5.8 Hz, 2H), 7.11 (t, J = 6.8 Hz, 2H), 0.18 (s, 9H). ESI-MS: m/z 403.1 $[M–2PF_6]^{2+}$, 950.9 $[M–PF_6]^+$. No titrations measurements were performed for the identification of the protonation state of the imidazole unit.

[Ru(bpy)$_2$(EPIP)](PF6)$_2$ (Ru-EPIP)

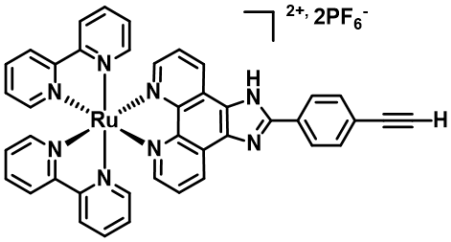

Ru-TMS-EPIP (160 mg, 0.15 mmol) was dissolved in 5 ml THF. K_2CO_3 (20 mg, 0.15) in 5 ml MeOH was added dropwise and the reaction mixture was stirred at room temperature for 4 hours. The crude product was purified by column chromatography on silica gel (gradient elution of MeCN/0.4 M aqueous KNO_3, from 98:2 to 90:10). The fractions were concentrated and the product was precipitated by dropwise addition of a saturated KPF_6 aqueous solution. The orange precipitate was filtered, washed with water and dried under vacuum. Yield: 87% (130 mg). ^{1}H-NMR (300 MHz, CD_3CN): δ (ppm) 8.94 (d, J = 8.3 Hz, 2H), 8.50 - 8.44 (m, 4H), 8.32 (d, J = 8.1 Hz, 2H), 8.05 (t, J = 8.3 Hz, 2H), 7.90 (t, J = 7.9 Hz, 2H), 7.81 (d, J = 7.7 Hz, 2H), 7.78 (d, J = 4.5 Hz, 2H), 7.60 – 7.55 (m, 4H), 7.48 (d, J = 8.2 Hz, 2H), 7.40 (t, J = 6.7 Hz, 2H), 7.18 (t, J = 6.3 Hz, 2H), 3.60 (s, 1H). ESI-MS: m/z 367.0 $[M–2PF_6]^{2+}$, 879.0 $[M–PF_6]^{+}$. No titrations measurements were performed for the identification of the protonation state of the imidazole unit.

[Ru(4,4´-(CH$_2$PO$_3$Et$_2$)$_2$-bpy)$_2$(TMS-EPIP)](PF$_6$)$_2$ (RuP$_4^{OEt}$-TMS-EPIP)

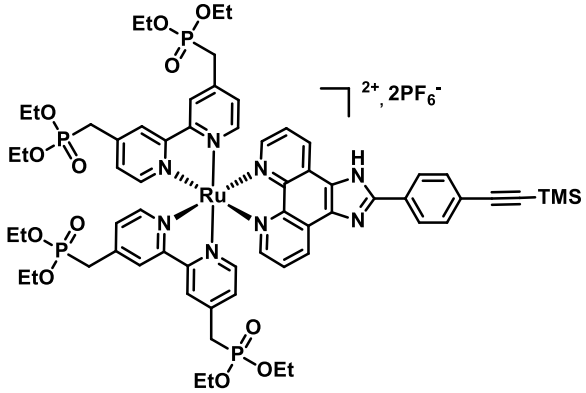

A solution of commercially available $Ru(dmso)_4Cl_2$ (105 mg, 0.22 mmol) and 4,4´-$(CH_2PO_3Et_2)_2$-bpy (200 mg, 0.44 mmol) in methanol (25 ml) was refluxed overnight under argon. Removal of the solvent and drying under vacuum yielded the dark-red highly hygroscopic intermediate [Ru(4,4´-$(CH_2PO_3Et_2)_2$-bpy)$_2$Cl$_x$(DMSO)$_{2–x}$]Cl$_{2–x}$. A solution of crude [Ru(4,4´-$(CH_2PO_3Et_2)_2$-bpy)$_2$Cl$_x$(DMSO)$_{2–x}$]Cl$_{2–x}$ (1 equivalent, using an average molecular weight of 1164) and TMS-EPIP (75 mg, 0.33 mmol) in a water/ethanol (1:3) mixture was refluxed overnight. After cooling down to room temperature, 5 ml of a saturated NH_4PF_6 aqueous solution was added to the reaction mixture. Extraction with dichloromethane and removal of the organic solvent yield a crude reddish solid. After purification by column chromatography on silica gel with gradient elution MeCN/0.4 M aqueous KNO_3 (from 98:2 to 90:10) and removal of volatiles, dropwise addition of a saturated NH_4PF_6 aqueous solution and extraction with dichloromethane, gave an orange powder. Yield: 20% (75 mg). ^{1}H NMR (300 MHz, CD_3CN): δ (ppm) 9.04 – 8.91 (m, 2H), 8.43 (d, *J* = 14.7 Hz, 4H), 8.26 (d, *J* = 8.1 Hz,

2H), 7.99 (d, *J* = 4.2 Hz, 2H), 7.79 – 7.66 (m, 4H), 7.50 (d, *J* = 5.7 Hz, 2H), 7.40 (dd, *J* = 5.4, 1.8 Hz, 4H), 7.15 (d, *J* = 5.7 Hz, 2H), 4.10 – 3.89 (m, 16H), 3.43 (d, J = 22.5 Hz, 4H), 3.33 (d, J = 22.5 Hz, 4H), 1.23 – 1.05 (m, 24H), 0.28 (s, 9H). ^{13}C-NMR (75 MHz, CD_3CN): δ (ppm): 157.7, 157.5, 152.6, 152.4, 151.1, 146.8, 145.9, 133.4, 131.5, 129.6, 127.6, 127.0, 126.1, 125.7, 105.1, 97.6, 63.6, 34.3, 32.5, 16.6, 1.4. ESI-MS: m/z 703.4 $[M\text{-}2PF_6]^{2+}$, 1405.4 $[M]^+$, 1551.2 $[M\text{-}PF_6]^+$. HR-MS (ESI^+): m/z calcd for $C_{64}H_{80}N_8O_{12}P_4RuSi$ 703.1824; found 703.1831 $[M\text{-}H\text{-}2PF_6]^{2+}$. E.A.: calcd for $C_{64}H_{80}N_8O_{12}P_6F_{12}RuSi$ + 0.2 NH_4PF_6 + 0.5 H_2O: C, 44.23; H, 4.74; N, 6.61; found: C, 44.26; H, 4.82; N, 6.53. No titrations measurements were performed for the identification of the protonation state of the imidazole unit.

[Ru(4,4´-($CH_2PO_3Et_2$)$_2$-bpy)$_2$(EPIP)](PF_6)$_2$ (RuP_4^{OEt}-EPIP)

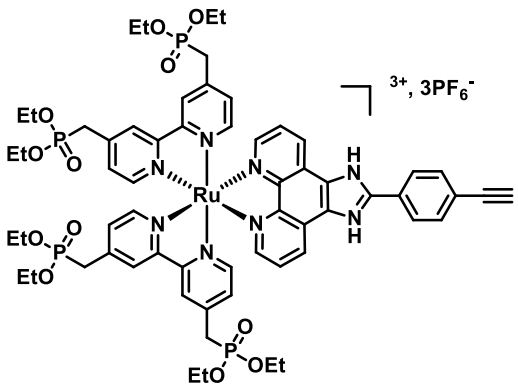

A solution of commercially available $Ru(dmso)_4Cl_2$ (420 mg, 0.88 mmol) and 4,4´-($CH_2PO_3Et_2$)$_2$-bpy (800 mg, 1.75 mmol) in methanol (100 ml) was refluxed overnight under argon. Removal of the solvent and drying under vacuum yielded the dark-red highly hygroscopic intermediate [Ru(4,4´-($CH_2PO_3Et_2$)$_2$-bpy)$_2$$Cl_x$$(DMSO)_{2-x}$]$Cl_{2-x}$. A solution of crude [Ru(4,4´-($CH_2PO_3Et_2$)$_2$-bpy)$_2$$Cl_x$$(DMSO)_{2-x}$]$Cl_{2-x}$ (1 equivalent, 600 mg, 0.52 mmol, using an average molecular weight of 1164) and EPIP (260 mg, 0.8 mmol) in a water/ethanol (1:3) mixture was refluxed overnight. After cooling down to room temperature, 5 ml of a saturated KPF_6 aqueous solution was added to the reaction mixture. Extraction with dichloromethane and removal of the organic solvent yielded a crude reddish solid. After purification by column chromatography on silica gel (gradient elution of MeCN/aqueous 0.4 M KNO_3, from 98:2 to 90:10) and removal of volatiles, dropwise addition of a saturated KPF_6 aqueous solution and extraction with dichloromethane, gave an orange powder. Yield: 30% (465 mg). ^{1}H NMR (300 MHz, CD_3CN): δ (ppm) 9.09 (d, *J* = 8.5 Hz, 1H), 8.87 (d, *J* = 8.1 Hz, 1H), 8.42 (d, *J* = 15.4 Hz, 4H), 8.28 (d, *J* = 8.5 Hz, 2H), 8.00 (d, *J* = 5.1 Hz, 2H), 7.81 – 7.74 (m, 6H), 7.49 (t, *J* = 6.0 Hz, 2H), 7.40 (d, *J* = 5.4 Hz, 2H), 7.15 (s broad, 2H), 4.10 – 3.88 (m, 16H), 3.60 (s, 1H), 3.42 (d, *J* = 22.6 Hz, 4H), 3.32 (d, *J* = 22.6 Hz, 4H), 1.23 – 1.05 (m, 24H). ^{13}C-NMR (75 MHz, CD_3CN): δ (ppm): 157.5, 157.1, 152.2, 152.0, 150.7, 145.6, 133.3, 131.1, 130.2, 129.2, 127.2, 125.8, 83.2, 80.8, 63.0, 34.1, 32.3, 16.2. ESI-MS: m/z 667.3 $[M\text{-}H\text{-}3PF_6]^{2+}$. HR-MS ($ESI^+$): m/z calcd for $C_{61}H_{72}N_8O_{12}P_4Ru$ 667.1626; found 667.1624 $[M\text{-}H\text{-}3PF_6]^{2+}$. E.A.: calcd for

$C_{61}H_{73}N_8O_{12}P_7F_{18}Ru$ + 0.8 KPF_6: C, 38.21; H, 3.84; N, 5.84; found: C, 38.40; H, 4.19; N, 5.64. **RuP_4^{OEt}-EPIP** has also been synthesized by deprotection of the triple bond of **RuP_4^{OEt}-TMS-EPIP** in 75% yield with similar procedure for Ru-EPIP.

N_3-Cu(DO)(DOH)pn(OH_2)](ClO_4) (Cu-N_3)

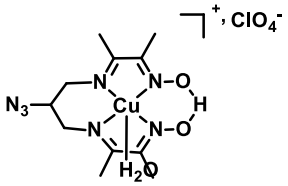

To a hot *N2,N2'*-2-azidopropanediylbis(2,3-butadione-2-imine-3-oxime) ligand (147 mg, 0.52 mmol) solution in acetone (1 ml), a concentrated solution of $Cu(ClO_4)_2.6H_2O$ (114 mg, 0.31 mmol) in acetone (0.5 ml) was added dropwise. The dark brown reaction mixture was left overnight at room temperature. Then, the precipitate was filtrated, washed with some acetone and dried under vacuum. Yield: 75% (83 mg).

Ru-Cu

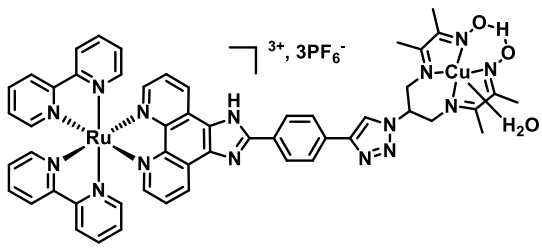

In a round bottom flask, Ru-EPIP (70 mg, 0.07 mmol) and Cu-N_3 (65 mg, 0.16 mmol) were dissolved in a homogeneous solvent mixture of MeOH, CH_2Cl_2 and H_2O (3:3:1, 15 ml). Sodium ascorbate (67 mg, 0.34 mmol) and copper sulfate (7 mg, 0.03 mmol) were added under argon. The reaction mixture was stirred at room temperature under argon in the dark over the weekend. The organic solvents were evaporated and the desired compound was precipitated by dropwise addition of 5ml saturated KPF_6 aqueous solution. The orange precipitate was filtered, washed with water and dried under vacuum. The crude product was purified by column chromatography on silica gel (gradient elution of MeCN/0.4 M aqueous KNO_3, from 98:5 to 80 : 20). The fractions were concentrated and the product was precipitated by dropwise addition of a saturated KPF_6 aqueous solution. The precipitate was filtered, washed with water and dried under vacuum. Yield: 55% (60 mgr). ESI-MS: m/z 1368 $[M\text{-}H_2O\text{-}PF_6]^+$, m/z 611 $[M\text{-}H_2O\text{-}2PF_6]^{2+}$, m/z 538 $[M\text{-}H_2O\text{-}H\text{-}3PF_6]^{2+}$, m/z 359 $[M\text{-}H_2O\text{-}PF_6]^{3+}$. No titrations measurements were performed for the identification of the protonation state of the imidazole unit.

Ru-Co

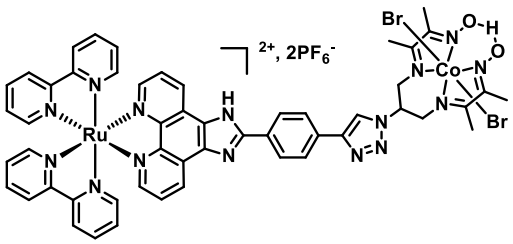

Ru-Cu (50 mgr, 0.033 mmol) and $CoBr_2$.hydrate (50 mgr, 0.23 mmol) were solubilized in a mixture of acetone/methanol 9/1 (15 ml) and stirred under air bubbling overnight. The organic solvents were evaporated and the crude product was purified by column chromatography on siliga gel (acetone/H_2O/KBr (sat. aq.) 90/9/1. After removal of the volatiles, the product was precipitated after the dropwise addition of KPF_6-saturated aqueous solution. The final compound was filtered, washed with water and dried under vacuum to give an orange powder. Yield: 60% (30mgr). ^{1}H NMR (300 MHz, CD_3CN): δ (ppm) 19.32 (s, 1H), 9.09 (d, *J* = 7.2 Hz, 1H), 8.93 (d, *J* = 7.4 Hz, 1H), 8.53-8.38 (m, 7H), 8.16-7.95 (m, 8H), 7.85-7.75 (m, 4H), 7.58 (t, *J* = 6.5 Hz, 2H), 7.43 (t, *J* = 6.2 Hz, 2H), 7.20 (t, *J* = 5.5 Hz, 2H), 5.88 (t, *J* = 11.5 Hz, 1H), 4.75-4.51 (m, 4H), 2.61 (s, 6H), 2.56 (s, 6H). ESI-MS: m/z 616.5 $[M-2PF_6]^{2+}$. HR-MS (ESI+): m/z calcd for $C_{52}H_{46}Br_2CoN_{15}O_2Ru$ 616.5345; found 616.5335 $[M-2PF_6]^{2+}$. No titrations measurements were performed for the identification of the protonation state of the imidazole unit.

RuP_4^{OEt}-Cu

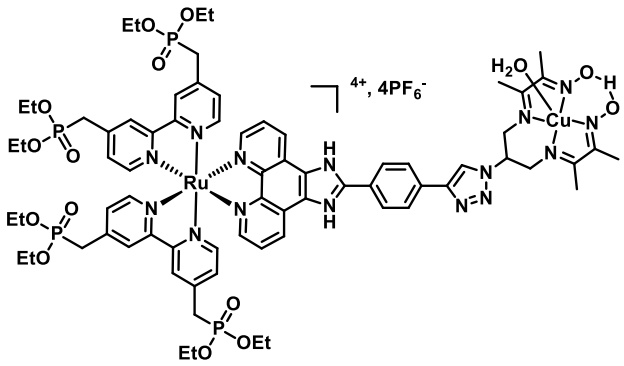

In an argon-purged round bottom flask, RuP_4^{OEt}-EPIP (150 mg, 0.09 mmol) and CuN_3 (86 mg, 0.18 mmol) were dissolved in a 15 ml of a degassed homogeneous 3:3:1 MeOH/CH_2Cl_2/H_2O solvent mixture. Sodium ascorbate (93 mg, 0.46 mmol) and copper sulfate (11 mg, 0.05 mmol) were added under argon and the reaction mixture was stirred at room temperature in the dark over the weekend. After evaporation of the organic solvents and dropwise addition of 5ml saturated KPF_6 aqueous solution, the orange solution was extracted with dichloromethane. DCM was evaporated and the dark orange compound was dried under vacuum. The crude product was purified by column chromatography on silica gel (gradient elution of MeCN/0.4 M aqueous KNO_3, from 95:5 to 80:20). The organic solvents were evaporated and the product was extracted with dichloromethane after the dropwise addition of 5 ml of saturated KPF_6 aqueous solution. Addition of Na_2SO_4, filtration and evaporation of dichloromethane under reduced vacuum gave a dark orange powder. Yield: 55% (110 mg). ESI-MS: m/z 559.3 [M-H_2O-H-

$4PF_6]^{3+}$, 911,0 $[M\text{-}H_2O\text{-}H\text{-}3PF_6]^{2+}$. HR-MS (ESI+): m/z calcd for $C_{72}H_{90}CuN_{15}O_{14}P_4Ru$ 559.1355; found 559.1356 $[M\text{-}H_2O\text{-}H\text{-}4PF_6]^{3+}$. E.A.: calcd for $C_{72}H_{93}CuN_{15}O_{15}P_8F_{24}Ru$: C, 37.98; H, 4.12; N, 9.23; found: C, 39.01; H, 4.53; N, 8.74.

RuP_4^{OEt}-Co

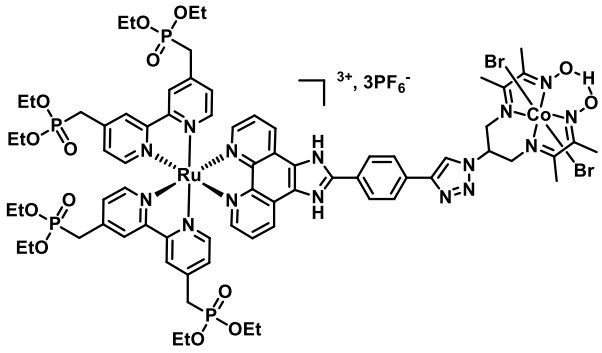

RuP_4^{OEt}-Cu (110 mg, 0.05 mmol) and $CoBr_2$.hydrate (100 mg, 0.45 mmol) were solubilized in a mixture of acetone/methanol 9/1 (15 ml) and stirred under air bubbling overnight. The organic solvents were evaporated and the crude product was purified by flash chromatography on siliga gel using a 90:9:1 acetone/H_2O/KBr (sat. aq. solution) eluent mixture. The organic solvents were evaporated and the product was extracted with dichloromethane after the dropwise addition of a saturated KPF_6 aqueous solution. Addition of Na_2SO_4, filtration and evaporation of dichloromethane under reduced vacuum resulted in an orange powder. Yield: 60% (70 mg). ^{1}H NMR (300 MHz, CD_3CN): δ (ppm) 19.35 (s, 1H), 9.67 (d, *J* = 8.1 Hz, 1H), 9.10 (d, *J* = 8.73 Hz, 1H), 8.66 (d, *J* = 8.7 Hz, 2H), 8.53 (s, 1H), 8.43 (d, *J* = 14.4 Hz, 4H), 8.12 (t, *J* = 8.28 Hz, 2H), 7.98 (d, *J* = 6.8 Hz, 2H), 7.81-7.76 (m, 4H), 7.52 (t, *J* = 4.6 Hz, 2H), 7.40 (d, *J* = 5.6 Hz, 2H), 7.16 (d, *J* = 6.2 Hz, 2H), 5.89 (t, *J* = 11.2 Hz, 1H), 4.78-4.57 (m, 4H). 4.10-3.88 (m, 16H), 3.46-3.29 (m, 8H), 2.67 (s, 1H), 2.60 (s, 1H), 1.22-1.10 (m, 24H). ESI-MS: m/z 584.8 $[M\text{-}Br\text{-}H\text{-}3PF_6]^{3+}$, 916.6 $[M\text{-}H\text{-}3PF_6]^{2+}$. HR-MS (ESI+): m/z calcd for $C_{72}H_{90}Br_2CoN_{15}O_{14}P_4Ru$ 915.6237; found 915.6230 $[M\text{-}H\text{-}3PF6]^{2+}$. E.A.: calcd for $C_{72}H_{91}Br_2CoN_{15}O_{14}F_{18}P_7Ru$: C, 38.11; H, 4.04; N, 9.26; found: C, 39.21; H, 4.44; N, 8.93.

General procedure for the hydrolysis of the phosphonate ester groups. The ruthenium complex (1 eq.) was added in an oven-dried schlenk under argon and was solubilized in 2 ml of dry dichloromethane or acetonitrile. Under argon, TMSBr (roughly 20 eq.) was added and the reaction mixture was stirred at room temperature for 3 days. After evaporation of the solvent, 5 ml of methanol was added and the solution was stirred for 3 hours in order to hydrolyze the silyl ester. Methanol was removed and the orange powder was dried under vacuum. Yield: 90%.

4-chloropyridine-2,6-diyl)bis(morpholinomethanone (1)

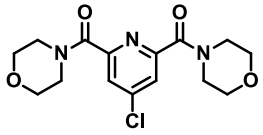

Chelidamic acid monohydrate (2.0 g, 10.93 mmol) was dissolved in $SOCl_2$ (20 ml). Dry DMF (0.3 ml) was added at 0°C and the pale-yellow reaction mixture was refluxed overnight under argon. The solvent was removed under vacuum with a liquid nitrogen trap and a white solid was obtained. The crude product was dissolved in dry $CHCl_3$ (20 ml) and a morpholine (3.8 ml, 43.72 mmol) solution in dry chloroform (3.8 ml) was added dropwise at 0°C. The mixture was stirred at room temperature for 3 hours. The solvent was removed under vacuum, aqueous saturated $NaHCO_3$ solution (10 ml) was added and extractions with ethyl acetate were realized, followed by extractions with brine solution and water. The organic layer was dried with Na_2SO_4, filtered, and the solvent was removed in vacuum to obtain a white solid. Yield: 65% (2.3 g). ^{1}H NMR (300 MHz, $CDCl_3$): δ (ppm) 7.74 (s, 2H), 3.80 (br, 8H), 3.68-3.64 (m, 4H), 3.60-3.56 (m, 4H). ^{13}C NMR (300 MHz, $CDCl_3$): δ (ppm) 165.3, 153.4, 146.6, 125.4, 66.8, 47.6. ESI-MS: m/z 340.1 $[M+H]^+$, 362.1 $[M+Na]^+$.

4-chloro-2,6-diacetylpyridine (2)

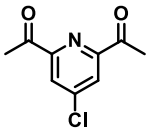

1 (2.3 g, 6.78 mmol) was dissolved under argon in 60 ml of freshly distilled THF. MeMgCl 3M solution in THF (7 ml, 17 mmol) was added dropwise at 0°C. The reaction mixture was stirred for 30 min under argon at 0°C, followed by quenching with aqueous saturated NH_4Cl solution (50 ml) and extraction with CH_2Cl_2. The organic layer was dried on Na_2SO_4, filtered and evaporated under vacuum. The crude product was purified by column chromatography on silica gel (CH_2Cl_2) to obtain white crystals. Yield: 64% (0.85 g). ^{1}H NMR (300 MHz, $CDCl_3$): δ (ppm) 8.18 (s, 2H), 2.78 (s, 6H). ^{13}C NMR (300 MHz, $CDCl_3$): δ (ppm) 198.1, 153.9, 146.9, 124.9, 25.6. ESI-MS: m/z 197.9 $[M+H]^+$, 219.9 $[M+Na]^+$, 235.9 $[M+K]^+$.

4-azido-2,6-diacetylpyridine (N_3-DPA)

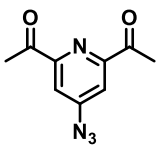

2 (600 mg, 3.04 mmol) and NaN_3 (3.9 g, 60 mmol) were mixed in DMF (10 ml) and heated to 55°C. After 24 hours, DMF was removed by distillation under reduced pressure. The crude product was purified on silica gel column chromatography using 50% pentane in CH_2Cl_2 as eluent to give a white solid. Yield: 30% (200 mg). ^{1}H NMR (300 MHz, $CDCl_3$): δ (ppm) 7.83 (s, 2H), 2.78 (s, 6H). ^{13}C NMR (300 MHz, $CDCl_3$): δ (ppm) 198.6, 154.5, 151.5, 114.7, 25.6. ESI-MS: m/z 205.0 $[M+H]^+$, 227.0 $[M+Na]$

$^{+}$, 243.0 [M+K] $^{+}$. The same experimental protocol was followed, when we used the Br-derivative of 2.

Cat1

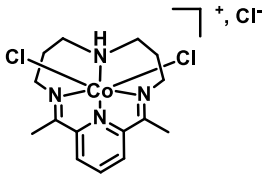

2,6-diacetyl-pyridine (50 mg, 0.31 mmol) was dissolved in ethanol (1 ml) and heated to 40°C under argon. $CoCl_2 \cdot 6H_2O$ (71 mg, 0.31 mmol) and water (0.8 ml) were added and the mixture was stirred at 55°C to dissolve the salt. The reaction mixture was warmed at 75°C and 3,3'-diaminodipropylamine (43 µl, 0.31 mmol) was added. Glacial acetic acid (0.1 ml) was added for solubility reasons and the solution was stirred at 75°C for 5 hours under argon. Concentrated HCl aqueous solution (30 µl, 0.73 mmol, 37 %) was added and the mixture was aerated overnight. The volume was reduced on the rotary evaporator, then cold ethanol was added slowly and green-brownish solid was obtained. The precipitate was filtered off, washed with cold ethanol and dried under vacuum. Yield: 30% (40 mg). ^{1}H NMR (300 MHz, CD_3CN): δ (ppm) 8.57 (br, 1H), 8.37 (d, *J* = 8.0 Hz, 2H), 6.01 (br, 1H), 4.05 (br, 2H), 3.65 (br t, *J* = 13.4 Hz, 2H), 3.40 (br, 2H), 3.00 (br, 2H), 2.80 (s, 6H), 2.30 (br d, *J* = 15.6 Hz, 2H), 2.11 (br, 2H). ESI-MS: m/z 387.1 [M-Cl] $^{+}$.

N_3-Cat1

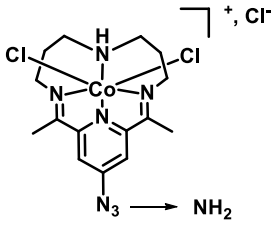

N_3-DPA (40 mg, 0.20 mmol) was dissolved in ethanol (1 ml) and CH_2Cl_2 (0.5 ml) and heated to 40°C under argon. $CoCl_2 \cdot 6H_2O$ (48 mg, 0.20 mmol) and water (0.4 ml) were added and the pale orange mixture was stirred at 55°C. The reaction mixture was warmed at 75°C and 3,3'-diaminodipropylamine (28 µl, 0.20 mmol) was added, resulting in a dark solution. Glacial acetic acid (20 µl) was added and the solution was stirred at 75°C for 5 hours under argon. Then, concentrated HCl aqueous solution (40 µl, 37 %) was added and the mixture was aerated overnight, turning into green. The volume was reduced, cold ethanol was then added slowly and green crystals were obtained. The precipitate was filtered, washed with cold ethanol and dried under vacuum. Yield: 45% (40 mg). The final compound is reduced from $-N_3$ to $-NH_2$ during the synthetic procedure as evidenced by ESI-MS. ESI-MS: m/z 330.2 [M-3Cl-2H] $^{+}$, 366.1 [M-2Cl-H] $^{+}$, 402,1 [M-Cl] $^{+}$.

RuP_4^{OEt}-DAP

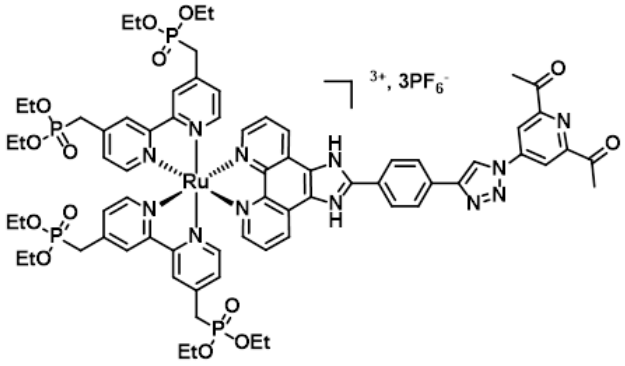

In an Ar-degassed round bottom flask, RuP_4^{OEt}-EPIP (130 mg, 0.07 mmol) and N_3-DPA (32 mg, 0.15 mmol) were dissolved in a degassed homogeneous solvent mixture of MeOH/CH_2Cl_2/H_2O (3:3:1; 14 ml). Sodium ascorbate (79 mg, 0.40 mmol) and copper sulfate (8 mg, 0.03 mmol) were added under argon. The reaction mixture was stirred at room temperature under argon in the dark for 2 days. The organic solvents were evaporated and the orange solution was extracted with CH_2Cl_2 after addition of 5ml saturated KPF_6 aqueous solution. The crude product was purified by column chromatography on silica gel (gradient elution of MeCN/0.4 M aqueous KNO_3, from 98:2 to 85:15). The organic solvents were evaporated and the product was extracted with dichloromethane after the addition of 5ml of saturated KPF_6 aqueous solution. The organic layer was evaporated and dried under vacuum to give an orange powder. Yield: 60% (85 mg)**.** ^{1}H NMR (300 MHz, CD_3CN): δ (ppm) 9.07 (s, 1H), 9.00 (t, *J* = 8.9 Hz, 2H), 8.65 (s, 1H), 8.42 (d, *J* = 7.1 Hz, 6H), 8.20-8.14 (m, 2H), 7.99-7.91 (m, 2H), 7.79-7.64 (m, 4H), 7.51 (t, *J* = 6.5 Hz, 3H), 7.40 (br, 2H), 7.15 (br, 2H), 4.10-3.89 (m, 16H), 3.37 (dd, *J* = 22.7 Hz, 8H), 2.79 (s, 6H), 1.23-1.05 (m, 24H). ESI-MS: m/z 769.1 $[M\text{-}H\text{-}3PF_6]^{2+}$. HR-MS ($ESI^+$): m/z calcd for $C_{70}H_{80}N_{12}O_{14}P_4Ru$ 769.1950; found 769.1951 $[M\text{-}H\text{-}3PF_6]^{2+}$.

RuP_4^{OEt}-Cat1

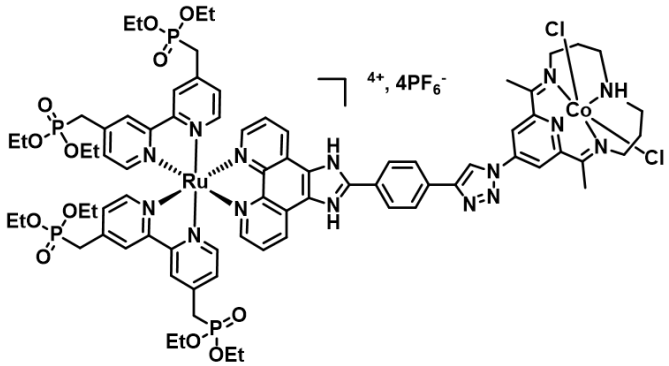

RuP_4^{OEt}-DAP (50 mg, 0.025 mmol) was dissolved in ethanol (1 ml) and dichloromethane (0.5 ml) and heated to 40°C under argon. $CoCl_2.6H_2O$ (7.5 mg, 0.031 mmol) and water (0.3 ml) were added and the mixture was stirred at 55°C. The reaction mixture was warmed at 75°C and 3,3'-diaminodipropylamine (4 µl, 0.028 mmol) was added resulting in a dark solution. For convenience, we diluted 40 µl of the amine in 1 ml of ethanol and from this stock solution we added 100 µl in the reaction mixture. Glacial acetic acid (10 µl) was added and the solution was stirred at 75°C overnight under argon. Then, concentrated HCl aqueous solution (50 µl, 37 %) was added and the mixture was aerated overnight. Addition of some drops of

aqueous saturated KPF_6, resulted in partial precipitation and further extraction with DCM was realized. The crude product was purified by column chromatography on silica gel (MeCN/0.4 M aqueous KNO_3, 85:15). Then, a mixture of acetone/H_2O aqueous solution of KCl (90/9/1) was used to completely desorb the product from the silica gel. The organic solvents were evaporated and the product was precipitated after the addition of 5ml of saturated KPF_6 aqueous solution. The precipitate was filtered and dried under vacuum to give an orange powder. Yield: 17% (10 mg)**.** ESI-MS: m/z 588.1 $[M\text{-}H\text{-}4PF_6]^{3+}$, 881.5 $[M\text{-}2H\text{-}4PF_6]^{2+}$, 954.7 $[M\text{-}H\text{-}3PF_6]^{2+}$. HR-MS ($ESI^+$): m/z calcd for $C_{76}H_{93}N_{15}O_{12}P_4CoCl_2Ru$ 587.4605; found 587.4599 $[M\text{-}H\text{-}4PF_6]^{3+}$.

Annexes

I. ESI-MS spectra of RuP_4^{OEt}-Cat1

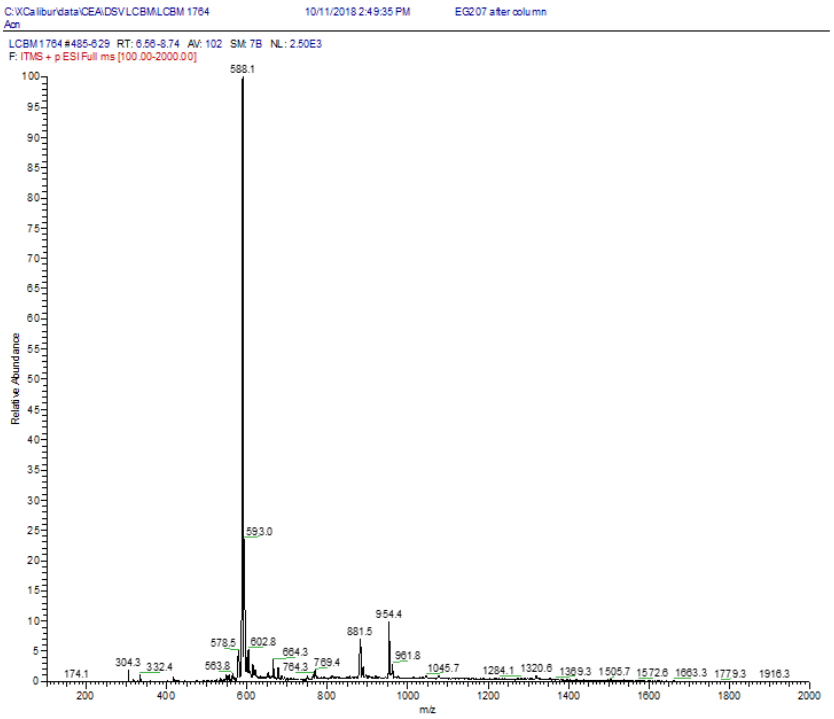

RuP_4^{OEt}-Cat1 batch fully hydrolyzed for photoelectrochemical experiments.

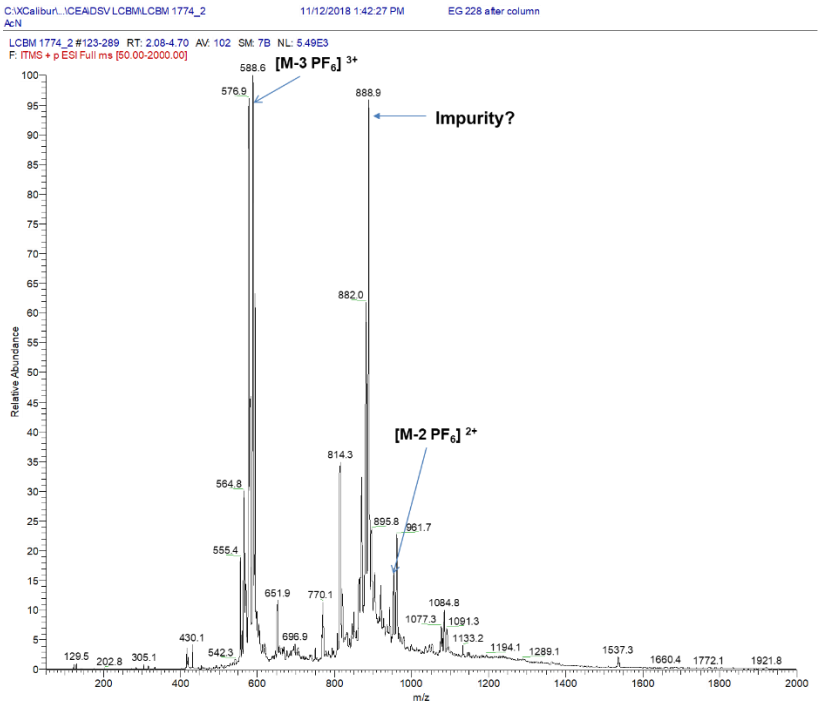

RuP_4^{OEt}-Cat1 batch used for CV and UV-Vis characterization.

II. Porphyrin-cobalt dyad for photoelectrochemical proton reduction

In collaboration with the group of Pr. A. Coutsolelos, I assessed the photoelectrochemical activity for proton reduction of a novel dyad based on porphyrin photosensitizer and the cobalt diimine-dioxime (**ZnP-Co**), synthesized and characterized by our collaborators. The results of this project have been submitted for publication (**P3**).

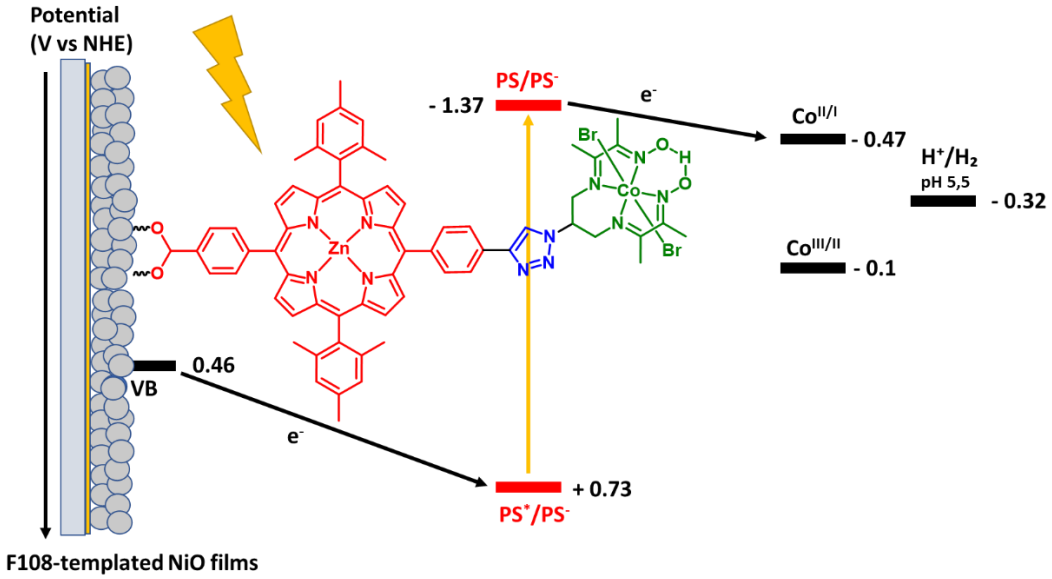

ZnP-Co was anchored onto homemade F108-templated NiO films. A dye loading of 6.4 ± 0.9 nmol.cm^{-2} was determined by desorption of the dyad from freshly-functionalized films in a THF solution of 1 M phenyl phosphonic acid. Linear sweep voltammograms were recorded in a MES buffer electrolyte at pH 5.5 under dark, chopped-light and full irradiation conditions, using the **ZnP-Co**-sensitized photocathode as working electrode in a three-electrode setup. Cathodic photocurrents of up to 11 µA.cm^{-2} (dark current subtracted) are clearly generated under visible light irradiation from +0.94 V vs RHE.

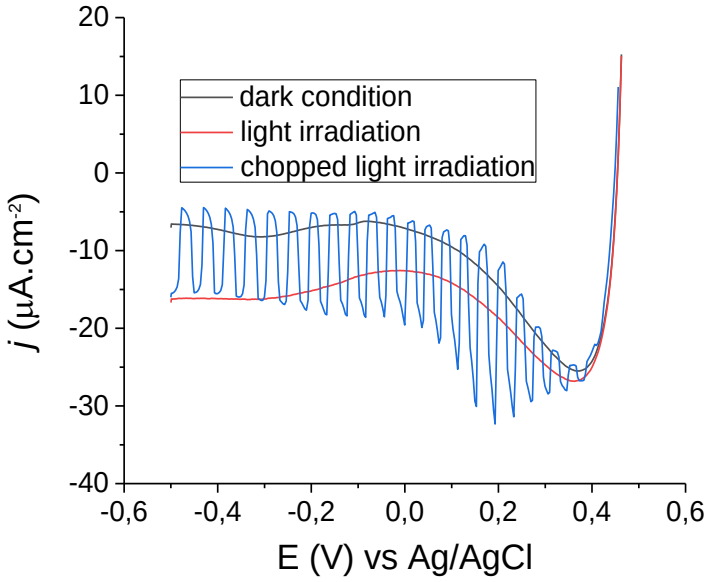

Linear sweep voltammograms of **ZnP-Co** –sensitized NiO electrodes , recorded in a pH 5.5 MES 0.1 M/NaCl 0.1 M buffer under dark conditions (black line), continuous visible light irradiation (red line) or chopped light irradiation (blue line).

To assess whether these photocurrents are correlated with photoelectrocatalytic hydrogen production, two hours chronoamperometric measurements coupled to hydrogen detection were carried out at -0.4 V vs Ag/AgCl for direct comparison with our previously-reported photocathodes based on the same cobalt diimine-dioxime catalyst. At the end of the experiments, the amount of hydrogen produced was measured in the headspace and in the electrolyte solution with 8 ± 1 % F.E. and 7 ± 1 nmol.cm^{-2}. By comparison, control experiments performed with **ZnP-ref**-sensitized (just the photosensitizer) NiO films under identical conditions produced only 3 nmol.cm^{-2}.

Post-operando characterization of the dyad was performed after desorption from the film in a 1 M phenylphosphonic acid solution in THF. The UV-vis spectrum of the solution displays an overall lower intensity of the signals by comparison with the spectrum of the freshly-grafted film attributed to some desorption of **ZnP-Co** from the NiO surface (estimated to ≈ 40 %) during the course of the two-hours PEC experiment. In addition, a clear evolution of four Q bands is observed, suggesting a demetallation of the porphyrin core. As demetallation of porphyrins is reported to take place under acidic conditions, the photoelectrocatalytic activity of the films was also assessed at pH 7. Although the **ZnP-Co**-sensitized film displays improved stability at this less acidic pH (less desorption and demetallation), the activity was not enhanced and the same amount of hydrogen was produced (Table above).

Film	pH	Surface Area (cm^2)	Dye loading ($nmol.cm^{-2}$)	Total H_2 (nmol)[a]	Total H_2 ($nmol.cm^{-2}$)	Charge passed ($mC.cm^{-2}$)	F.E. (%)	TON	% desorp.
ZnP-Co	5.5	3.3	7.4	25	8	17	9	1	30
		3.1	6.1	17	6	19	6	1	48
average					**7 ± 1**	**18 ± 1**	**8 ± 1**	**1**	**39 ± 9**
ZnP-Co	7	3.2	7.1	23	7	13	11	1	19
		3.2	5.1	15	5	21	5	1	31
average					**6 ± 1**	**17 ± 4**	**8 ± 3**	**1**	**25 ± 6**
ZnP-ref	5.5	3.0	3.6	10	3	4	17	-	35
		3.2	3.1	8	3	10	8	-	67
average					**3**	**7 ± 3**	**13 ± 4**		**51 ± 16**

H_2 measurements at the end of the photoelectrolysis experiments (continuous irradiation for 2 hours; MES buffer, pH 5.5 or B.R. buffer pH 7; applied potential: +0.14 V vs RHE).

a) Measured by gas chromatography and micro-clark type electrode.

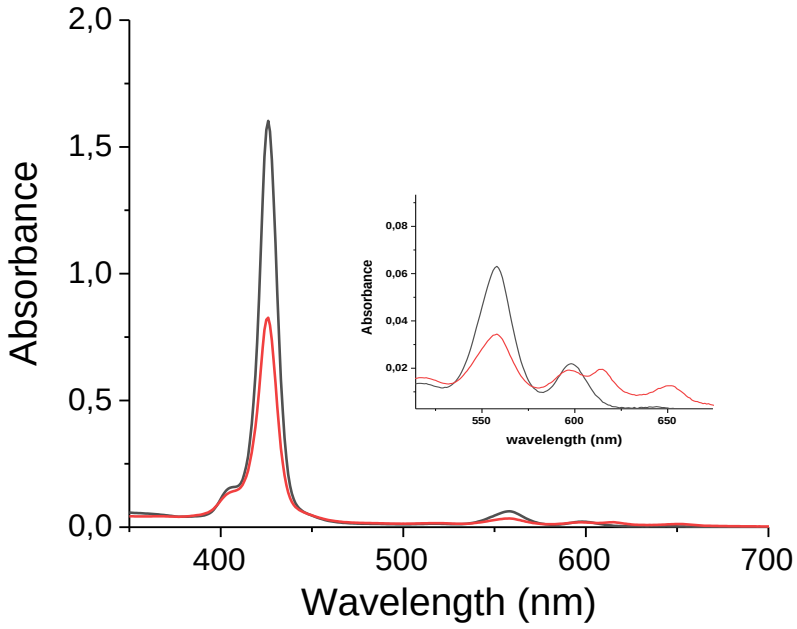

UV-Visible spectra of **ZnP-Co** in a THF solution of 1 M phenylphosphonic acid, where half of a fresh NiO film was dipped (black line) and the other half was dipped after 2 hours of PEC experiment (red line). Zoom in the region of the Q bands.

The overall performances of this novel dyad are slightly lower than the ones previously reported for a NiO-based photocathode based on the same cobalt diimine-dioxime complex covalently coupled with a push-pull organic dye. This might be due to a lack of directionality in the structure. Indeed, the electron-withdrawing ability of the carboxylate anchoring group can stabilize the electron on the opposite side of the catalytic center, preventing the generation of the catalytically active species.

III. Push-pull organic dye-catalyst assemblies

1) Synthesis of ^{tBu}T1-Cat1

During my thesis, I also participated in the project related to the construction of dye-catalyst assemblies based on the previous expertise of the group. As already presented in Chapter IV, I optimized the synthesis and purification of **^{tBu}T1-Cat1** based on the synthetic procedure developed by Q. Vacher and J. Massin. This dyad has been characterized and the corresponding NiO photocathode was studied by S. Bold. The results of this project have been submitted for publication (**P2**).

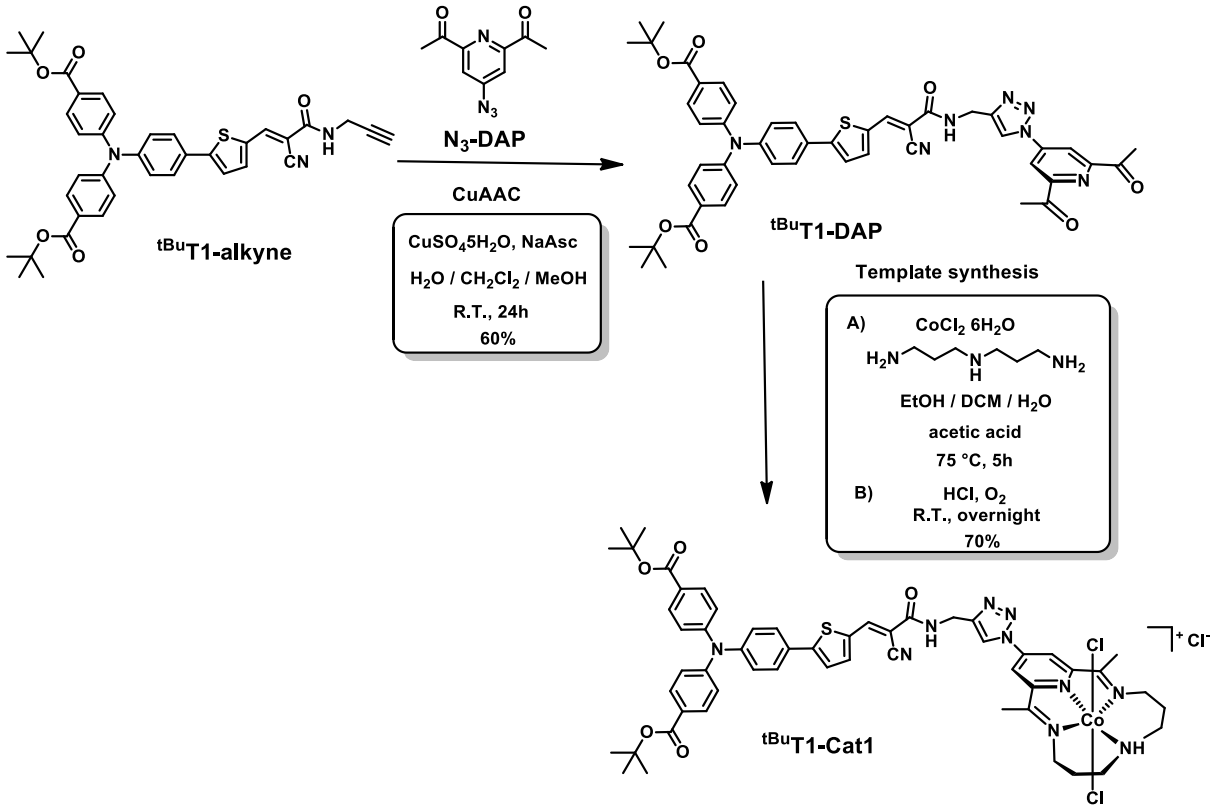

^{tBu}T1-diacetylpyridine (^{tBu}T1-DAP)

^{tBu}T1-alkyne (200 mg, 0.30 mmol) and N_3-DAP (60 mg, 0.30 mmol) were dissolved in 10 ml of degassed CH_2Cl_2. Sodium ascorbate (50 mg, 0.26 mmol) and $CuSO_4.5H_2O$ (22 mg, 0.09 mmol) were dissolved in 5 ml of degassed H_2O and then added to the reaction mixture. 15 ml of degassed MeOH were added until a single phase was obtained. The reaction mixture was stirred at room temperature for 18 hours. After removal of the volatile solvents, the mixture was extracted with CH_2Cl_2, washed with brine solution, dried over Na_2SO_4 and filtered. The crude product was purified on silica gel column using CH_2Cl_2/AcOEt (7:3) as eluent and dried under vaccum to give a red solid. Yield: 60% (150 mg). ^{1}H NMR (300 MHz, $CDCl_3$): δ 8.61 (s, 2H), 8.39 (s, 1H), 8.28 (s, 1H), 7.90 (d, *J* = 8.5 Hz, 4H), 7.71 (d, *J* = 3.7 Hz, 1H), 7.60 (d, *J* = 8.5

Hz, 2H), 7.35 (d, *J* = 4.2 Hz, 1H), 7.08 -7.14 (m, 7H), 4.79 (d, *J* = 5.8 Hz, 2H), 2.84 (s, 6H), 1.59 (s, 18H). ESI-MS: m/z positive mode 886.2 $[M+Na]^+$, negative mode 898.2 $[M+Cl]^-$. HR-MS (ESI+): m/z calcd for $C_{48}H_{46}N_7O_7S$ 864.3174; found: 864.3173 $[M+H]^+$. E.A.: calcd for $C_{48}H_{45}N_7O_7S$ + 1 H_2O: C, 65.37; H, 5.37; N, 11.12; found: C, 65.35; H, 5.31; N, 10.99.

^{tBu}T1-Cat1

^{tBu}T1-DPA (50 mg, 0.058 mmol) was dissolved in EtOH (1 ml) and CH_2Cl_2 (0.5 ml) and kept at 40°C under argon. $CoCl_2.6H_2O$ (14 mg, 0.058 mmol) and water (0.56 ml) were added and the mixture was stirred at 55°C to dissolve the salt. The reaction mixture was warmed at 75°C and 3,3'-diaminodipropylamine (0.008 ml, 0.058 mmol) and glacial acetic acid (0.005 ml) were added. The solution was stirred at 75°C for 5 hours under argon. After cooling down to room temperature, 0.01 ml of concentrated HCl was added and the mixture was aerated at room temperature for 16 hours. After evaporation of the solvents, precipitation was carried out with addition of cold saturated aqueous solution of KCl. The crude product was purified on silica gel column using CH_2Cl_2/AcOEt (7:3) as eluent to remove the starting material. The desired compound was desorbed from silica by addition of acetone/H_2O/aq. KCl (90/9/1). Precipitation was realized by addition of aqueous saturated solution of KCl. The precipitate was washed with water and dried under vacuum resulting in a red solid. Yield: 70% (45 mg). ^{1}H NMR (300 MHz, $(CD_3)_3CO$): δ 9.25 (s, 2H), 9.11 (s, 1H), 8.46 (s, 1H), 8.25 (s (br), 1H), 7.93 (d, *J* = 7.9 Hz, 4H), 7.82 (d, *J* = 8.3 Hz, 2H), 7.67 (s (br), 1H), 7.28-7.18 (m, 6H), 6.30 (br, 1H), 4.82 (br, 2H), 4.40 (d, *J* = 16.0 Hz, 2H), 3.78-3.68 (m, 2H), 3.50-3.40 (m, 2H), 3.36-3.31 (m, 2H), 3.18 (s, 6H), 2.43 (br, 2H), 2.31-2.28 (m, 2H), 1.58 (s, 18H). ESI-MS: m/z 1087.3 $[M-Cl]^+$. HR-MS (ESI^+): m/z calcd for $C_{54}H_{58}Cl_2CoN_{10}O_5S$ 1087.3016; found 1087.3014 $[M-Cl]^+$.

2) Synthesis of T1P-Co

One of the initial aims of my PhD was to assess the stability of the anchoring groups for grafting onto NiO films. In this sense, we decided to synthesize **Dyad 2a** but with methyl phosphonate instead of carboxylate anchoring groups (**T1P-Co**). The assessment of the photoelectrocatalytic activity of the dyad was carried out by S. Bold with no significant differences compared to **Dyad 2** under identical experimental conditions. Faradaic efficiencies and TON lower than 10% and 1 were determined accordingly.

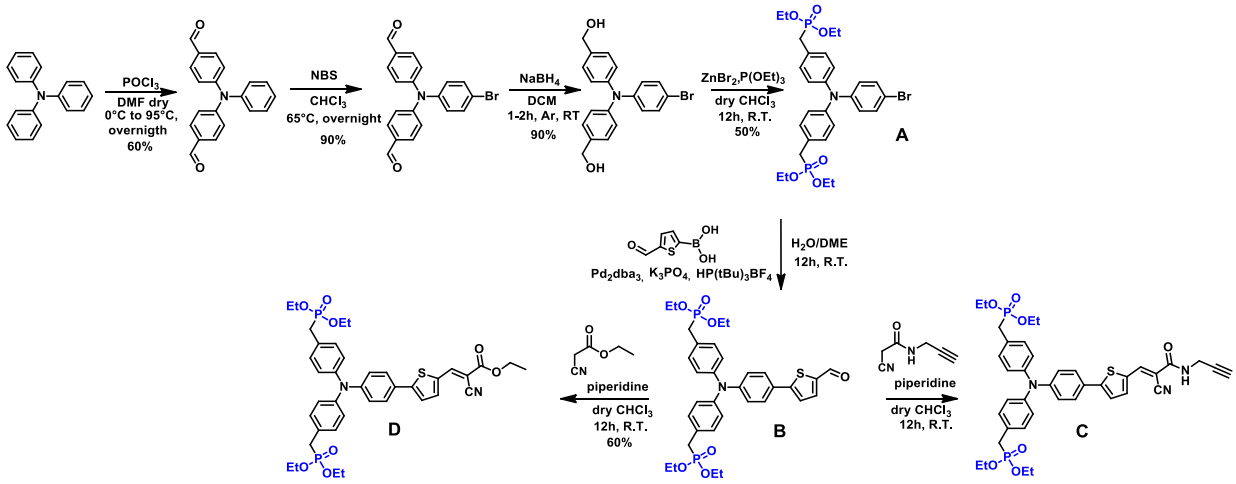

N,N-bis(4-carboxyphenyl)aniline

N,N,N-Triphenyamine (2.0 g, 8.16 mmol) was suspended in anhydrous DMF (15 ml) and the mixture was cooled down to 0ºC using a $CaCl_2$ guard to isolate the mixture from the atmospheric moisture. Excess phosphorous oxychloride (8 ml, 85.60 mmol) was added dropwise, keeping the temperature low with an ice bath. After complete addition, the mixture was heated to room temperature, before being stirred at 95ºC overnight. The reaction mixture was cooled down to room temperature, then poured in ice water (50 ml) and the pH of the medium was neutralized (pH 7) by slow addition of aqueous KOH solution. The aqueous phase was extracted with dichloromethane. Then, extraction with 10% aqueous LiCl solution was realized to remove most of DMF from the organic phase. The procedure was repeated three times. The combined organic layer was further washed with water and brine, dried over sodium sulfate, filtered and the solvent was evaporated. The crude material was purified over a silica short plug using a mixture of CH_2Cl_2 - 10 % hexane as the eluent. After evaporation of the solvents and dried under vacuum, a yellow solid was isolated. Yield: 60% (1.5 g). ^{1}H NMR (300 MHz, $CDCl_3$): δ (ppm) 9.92 (s, 2H), 7.85 (d, *J* = 8.7 Hz, 4H), 7.51 (d, *J* = 8.8 Hz, 2H), 7.18 (m, 7H).

N,N-bis(4-carboxyphenyl)-4-bromoaniline

N,N-bis(4-carboxyphenyl)aniline (1.50 g, 4.98 mmol) and N-bromosuccinimide (1.02 g, 5.73 mmol) were dissolved in anhydrous chloroform (100 ml) and the mixture was refluxed (65ºC) overnight, using a $CaCl_2$ tube to isolate the mixture from the atmospheric moisture. After cooling down to room temperature, the mixture was extracted with aqueous sodium bicarbonate (10% $NaHCO_3$, 3 x 100 ml) and brine. The organic layer was collected, dried over Na_2SO_4 and filtered. After removal of the solvents, a yellow solid was obtained. Yield: 90% (1.7 g). ^{1}H

NMR (300 MHz, $CDCl_3$): δ 9.84 (s, 2H), 7.72 (d, *J* = 8.7 Hz, 4H), 7.43 (d, *J* = 8.8 Hz, 2H), 7.11 (d, *J* = 8.6 Hz, 4H), 6.98 (d, *J* = 8.8 Hz, 2H).

N,N-bis(4-hydroxymethylphenyl)-4-bromoaniline

N,N-bis(4-carboxyphenyl)-4-bromoaniline (1.7 g, 4.47 mmol) was dissolved in 60 ml CH_2Cl_2. 25 ml of absolute ethanol was added followed by sodium borohydride (600 mg, 15.86 mmol). The mixture was stirred under argon, at room temperature, for 2 hours with a color change from yellow to almost colorless. The reaction was quenched by the addition of 50 ml water. After extractions with brine, the organic layer was dried over Na_2SO_4, filtered and the solvent was evaporated. Yield: 90% (1.5 g). ^{1}H NMR (300 MHz, CD_2Cl_2): δ (ppm) 7.32 (d, *J* = 8.8 Hz, 2H), 7.25 (d, *J* = 8.3 Hz, 4H), 7.04 (d, *J* = 8.4 Hz, 4H), 6.92 (d, *J* = 8.8 Hz, 2H), 4.59 (s, 4H).

TPA-phosphonate derivative (A)

In a oven dried schlenk N,N-bis(4-hydroxymethylphenyl)-4-bromoaniline (1.1 gr, 2.86 mmol), $ZnBr_2$ (1.5 gr, 6.70 mmol) and $P(OCH_2CH_3)_3$ (10 ml, 58 mmol) were added under argon. The solution was purged with argon and 20 ml dry $CHCl_3$ was added. The reaction mixture was stirred overnight, at room temperature, using a balloon filled with argon and protected from night. After the addition of 300 ml of hexane, the mixture was stirred vigorously for at least 5 minutes until the appearance of a waxy solid. The supernatant was removed and the precipitate was extracted with dichloromethane and washed with water. The organic layer was dried over Na_2SO_4, filtered and the solvent was evaporated. The crude product was purified by column chromatography on silica gel using dichloromethane/ethanol (98/2) as eluent to give a yellowish oil. The product was placed in a refrigerator overnight until a white solid (**A**) was obtained. Yield: 50% (900 mg). ^{1}H NMR ($CDCl_3$, 300 MHz): δ (ppm) 7.31 (d, *J* = 8.2 Hz, 2H), 7.18 (d, *J* = 8.4 Hz, 4H), 6.99 (d, *J* = 8.0 Hz, 4H), 6.90 (d, *J* = 8.2 Hz, 2H), 4.04 (quint., *J* = 7.35 Hz, 8H), 3.13 (s, 2H), 3.06 (s, 2H), 1.26 (t, *J* = 7.0 Hz, 12H). ^{13}C NMR (75 MHz, $CDCl_3$) δ 146.78, 146.04, 132.17, 130.78, 126.32, 125.13, 124.31, 114.92, 62.09, 33.09, 16.39.

TPA-aldehyde derivative (B)

(**A**) (300 mg, 0.48 mmol), 5-formyl-2-thiophene boronic acid (118 mg, 0.76 mmol), Pd_2dba_3 (9.3 mg, 0.01 mmol), $HP(tBu)_3BF_4$ (9.3 mg, 0.03 mmol), and K_3PO_4 (0.75 mL, 1 M) were added in 6 ml DME. The mixture was stirred at room temperature under argon for 24 hours, protected from light. After addition of H_2O (20 ml), the mixture was extracted with CH_2Cl_2 and dried over Na_2SO_4. The crude product was purified by column chromatography on silica gel

using dichloromethane/ethanol (98/2) as eluent to give yellow oil (**B**). From the ^{1}H NMR ($CDCl_3$, 300 MHz), the peak at 9.81 ppm confirmed the presence of the aldehyde derivative. Although many efforts were made (increasing temperature, reaction time, different mixture of solvents for column chromatography), we always observed the starting material. Thus, the crude product was used for the next reaction.

Propargyl cyanoacetamide

To a solution of 1-cyanoacetyl-3,5-dimethylpyrazole (5.1 g, 31.2 mmol) in toluene (40 ml), propargylamine (2 ml, 31.2 mmol) was added. The mixture was refluxed for 2 min and then stirred at room temperature. The precipitate was filtered, washed with pentane and dried to obtain a yellow-brownish solid. Yield: 83% (3.3 g). ^{1}H NMR (Acetone-d6, 300 MHz): δ (ppm) 5.75 (s, 1H), 4.02 (br, 2H), 3.61 (s, 2H), 2.69 (br, 1H). ESI-MS: m/z 123.1 $[M+H]^{+}$, 145.1 $[M+Na]^{+}$, 161.0 $[M+K]^{+}$.

TPA-alkyne derivative (C)

(**B**) (200 mg, 0.31 mmol) and propargyl cyanoacetamide (45 mg, 0.37 mmol) were solubilized in 15 ml dry $CHCl_3$ and piperidine (0.2 ml, 1.4 mmol) was added dropwise. The reaction mixture was stirred overnight under argon and protected from light. 1 M aqueous HCl was added and the mixture was extracted and washed with water. After evaporation of the solvent, the crude product was purified by column chromatography on silica gel using dichloromethane/ethanol (98/2) as eluent and the orange solid (**C**) was dried under vacuum. ESI-MS: m/z 759.1 $[M+H]^{+}$. From the ^{1}H NMR ($CDCl_3$, 300 MHz), the new peaks at 8.36 (s, 1H) and 2.30 (s, 1H) ppm confirmed the presence of the alkyne derivative. Although many efforts were made, we always observed the starting material with a peak at 9.85 ppm. The crude product was used for the next reaction.

Reference dye (D)

(**B**) (25 mg, 0.038 mmol) and ethyl cyanoacetate (0.1 ml, 1.33 mmol) were solubilized in 5 ml dry $CHCl_3$ and piperidine (0.1 ml, 0.95 mmol) was added dropwise. The reaction mixture was stirred overnight under argon and protected from light. 1 M aqueous HCl was added and the mixture was extracted and washed with water. After evaporation of the solvent, the crude product was purified by column chromatography on silica gel using dichloromethane/ethanol (98/2) as eluent. The excess ethyl cyanoacetate was removed by precipitation of the compound in a mixture of ethanol/water and filtration with celite. The red solid (**D**) was dried under

vacuum. Yield: 60% with some starting material (17 mg). ^{1}H NMR ($CDCl_3$, 300 MHz): δ (ppm) 8.11 (s, 1H), 7.57 (br, 1H), 7.38 (d, *J* = 8.1 Hz, 2H), 7.19 (br, 1H), 7.08 (d, *J* = 8.1 Hz, 4H), 6.91-6.84 (m, 6H), 3.90 (quint., *J* = 7.1 Hz, 10H), 3.01 (s, 2H), 2.94 (s, 2H), 1.17-1.09 (m, 15H). HR-MS (ESI+): m/z calcd for $C_{38}H_{45}N_2O_8P_2S$ 751.2366; found: 751.2357 $[M+H]^+$.

*Following the synthetic protocol for **Dyad 2**, we synthetized **T1P-Co** as follows:*

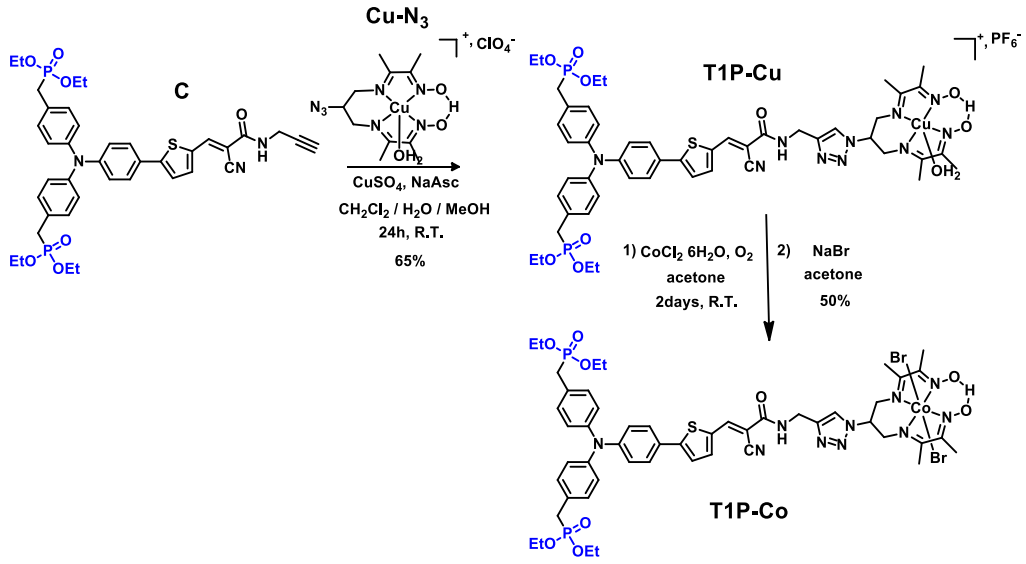

T1P-Cu

(**C**) (110 mg, 0.14 mmol) and Cu-N_3 (60 mg, 0.14 mmol) were dissolved in 7.3 ml of degassed CH_2Cl_2. Sodium ascorbate (26 mg, 0.13 mmol) and $CuSO_4.5H_2O$ (10 mg, 0.04 mmol) were dissolved in 2.5 ml of degassed H_2O and then added to the reaction mixture. 8 ml of degassed MeOH was added until a single phase was obtained. The reaction mixture was stirred at room temperature for 24 hours under argon and dark conditions. After removal of the organic solvents, aqueous saturated KPF_6 solution was added and the mixture was extracted with CH_2Cl_2. The crude product was purified by column chromatography on silica gel using as eluent a mixture of CH_3CN/aqueous KNO_3 solution at 10% of the saturating concentration. The product was obtained after evaporation of the organic solvents, addition of KPF_6-saturated aqueous solution and extraction with CH_2Cl_2. The final compound was dried under vacuum to give a brown solid, Yield: 65% (115 mg). HR-MS (ESI+): m/z calcd for $C_{50}H_{62}N_{10}O_9CuP_2S$ 551.6591; found 551.6584 $[M-H_2O-PF_6]^{2+}$ and m/z calcd for $C_{50}H_{61}N_{10}O_9CuP_2S$ 1102.3109; found 1102.3102 $[M-H_2O-PF_6]^+$. E.A.: calcd for $C_{50}H_{63}N_{10}O_{10}CuP_3SF_6$ + 1.2 KPF_6: C, 44.46; H, 4.70; N, 10.37; found: C, 44.47; H, 4.74; N, 9.83.

T1P-Co

T1P-Cu (80 mg, 0.06 mmol) and $CoCl_2.6H_2O$ (100 mg, 0.42 mmol) were solubilized in acetone (10 ml) and stirred under air bubbling for two days. The solution was evaporated under vacuum and the solid was purified by column chromatography on silica gel using as eluent a mixture of acetone/water/aq. saturated KBr solution (94/5/1). The organic solvents were evaporated under vacuum, yielding a precipitate. The dark orange precipitate was filtered, washed with water and diethyl ether and dried under vacuum to obtain the expected product as solid. Yield: 50% (40 mg). ^{1}H NMR (CD_3CN, 300 MHz): δ (ppm) 19.32 (s, 1H), 8.35 (s, 1H), 8.00 (s, 1H), 7.73 (d, *J* = 3.7 Hz, 2H), 7.59 (d, *J* = 8.8 Hz, 2H), 7.25 (m, 4H), 7.04 (d, *J* = 8.0 Hz, 4H), 6.96 (d, *J* = 8.7 Hz, 2H), 5.77 (t, *J* = 11.0 Hz, 1H), 4.64-4.43 (m, 6H), 4.04-3.95 (m, 8H), 3.17 (s, 2H), 3.09 (s, 2H), 2.59 (s, 6H), 2.54 (s, 6H), 1.22 (t, *J* = 7.0 Hz, 12H). ESI-MS: m/z 549.3 $[M–2Br]^{2+}$, 1179.1 $[M–Br]^+$. HR-MS (ESI+): m/z calcd for $C_{50}H_{61}N_{10}O_9CoP_2S$ 549.1570; found 549.1564 $[M-2Br]^{2+}$. E.A.: calcd for $C_{50}H_{61}N_{10}O_9CoP_2SBr_2$ + 10.3 acetone: C, 52.32; H, 6.66; N, 7.54; found: C, 52.98; H, 5.99; N, 7.56.

3) Synthesis of T2RP-Cat1

Based on the promising activity of the new dyads based on **Cat1** (**T1-Cat1** and **T2R-Cat1**) for PEC proton reduction (**Chart IV.2**) and in order to further compare the stability of the different anchoring groups (carboxylate vs phosphonate) with more active systems, the functionalization of the most efficient dyad (**T2R-Cat1**) with methyl phosphonate anchoring groups was an objective during my PhD. In the following scheme, the synthetic procedure to obtain **T2RP-Cat1** is presented. Unfortunately, the last step to perform the metal-templated synthesis was not successful. Different experimental conditions were employed (solvents, reaction time, temperature), but we could not isolate our final dyad. Nevertheless, due to time limitation, the synthesis of this dyad was not a priority.

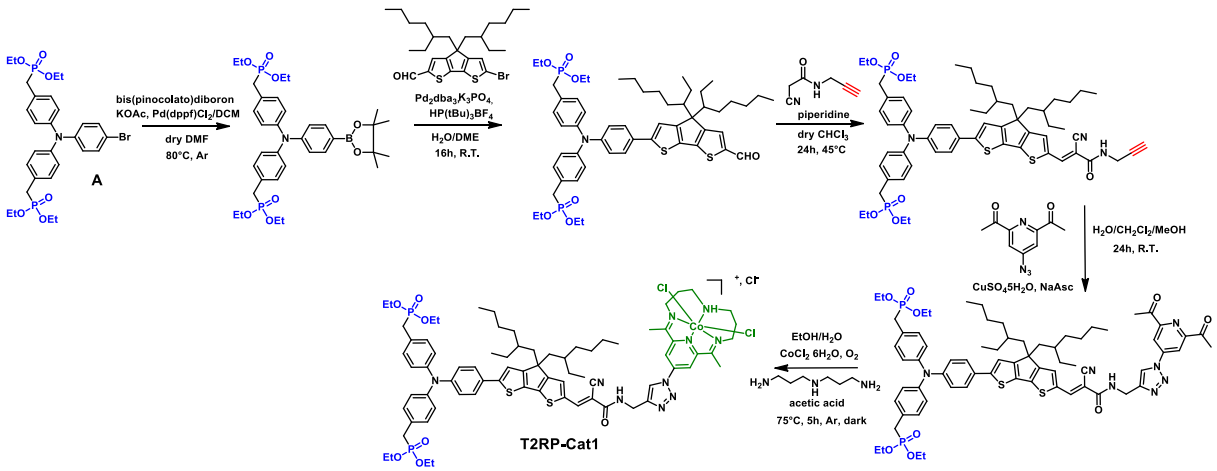

As a perspective, an alternative approach could be followed. As already explained in Chapter IV, the hydrolysis of the phosphonate groups in **T2RP-Cat1** and **RuP$_4^{OH}$-Cat1**, could be the main issue for the isolation of the final dyads. Thus, the template synthesis of the cobalt catalyst could be performed using first a precursor without the phosphonate anchors. The last reaction would be the Knoevenagel condensation to couple the dye with the catalyst, as presented below.

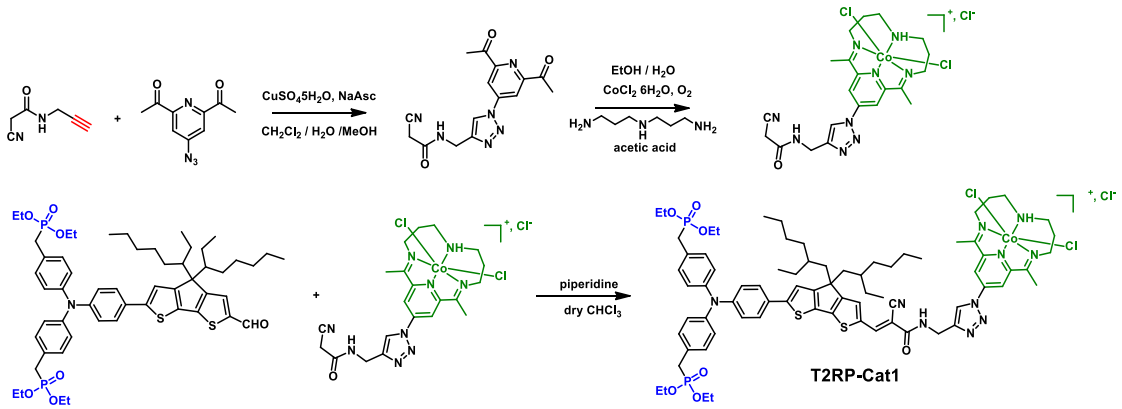

IV. Publications related to the PhD thesis project

P1. *Synthesis of Ruthenium Tris-Diimine Photosensitizers Substituted by Four Methylphosphonate Anchoring Groups for Dye-Sensitized Photoelectrochemical Cell Applications*

N. Queyriaux, **E. Giannoudis**, J.-F. Lefebvre, V. Artero, M. Chavarot-Kerlidou*

European Journal of Inorganic chemistry, 2019

DOI: 10.1002/ejic.201900151

P2. *A cobalt tetraazomacrocyclic catalyst as a game changer for hydrogen production at dye-sensitized NiO photocathodes*

S. Bold, J. Massin, **E. Giannoudis**, M. Koepf, V. Artero, B. Dietzek,* M. Chavarot-Kerlidou*

Submitted for publication.

P3. *Synthesis and Characterization of a Covalent Porphyrin-Cobalt Diimine-Dioxime Dyad towards Photoelectrochemical H_2 Evolution*

A. Charisiadis, **E. Giannoudis**, Z. Pournara, A. Kosma, V. Nikolaou, G. Charalambidis, V. Artero, M. Chavarot-Kerlidou,* A. G. Coutsolelos*

Submitted for publication

P4. *Key insights into the performances of a novel H_2-evolving NiO photocathode based on a ruthenium dye – cobalt diimine dioxime catalyst assembly*

E. Giannoudis, S. Bold, C. Müller, N. Queyriaux, J. Bruhnke, S. Kupfer, C. Gablin, D. Leonard, D. Aldakov, C. Saint-Pierre, D. Gasparutto, V. Artero, B. Dietzek, M. Chavarot-Kerlidou*

Manuscript in preparation.

Résumé en français des travaux

L'énergie est l'outil le plus important des communautés modernes afin de faciliter leur vie quotidienne avec une consommation d'énergie mondiale annuelle d'environ 18 TW, qui devrait atteindre 43 TW en 2100. L'économie énergétique moderne repose sur les combustibles fossiles qui causent de graves problèmes environnementaux (changement climatique, fonte des calottes polaires, pollution de l'air, baisse de la biodiversité) en raison de leur combustion qui produit du dioxyde de carbone. Ce fait, associé à l'épuisement des combustibles fossiles en raison de leur utilisation continue, a contraint la communauté scientifique à trouver des alternatives basées sur des sources d'énergie renouvelables et abondantes, comme le solaire, la géothermie, l'énergie éolienne, etc. (**Figure 1**).

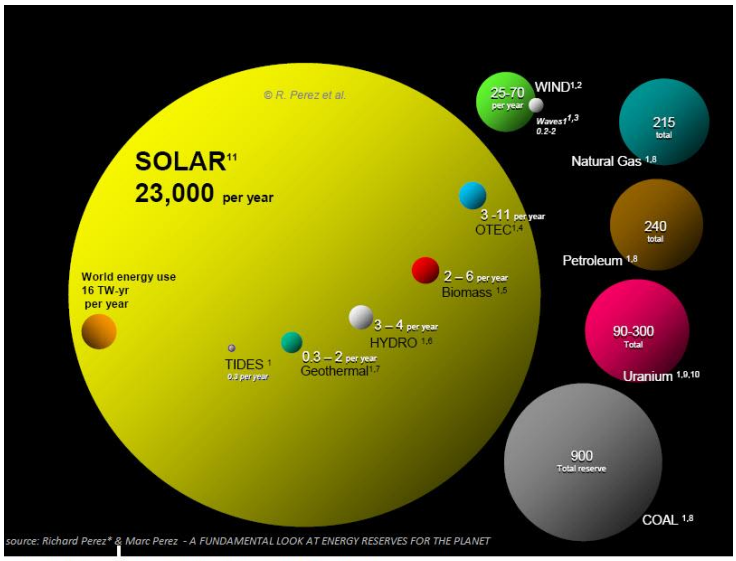

Comparing finite and renewale planetary energy reserves)Terawatt-years).
Total recoverable reserves are shown for the finate resources.

Figure 1. Réserves énergétiques totales (sources d'énergie renouvelables et combustibles fossiles).

L'énergie solaire est extrêmement avantageuse, car la source d'énergie la plus abondante. Le soleil délivre sur terre en environ une heure, la même quantité d'énergie que nous utilisons actuellement en un an. Malheureusement, l'énergie solaire est intermittente et diffuse. Ainsi, il est urgent de trouver un moyen de stocker et de convertir cette source d'énergie inépuisable. La photovoltaïque est une technologie existante mature pour capter la lumière du soleil et la convertir en électricité.

L'électricité peut répondre aux besoins énergétiques immédiats. Cependant, il ne peut pas être stocké. Pour parvenir à un stockage à long terme de l'énergie solaire, différentes approches

ont été proposées. Le convertir en une forme chimique, comme un carburant, semble être un moyen prometteur et il est absolument nécessaire en raison de l'infrastructure technologique actuelle. Les carburants qui peuvent être produits directement ou indirectement par l'énergie solaire par des réactions photo-, thermo- ou électrochimiques sont appelés carburants solaires. Utiliser l'énergie solaire pour leur production est un défi de taille et les scientifiques s'inspirent du processus naturel le plus courant, la photosynthèse.

Dans la nature, il existe de nombreux organismes photosynthétiques, comme les algues, les cyanobactéries et les plantes, appelés photoautotrophes, qui sont capables de synthétiser la biomasse directement à partir du dioxyde de carbone et de l'eau en utilisant l'énergie du soleil. Ils utilisent les électrons photogénérés pour réduire le dioxyde de carbone et produire des glucides via le cycle de Calvin, qui sont les réserves énergétiques de la cellule. De plus, certaines cyanobactéries et microalgues sont capables de réduire les protons en hydrogène, à l'aide d'enzymes appelées hydrogénases. Toutes ces transformations sont réalisées grâce à une étonnante machinerie biologique, présentée schématiquement sur la **Figure 2**, constituée de deux grands complexes protéiques, le photosystème I (PS I) et le photosystème II (PS II), assistés par divers cofacteurs redox et enzymes.

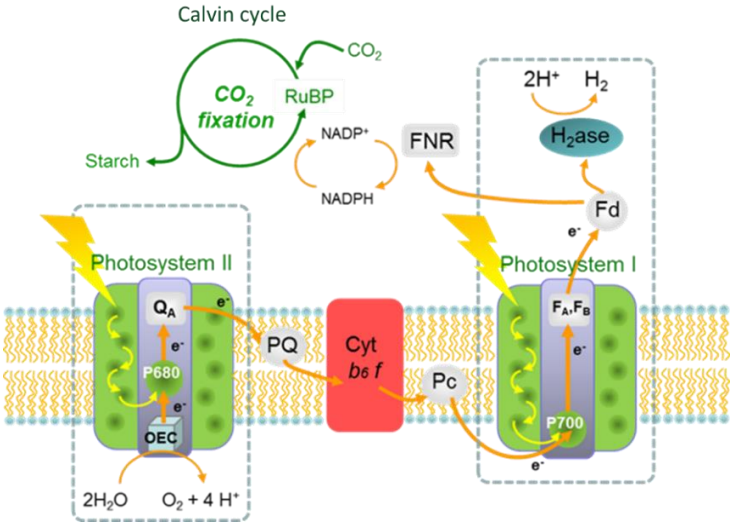

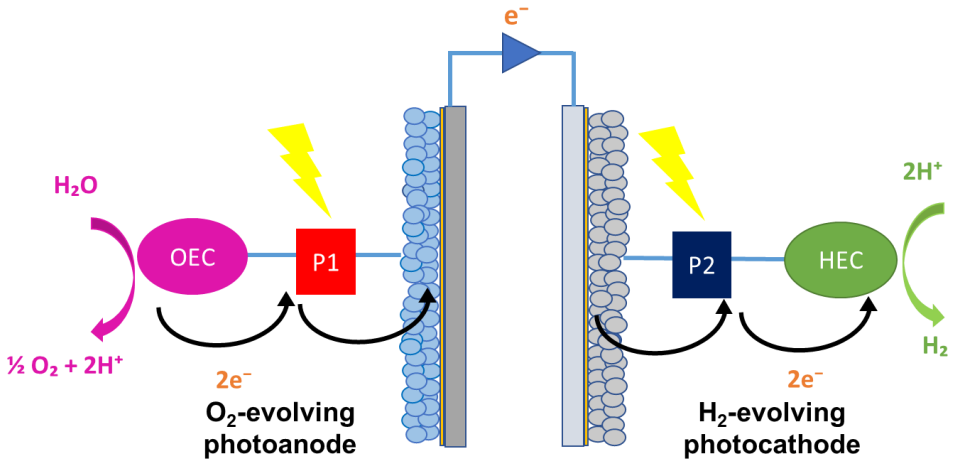

Figure 2. Représentation schématique du processus photosynthétique naturel (en haut) et cellule photoélectrochimique de division de l'eau, DSPEC (en bas). Les cubes correspondent aux collecteurs de lumière (P1, P2) et les sphères à l'oxygène ou aux catalyseurs dégageant de l'hydrogène (OEC, HEC) en conséquence.

La communauté scientifique tente d'imiter le mécanisme de base de la photosynthèse (photosynthèse artificielle) qui se compose de trois étapes élémentaires:

- récupération initiale de la lumière grâce à des photosensibilisateurs moléculaires situés au PSII et au PSI
- transferts d'électrons couplés au proton entre les cofacteurs redox pour réaliser une séparation de charge à longue durée de vie
- catalyse redox multielectronique impliquant des enzymes et des cofacteurs spécifiques (OEC au PSII, RuBP, hydrogénases, etc.)

En prenant la photosynthèse comme modèle, trois grandes approches existent pour produire des énergies solaires: les systèmes photocatalytiques homogènes utilisant des colloïdes, le photovoltaïque couplé à l'électrolyse et les cellules photoélectrochimiques. Ces systèmes présentent différents degrés de maturité technologique et de coût de fabrication. Cellule photoélectrochimique sensibilisée à un colorant (DSPEC, **Figure 2**), qui combine une photoanode par analogie avec le PSII, où l'oxydation de l'eau a lieu pour alimenter en électrons et protons la photocathode (similaire au PSI), où la réduction des protons (ou dioxyde de carbone) se produit, a gagné une attention accrue de la part des chimistes moléculaires. Une première preuve de concept a été faite en 1972, comprenant une photoanode de TiO_2 et du Pt comme contre-électrode. Depuis lors, de nombreux efforts de différents groupes de recherche

ont été consacrés à la préparation de photoanodes et de photocathodes sensibles aux colorants fonctionnels séparément. Comprendre les principes qui régissent l'activité et optimiser les performances de chaque composant ouvrira la voie à la préparation d'un DSPEC compétent.

Jusqu'à aujourd'hui, le goulot d'étranglement d'un appareil DSPEC complet en termes de performances est la partie photocathode. En ce sens, au cours de ma thèse, je me suis concentré sur la construction de photocathodes sensibilisées aux colorants pour le dégagement d'hydrogène. Ce travail s'inscrit dans la continuité de ce qui a déjà été fait dans le groupe «SolHyCat» du Laboratoire de Chimie et Biologie des Métaux. Sur la base de l'expertise précédente du laboratoire, les principaux objectifs de mon projet de doctorat étaient:

- Comparer l'efficacité de différents collecteurs de lumière (P2) et unités catalytiques (HEC) pour des photocathodes à dégagement d'hydrogène
- Pour aborder la stabilité des photocathodes à base moléculaire en effectuant une analyse post-operando

Dans le premier chapitre, nous présenterons les principes des photocathodes à colorant pour la production d'hydrogène. Ensuite, la contribution du groupe à ce champ sera mise en évidence. Nous montrerons un catalyseur au cobalt qui a été utilisé pour le premier assemblage de colorant-catalyseur covalent et sans métal noble et des modèles de photocathodes à base de complexes de ruthénium. Ensuite, les exemples déjà rapportés de photocathodes fonctionnelles seront analysés, y compris les travaux du groupe. Enfin, des chiffres de mérite seront présentés pour tous les différents systèmes, ainsi que les limitations actuelles.

Dans le deuxième chapitre, la synthèse et la caractérisation d'un nouvel assemblage colorant-catalyseur constitué d'un photosensibilisateur au ruthénium fonctionnalisé avec des groupements méthylphosphonate et d'un catalyseur au cobalt diimine-dioxime seront démontrées.

Le troisième chapitre est dédié à l'évaluation de l'activité photoélectrochimique pour le dégagement d'hydrogène d'une photocathode NiO en milieu aqueux sensibilisé par la première dyade. Une caractérisation post-operando pour étudier le destin de nos composants moléculaires sera réalisée.

Le quatrième chapitre se concentrera sur la préparation d'un deuxième assemblage colorant-catalyseur avec le même photosensibilisateur et un complexe cobalt tétraazomacrocyclique différent comme catalyseur.

Dans le dernier chapitre, la deuxième dyade sera examinée pour la réduction des protons dans les mêmes conditions expérimentales avec la première photocathode pour comparaison

directe. En outre, des tentatives préliminaires d'utilisation de notre nouvel assemblage colorant-catalyseur pour la réduction du dioxyde de carbone PEC seront présentées.

Abstract

Production of solar fuels in water splitting dye-sensitized photoelectrochemical cells is a highly promising approach in order to fulfill future energy demands and to face the environmental problems arising from the combustion of fossil fuels. Our group previously constructed NiO-based dye-sensitized photocathodes for H_2 evolution, based on the first covalent organic dye-catalyst assemblies. Here, we report the synthesis and characterization of two novel dyads, both relying on a ruthenium tris-diimine photosensitizer covalently linked via copper-catalyzed azide-alkyne cycloaddition (CuAAC) to two different H_2-evolving cobalt catalysts. The H_2-evolving photoelectrochemical activities of the resulting photocathodes were assessed under standardized conditions. This allowed us to establish that *i*) the dyads based on a Ru photosensitizer outperform the previous ones relying on push-pull organic dyes; *ii*) replacing the cobalt diimine-dioxime catalyst previously employed by the group by a more robust cobalt tetraazamacrocyclic catalyst was crucial to improve the activity, with the highest TON so far reported for hydrogen-evolving dye-sensitized photocathodes. Transient absorption spectroelectrochemical measurements revealed that the performances are limited by the low efficiency of the electron transfer from the reduced dye to the catalytic unit. In addition, long-term stability is strongly affected by the desorption of the dyads from the surface of the electrode during the course of the photoelectrochemical tests. Finally, promising preliminary results were also obtained for photoelectrochemical CO_2 reduction to CO in aqueous medium, thus opening interesting perspectives in the field.

Résumé

La production de carburants solaires dans des cellules photo-électrochimiques à colorant réalisant la photodissociation de l'eau est une approche extrêmement prometteuse pour répondre aux futures demandes énergétiques et faire face aux problèmes environnementaux liés à l'utilisation de combustibles fossiles. Au laboratoire, de premières photocathodes de production d'hydrogène à colorant ont été construites, basées sur le premier assemblage colorant-catalyseur covalent sans métal noble. Dans ces travaux, la synthèse et la caractérisation de deux nouveaux assemblages colorant-catalyseur est décrite, tous deux reposant sur le même photosensibilisateur de ruthénium lié de façon covalente via une cycloaddition azoture-alcyne catalysée au cuivre (CuAAC) à deux catalyseurs de cobalt différents. Les activités photo-électrochimiques de production d'hydrogène des photocathodes correspondantes ont été déterminées dans des conditions standardisées. Ceci nous a permis d'établir que *i*) les dyades à base de ruthénium surpassent celles précédemment décrites à base de colorants organiques ; *ii*) remplacer le catalyseur diimine dioxime de cobalt précédemment utilisé dans le groupe par un catalyseur tétraazamacrocyclique de cobalt s'est révélé crucial pour améliorer l'activité, et a permis d'obtenir les TONs les plus élevés à ce jour pour des photocathodes de production d'hydrogène à colorant. Des caractérisations spectroscopiques avancées ont révélé que les performances sont limitées par le manque d'efficacité du transfert d'électrons du colorant réduit vers le catalyseur. Par ailleurs, la stabilité est fortement impactée par la désorption de la dyade de la surface de l'électrode au cours des tests photo-électrochimiques. Enfin, de premiers résultats préliminaires sur la réduction photo-électrochimique du CO_2 en CO en milieu aqueux ont été obtenus et ouvrent des perspectives intéressantes dans le domaine.